# Investigation of heat conduction through PMC components made using resin transfer moulding

Aymen Sakka

A thesis submitted to the Faculty of Graduate and Postdoctoral Studies in partial fulfilment of the requirements for the Degree of

**MASTER OF APPLIED SCIENCE**

In Mechanical Engineering

Ottawa-Carleton Institute for Mechanical and Aerospace Engineering

University of Ottawa

Ottawa, Canada

August 2012

# Abstract

The increasing demand for polymer matrix composites (PMCs) from the airframe industry raises the issues of productivity, cost and reproducibility of manufactured PMC components. Performance reproducibility is closely related to the manufacturing technique. Resin transfer moulding (RTM) offers the advantage of flexible manufacturing of net-shape PMC components with superior repeatability starting from ready-to-impregnate dry reinforcements. An RTM apparatus was developed for manufacturing PMC plates and demonstrator components representative of actual, PMC components and PMC moulds made and used in the airframe industry. The RTM process developed in this work involved making net-shape dry carbon fibre preforms and impregnating them an epoxy resin, targeting mould applications. Thermal repeatability of different net-shape PMC components manufactured using the RTM apparatus developed in-house was investigated. Effects of bonding an outer copper plate onto the PMC material, targeting mould applications known as integrally heated copper tooling (IHCT), were explored. Heat conduction through the PMC components was studied using simulation models validated by experimental data obtained primarily by thermography. Manufactured PMC components showed good repeatability, particularly in terms of thermal behaviour. The IHCT technique was found to be well suited for mould applications. Expected advantages of thermography were materialised. Finally, the simulation models developed were in good agreement with experimental data.

# Dedication

I would like to dedicate this thesis to my mother, who, through her patience and unwavering support throughout all my education, made this experience worthwhile. Words can barely express my gratitude to her unbounded devotion.

# Acknowledgments

I am grateful to my supervisor, Dr. François Robitaille, for his guidance, encouragement and patience throughout this research. He consistently allowed this thesis to be my own work along with encouraging me to push the boundaries of excellence.

Foremost, I would like to thank my mother and my family whose firm support, patience and belief in me strengthened my motivation for accomplishing my education goals.

My appreciations go to fellow graduate students Andrew Stewart and Scott Audette for their contribution to the design of the RTM setup. I owe many thanks to the advanced composite lab group, Reza Samadi in particular, for their unending help and support. I sincerely appreciate Dr. Mohammed Yandouzi who helped me with the optical microscopy and SEM. Many thanks go to those whose names are not mentioned but who contributed through support or friendship.

# Table of contents

# List of figures

# List of tables

# Chapter 1: Background and motivation

## 1.1. Introduction

Composite materials are defined as engineered materials composed of two or more phases that remain distinct at the macroscopic level. They typically involve two constituents, the reinforcement and the matrix, which by adequate synergism may lead to enhanced material properties. The outcome material offers usually a high strength-to-weight ratio with the reinforcement supplying the strength and stiffness and the matrix transferring the load to the reinforcement.

Polymer-matrix composites (PMCs) in particular are becoming a driving force in the development of technology, especially in the aerospace industry. The airframe industry's continuous demand for higher performance-to-cost ratios has ushered in the development of more mature manufacturing processes. Resin transfer moulding is a promising manufacturing method that offers major advantages over competing methods including its cost, capability of producing complex net-shape 3D components with good surface finish, full control of fibre placement which can be tailored to the load bearing requirements, and thorough control over resin volume fraction.

## 1.2. Literature review

### 1.2.1. Polymer-matrix composites

#### 1.2.1.1. Polymer-matrix composites for aerospace

Polymer-matrix composite materials (PMCs) have a wide variety of applications due to their unique structural and thermal properties. The main characteristics of PMCs include a high

strength-to-weight ratios, non-corrosiveness, high electrical resistance and electromagnetic transparency. PMCs are available in various types with properties depending essentially on the nature and configuration of the reinforcement, on the resin used and on the manufacturing process. Reinforcements come in three basic types: particulates, short fibres and continuous fibres. The matrix or resin used in the PMC partly determines its possible applications, especially with regards to the maximum temperature that the material can withstand [1]. Carbon fibre reinforced PMCs used in airframe construction are manufactured by embedding carbon fibres in a matrix constituted of a polymeric resin, typically thermosetting. Whilst aerospace PMC parts are typically made from prepreg, dry carbon fibre fabric reinforcements are also used for making aerospace-grade composites, notably for making PMC moulds. Fibre preforms can be produced by several techniques including weaving, braiding, knitting and stitching [2].

PMCs can also be classified according to the type of polymer matrix used. Matthews and Rawlings [3] state that thermosetting matrix like epoxies, polyesters and phenolics are the most used in industry followed by thermoplastics such as polyether ether ketone (PEEK) and polyphenylenesulfide (PPS). Thermosetting polymers are long-chain molecules that cure by cross-linking to form a fully three-dimensional network.

Composites can be manufactured in different ways depending upon matrix, reinforcement and application. Manufacturing processes include hand-lay-up, resin transfer moulding (RTM), vacuum-assisted resin transfer moulding (VARTM), resin film infusion (RFI), pultrusion and filament winding [2]. Some processes relevant to this thesis are discussed further in the text.

#### 1.2.1.2. Reinforcements and resins for PMCs

A dry preform is a manufactured assembly of long carbon fibres making either a flat sheet or a shape defined in 3D, featuring typically one or more stratified layers of fibres. These layers can

be held together using textile manufacturing techniques such as knitting, weaving and braiding. Chemical binders are also used in some cases. Fabrics can be categorized according to the orientation of fibres and the method used for holding the fibres together, Figure 1.1.

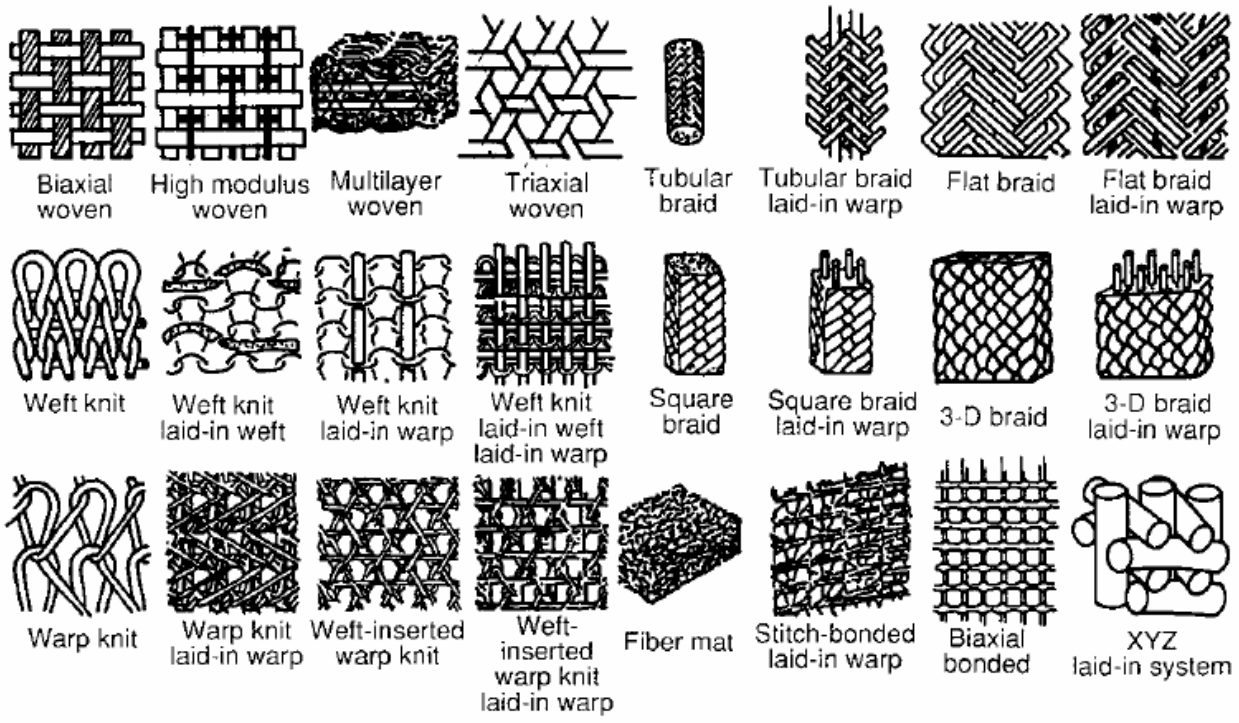


Figure 1.1: Diverse types of dry reinforcements and preforms [4]

Woven fabrics made from carbon fibre tows are commonly used in the aerospace industry. There are three prevalent types of woven fabric reinforcements: plain, twill and satin fabrics. The weave is made of warp fibres that run in the direction of the loom and weft fibres that are normal to the direction of the warp. In a plain weave the weft passes over alternate warp threads requiring two harnesses only, while a twill weave is made by causing weft threads to interlace two to four warp threads.

Non-crimp fabrics (NCFs) are made of fibres that are held straight and in-plane by light, stitched

or knitted thermoplastic polymer threads, typically nylon or polyester, or sometimes by light threads of strong fibre such as glass, aramid or carbon. In non-crimp fabrics, in-plane alignment of carbon fibres is closer to optimal in terms of stiffness and strength, Figure 1.2. Because of the non-crimped configuration of the yarns, laminates using NCF exhibit improved in-plane properties compared to laminates using woven or braided fabrics [5].

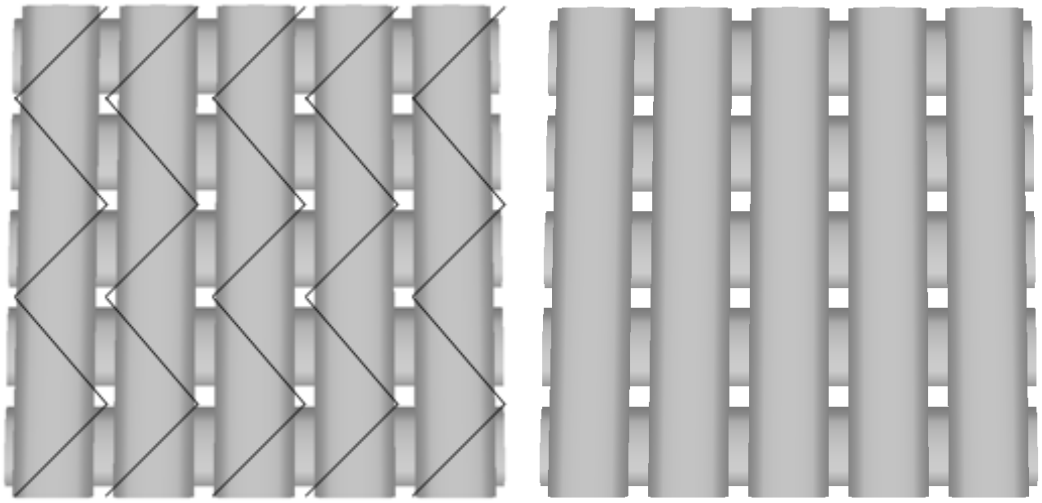

Figure 1.2: Schematic of a NCF structure (left) and plain-weave structure (right)

Stitching techniques are highly flexible production methods for manufacturing complex dry preforms. Their main benefit resides in the delivery of ready-to-impregnate dry preforms which dramatically reduce the cost of manufacturing PMC components using RTM or VARTM. Stitching refers to the operation of inserting a needle carrying a thread, through stratified fabric layers, assembling them into a 2D or a 3D dry preform, Figure 1.3. Regular stitching machines using lock-stitch technique can be used for stitching NCF dry preforms; more sophisticated equipment designed specifically for carbon fibre performs was also developed. Some use computer-controlled robotic stitching heads that are capable of stitching complex 2D and 3D dry preforms and can be adjusted for optimising the sewing parameters for improved overall PMC component properties [6]. Amongst the many stitching techniques, lock-stitch is widely used for

preform engineering [6]. As the stitch geometry should accommodate the application of a given PMC component, lock-stitch was modified for preform engineering, to move the interlocking knot between the bobbin thread and the needle thread from the inside of the preform to the outside [7]. Hence, the aggregation of sewing thread between the fibre packages was dramatically reduced. Figure 1.3 shows the geometry of the lock-stitch (a) and modified lock-stitch (b). Making this modification along with setting the proper thread tension was found to prevent the fibres from spreading apart locally, creating resin-rich zones [6, 9].

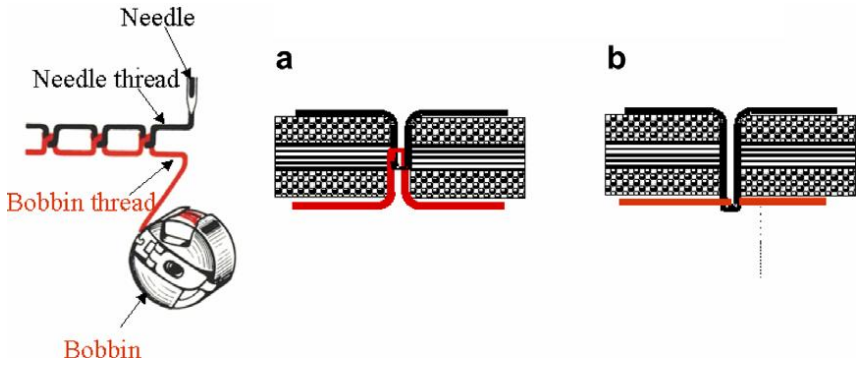


Figure 1.3: Schematic of the lock-stitch geometry modification [7]

Ogale and Mitschang [6] presented a classification of seam types and stitch geometries. Seam types were summarised in three categories; fixing and positioning seams, assembly seams and joining seams, Figure 1.4. Fixing and positioning seams are useful in the production of 3D net-shape preforms. They are intended for making tailored sub-preforms with minimised fray and fibre wrinkling, as well as precise contours. The assembly seams aim at facilitating mould loading and the injection process by attaching the sub-preforms to make the final net-shape dry preform. Joining seams are also known as structural seams [5]. The choice of parameters such as seam pattern and density, presser-foot pressure and thread material permits to make dry preforms with improved through-thickness properties [10]. Seam types or combinations of types can be selected to tailor the ready-to-impregnate dry preform to the final PMC product [6]. The choice of a seam type can also be influenced by the preforming technique, handling process and RTM process compatibility [10]. Commercially available 100% polyester sewing thread is highly

suitable for fixing and positioning seams applications. Recent advances in preforming technology boosted stitching speed using polyester thread up to 5000 stitches/min [6]. A classification of the seam types, their corresponding application and thread tensions appears in Figure 1.4.

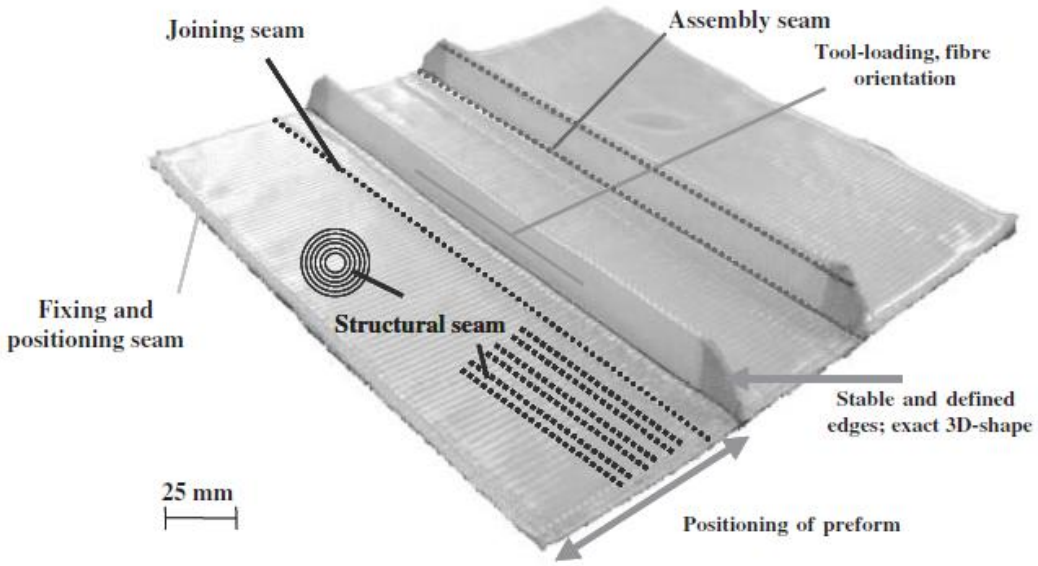


Figure 1.4: Schematic summarising seam types [10]

Table 1.1: Different seam types according to their application and required thread tensions [9]

| Seam type | Application | Thread tension |
|---|---|---|
| Fixing and positioning | 2D preforming | Moderately low |
| Assembly | 2D/3D assembling | Medium to high |
| Structural | 3D reinforcement | High |

NCFs have been found suitable for making complex shapes with relatively less fabric wrinkling than plain weave preforms, due to lower in-plane shear forces allowed by the loops of knitted stitches for deformations perpendicular to the seam [10]. However, stitching induces problems

such as gaps and local in-plane fibre and tow dislocations leading to resin-rich pockets in the laminate [5]. These dislocations affect the mechanical properties, fatigue behaviour and impregnation behaviour of the dry NCF preform [10]. However, they are limited in size and do not form continuous channels where the resin can race-track [11]. Loendersloot et al. [11] presented a geometrical analysis of NCFs subjected to shear deformation. The study focused on the effect of shear deformation as the main deformation mode of draped fabrics on the stitch-induced local tow dislocations (LTDs). Several fabrics were analysed for unveiling the dependence of the width and length of the LTDs as a function of the shear angle, up to 60°. The authors found that increasing the in-plane shear on a given dry preform results in fibre bundle compaction rather than a change in the dimensions of LTDs. Dry preform compaction was found to be an effective remedy to the problems caused by LTDs. Subjecting dry preforms to high pressure compaction cycles was proven to reduce the size of LTDs considerably, by reorganising the fibre network [7]. Compaction of dry preforms can also reduce the void content inside the PMC laminate [13].

#### 1.2.1.3. General properties of PMCs

PMCs are increasingly used in the aerospace industry due to their good specific structural properties and high strength-to-weight ratios obtained by incorporating strong, stiff but brittle fibres bonded by a polymer matrix. Chung [1] listed other advantageous properties of PMCs; the main structural advantages are the low density, high strength, high stiffness, an almost infinite life under fatigue loading, creep and corrosion resistance, toughness and damage tolerance. In addition to its main role as a medium to transfer loads to the fibres which carry most of the applied load, the matrix protects the fibres from the external environment. Their low process temperatures and capability to be put into a given shape, are also important advantages of PMCs.

Carbon fibres are made from organic precursors processed through different manufacturing steps including carbonisation, graphitization, surface treatment and sizing [14]. These precursor materials are primarily polyacrylonitrile (PAN), coal tar pitches, rayon and petroleum. Based

mainly on strength and stiffness, carbon fibres can be classified into three main categories: high modulus (HTM, Type I), high strength (HTS, Type II) and intermediate modulus (ITM, Type III). Typical properties of commercially available carbon fibres are summarized in Table 1.2.

Table 1.2: Typical properties for the major types of commercial carbon fibres [1]

| Property | HTM, Type I | HTS, Type II | ITM, Type III |
|---|---|---|---|
| Specific gravity | 1.9 | 1.8 | 1.8 |
| Tensile modulus (GPa) | 267-380 | 228-241 | 296 |
| Tensile strength (MPa) | 2415-2555 | 3105-4555 | 4800 |
| Ultimate strain (%) | 0.6-0.7 | 1.3-1.8 | 2 |
| Coefficient of thermal expansion ($\times 10^{-6}$ /mm K) | -0.7 | -0.5 | N/A |
| Axial thermal conductivity (W/m K) | 64-70 | 8.1-9.3 | N/A |
| Electrical resistivity ($\mu\Omega$ m) | 09-10 | 15-18 | N/A |

The high strength and moduli of PMCs depend not only on the properties of fibres but also on their orientation, fibre volume fraction and quality of bonding to the matrix. Good bonding between fibres and resin is required for obtaining an effective reinforcement.

#### 1.2.1.4. Selected PMC manufacturing processes

To make PMC components using any of the liquid moulding processes, dry preforms are infused by the polymer resin and the wetted component is cured; fibres are bonded to the matrix to make the composite part. PMC components made with thermosetting resins can be “staged”, meaning

that the resin can be retained in a partially cured condition, within temperature and pressure ranges specified by the supplier. Another advantage of thermosetting resins is that the manufacturing of composite components can be conducted at relatively low temperatures and pressures as thermosetting polymers exhibit low viscosities especially at increasing temperatures, prior to the cross-linking process.

The most widely used thermosetting resins for aerospace-grade PMCs are epoxies. Epoxies have excellent mechanical properties, high tensile strength and modulus. With an adequate sizing applied to the fibres, epoxies bond very well to the reinforcement. Epoxy PMCs cured at temperatures of 120°C and 180°C have upper limit service temperatures of 100°C and 130°C - 150°C respectively [2]. Epoxies offer similar stiffness and strength qualities as thermoplastics, as shown in Table 1.3, but offer lower prices and are more convenient processed.

Table 1.3: Stiffness and strength data for main aerospace-grade resins [15]

| Resin material | Density ($g/cm^3$) | Tensile modulus (GPa) | Tensile strength (MPa) |
|---|---|---|---|
| Epoxy | 1.2-1.4 | 2.5-5.0 | 50-110 |
| PEEK | 1.3-1.35 | 3.5-4.4 | 100 |
| PPS | 1.3-1.4 | 3.4 | 80 |

PMCs made from pre-impregnated (Prepreg) semi-products, typically tape, are extensively used in primary load-bearing aircraft components. Such components are often consolidated in autoclave using PMC moulds that may be built using reinforcements such as those discussed in this thesis; the process requires the use of a mould to impart a shape to the PMC component. Prepreg increases reproducibility and consistency, especially control of fibre volume fraction, thickness and mechanical properties of the composite component.

Prior to their use, frozen prepreg tapes are unrolled then thawed to room temperature whilst protected from condensation in a bag. The backing film is removed and the prepreg is laid on the surface of a mould. Prepreg material is laid up in different directions to account for loads expected on the part. Prepreg lay-up is often automated in the aerospace industry but hand lay-up is also in use, especially in small production lines. After laying up all the prepreg sheets in the required directions, the assembly is vacuum-bagged then put inside an autoclave under an inert gas, Figure 1.5. A combination of high pressure and temperature profiles is used for shaping and curing the PMC component. Autoclave curing of PMC parts is a traditional technique in the aerospace industry. It allows for the manufacturing of parts with high dimensional accuracy and very low void content with very high fibre volume fractions. All these advantages combined with high processing temperatures leading to high glass transition temperatures, make autoclave manufacturing the preferred technique for aerospace-grade PMC production. However, high costs due to prepreg expensive equipment and long cure cycles time constitute disadvantages of the process.

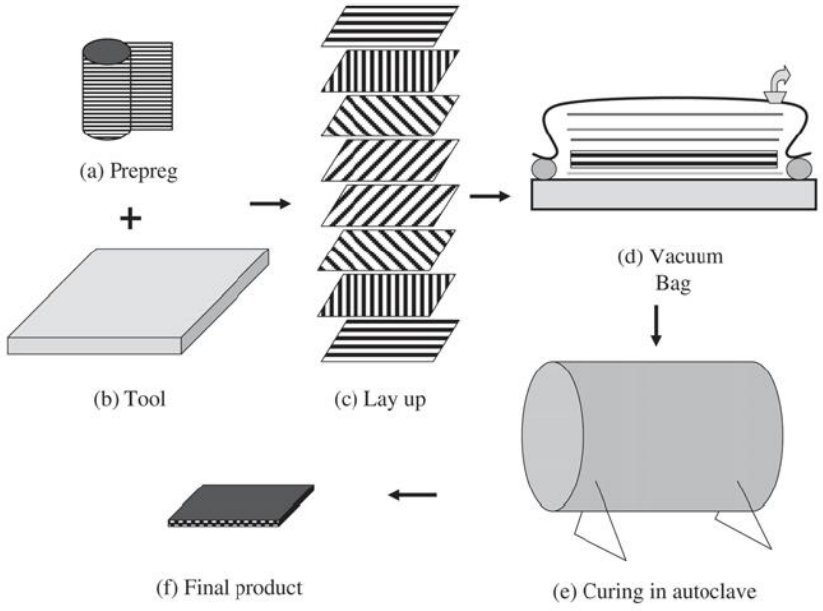


Figure 1.5: Autoclave manufacturing process [16]

Resin transfer moulding (RTM) is a liquid moulding process using a cavity made of a male and a female half moulds. RTM involves injecting a thermosetting liquid resin in the mould cavity loaded with a dry preform [17], Figure 1.6. The mould and the resin are typically pre-heated before injection. Epoxies reach a low resin viscosity stage after heating, which translates in a lower resistance to the flow of resin through the dry preform. This advantage of epoxies over thermoplastic resins like PEEK, leads to fully impregnated carbon fibre preforms requiring lower injection temperatures and pressures. However, attention must be paid to the pre-heating temperature of the resin since high temperatures may lead to premature cross-linking of the epoxy. After saturating the preform with resin and expelling air from the cavity, curing is initiated. Optimal resin pre-heating temperature, injection time and mould temperature depend mainly on the resin used [2]. After the resin is cured, the finished composite component can be de-moulded.

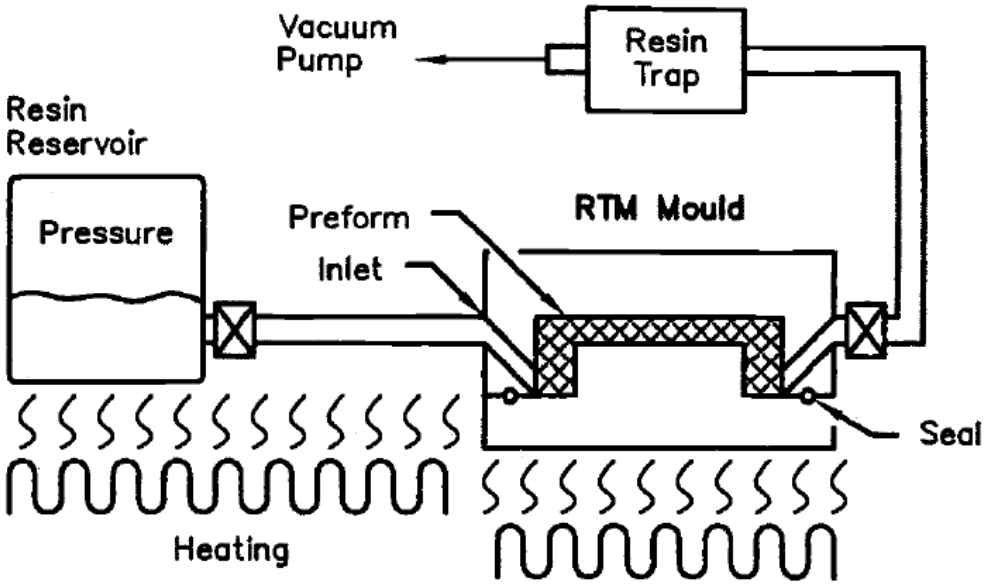


Figure 1.6: Schematic of a typical RTM process [2]

RTM is highly sensitive to the preforming process, impregnation and curing method [18]. Manufacturing good, aerospace-grade PMC components requires the successful filling of the

mould cavity and expulsion of entrapped air. Changes in preform architecture, local preform deformation and mould curvatures have dramatic effects on mould filling. Injection pressures were found to be dependent on parameters such as the mould corner radii [18]. Post-impregnation processes involve curing the PMC component as described earlier in this section, followed by de-moulding of the final product. The de-moulding operation can cause strains and even defects during component removal from the mould cavity. Hence, when making aerospace grade composites, ease of demoulding must be considered during component and mould design [19].

RTM offers excellent dimensional control, high quality surface finish on both surfaces of the part, good bonding between the matrix and the fibres, and repeatability in manufacturing [2]. These advantages are highly sought in the airframe industry. Another asset of RTM is its good compatibility with net-shape production [10,20]. Adding net-shape preform manufacturing to a RTM process makes it more effective as quick and accurate loading of a net-shape, fault-free preform inside the mould cavity renders the single shot resin impregnation task uncritical [10].

### 1.2.2. Heat conduction in PMCs

#### 1.2.2.1. Heat conduction theory

This section introduces fundamental concepts and equations which govern heat transfer by conduction and natural convection. Heat conduction occurs within a medium at a molecular scale from regions of high temperatures to regions of lower temperatures. It is governed by Fourier's law (Equation 1.1):

$$\boldsymbol{q} = -\boldsymbol{K}(T)\boldsymbol{\nabla} T \qquad 1.1$$

where **q** is the heat flux vector through the medium, **K** is the thermal conductivity tensor and **∇**T is the temperature gradient vector. The thermal conductivity serves as a quantitative indicator of the ease of heat transfer through a solid material. It is influenced by temperature [21].

Transient conductive heat transfer through PMCs is the main interest of this thesis. It is of relevance to airframe manufacturers as changes in temperatures within composite components in service as well as during manufacturing must imperatively be taken into account, because of their ability to alter the mechanical behaviour of the material. The transient heat transfer problem is governed by Equation 1.2:

$$\frac{\partial}{\partial t}\left(\rho\, C_p T\right) = \nabla(\boldsymbol{K}\boldsymbol{\nabla} T) + \dot{q} \qquad 1.2$$

For an orthotropic material, the three dimensional transient heat conduction problem with no internal heat source can be described by Equation 1.3:

$$\rho C_p \frac{\partial T}{\partial t} = \frac{\partial}{\partial x}\left(K_x(T)\frac{\partial T}{\partial x}\right) + \frac{\partial}{\partial y}\left(K_y(T)\frac{\partial T}{\partial y}\right) + \frac{\partial}{\partial z}\left(K_z(T)\frac{\partial T}{\partial z}\right) + \dot{q} \qquad 1.3$$

where $K_x$, $K_y$ and $K_z$ are the directional thermal conductivities of the orthotropic material in the x, y and z directions respectively, ρ is the density, $C_p$ is the specific heat of the material and $\dot{q}$ is the rate of heat generated within the material.

Thermal conductivity and specific heat are temperature dependant. Unlike thermal conductivity, specific heat in PMCs does not have directional dependency. To solve Equation 1.3 for a composite material, the specific heat must be known. For a two-phase composite material the

specific heat can be calculated using the rule of mixtures given by Equation 1.4 [22]:

$$\rho C_p = \rho_f V_f C_{pf} + \rho_m (1 - V_f) C_{pm} \quad 1.4$$

where $\rho_f$, $\rho_m$ and $C_{pf}$, $C_{pm}$ are the fibre and matrix densities and the fibre and matrix specific heat, respectively. $V_f$ is the fibre volume fraction in the laminate.

Perturbation to the temperature field resulting from a discontinuity in the material is termed thermal contact resistance. Perfect contact between two solid materials cannot be achieved due to microstructures present at the interface. The reciprocal of thermal resistance is called thermal conductance. The thermal resistance can be obtained from Equation 1.5:

$$R_c = \frac{\Delta T}{q} \quad 1.5$$

where $\Delta T$ is the temperature difference across the interface and q is the heat flux. $R_c$ units are in $m^2K/W$.

Thermal stresses arise in airframe sub-units consisting of a set of PMC components fixed rigidly together. Thermal expansion is a major cause of internal thermal stresses in PMCs. Thermal stresses induced by thermal expansion within PMC components result from a considerable mismatch in values between the coefficients of thermal expansion (CTEs) of the reinforcement and the matrix, from a non-balanced laminate, or from resin-rich zones [2,23]. Thermal stresses

can also appear in the vicinity of bonded joints between dissimilar materials such as PMC components with different inherent properties, or PMC and metallic parts [24-26]. The CTE describes the unit change in length L of a material as a response to a change in temperature. It is a directional property in the case of PMCs. The linear CTE, $\alpha_L$, is given by Equation 1.6 [21].

$$\alpha_L = \frac{1}{L}\frac{dL}{dT} \qquad 1.6$$

#### 1.2.2.2. Analytical and numerical models for predicting thermal conductivity of PMCs

Numerical simulations of heat transfer are widely used in aerospace design for predicting the thermo-mechanical behaviour of PMC components and hence, to assess the reliability, durability and integrity of a given aircraft structural PMC component [27]. Carbon fibre manufacturing processes mentioned in section 1.2.1.3 lead to an orthotropic arrangement of the material's microstructures within carbon fibres [28]. Consequently, thermal properties of carbon fibres are orthotropic and so are those of continuous fibre-reinforced PMCs. This fact stems from the isotropy of polymers and the orthotropic nature of carbon fibres. Analytical and/or numerical models for predicting the effective thermal conductivity of PMCs are then required [29]. Knowledge of the thermal properties of orthotropic laminated composite materials and of their variability is crucial to performing accurate predictive numerical simulations of temperature maps and thermal stresses in PMC components [27]. The thermal conductivity of an orthotropic composite material depends on the nature of the resin, fibre type, reinforcement architecture, fibre volume fraction, manufacturing technique, direction of heat flow and operating temperature. These factors lead to a high degree of complexity in understanding the thermal behaviour of PMCs.

Heat transfer through PMCs was not investigated as thoroughly as their structural behaviour or manufacturing [30]. For thermally stable post-cured thermosetting laminates, changes in

properties with temperature can be considered reversible up to the point where decomposition of one of the phases, usually the resin, begins. This thesis covers temperature ranges below the glass transition temperature of the resin. In other cases of heat transfer through PMCs, such as exposition to fire, it is necessary to consider major changes in thermal properties beyond the glass transition temperature [30].

Generally, analytical and semi-empirical thermal conductivity prediction models require the thermal conductivity of the carbon fibre and resin as an input. Nevertheless, data for thermal conductivities of commercially available carbon fibres are scarce in the literature [31] and they are seldom supplied by manufacturers. Direct measurement of the thermal conductivity of carbon fibres is intrinsically difficult. The trend has been to carry out thermal conductivity measurements on PMC samples, and then back-calculate the thermal conductivity of the fibres. This method presents the advantage of enabling the assessment uncertainties introduced by the back-calculation of fibres conductivity, as opposed to data supplied by manufacturers which most likely used similar but unknown assumptions, introducing uncertainty on real values.

Pilling et al. [32] proposed a model for predicting the transverse thermal conductivity of carbon fibres, which was found to overestimate this property, Equation 1.7. This model uses the transverse thermal conductivity of PMC samples obtained by direct measurement to back-calculate the fibre data:

$$K_{ft} = \frac{K_m(1-V_f) - K_2(1+V_f)}{\frac{(1-V_f)K_2}{K_m} - (1+V_f)} \qquad 1.7$$

where $K_{ft}$ is the transverse thermal conductivity of the fibre, $K_2$ is the through-thickness thermal

conductivity of the PMC, $K_m$ is the thermal conductivity of the resin and $V_f$ is the fibre volume fraction.

Al-Sulaiman et al. [33] developed a correlation model predicting the transverse thermal conductivity of fibres as a function of the thermal conductivity of PMCs and their matrix. The model was based on the parallel thermal model and accounted for void content in PMCs, Equation 1.8. It was validated using finite element analysis. Polynomial coefficients $C_i$ were introduced in creating two sub-models validated over $V_f$ ranging from 0.30 to 0.75 and thermal conductivity ratios $K_f/K_m$ ranging from 0.5 to 5.0. The coefficients were function of fibre and void volume fractions:

$$\frac{K_{ft}}{K_m} = C_0 + C_1\left(\frac{K_{fp}}{K_m}\right) + C_2\left(\frac{K_{fp}}{K_m}\right)^2 + C_3\left(\frac{K_{fp}}{K_m}\right)^3 \quad 1.8$$

where $K_{fp}$ is the transverse thermal conductivity of the fibre using the parallel model.

Simulating conduction in a PMC component for specific application cases requires approximation of the orthotropic material as a homogeneous medium, in the sense that fibre distribution in the resin is considered macroscopically homogeneous. Other assumptions to be made are negligible thermal contact resistance between fibres and resin, and low operation temperatures enabling radiation heat transfer to be neglected. Different analytical approaches for calculating and predicting the thermal conductivity of a PMC are presented in this section.

The rule of mixture (ROM) is a simple way of modelling the thermal conductivity of unidirectional PMCs along the axis of the fibres. The ROM, Equation 1.9, was thoroughly

validated for on-axis thermal conduction in unidirectional composites [31-32,34]:

$$K_1 = V_f \times K_{fa} + \left(1 - V_f\right) \times K_m \quad 1.9$$

where $K_1$ is the axial in-plane conductivity of the composite material and $K_{fa}$ is the axial conductivity of the fibres.

PMCs exhibit discontinuity in the transverse direction. Numerous models were developed for predicting the transverse conductivity of PMCs. Most make assumptions regarding the fibre packing geometry in the laminate. Fibres are generally assumed to pack following a specific pattern which is not the case in real PMCs where the continuous fibres pack randomly. A widely applied model for predicting the transverse thermal conductivity of unidirectional PMCs was developed in analogy to electrical circuits where the components, here the fibres and resin, are connected in parallel [35]:

$$K_2 = \frac{K_{ft} K_m}{V_f K_m + \left(1 - V_f\right) K_{ft}} \quad 1.10$$

where $K_2$ is the transverse thermal conductivity of the composite and $K_{ft}$ is the transverse thermal conductivity of the fibres.

Thornburgh and Pears [34] predicted the transverse conductivity of unidirectional dual-phase composites by using a simple series model, giving a lower limit expressed by Equation 1.11:

$$K_2 = \left(V_f/K_{fa} + \left(1 - V_f\right)/K_m\right) \quad 1.11$$

An upper limit for the value was given by James et al. [36], Equation 1.12. Although the thermal conductivity model is for a two-phase composite material in the direction transverse to the fibres, a matrix volume fraction coefficient ($V_m$) was introduced to account for the void content. $V_m$ is to be adjusted to fit results obtained by experiments.

$$K_2 = V_m K_m\left(1 - V_f\right) + \frac{\left(V_f + (1-V_m)\left(1-V_f\right)K_f K_m\right)}{\left(V_f K_m + (1-V_m)\left(1-V_f\right)K_f\right)} \quad 1.12$$

Springer and Tsai [37] developed an expression for the transverse thermal conductivity of unidirectional composites based on the analogy between the longitudinal shear loading and heat transfer equations. This analogy allowed for the application of the same numerical method used for solving. Geometrical configurations considered fibres in square packing with square cross-sections, and fibres in square packing with circular cross-sections. An analogy between the response of a unidirectional composite to longitudinal shear loading and heat transfer equations lead to the following system of equations; expressions for the effective conductivity for square fibre cross-section and for cylindrical fibres in a square array are given by Equations 1.13 and 1.14, respectively [38]. Zinmeister et al. [39] showed that the model is accurate only at high $V_f$ with relatively low transverse conductivity PAN fibres.

$$K_2 = K_m\left[\left(1 - \sqrt{V_f}\right) + \frac{1}{\sqrt{\frac{1}{V_f} + \frac{B}{2}}}\right] \quad 1.13$$

$$K_2 = K_m \left( 1 - 2\sqrt{\frac{V_f}{\pi}} + \frac{1}{B}\left[ \pi - \frac{4}{\sqrt{1-\left(\frac{B^2 V_f}{\pi}\right)}} \, Tan^{-1} \frac{\sqrt{1-\frac{B^2 V_f}{\pi}}}{1+\sqrt{\frac{B^2 V_f}{\pi}}} \right] \right) \quad 1.14$$

where

$$B = 2\left(\frac{K_m}{K_{ft}} - 1\right) \quad 1.15$$

Halpin and Tsai [35] reached the following approximation for the transverse conductivity $K_2$ of unidirectional composites. The model was devised theoretically by analogy with electrical circuits with the assumption of fibres with uniform cross-section arranged in parallel. Fibres were assumed to have an elliptical cross-section. This approximation is known to give good predictions up to a $V_f$ of 60% [35]:

$$K_2 = K_m \left[ \frac{1+ \xi \, \eta \, V_f}{1- \eta \, V_f} \right] \quad 1.16$$

$$\eta = \frac{(K_{fa}/K_m)-1}{(K_{fa}/K_m)+\xi} \quad 1.17$$

$$\xi = \sqrt{3} \, log \frac{a}{b} \quad 1.18$$

where a/b is the aspect ratio of the cross-sectional dimensions of the fibre, a along the direction of heat conduction and b transverse to it. ξ equals to unity for circular or square fibres.

Nielsen [40] considered the effect of aggregation of fibres into yarns, in the sense that the reinforcement is considered to be made of yarns with potential resin rich zones between them. This reinforcement configuration can lead to large variations in local thermal properties of the composite component [31], whilst the overall transverse thermal conductivity may not show large variations. Also, for the same fibre volume fraction, the effective transverse conductivity variation is narrow for different yarn packing schemes. The semi-empirical model for transverse conductivity is given by Equation 1.19. The model accounts for the effect of the shape of the fibre cross-section as well as for its orientation:

$$K_2 = K_m \left[\frac{1+A\ B\ V_f}{1-B\ \varphi\ V_f}\right] \tag{1.19}$$

where A is a constant determined by the direction of the heat flow and $V_{f,max}$ is the maximum volume fraction given as a function of the type of packing:

$$A = K_e - 1 \tag{1.20}$$

where $K_e$ is the generalized Einstein coefficient. B and φ are given by equations 1.21 and 1.22, respectively.

$$B = \frac{\frac{K_f}{K_m}-1}{\frac{K_f}{K_m}+A} \tag{1.21}$$

$$\varphi = 1 + \left(\frac{1-V_{f,max}}{{V_{f,max}}^2}\right) V_f \qquad 1.22$$

For uniaxially oriented fibres with heat flow perpendicular to the fibres, A = 0.5 and $V_{f,max}$ = 0.82. According to Progelhof et al. [35], results given by Clayton [41] and Nielsen [40] are close. However, in the author's attempt to validate these models using published experimental data, a strong conclusion was not reached for continuous unidirectional fibres since experimental data enabling robust validation could not be sourced.

Hashin [14] extended the shear property approach into the cylindrical assemblage model which was developed based on random packing of composite cylinders. These consisted in an inner cylinder representing the fibre surrounded by an outer cylindrical shell representing the matrix. The combined concentric cylinders were assumed to be transversely isotropic and continuous. The packing pattern was formed by randomly filling the entire cross-sectional area of a given domain with non-overlapping composite cylinders of varying radii. The overall volume of voids was taken into account and consequently the summation of $V_f$ and $V_m$ does not equal to unity. The ratio of radii of the concentric cylinders was considered to be constant. A mathematical analogy was made between the axial shear problem and the transverse conductivity. This analogy accounted for the transversely isotropic phases of fibres and resin in unidirectional PMCs, leading to the following equation for transverse conductivity:

$$K_2 = K_m \left[\frac{K_m V_m + K_{ft}(1+V_f)}{K_m(1+V_f) + K_{ft} V_m}\right] \qquad 1.23$$

Grove [42] combined a finite element analysis model and spatial statistical techniques to model the case of a real PMC with random fibre packing. Figure 1.7 shows a comparison of the

variation of relative thermal conductivity with fibre volume fraction, between results of the pure finite element model and the combined model. The combined model gave lower effective transverse conductivities for fibre volumes fractions up to 50%. Differences between values were found to be significant especially at higher fibre volume fractions. The maximum difference in values was found to range between 7% and 8%.

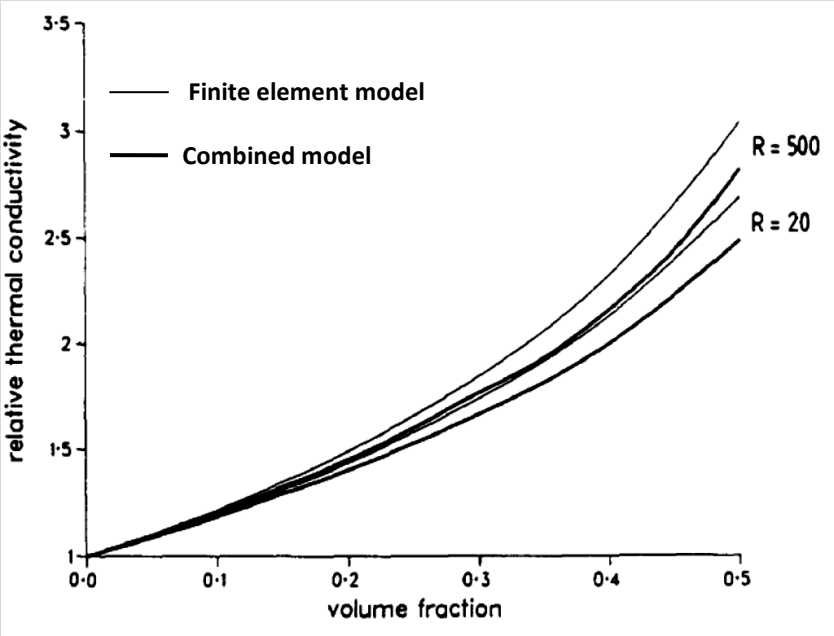


Figure 1.7: Relative transverse composite thermal conductivity, $K_2/K_m$, as a function of fibre volume fraction for values of $R = K_f/K_m$ of 20 and 500 [42]

Dasgupta et al. [31] validated experimentally and numerically the semi-empirical closed-form model presented by Clayton [41] and given by Equation 1.24. Model validation was done at the micro-scale for a plain-weave fabric PMC. Their 3D steady-state finite element model was applied on a quarter of a unit cell; the principal in-plane axes of the laminate coincided with the warp and fill directions, and the resin-impregnated yarns had a thermal behaviour similar to that of unidirectional composites. Equation 1.24 was found to be in good agreement with experimental values for transverse conductivities of unidirectional composites [31].

$$K_2 = \frac{K_m}{4}\left[\sqrt{\left(1-V_f\right)^2\left(\frac{K_{ft}}{K_m}-1\right)^2+\frac{4K_{ft}}{K_m}}-\left(1-V_f\right)\left(\frac{K_{ft}}{K_m}-1\right)\right]^2 \quad 1.24$$

Hasselman et al. [43] considered the interfacial thermal contact resistance in defining the effective transverse thermal conductivity of the composite material. The numerical model, given by Equation 1.25, was devised using the shear loading analogy for unidirectional PMCs. The model assumed circular fibres completely covered with the matrix, accounting for the radius of the fibre and its anisotropy in the transverse direction, by introducing radial and tangential conductivities $K_r$ and $K_\theta$ respectively:

$$K_2 = K_m\left[\frac{\left(\frac{\sqrt{K_rK_\theta}}{K_m}+\frac{\sqrt{K_rK_\theta}}{rC}+1\right)+V_f\left(\frac{\sqrt{K_rK_\theta}}{K_m}-\frac{\sqrt{K_rK_\theta}}{rC}-1\right)}{\left(\frac{\sqrt{K_rK_\theta}}{K_m}+\frac{\sqrt{K_rK_\theta}}{rC}+1\right)+V_f\left(\frac{\sqrt{K_rK_\theta}}{K_m}-\frac{\sqrt{K_rK_\theta}}{rC}+1\right)}\right] \quad 1.25$$

where r is the radius of the fibre and C is the contact thermal conductance between the fibres and matrix. Mirmira and Fletcher [44] modified this model to include the effect of porosity of the PMC on the predicted transverse thermal conductivity:

$$\frac{K_2}{K_m} = \left[\frac{\left(\frac{\sqrt{K_rK_\theta}}{K_m}+\frac{\sqrt{K_rK_\theta}}{rC}+1\right)+V_f\left(\frac{\sqrt{K_rK_\theta}}{K_m}-\frac{\sqrt{K_rK_\theta}}{rC}-1\right)}{\left(\frac{\sqrt{K_rK_\theta}}{K_m}+\frac{\sqrt{K_rK_\theta}}{rC}+1\right)+V_f\left(\frac{\sqrt{K_rK_\theta}}{K_m}-\frac{\sqrt{K_rK_\theta}}{rC}+1\right)}\right]\left(1-V_p\right)^2 \quad 1.26$$

where $V_p$ is the porosity volume fraction.

Lim [29] developed an analytical model based on the boundary solution method for predicting the upper and lower bounds of thermal conductivity of a composite material with random reinforcement phase geometry. The model includes a reinforcement parameter which depends on the reinforcement aspect ratio and conductivity directionality. The parameter ranges between 0 and 1 in general and takes values of 1 and 0.5 for a unidirectional continuous fibre composite in the longitudinal and transverse directions, respectively. Even though the model used a highly idealised geometry, verification with experimental data showed its good applicability even at a high $K_f/K_m$ ratio. These upper and lower limits of the transverse conductivity are given by Equations 1.27 and 1.28, respectively:

$$K_{2l} = K_m \left\{ 1 - V_f^{0.5} \left[ 1 - \frac{1}{1 - V_f^{0.5}\left[1 - \frac{K_m}{K_f}\right]} \right] \right\}^{-1} \quad 1.27$$

$$K_{2u} = K_m \left\{ 1 - V_f^{0.5} \left[ 1 - \frac{1}{1 - V_f^{0.5}\left[1 - \frac{K_f}{K_m}\right]} \right] \right\}^{-1} \quad 1.28$$

where $K_{2l}$ and $K_{2u}$ are the lower and upper bounds of the transverse thermal conductivity, respectively.

Models predicting the transverse thermal conductivity of PMCs described earlier in this section are compared in Figure 1.8. The ratio of the transverse thermal conductivity to the thermal conductivity of the matrix was plotted against the $V_f$. A value of 500 was set for the ratio of the

transverse thermal conductivity of carbon fibres to the thermal conductivity of the matrix. $V_f$ values ranged from 0.3 to 0.7. The predictive models of Hasselman et al. [43] and James et el. [36] were omitted from this comparison as their expressions could not be expressed in terms of $K_2/K_m$ only.

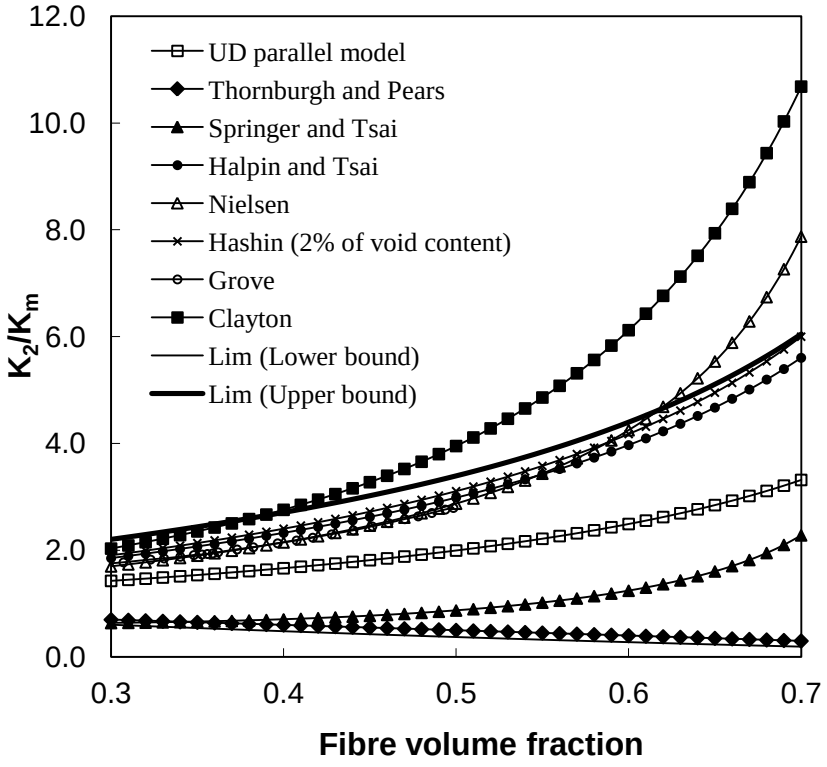


Figure 1.8: Comparison of transverse thermal conductivity ratio for different prediction models

Models given by Hashin [14], Halpin and Tsai [35], Nielsen [40] and Grove [42] exhibited good concordance throughout a $V_f$ range from 0.3 to 0.6. They slightly under-estimated Lim's upper bound model for transverse thermal conductivity ratio $K_2/K_m$, reaching a thermal conductivity ratio of 4.2. Nielsen's model exhibited a relatively fast increase in the thermal conductivity ratio after a $V_f = 0.6$, reaching a value of 7.87 at $V_f = 0.7$ compared to a value of roughly 6.4 reached by the Hashin, Halpin and Tsai and Grove prediction models. Nielsen's model also exceeded Lim's upper bound model over the same $V_f$ range. Clayton's prediction model matched Lim's

upper bound model values up to $V_f = 0.4$, then showed a relatively fast increase of the transverse thermal conductivity ratio. The parallel model showed a slow increase over the whole $V_f$ range to reach a maximum value of $K_2/K_m$ of about 3.1. Springer and Tsai's predicted conductivity ratios were also similar to the unidirectional parallel model in behaviour with an under-estimation of roughly 1.0. On the other hand, Thornburgh's and Pears's [34] predictive model showed significantly lower values of $K_2/K_m$ but an overall behaviour similar to Lim's lower bound model. It is interesting to note that these two models returned decreasing $K_2/K_m$ values with increasing $V_f$. Again, Lim's models were meant to serve as general prediction tools for all types of composites featuring varied types of reinforcements, and deemed not to be an accurate prediction tool for the transverse thermal conductivity of structural fibre-reinforced PMCs.

#### 1.2.2.3. Experimental determination of thermal properties of PMCs

Analytical and numerical models have been used routinely for predicting the thermal conductivity of PMCs. It can be concluded from the previous section that the trend is to compare and combine analytical and numerical models found in the literature in order to develop a more accurate predictive model. Published experimental thermal conductivity data for carbon fibre PMCs aimed at airframe applications are limited in the literature [45]. Various steady-state and transient measurement methods were developed for determining the thermal conductivity of specific PMCs. Many of these methods are set as standards by the American Society for Testing and Materials (ASTM).

Steady-state methods require long test times for attaining steady-state conditions, but they are suitable for testing low conductivity materials [46]. They can be grouped into two categories, namely absolute methods of measurement in which no heat flux or material reference is required to carry out the thermal conductivity measurement, and comparative test methods in which the thermal conductivity is derived from a heat flux reference standard [47].

The ASTM C177-97 standard method, known as guarded-hot-plate method, uses an absolute steady-state technique based on two flat specimens of the PMC to be tested. A schematic of the general components of a guarded-hot-plate apparatus is shown in Figure 1.9.

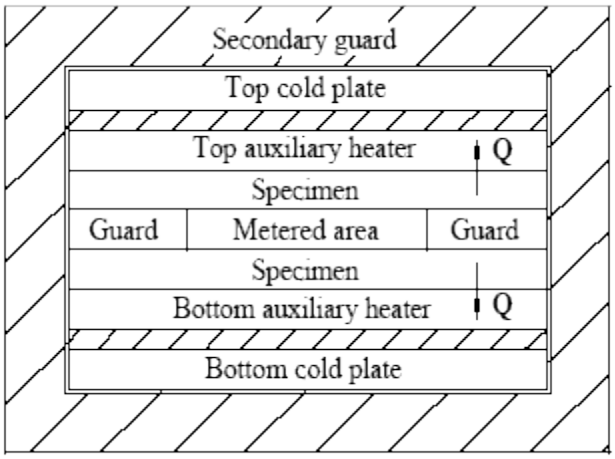


Figure 1.9: Schematic of a guarded parallel plate instrument [47]

The apparatus features two isothermal cold plates and a guarded hot plate, also called the metered section. The metered section generates the heat flux for the test and is surrounded by a thermal guard ring used for directing the heat flux normally through all the components of the assembly, i.e. the metered section, the specimens and the isothermal cold plates. A secondary guard acts as insulation of the apparatus from its surrounding. As the test outcome is an average of the thermal conductivities of the two specimens, these must be as identical as possible with completely flat sides to ensure a normal and uniform heat flow. The two specimens are placed at either sides of the guarded-hot-plate, and a considerable constant clamping force is applied to the guarded-hot-plate apparatus to improve thermal contact between all surfaces of the plates and specimens. Upon reaching steady-state, the unidirectional heat flow and temperature difference between the hot and cold plates are recorded. Hence, the average thermal conductivity of the specimens can be calculated using equation 1.29. A calibration constant is usually added to account for parameters which may affect the heat flux in the vicinity of the metered section area.

It is important to note that a single-sided configuration of the apparatus is also possible, where a single specimen is squeezed between the guarded hot plate and the isothermal cold surfaces:

$$k = \frac{QL}{A\Delta T} \tag{1.29}$$

where Q is the unidirectional heat flow normal to the specimen, L is the specimen thickness, A is the metered section area and $\Delta T$ is the temperature difference across the specimen.

Amongst numerous ASTM steady-state thermal conductivity measurement methods for PMCs, the guarded longitudinal heat flow method, known as ASTM E1225-99 standard method, is widely used, followed by ASTM C518-98 standard method [47]. Both methods are comparative test methods. The guarded longitudinal heat flow method consists in inserting the PMC specimen subject to high clamping pressure between two similar specimens of a reference material of known thermal properties, termed meter bars. A constant heat flux is imposed through the assembly with lateral heat losses being minimised by a longitudinal guard heater subjected to the same temperature gradient. Once steady-state conditions are reached, the thermal conductivity of the PMC specimen can be derived from established temperature gradients across all the specimens as well the thermal conductivity of the reference materials. ASTM E1225-99 standard method gives very good accuracy for PMCs with thermal conductivities ranging between 0.2 W/mK and 200 W/mK over a temperature range between 10 K and 1300 K, if the areas of specimens in contact are equal and if the thermal conductance of the PMC specimens and reference material are close.

ASTM C518 standard method involves the same setup as ASTM E1225-99 standard method, with added heat flow transducers covering the contact surfaces between specimen and meter

bars. The specimen to be tested is mounted between two meter bars with a high clamping pressure. The measurement starts with imposing constant temperatures on the meter bars; a cold meter bar at a low temperature and hot meter bar at a higher temperature. Upon establishment of a steady-state unidirectional heat flow through the stack, the heat flow is obtained from the transducers and the thermal conductivity of the specimen, as calculated using Equation 1.29. For good measurement accuracy, the standard requires very limited lateral heat losses and a thermal resistance of the specimen greater than 0.10 $m^2K/W$ in the direction of the heat flow [47]. Opting for a specific measurement method generally depends on the directionality of the thermal conductivity to be measured, but ASTM C177 standard method is generally preferred to ASTM E1225 standard method for both in-plane and out-of-plane thermal conductivity measurements [47].

Among transient techniques, the laser-flash method has been used widely and validated as accurate for the thermal conductivity of PMCs [46]. Parker et al. [48] were the first to describe the flash method. Taylor et al. [49] applied the laser-flash method to evaluate the thermal diffusivity of PMCs. The laser-flash method consists of a light source, a furnace and an IR detector, Figure 1.10.

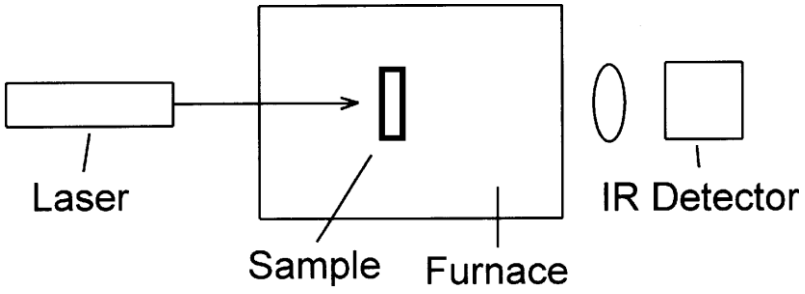


Figure 1.10: Schematic diagram for the laser-flash measurement system [46]

A high intensity laser pulse hits the front face of the material specimen generating heat at the surface. The heat flows to the back face of the specimen where the temperature rise is sensed

using an infrared detector. Solving the heat equation with the initial condition of an instantaneous laser pulse for a specimen of thickness L leads to the following equation for the thermal conductivity [50]:

$$K = \frac{1.38\ \rho\ C_p L^2}{\pi^2 t_{1/2}} \tag{1.30}$$

where K is the thermal conductivity, $C_p$ the specific heat of the specimen and $t_{1/2}$ is the time taken for the back face of the specimen to reach one half of its maximum temperature.

The main advantage of this technique is the absence of contact between the heater, detector and sample. Thermal contact resistance issues are eliminated and relatively high temperatures can be used. However, attention should be given to radiation penetration through the specimen, which can reach the back face and affect the results. Also, temperatures at the front face have to be kept below the glass transition temperature of the PMC to prevent distortions in results [46]. The laser-flash method is commonly used for both fibre orientations and offers the convenience of shorter testing times and smaller specimen sizes [47].

Searle's bar and Lees' disc systems are transient measurement methods that have been widely used for measuring the thermal conductivity of both highly and poorly conductive materials, respectively [51-54]. Pilling et al. [32] used Searle's bar system and Lees' disc system for determining the in-plane and through-thickness thermal conductivities, respectively, of various PMCs by heating one end of the specimens and measuring the temperature gradient along them. The thermal conductivity can be derived from the temperature gradient and the time at which temperatures are recorded. Schematics of both apparatus are presented in Figure 1.11 and Figure 1.12.

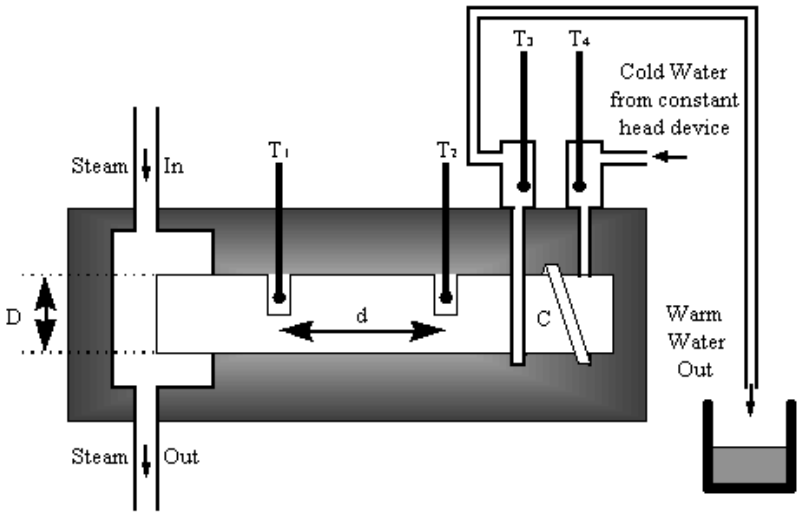


Figure 1.11: Schematic of Searle's bar apparatus [55]

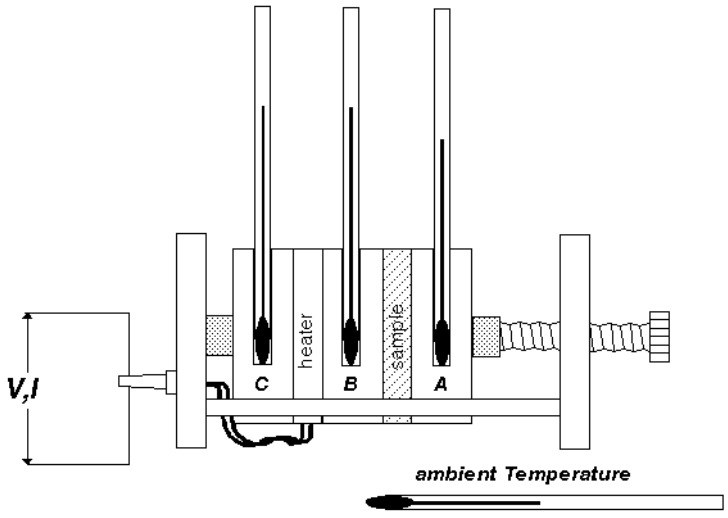


Figure 1.12: Schematic of Lee's disk apparatus [56]

Transient hot-wire techniques use the time-dependent temperature increase in a very thin metallic wire, generally platinum, after the onset of a heating current, to measure the thermal conductivity of a material specimen. This method allows for the absolute determination of

thermal conductivity of the tested material, i.e. without the need for a reference material, Figure 1.13 [57]. The conductivity can be determined directly from the slope of the plot of temperature increase as a function of the logarithm of time [46]. This method was found to offer high accuracy with less than 1% uncertainty for in-plane thermal conductivity of PMCs made of macroscopic and nanoscopic reinforcements [57].

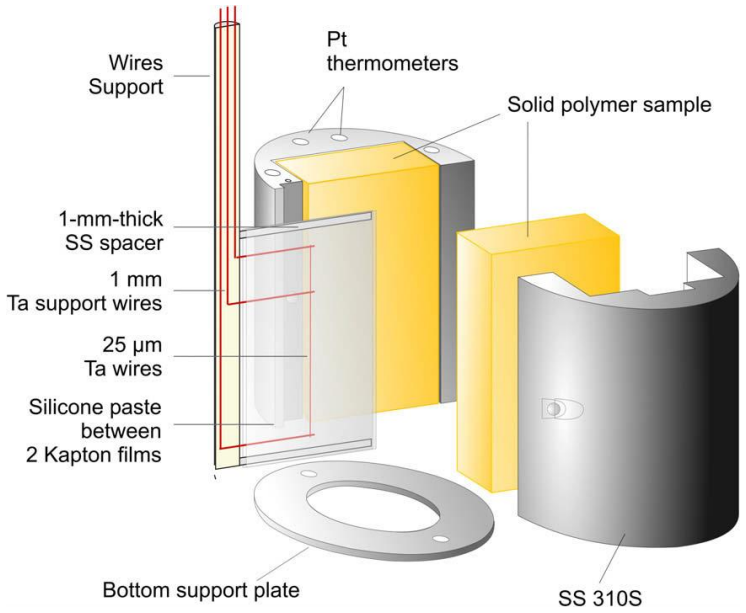


Figure 1.13: Sensor of the transient hot-wire apparatus [57]

The surface probe method is a transient state comparative method used for measuring the in-plane thermal conductivity of a PMC specimen. The probe consists of three parallel strips of a highly conductive material, usually nickel or platinum, connected to an electric circuit ensuring a constant heating rate in the strips. A low electric conductivity backing material is applied to the strips. The two outer strips are kept at constant low and high temperatures. They act as heat guards by keeping the heat flow unidirectional and perpendicular to their plane. The middle strip acts as a sensor. After placing a flat material specimen adjacent to the central strip, a data acquisition system monitors the temperature increase in the central strip. According to the literature [46], this temperature variation depends on the thermal properties of the material being

tested:

$$T \propto \frac{Q\, t^{1/2}}{\left(K\, \rho\, C_p\right)^{1/2}} \qquad 1.31$$

where T is the surface temperature of the sensor, Q is the constant heat flux in the central strip, t is the time, K is the thermal conductivity of the specimen, ρ is the density of the material being tested and $C_p$ its heat capacity. Calibration is required for compensating heat loss to the backing material. Calibration of the system leads to a relationship that links the temperature increase to the elapsed time. The thermal conductivity can be determined from the slope of the plot relating temperature variation to elapsed time.

Other thermal conductivity measurement methods that conform to ASTM standards have been used. Miller et al. [58] compared results for transverse thermal conductivity given by the guarded heat flow method corresponding to ASTM F433 standard method, and a transient plane source method developed by Mathis Instruments (Fredericton, NB, CANADA). The latter method was considered more accurate for in-plane heat conductivity measurements in PMCs. Keith et al. [59] used a Holometrix TCA-300 guarded heat flow meter conform to ASTM F433 standard method for transverse conductivity measurements, whilst a Mathis hot disk thermal analyser was used for measurements in the in-plane direction.

#### 1.2.2.4. Available thermal conductivity data for PMCs and their reinforcements

The thermal properties of carbon fibres were not investigated as thoroughly as their mechanical properties. The thermal conductivity of carbon fibres is usually back-calculated from measurements made on PMCs using analytical or numerical models, as direct measurement of

the effective thermal conductivity of PMCs is more straightforward. Pilling et al. [32] calculated axial conductivities, $K_{fa}$, of diverse HTS and HMS fibres from measurements made on unidirectional composite, using the ROM. Conductivities varied from less than 10 W/mK up to 300 W/mK over temperatures ranging from 80 K to 270 K. The transverse conductivity, $K_{ft}$, of HTS fibres was determined as 1.7 W/mK, 3.5 W/mK and 10 W/mK at 180 K, 225 K and 270 K respectively. Bigaud et al. [33] predicted thermal conductivities for PAN fibres as $K_{fa}$ = 7 W/mK and $K_{ft}$ = 0.7 W/mK. Gowayed et al. [60] calculated thermal conductivity values of $K_{fa}$ = 6.69 W/mK and $K_{ft}$= 0.53 W/mK for Toho carbon fibres.

The orthotropic nature of the thermal conductivity of carbon fibres was investigated. James et al. [36] reported a $K_{fa}/K_{ft}$ ratio of 60. Dasgupta [31] predicted a ratio of 10 between the axial and transverse conductivity for T300 graphite fibres. Reported values were $K_{fa}$ = 8.40 W/mK and $K_{ft}$ = 0.84 W/mK. Al-Sulaiman et al. [33] measured a transverse fibre conductivity of 1.9 W/mK using photo-thermal microscopy. Al-Sulaiman et al. [33,61-62] discussed the back-calculation method for calculating the thermal conductivity of carbon fibres. Authors found that the accuracy of predicting the thermal conductivity of fibres using a developed correlation improved with decreasing fibre volume fraction. Nevertheless, the developed correlation was deemed valid for industrial applications of PMCs.

Manufacturer's thermal conductivity data for carbon fibres exists but is very limited. It is important to note that most manufacturers do not mention whether the provided conductivity value is in the longitudinal or the transverse direction. A survey of carbon fibre thermal conductivities from literature and manufacturers is summarized in Table 1.4 [63].

Table 1.4: Carbon fibre thermal conductivities from literature and manufacturers [63]

| Fibre | $K_{fa}$ (W/mK) | $K_{ft}$ (W/mK) | Reference |
|---|---|---|---|
| AS | | 26 | Loos and Springer (1983)[64] |
| AS4 | 7.7 | 2.4 | Johnston (1997)[65] |
| AS4 | | 6.8 | Hexcel Corporation (2010a)[66] |
| CN80 | 320 | 11 | Schuster, et al. (2008) [67] |
| IM7 | | 5.4 | Hexcel Corporation (2010c)[68] |
| IM10 | | 6.1 | Hexcel Corporation (2010b)[69] |
| M35J | | 39 | Toray Inc. (2010a)[70] |
| M40J | | 68.6 | Toray Inc. (2010b)[71] |
| M46J | | 84.5 | Toray Inc. (2010c)[72] |
| M50J | | 97.9 | Toray Inc. (2010d)[73] |
| M55J | | 155.6 | Toray Inc. (2010e)[74] |
| M60J | | 151.8 | Toray Inc. (2010f)[75] |
| P-25 | | 26-36 | Cytec Industries Inc. (2003a)[76] |
| P-30 | | 62 | Cytec Industries Inc. (2003b)[77] |
| T300 | | 2.5 | Guo, Du and Zhang, (2005)[78] |
| T300 | 100 | 11 | Schuster, et al. (2008)[67] |
| T300 | | 10.5 | Toray Inc. (2010h)[79] |
| T300J | | 9.3 | Toray Inc. (2005)[80] |
| T-300 | | 5 | Cytec Industries Inc. (2003c)[81] |
| T400H | | 10.5 | Toray Inc. (2005)[80] |
| T650 | 14 | 5 | Cytec Industries Inc. (2003d)[81] |
| T700 | 100 | 11 | Schuster, et al. (2008)[67] |
| T700S | | 9.4 | Toray Inc. (2010i)[83] |
| T800H | | 35.1 | Toray Inc. (2010j)[84] |
| T1000G | | 32 | Toray Inc. (2010g)[85] |
| YS80 | 320 | 11 | Schuster, et al. (2008)[67] |

Pilling et al. [32] used the methods described in section 1.2.2.4 for measuring directional thermal conductivities of unidirectional and bidirectional PMCs. The specimens were made of PAN-based Morganite HMS and HTS carbon fibres reinforced DX210/$BF_3$ 400 epoxy resin. For transverse thermal conductivity measurements, 3 composite specimens were tested with 45.9%, 59.1 % and 71.9% $V_f$ within a temperature range from 175 K up to 270 K. Throughout this temperature range, the transverse thermal conductivity lower bounds were 0.457 W/mK, 0.506 W/mK and 0.746 W/mK. Upper bounds reached 0.607 W/mK, 0.747 W/mK and 1.133 W/mK,

respectively. Axial conductivity of unidirectional HMS and HTS PMCs with $V_f$s of 60.7% and 58.4% respectively, ranged from 9.4 W/mK to 50.6 W/mK in HMS PMC specimens and from 1.55 W/mK to 9.33 W/mK for HTS PMCs, with temperatures varying from 90 K to 270 K. Similar in-plane conductivities along the 0° direction were reported for bidirectional HMS and HTS PMCs laid at [0°/90°] and [45°/45°] throughout the temperature range extending from 80 K to 270 K. Finally, comparison of the results with scarce data found in the literature, using extrapolation and taking into account differences in materials, showed good concordance.

James et al. [36] conducted axial and through-thickness transverse conductivity measurements on GY70 pitch fibre reinforced code 69 resin with $V_f$ = 50% over a temperature range of -183°C to +100°C. A comparative thermal conductivity measurement system was used. The measurement apparatus was essentially based on the guarded heat flow method with squeezing the PMC specimen between two metallic slabs of known thermal conductivity. The materials of known thermal conductivity were used for measuring the heat flow. Values of axial and through-thickness conductivities, $K_1$ and $K_2$, varied from 30 W/mK to 120 W/mK, and from 1.2 W/mK to 1.5 W/mK, respectively.

Scott and Beck [86] presented experimental data for transverse thermal conductivity of AS4/BADGE-mPDA prepreg composite. The effects of temperature and stacking sequence were studied. Two fibre orientations were used, namely unidirectional $[0°]_{24}$ and $[0°/30°/-30°/60°/-60°/90°]_{2s}$. For the unidirectional laminates, through thickness conductivity $K_2$ went from 0.72 W/mK to 0.95 W/mK over temperatures ranging from about 33°C to about 133°C. For the quasi-isotropic laminates, $K_2$ went from 0.64 W/mK to 0.82 W/mK for temperatures ranging from about 25°C to about 80°C. Data scatter was very high at all but the highest temperatures. It should be noted that no information was provided for $V_f$.

Gowayed [60] presented measurements for through-thickness conductivity in plain weave and

3D weave textile epoxy composites. Resin was Ciba-Geigy Araldite epoxy HY 956 with a conductivity of 0.196 W/mK. Holometrix k-Matic 75 apparatus conform to ASTM C518 standard method was used for measurements. AS4 plain weave graphite epoxy composites were made with $V_f$ = 26.8%, 37.5%, 47.1%, 54.0% and 55.7%. Through-thickness conductivity varied between 0.28 W/mK and 0.45 W/mK from $V_f$ = 26.8% to $V_f$ = 55.7%.

Kalogiannakis et al. [87] published thermal conductivity and heat capacity measurements for cross-ply laminates made of Hexcel (Fibredux 920CX-TS-5-42) reinforced epoxy. Tested specimens were presented in terms of thickness and weight. No reference was made to the $V_f$ of the PMCs. Modulated temperature differential scanning calorimetry was applied for studying the thermal conductivity and heat capacity variation over 3 phases: before, at and above the glass transition temperature. Thermal properties were presented for temperatures ranging from -50°C to 125°C. The stage prior to glass transition, which is of interest in this thesis, was identified for all PMC specimens results as a range between -50°C and 77.7°C. Corresponding thermal conductivities and heat capacity ranged from 0.530 W/mK up to 0.627 W/mK and from 0.808 J/gK and 1.091 J/gK.

Sweeting et al. [88] developed an experimental method for determining the in-plane and though-thickness thermal conductivities of polymer composites based on a steady-state method. The directional temperature gradient was recorded using thermocouples, and results were processed numerically by an inverse approach to determine the directional thermal conductivity. Thermal conductivities were provided for Hexcel F593 carbon-epoxy plain weave prepreg laminates with a fibre volume fraction of 49%, cured in an autoclave for 2 hours at 180°C under a pressure of 680 KPa. As shown in Figure 1.14, conductivity varies linearly with temperature, and in-plane conductivities are about four times higher than through-thickness conductivities.

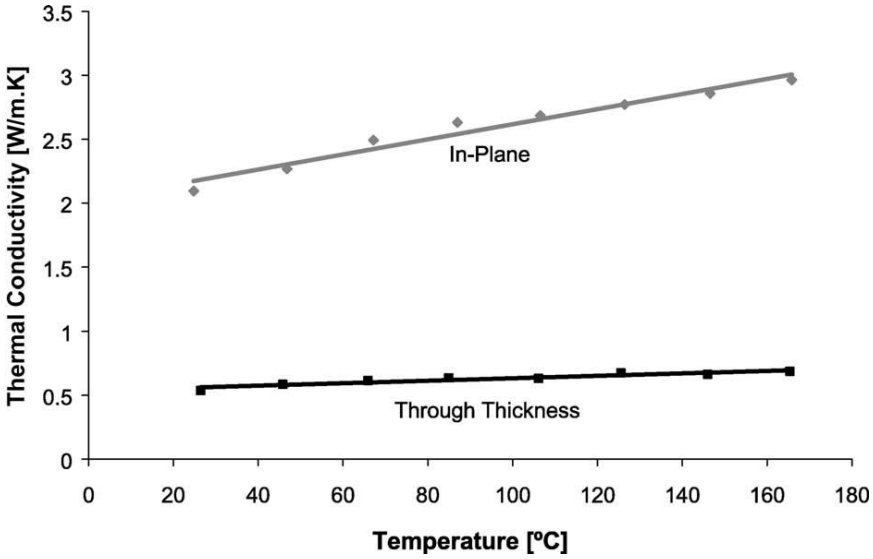


Figure 1.14: Thermal conductivity of F593 plain weave composite [88]

Robitaille and Hind [89] presented in-plane and through-thickness thermal conductivity data for PMC laminates made from three type of materials: Hexcel AS4/3501-6, prepreg T-300 carbon fibres Hexcel F263 plain weave prepreg and Fabric Development 1152 quasi-unidirectional carbon fabric infused with MF composites Mia 100/95 epoxy resin. The latter material consists in woven low-crimp T-300 carbon yarns held with very low density glass yarns. Average $V_f$ values were 62%, 61% and 55% for the cited materials, respectively. Autoclave manufacturing under controlled thickness using a caul plate and vacuum bagging was used for making laminates from the Hexcel prepregs. Laminates manufactured using the Fabric Development 1152 woven fabric were hand laid-up then cured under a hot press. Different lamination sequences and thicknesses were used for making the specimens. Measurement procedure followed ASTM C1114-06 standard method. In-plane and through-thickness conductivities ranged from 0.36 W/mK to 7.33 W/mK and from 0.45 W/mK to 0.81 W/mK, respectively. Results showed orthotropy ratios in line with literature, low variability, and an expected decrease in thermal conductivity values for lower fibre volume fraction specimens.

### 1.2.2.5. Introduction to lamination theory for conduction

An analogy between the governing equations of the thermal and the micromechanical problems in orthotropic materials can be established. The conductivity matrix of an orthotropic material is given by Equation 1.32:

$$K = \begin{bmatrix} K_{xx} & K_{xy} & K_{xz} \\ K_{yx} & K_{yy} & K_{yz} \\ K_{zx} & K_{zy} & K_{zz} \end{bmatrix} \quad 1.32$$

The difference between the thermal and micromechanical problems is that Poisson's ratio does not have an equivalent in the thermal problem; the coupling between axial directions is not present. Thus, the conductivity matrix expressed along the principal directions for a single ply can be reduced to a diagonal matrix:

$$K = \begin{bmatrix} K_{xx} & 0 & 0 \\ 0 & K_{yy} & 0 \\ 0 & 0 & K_{zz} \end{bmatrix} \quad 1.33$$

Different numerical and analytical models can predict the axial and transverse thermal conductivities of unidirectional PMCs as seen in section 1.2.2.2. Once obtained, these values can be used in predicting the effective thermal conductivity of an individual lamina positioned at an angle θ of the reference axis i.e. θ = 0°, using equations 1.34, 1.35 and 1.36 [42]:

$$K' = [T_\theta]^T \, K \, [T_\theta] \quad 1.34$$

where

$$[T_\theta] = \begin{bmatrix} cos\theta & sin\theta & 0 \\ -sin\theta & cos\theta & 0 \\ 0 & 0 & 1 \end{bmatrix} \quad 1.35$$

Hence, the matrix of conductivity of the single ply along an axis oriented at an angle θ is given by:

$$K' = \begin{bmatrix} K_{xx}cos^2\theta + K_{yy}sin^2\theta & (K_{xx} - K_{yy})cos\theta sin\theta & 0 \\ 0 & K_{xx}cos^2\theta + K_{yy}sin^2\theta & 0 \\ 0 & 0 & K_{zz} \end{bmatrix} \quad 1.36$$

where K' is the global directional thermal conductivity of the single lamina at an angle θ and θ is the fibre orientation relative to the reference axis. $K_{xx}$ and $K_{yy}$ are the single lamina thermal conductivity in the 0° and 90° directions respectively while $K_{zz}$ is its through-thickness thermal conductivity.

The classical lamination theory (CLT) requires that some assumptions be made; each ply is assumed to show the thermal behaviour of an orthotropic and homogeneous material. Bonding between lamina is assumed perfect with infinitesimally thin layers [41]. Finally, the CLT is only valid for thin laminates. The thermal conductivity of the laminate in the reference direction, i.e. θ = 0° $K_x$ can be determined using Equation 1.37:

$$K_x = \frac{1}{2h} \sum_{i=1}^{N} (K_1 (cos\,\theta_i)^2 + K_2 (sin\,\theta_i)^2) t_i \quad 1.37$$

where 2h is the laminate total thickness, N is the number of plies, $t_i$ is the ply thickness and $\theta_i$ is the ply orientation with respect to the reference axis. $K_1$ and $K_2$ are the in-plane principal thermal conductivities of the single ply respectively.

In particular, the thermal conductivities of the laminate in the reference and in-plane transverse orientations, namely $K_x$ and $K_y$, become equal in the case of a symmetric balanced cross-directional laminate. Hence, equation 1.37 suggests that the thermal conductivity $K_x$ does not undergo any change in value for any rotation angle $\theta_i$ for 0°/90° laminates. One can conclude that the condition of in-plane thermal isotropy of symmetric balanced PMCs can be achieved using a 0°/90° laminating sequence as opposed to mechanical isotropy which requires a 0°/60°/120° laminating sequence.

#### 1.2.2.6. Infrared imaging temperature measurement

Infrared non-contact thermal sensors are classified as infrared radiation thermometers by the ASTM [90]. The associated measurement technique, termed thermography, is achieved by gauging the self-emitted radiation in the IR portion of the electromagnetic spectrum from target surfaces and converting them into electrical signals. These signals are then processed for converting the information into radiation measurements. The derivation of the Stefan–Boltzmann law, Equation 1.38, enables the conversion of IR radiation measurements into temperature measurements [21,90]:

$$E = \varepsilon \sigma T_s^4 \quad 1.38$$

where E is the heat flux emitted by the surface, $T_s$ is the absolute temperature of the surface, $\sigma$ is the Stefan-Boltzmann constant and $\varepsilon$ is the surface emissivity.

A body at temperature greater than absolute zero emits electromagnetic radiation. Absolute zero temperature corresponds to a state of lowest quantum energy for electrons, atoms and molecules. No transitions to lower energy states are possible, which would result in the emission of electromagnetic radiations [21]. Incident thermal IR radiation on a surface can be reflected, transmitted or absorbed. Kirchhoff's law indicates that the sum of the three components is always equal to unity [21]:

$$\alpha(\text{absorptivity}) + \rho(\text{reflectivity}) + \tau(\text{transmissivity}) = 1 \qquad 1.39$$

The quantity and distribution of radiation over the wavelength spectrum depend mainly on the temperature of the body target surface and its emissivity. The latter characteristic of a real surface is generally a function of the wavelength and may also depend, to a lesser extent, on the temperature of the object [91]. Infrared detectors can sense IR radiation and produce electrical signals that are proportional to the temperature of target surfaces. Instruments using IR detectors and optics to gather and focus energy from the targets onto these detectors are capable of measuring target surface spot temperatures with sensitivities down to 0.1°C and with microsecond-range response times. Basic instruments are called point sensors or spot radiometers. Instruments that combine this measurement capability with mechanisms for scanning target surfaces are called infrared thermal imagers or infrared cameras. These can produce thermal maps or thermograms where, typically, brightness or color hue of any spot on the map is representative of surface temperature at that point.

It must be noted that temperatures referred to in the above paragraphs are apparent temperatures,

which correspond to actual temperatures only if the object of interest has an emissivity equal to unity and atmospheric absorption is zero at the distance and within the wavelength range used. Emissivity data may be found in reference texts [21] or determined by calibration, varying input emissivity in an IR camera and comparing the results with direct thermocouple measurements. The apparent temperature results from the reflection of background energy on the target. The reflection of background energy appears in the image and affects temperature measurements. The apparent temperature depends not only on the emissivity of the object but also on the temperature of the surrounding objects and on atmospheric absorption [92]. The effect could be particularly strong for the targets with low emissivity, such as metals, or when the camera is at a relatively distant position from the object [93]. In theory the atmosphere itself can contribute to radiation received by the IR camera. However, under most conditions this effect is small and can be ignored. The contribution from atmosphere radiation is only significant when working in the 3 μm - 5 μm range, whereas most commercial IR cameras have a spectral range from 7.5 μm to 13 μm. Therefore, making measurements in daylight does not have any significant effect on the results [91].

The 4 most commonly stated advantages of thermography over contact measurement are that it is nonintrusive, remote, much faster than conventional methods, and that it measures temperature at the surface of the object of interest with relatively minor intrusion from the environment. Furthermore, IR radiant energy travels from the target to the sensor at light speed, hence rapidly changing temperatures can be monitored in real time. As well, when temperature must be measured at many points on a target or there is a need to relocate these points, it is more practical to re-aim an IR sensor than to reposition a thermocouple or deploy a great number of thermocouples. A thermogram of a target may be presented in terms of surface radiant energy contrast, in which case it is called a qualitative thermogram. It is more often presented in terms of apparent surface temperature distribution, in which case it is called a quantitative thermogram [90].

In this work, thermal imaging was used for documenting heat transfer through PMCs and validating heat transfer simulations. Hunyar et al. [53] used thermography along with thermocouple measurements for comparing temperature distribution with simulations done on PMC samples heated by millimetre-waves. Results from thermograms showed good agreement with simulations and thermocouple measurements. Advani and Corlay [54] carried out heat conduction simulations through various PMCs and compared the thermal maps with thermograms. PMC samples, placed horizontally, were subjected to a concentrated heat source. Two types of heat sources were used, namely a gas burner and a radiant heater. Material properties, geometry, heat flux and distance were varied for each type of heat source. The IR camera used in the experiments recorded temperatures of the PMC sample surface as a function of time. Numerical and experimental results were deemed in agreement to various degrees of accuracy depending on the type of heater, its intensity, its distance from the PMC sample, the assumptions made about convection heat transfer in the vicinity of the sample and the approximation of the samples emissivity. Simulations were found to be limited to a range of distances from 62 mm to 440 mm and heat flux up to 200 $W/m^2$ for the gas flame, and to a maximum temperature of 600°C for the radiant heater.

## 1.3. Previous work done at the University of Ottawa

### 1.3.1. Carbon fibre composite tooling optimization for heat transfer using CFD modeling

An out-of-autoclave heat conduction based process for manufacturing composites from prepreg was presented. The process named integrally heated conductive tooling (IHCT) was developed by the National Research Council (NRC), Institute of Aerospace Research (IAR) as an alternative to the costly current industry standard autoclave moulding processes. The process model is portrayed in Figure 1.15. Robust parameter design, namely the Taguchi method, was used for analysing results from CFD modelling. Seventeen input parameters were considered. They included nine geometrical, five thermal and one process parameter. The Taguchi simulation plan was generated using Design Ease 7.0.2 software package. 32 iterations were identified as required for studying the process. The output parameters deemed to be the most significant to

optimize the process input parameters were the heating and cooling times, the temperature difference throughout the domain, temperature difference at the tooling and part interface and temperature difference through the thickness of the part.

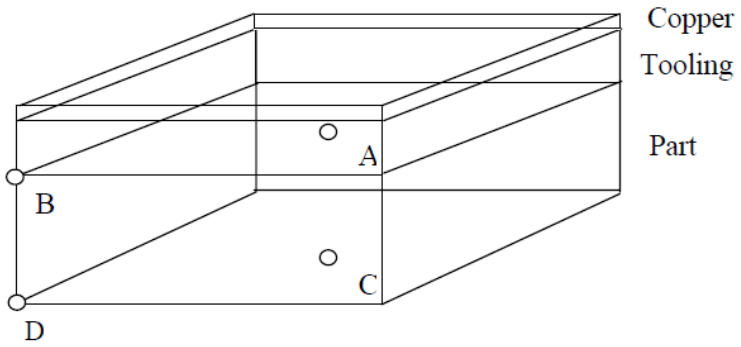


Figure 1.15: Sketch of the out-of-autoclave simulation model

32 iterations following the Taguchi simulation plan were done on the model shown in Figure 1.15. Factored effect analysis using Pareto charts and normal charts, led to the identification of the main input parameters whose effect is strongest on the variation of the output stated earlier. These parameters are, by order of importance,1) the cure temperature, 2) heater power rating and 3) interaction between the overall width and silicone thickness. These were recognized as having the largest effect on the heating time of the assembly, whereas 1) the convection coefficient and 2) cure temperature were identified to mainly drive cooling times. Maximum temperature difference values were proven to be governed mainly by 1) the heater adhesive thickness, 2) heater power rating, 3) ambient air temperature and 4) cure temperature. Regarding the maximum temperature difference between points C and D, many parameters were considered to have a considerable effect on the results. These parameters are, by order of prominence; 1) part thickness, 2) ambient air temperature, 3) heater power rating, 4) cure temperature, 5) heater adhesive thickness, 6) overall width, 7) overall length and 8) interaction between the overall length and copper thickness. Finally, regarding the temperature difference between points A and C, the study revealed that only two input parameters had prominent effect on the results, namely

1) part thickness and 2) ambient air temperature.

To validate the temperature variation trends over time, Houde conducted experimental trials on the setup portrayed in Figure 1.16. Qualitative agreement was reached despite a difference in heating ramp rate. The heating power was applied constantly in the simulation, while in experiments conducted at NRC the heating power was controlled using a predefined temperature ramp.

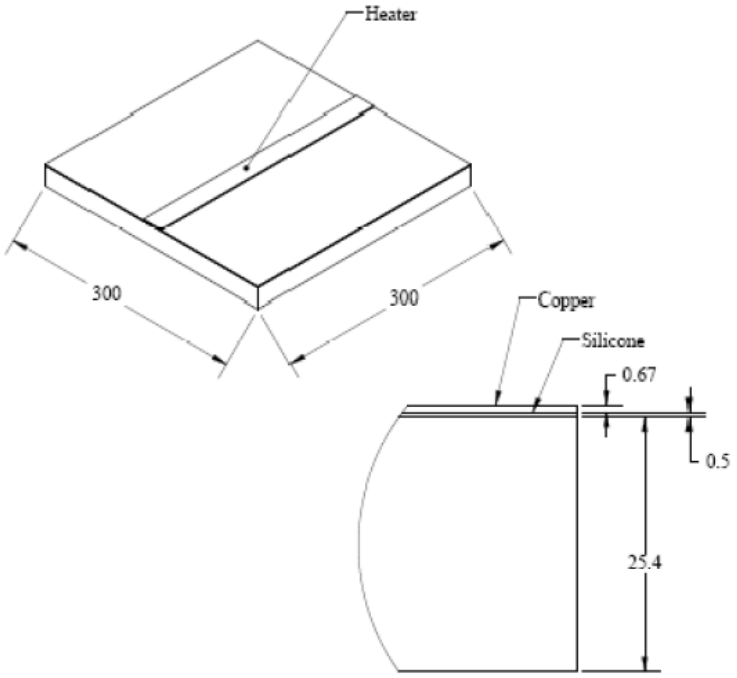


Figure 1.16: Schematic of the experimental model (mm)

Results aimed at studying the effect of adhesive thickness on the thermal behaviour of the assembly confirmed its significance as an influential input parameter. Nevertheless, results were inconclusive on the mutual effect of power and part thickness on temperature variation. Temperature maps generated from the simulations were validated qualitatively using liquid

crystal sheets. Eventually, Houde concluded that the experimental study did not enable robust validation of the CFD model, even though results showed good qualitative agreement.

### 1.3.2. Using Plackett-Burman and Taguchi experimental designs to determine significant factors for the repair of thick section composite wing skins with aluminum substructure

Hind carried out a thermal study of the patch repair area of a PMC F-18 fighter wing. The results and conclusions of the work are applicable to all structures composed of thick section composite laminates with underlying metallic substructure. Various geometric and process-related variables were modified for each experimental trial. In order to study this problem, Taguchi statistical methods and Plackett-Burman experimental designs were used for reducing the number of experimental trials to 16 and were coupled with analytical tools for separating response signals from experimental noise.

NRC's IHCT model was used for heating the fictitious repair area. A heat transfer tile (HTT) was used for supplying a uniform heat flux into the PMC structure, Figure 1.17. A HTT is comprised of a copper sheet with strategically placed Minco$^{TM}$ wire wound strip heaters (10 W/in$^2$) and thermocouples. Experiments were done for 16 different locations and 8 different factors. The latter were spar under repair area, rib under repair area, distance between spars, distance between ribs, skin thickness, time at soak, the presence of a HTT gasketing material and the presence of Roxul$^{TM}$ blankets inserted between spars and ribs.

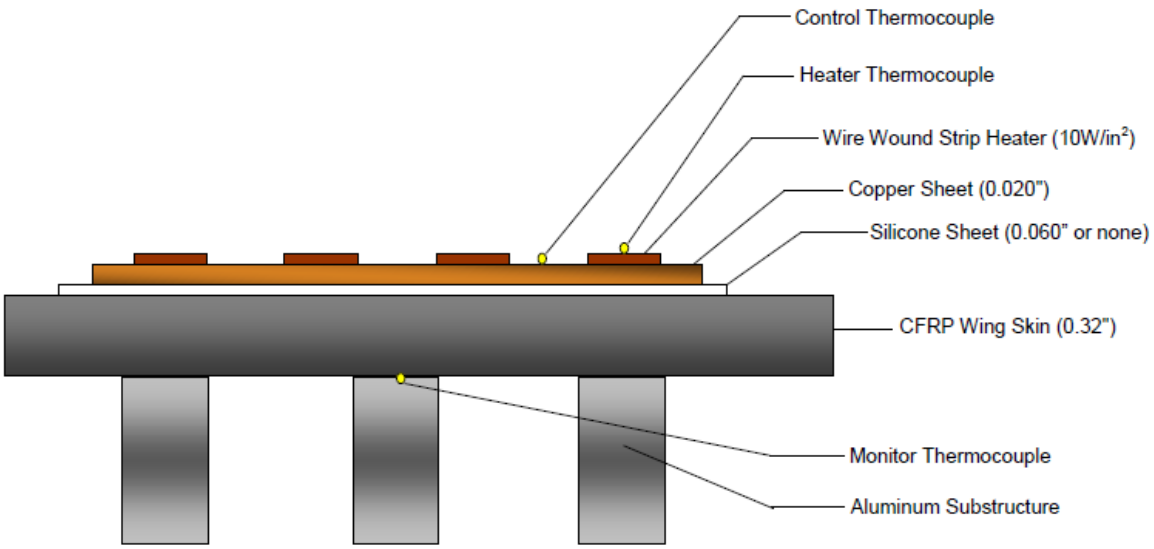


Figure 1.17: HTT setup components

Each experimental trial was run twice to gather data and separate noise from signal. A constant temperature ramp rate of 2 °C/min from room temperature to 177°C was applied to the heating process while imposing a maximum heater temperature of 220°C. The heating time was varied to either 30 or 60 minutes. Skin thickness was varied by vacuuming an AS4/3501-6 carbon epoxy laminate of 0.120" thickness on the wing. Accessories and local geometric features were considered as the cause of experimental noise. The HTT was moved to different locations on the wing skin with different underlying structural details. 5 responses were measured in experimental trials. These responses are the maximum temperature measured under and on the edge of the HTT, the difference between the maximum temperatures, the maximum temperature measured by the average of control thermocouples and the difference between the latter value and the average of aluminum monitoring thermocouples. Ultimately, it is important to note that all contrasts were based on temperatures taken at steady state.

The analysis of the most significant contrasts for every response type confirmed the expected behaviour of heat transfer in the composite wing with different underlying structural details. The

aluminum spars and ribs have the same effect on heat transfer by acting as a heat sink. This heat loss was validated by negative contrasts. The insulation blankets significantly reduced passive convection; therefore higher temperatures were recorded if the insulation was in place. The HTT gasketing material added a high thermal resistance compared no silicone sheet placed between the HTT and the wing skin. Finally the thicker wing skin was more resistant to heat transfer. This result was expected since the composite wing skin has a low conductivity and therefore the heat could not dissipate as quickly through it as through the thinner wing skin. Another goal of this study was to monitor maximum temperature in the aluminum structure. It was shown that a safety-limited temperature of 120°C was not exceeded in the trials conducted. Nevertheless, Hind recommended more trials to be performed, to ensure that the aluminum substructure would not be adversely affected during a 177°C cure.

### 1.3.3. Modeling heat transfer through complex shapes using computational fluid dynamics

This study focused on modelling heat conduction in the structure of aircraft fighter wings during their repair process, and on the effect of the wing structure geometry on heat flow. The intention was to further develop the work of Hind who tested the same structure experimentally. Furthermore, another objective of this work was to model more complex geometries using FLUENT to further develop simulations done by Houde.

Six different geometries were used for modelling various aluminum substructures under the composite skin patch repair areas. These were a C channel, a C channel with ribs, an I beam, an I beam with ribs, an I beam with flanges, and an I beam with both ribs and flanges. The temperature was monitored at 6 different points on each model. Choice of the location of points was done so that each temperature distribution could be thoroughly assessed and compared against each other for the different geometries. An additional temperature monitoring location was added between the composite and the aluminum structure to reveal any variations of the composite plate temperature relative to the aluminum beam temperature.

For each geometry created, heat transfer was modeled under 7 different thermal conditions. The conditions involved changing the convection coefficient, adhesive thickness, and conductivity of the composite. 2 values were used for each parameter. Heat flow through different geometries was investigated by modeling these geometries in solid modeller Solidworks then converting them into meshes using pre-processor GAMBIT. The meshed geometries were then exported to FLUENT to simulate the surface temperature distribution and its evolution in time.

Comparison of the evolution of heat distribution with time for the different geometries at the different monitoring locations showed the importance of in-plane heat conduction. Geometries with larger surface areas experienced a drop in temperatures. Larger surfaces led to more air being in contact with the member, and therefore to quicker and more effective convection cooling. Results revealed that a larger mass of material led to longer heating times for the same heat flux being imposed. The effect of taking off the ribs from the geometry reduced contact areas between the composite plate and aluminum structure; therefore, the heat transferred to the aluminum structure decreased, leading to lower temperatures at all locations except for those in direct contact with both the aluminum structure and composite part. On the other hand, flanges were found not to change relative temperatures between monitoring locations, but instead they lowered temperatures over the entire system. They were also found to cool the aluminum more efficiently than the ribs. Both ribs and flanges combined obviously optimized cooling and contributed to achieving lower temperatures in the aluminum structure. Comparison of heat transfer in all geometries showed that adding ribs to the C channel did not have an effect as significant effect as it did on the other geometries. This comparison also showed that flanges produced more effective cooling than ribs.

### 1.3.4. Optimization of heat transfer in carbon fibre epoxy composite tooling

Maksoud conducted an optimization study of the IHCT, the out-of-autoclave conduction-based process for manufacturing composites from prepregs mentioned in section 1.3.1. The IHCT model consisted of a composite plate bonded to a copper layer heated by an electrical heater as

shown in Figure 1.18.

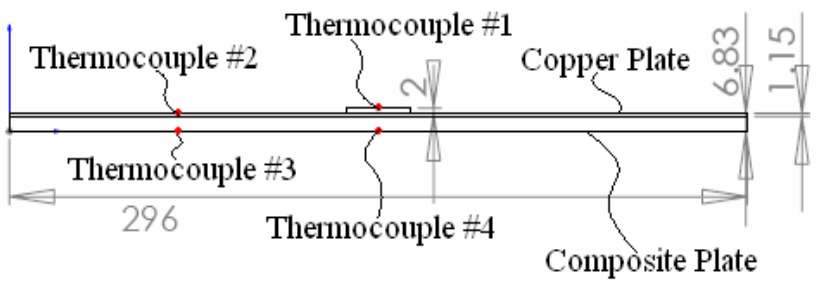


Figure 1.18: Schematic of the IHCT model (mm)

To investigate the effect of orientation of the plate and copper material in the IHCT model, Maksoud recorded heating and cooling temperature cycles on a copper plate heated by a rectangular electrical heater. The assembly was positioned in 4 different orientations as portrayed in Figure 1.19. Temperature readings were done using 4 thermocouples located as shown in Figure 1.18. The effect of plate orientation and relative orientation of the heater on the heating and cooling cycles was deemed to be negligible. Relative orientation of the heater did not have a significant effect on the free convection coefficient. In addition, the author also concluded that the through-thickness temperature gradient in the copper plate was negligible once steady state is reached.

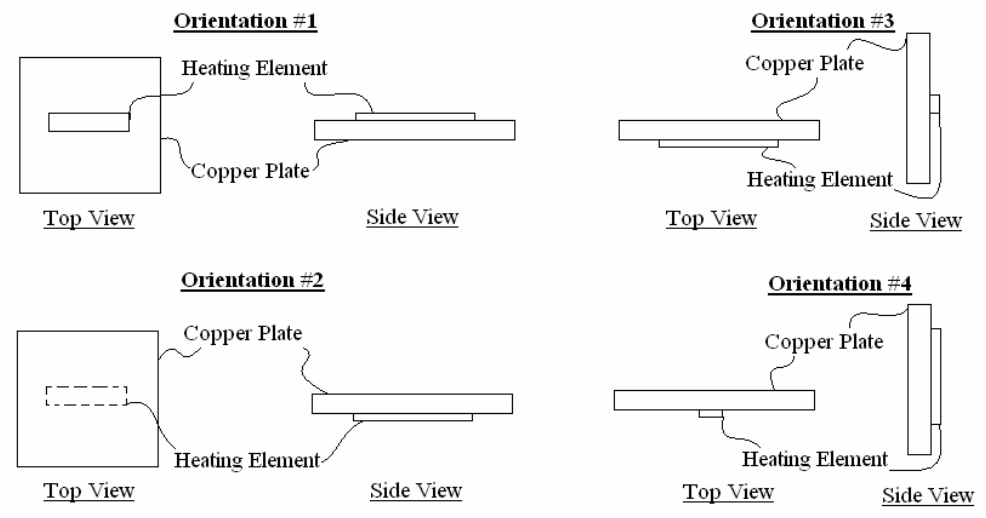


Figure 1.19: Orientations of the copper plate

To determine convection coefficients on the heater and plate, a series of FLUENT simulations was done. Modelling transient heat transfer using different convection coefficients, then trying to match heating and cooling cycles with experimental data revealed values of 5 W/mK and 10 W/mK for the convection coefficients of the heater and the copper plate, respectively. Three simulations using three different bonding tape thicknesses were carried out. The outcome of these simulations showed marginal effect of tape thickness on the temperature distribution. Heater conductivity influence on heat transfer was investigated by carrying out three simulations with 3 conductivity values, namely 10 W/mK, 387.6 W/mK and 1000 W/mK. It was shown that the variation of thermal conductivity of the heating element had almost no effect on the overall heat conduction process in the assembly.

The author investigated the influence of key parameters on heat conduction in the assembly and consequently, the surface temperature distribution in the different components of the IHCT model. In the experimental section, comments were made to confirm the expected advantage of bonding a copper layer to the composite plate for reducing the temperature gradient in the composite. However, the slow response of the temperature recorded at the surface of the

composite compared to the through-thickness copper surface temperature was noticed. Unlike the copper plate assembly, temperature variations in the IHCT assembly showed dependence to the orientation. Surprisingly, composite surface temperatures in the vertical orientations showed higher values than in the horizontal orientations. Using CFD modelling, variation of the thickness of the silicone bonding layer that separates the copper and the composite plates was deemed to have a negligible effect on temperature variations in heating and cooling cycles. Simulation cases using different through-thickness conductivities, namely 0.74 W/mK, 1.0 W/mK and 1.25 W/mK for the composite plate led to the conclusion that the through-thickness conductivity has little effect on the temperature of the composite. Eventually, CFD models used in the study were considered valid and able to represent the physical problem accurately.

### 1.3.5. Simulation and experimental measurement of heat transfer through composite laminates with integrated copper sheets

Brillant's study was focused on the optimization of the IHCT configuration, aiming at enhancing its conductive performance. The IHCT model described in the previous section was named heat transfer tile (HTT) in this thesis. The integration of copper sheets into the PMC plate used for making the IHCT and their effect on heat transfer was investigated. Various design parameters were explored, namely the location of copper sheets, quantity of copper sheets and cooling method. The effect of each parameter on heat conduction was studied experimentally and numerically using FLUENT. The HTT model consisted of PMC components of various thicknesses and 0.533 mm thick copper sheets bonded using a heat-curable silicone adhesive. PMC components were made from unidirectional or woven prepreg. Different configurations of copper sheet placement between the PMC shells were considered and up to 3 copper sheets per configuration were integrated in the tool. Heat supply was provided by a 25.4 cm × 2.54 cm, 50W electrical heater during a 90 minute period or until a maximum temperature of 210°C on the heater was reached. The heater was affixed on the back face. A total of eight thermocouples were used for the experimental study. Temperatures of the heating element, ambient air and the front and back face of the tool were monitored. Q420 VNRC control software developed by Hind at NRC-IAR was used for temperature monitoring. The assembly was maintained in place and

close together by applying vacuum and weight. Insulation was applied at the top and the bottom of the assembly. In the analysis of the results, the natural convection of air in the vicinity of the tooling was neglected and constant heating was used, to facilitate direct comparisons with numerical results.

First trials were done using the same quantity of copper sheets, heating elements and heating power. The variation in the location of the copper sheets was deemed to have a negligible effect on the magnitude as well as on the uniformity of temperatures at the tool face. This was explained by the fact that the uniformity of the temperatures was mainly governed by the high conductivity of the copper sheets in the lateral direction. On the contrary, the location of the copper sheets influenced the temperature of the heater. The temperature at the heater surface was decreased drastically when copper sheets were located closer to the heating element. According to the author, this was caused by the mismatch in heat capacities and dimensions between the copper sheets and heater. Thus, a relatively small increase in the heat transferred to the tool engendered a considerable decrease of heater temperature. On the other hand, variation of the volume of copper within the tool had a clear effect on the magnitude of temperatures at the tool face at a given time. Using more copper layers caused the introduction of an additional heat resistance into the assembly as well as an increase in the overall heat capacity of the assembly. In the case where the quantity of copper sheets was decreased, temperatures at the tool face were less uniform. Concerning the effect of the cooling method, natural convection and an adjustable cold air gun were used for cooling down the set-up. The cooling method did not affect the heat transfer behaviour of the tool. The replacement of multiple thin copper sheets by a thick one did not have considerable effects on the tool face temperatures. In contrast, the addition of a heating element increased the overall temperature by 50°C. The author concluded that the uniformity of temperature distribution was increased owing to the presence of the copper sheet.

Numerical simulations showed that the location and quantity of copper sheets had a direct effect on temperatures at the control surface and at the tool face, as opposed to observations from

experimental data. A constant heat rate was adopted for the CFD model for simplicity and the control of the heater was accomplished using the feedback signal from a control thermocouple on the back face. Comparison of experimental and numerical temperature profiles revealed that the CFD model's convection coefficient should be around 2.5 $W/m^2K$. A layer of silicone was applied to each composite-copper interface. A series of CFD analyses were conducted for various thicknesses. The results showed that the heater temperature increased as the resistance thickness increased. But since the effects of variation of the convection coefficient and resistance thickness are different, the combination of convection coefficient and resistance thickness merged into one parameter was studied. A convection coefficient of 2.88 $W/m^2K$ and a resistance thickness of $89.55x10^{-5}$ m were found to satisfy the boundary conditions of the CFD model.

The CFD model was able to mimic the experimental problem. Temperatures at the tool face were modeled accurately with a maximum difference in temperature of 2.5°C while heater temperatures were over-estimated by 6°C. The simulations confirmed conclusions made from the experimental study. In fact, it was shown that a lower the proportion of copper within the set-up lead to a higher temperature at the heater, whilst a larger volume lead to lower the temperatures at the tool face.

In a second phase of the numerical study, and to supply the desired heat rate value for a given iteration, a user defined function (UDF) was written with the objective of keeping temperatures within ±2°C of the target temperature as shown in Figure 1.20.

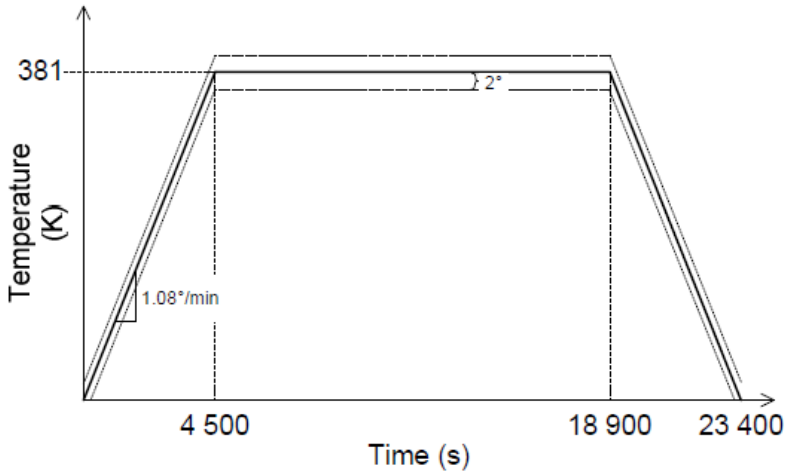


Figure 1.20: Temperature profile imposed by the UDF

A feedback thermocouple was placed on the top surface of the tool close to the heater. The control algorithm was adjusted to produce the proper temperatures at the tool face. The target control temperature was set to a ramp of 1.08 K/min for 75 min, a constant temperature of 381K for 240 min and a ramp of -1.08 K/min for another 75 min. The CFD model was deemed to be valid. Conclusions were made on the slow cooling rate, done by natural convection, for the desired decreasing temperature ramp. Therefore, a controlled external source for cooling was recommended to keep the cooling rate within the margins of the UDF.

### 1.3.6. Geometric modeling and heat transfer simulations for the reverse engineering of an aerospace carbon / epoxy back seat tool

Following on the objectives of Brillant and Maksoud, El Karafi investigated the heat transfer process in the IHCT, referred as HTT. An existing PMC seat back tool was reverse engineered. The 3D model coordinates data were acquired using a contact probe a connected to MicroScribe-G2 portable coordinate measuring machine (CMM). The 3D model was then generated using RHINOCEROS software package and transferred to FLUENT. Static and transient heat transfer simulations were conducted on the model. The HTT model consisted on a 1mm thick deformed

copper sheet bonded onto the back face of the PMC tool using a heat-curable silicone adhesive. The PMC tool measures 381 mm × 546 mm and is 63 mm thick. The assembly was positioned in a vertical orientation and five horizontal heaters were affixed to the copper sheet with an equal spacing of 101.6 mm. The top heater length was 304.8 mm and the remaining four measured 381 mm, Figure 1.21.

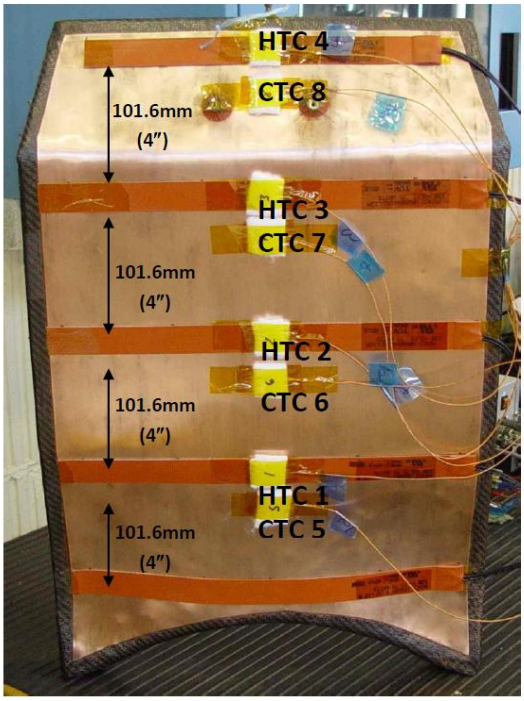


Figure 1.21: Experimental setup of the seat back tool with five heaters

Material properties were the same as in Houde's thesis and boundary conditions were set as in Maksoud's simulations. Validation of the model was conducted through heat transfer simulations in FLUENT, in both static and transient modes. Heaters were assigned a volumetric heat flux as in experimental trials. For the single heater model the volumetric heat flux was 3830 kW/m$^3$, whereas it was 3860 kW/m$^3$ for the five heaters arrangement model. The thickness of the silicone layer was 0.25 mm in simulation models where the silicone bonding was taken into account.

Preliminary simulations involved a steady-state heat transfer simulations in the tool using only one heater. For comparison purposes, the material was first assumed to be isotropic. The model incorporated the effect of natural convection, heat generation in the heaters and conduction through the model. Then the silicone layer was considered. The temperature distribution was slightly different. The silicone layer was considered to act as an additional thermal resistance at the interface. The temperature gradient through the tool at the heater location was increased by 6°C. At a later stage, simulations were done taking into account the orthotropic nature of composites. The effect of this property on heat transfer was noticed across the mould. The PMC shell inner temperatures were decreased and a 50°C temperature difference was reported through the thickness of the assembly. Temperatures were observed to be more uniform and no heat concentrations were observed between the heaters and copper sheet.

In the transient analysis stage, the temperature of the assembly was initialized to 300K and the temperature distributions were plotted after 45 minutes. The results were compared with trials conducted at NRC-IAR. PMC tool temperatures were controlled by a closed loop temperature controller. The overall temperature was about 82°C, reached after 20 minutes of heating. However, the CFD model did not match experimental results. The mesh was considered not to be sufficiently refined to give reliable results. Uncertainties introduced by reverse engineering, shortage of details about the generated geometry were considered to be important and contributed to overall errors.

### 1.3.7. Predicting and measuring thermal conductivity in carbon/epoxy unidirectional tape and textile reinforced composites

Hind presented experimental conductivity data for AS4 fibre unidirectional tape prepreg composites, and for T300 fibre unidirectional non-woven and plain weave textile reinforced composites. Lamination sequences of the samples included $[0°]_n$, $[0°/90°]_n$, $[0°/90°/0°]_n$, $[0°/60°/-60°]_n$ and $[0°/+45°/-45°/90°]_n$. Table 1.5 details the specifications of the manufactured composite plates. Composite samples 1 and 2 were manufactured using autoclave curing whilst

samples of material 3 were made by hand layup.

Table 1.5: Specifications of the manufactured PMCs, Hind [100]

| Material | 1 | 2 | 3 |
|---|---|---|---|
| Designation | AS4/3501-6 | HexPly F263 W3T282-42"-F263 | Tape weave Fabric style 1152 |
| Manufacturer | Hexcel | Hexcel | Fabric Development |
| Form | UD prepreg | Woven prepreg | UD dry fibre |
| Weave style | N/A | Plain weave | UD weave |
| Fibre | AS4 | T300 | T300 |
| Surface density ($g/m^2$) | 150 | 194 | 366.7 |
| Roll width (cm) | 107 | 107 | 7.5 |
| Cured ply thickness (mm) | 0.25 | 0.18 | 0.37 |
| Fibre volume fraction | 0.62 | 0.61 | 0.55 |
| Manufacturing method | Autoclave | Autoclave | Hand layup |

The experimental phase of the thesis consisted of directional conductivity measurements using THASYS and THISYS thermal conductivity measurement devices from Hukseflux (Delft, Netherlands). The devices' test methods were explained in detail by Hind. THASYS was used for measuring the through-thickness conductivity while THISYS was used for measuring the in-plane conductivity of flat specimens. Fourteen PMC panels were manufactured from the three polymer composite materials. Variability was quantified in all cases. Measurement data are summarized in Table 1.6. Through-thickness transmission ultrasonic c-scans of panels 1, 2 and 4 through 9 were carried out. C-scan images revealed suitable levels of quality for all panels with no discontinuities noticed.

Table 1.6: Summary of the experimental data, Hind [100]

| Panel | Material | Form | Layup sequence | Standard THYSIS | | | THASYS | Directional THYSIS | | |
|---|---|---|---|---|---|---|---|---|---|---|
| | | | | $k_x$ 0° | $k_y$ 90° | $k_{45}$ 45° | $k_z$ | $k_x$ 0° | $k_y$ 90° | $k_{45}$ 45° |
| 1 | 1 | UD Prepreg | $[0]_6$ | 3.16 ±0.03 | 3.10 ±0.15 | 2.94 ±0.05 | 0.73 ±0.06 | 6.4 ±0.30 | 0.7 ±0.08 | 2.74 ±0.03 |
| 2 | 1 | UD Prepreg | $[0]_6$ | 3.15 ±0.07 | 3.37 ±0.01 | 3.33 ±0.02 | 0.81 ±0.04 | 7.33 ±0.35 | 0.85 ±0.11 | 3.25 ±0.12 |
| 3 | 1 | UD Prepreg | $[0/90/0/90]_s$ | 2.90 ±0.01 | 3.06 ±0.03 | 3 ±0.10 | 0.74 ±0.02 | 3.87 ±0.02 | 3.73 ±0.06 | 3.89 ±0.02 |
| 4 | 1 | UD Prepreg | $[0/90/0]_s$ | 3.18 ±0.03 | 3.22 ±0.01 | 3.13 ±0.01 | 0.74 ±0.01 | 4.72 ±0.09 | 2.79 ±0.09 | 3.52 ±0.06 |
| 5 | 1 | UD Prepreg | $[0/45/-45/90]_s$ | 3.16 ±0.03 | 3.12 ±0.03 | 3.03 ±0.05 | 0.74 ±0.02 | 3.5 ±0.12 | 3.57 ±0.05 | 3.59 ±0.06 |
| 6 | 1 | UD Prepreg | $[0/30/-30]_s$ | 3.03 ±0.02 | 3.05 ±0.01 | 3.09 ±0.08 | 0.71 ±0.01 | 5.43 ±0.02 | 1.7 ±0.14 | 3.51 ±0.01 |
| 7 | 2 | Woven Prepreg | $[(0/90)]_8$ | 2.6 ±0.07 | 2.57 ±0.03 | 2.51 ±0.04 | 0.62 ±0.01 | 2.97 ±0.04 | 2.97 ±0.04 | 2.96 ±0.06 |
| 8 | 2 | Woven Prepreg | $[(0/90)_{]8}$ | 2.56 ±0.04 | 2.55 ±0.02 | 2.58 ±0.02 | 0.6 ≤0.01 | 3.04 ±0.02 | 2.9 ±0.05 | 2.9 ±0.19 |
| 9 | 2 | Woven Prepreg | [(0/90)/(45/45) /(45/45)/(0/90)]$_s$ | 2.42 ±0.03 | 2.42 ±0.04 | 2.37 ±0.03 | 0.58 ±0.01 | 2.81 ±0.08 | 2.79 ±0.02 | 2.74 ±0.04 |
| 10 | 3 | UD Woven | $[0]_6$ | 2.04 ≤0.01 | | | 0.45 ≤0.01 | 4.77 ±0.13 | | |
| 11 | 3 | UD Woven | $[0]_6$ | 2.05 ±0.02 | | | 0.46 ≤0.01 | 4.95 ±0.07 | 0.36 ≤0.01 | 1.68 ≤0.01 |
| 12 | 3 | UD Woven | $[0/90]_s$ | 2.27 ±0.01 | | | 0.45 ≤0.01 | 2.62 ±0.02 | 2.72 ±0.21 | 3.04 ±0.14 |
| 13 | 3 | UD Woven | $[0/90/0]_s$ | 2.43 ≤0.01 | | | 0.52 ≤0.01 | 3.53 ±0.01 | 2.03 ±0.03 | 2.77 ±0.02 |
| 14 | 3 | UD Woven | $[0/60/-60]_s$ | 2.42 ±0.01 | | | 0.51 ≤0.01 | 2.59 ±0.13 | 2.81 ±0.03 | 2.78 ±0.01 |

Measurement direction is indicated by the angle along which each specimen was cut from the panel. THISYS and THASYS in-plane specimen dimensions were 70 mm x 110 mm and directional THISYS specimens were 22 mm × 110 mm. Eighteen specimens were cut with a diamond saw from panels 1 through 9. These included three bulk THISYS and THASYS specimens in each of the three directions. Data presented in Table 1.6 are averages of a minimum

of three measurements and a maximum of 12 measurements. Differences in reinforcement architecture and variations in material microstructures are highlighted through micrographs of sample cross-sections. The results confirmed that THISYS was capable of quantifying the directional conductivity of composite materials. Experimental conductivity data showed variability ranging from less than 1% to more than 10%. In-plane and through-thickness transverse thermal conductivity values varied significantly depending on reinforcement type.

Predicting values of the directional in-plane and through-thickness transverse thermal conductivity of composite materials was the second objective of this thesis. CLT and models of the thermal conductivity applicable to homogeneous composites found in the literature were used in determining the thermal conductivity of tape prepreg laminates and impregnated textile fabrics. Simulations of heat transfer were done on unit cells of textile-based composites. Numerical models were developed to quantify the effect of changes in reinforcement architecture or local geometry on directional thermal conductivities. For this purpose, a code was developed for steady state finite element simulations conducted for non-crimped and crimped woven textile reinforced composites.

Results generated for radial thermal conductivity data of AS4 fibres produced by Hexcel used experimental data obtained earlier in the work, combined with the rule of mixtures by volume (ROMv) and Clayton's model for aligned fibres [9]. Finite element models of textile composite unit cells were developed as a predictive tool for the directional thermal conductivity as a function of the geometry of the reinforcement and constituent properties. Unidirectional modelling efforts focused on a three-dimensional meso-scale composite unit cell model which consisted of two layers of parallel non-crimp yarns embedded in an epoxy matrix. A convergence study was carried out to assess the discretisation error associated with the mesh density and geometry of the unit cell. To optimize computational resources a ¼ of a yarn crossover was modeled instead of the full crossover or multiple crossover unit cells. Variations of $V_f$ and reinforcement geometry had a significant effect on $k_z$ values. Simulations done on the

non-woven unidirectional and cross-ply unit cell revealed that $k_z$ does not vary significantly upon change of reinforcement geometry or lamination sequence based on the minimal variability. Lamination sequence was deemed to have an important effect on axial conductivity for non-woven reinforcements. Non-woven models simulated $k_z$ values ranged from 0.46 W/mK to 0.52 W/mK compared to the average experimental value of 0.48 W/mK. Yarn gap geometry had a major effect on the $k_z$ predictions. It is important to note that the yarn gap geometry was deliberately simplified to reduce bad mesh surfaces. The non-woven numerical conductivity values for unidirectional laminates ranged from 5.25 W/mK to 5.38 W/mK along the direction of the yarns and 0.49 W/mK to 0.50 W/mK across the yarns, compared to 4.86 W/mK and 0.36 W/mK obtained from the experimental trials, respectively. The non-woven numerical value for the axial conductivity for a cross-ply laminate was 3.25 W/mK whereas an average experimental value of 2.79 W/mK was obtained.

Material 2 was modelled using woven unit cell models with reinforcement geometric parameters obtained from experimental measurements obtained from the micrographs of the specimens. More accurate models were developed by cutting the upper and lower faces at mid-yarn. Woven unit cell simulations showed that these models were the most accurate to predict $k_z$ but in-plane conductivities were not obtained using these cut models. The non-cut models demonstrated the effect of the number of plies, degree of nesting and lamination sequence on $V_f$ for axial and transverse conductivity values. Woven unit cell models gave $k_z$ values of 0.32 W/mK to 0.49 W/mK whilst the average of experimental measurements was 0.60 W/mK. Generated models for woven textiles were not able to predict accurate directional thermal conductivity values for high $V_f$ materials. Micrographs of materials 2 and 3 exhibited an irregular, intricate geometry which requires better geometric modelling capabilities.

The author stated that the high $V_f$ of the woven composite along with the high yarn fibre volume fraction are limiting factors for a better accuracy of the generic model for the woven composite unit cell. This results from the limits of the analytical model to mimic yarn paths through simple

mathematical functions and regular cross-section shapes. This brought up the intricate nesting in real unit cells, which causes local thermal conductivity variability. Eventually, it was suggested that simplified predictive models could be used for predicting the directional thermal conductivities of PMCs in studying more complex textile reinforcement structures.

# Chapter 2: Experimental work

## 2.1. Resin transfer moulding manufacturing of PMC components

This section presents the materials and performing technique used for manufacturing PMC components for this research work. These were carefully chosen to replicate airframe industry practices as closely as possible. The manufacturing process for PMC components is also presented. Throughout the manufacturing operations, much effort was put towards minimizing the manufacturing cost and time, as well as towards mitigating in-process and post-process issues. Safety issues were also taken into account. The chosen methodology ensured that the PMC components made in-house were comparable, as realistically as possible, to PMC airframe industry practice.

### 2.1.1. Manufacturing materials

#### 2.1.1.1. Preforming process

This section presents the preforming process used in this thesis for making 2D stitched preforms. Five carbon preforms were made for manufacturing PMC components using the RTM process, as well as one fibreglass preform. Carbon fibre preforms featured 18 layers of carbon fibre tows; estimated $V_f$ for the manufactured PMC components was 0.52. The fibreglass preform counted only 6 layers, for an estimated a $V_f$ of 0.63. Owing to the design of the mould and limit on the mould cavity thickness, only one $V_f$ was studied since adding too many layers lead to the problems with mould closure while less layers caused an under packed mould cavity leading to preform buckling during injection.

Tenax-J HTS carbon fibre from Toho-Tenax America, Inc (Rockwood, TN, USA) was used for

manufacturing dry carbon fibre preforms. Fibres were manufactured from PAN precursor and had polyurethane based sizing. Their relevant characteristics are shown in Table 2.1, detailed specifications are presented in Appendix A. The fibres came in untwisted flat fibre tows containing 12000 carbon fibre filaments. Spools of the Toho-Tenax carbon fibre used for making composite components in this thesis appear in Figure 2.1. Owing to the flat ribbon-like arrangement of carbon tows, the fibres had some ability to spread on a given surface and to be laid down along selected orientations as required for making the NCF preform. These characteristics contributed to producing dry preforms with minor inter-yarn gaps. The linear density of the tows given in Table 2.1 was verified by measuring then averaging the mass of 6 tow samples, each 10 cm in length. The measured linear density was 805.5 Tex with a standard deviation of 0.47 Tex.

Table 2.1: Relevant characteristics of Toho-Tenax Tenax-J HTS carbon fibre tows

| Property | Unit | Value |
|---|---|---|
| Carbon fibre diameter [104-105] | μm | 7 |
| Size level [105] | % | 1.3 |
| Linear density [105] | Tex | 810 |
| Density [105] | g/cc | 1.76 |
| Axial thermal conductivity [104] | W/m K | 10 |
| Specific heat capacity [104] | J/Kg K | 710 |
| Coefficient of thermal expansion [104] | $10^{-6}$/K | -0.1 |
| Nominal tow width | mm | 4 |

Figure 2.1: Toho-Tenax Tenax-J HTS carbon fibre spools

Bi-axial dry preforms were made using the setup shown in Figure 2.2. A clear acrylic board was CNC-machined to host pins with 4 mm centre-to-centre spacing, in a 4 cm x 4 cm squared pattern. An aluminum frame was laid down around the pin-board. The frame, having roughly the same dimensions as the pin set mounted on the pin-board, served at a later stage as a clamp to hold the carbon fibre tows in place.

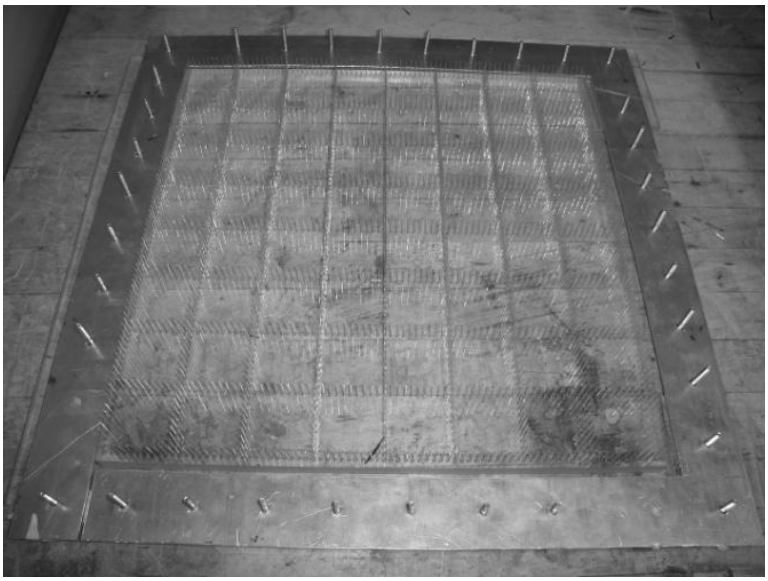

Figure 2.2: Pin-board and lower frame

Carbon fibre tows were unrolled from the spools and cut into segments of approximately 80 cm in length. Next, they were laid down manually in between the pins. Great care was taken in doing this operation, to reduce and remove any tow waviness present in the spools by manually applying tension on the tows before placing them between the pins. The operation did introduce some defects in brittle carbon fibre tows as they got caught in pin heads. 80 fibre tows were laid down next to each other for covering a full layer. Then this was repeated for a total of 18 times, for a final ply sequence $[0°/90°/0°/90°/0°/90°/0°/90°/0°]_s$. Making a single ply took roughly 1 hour.

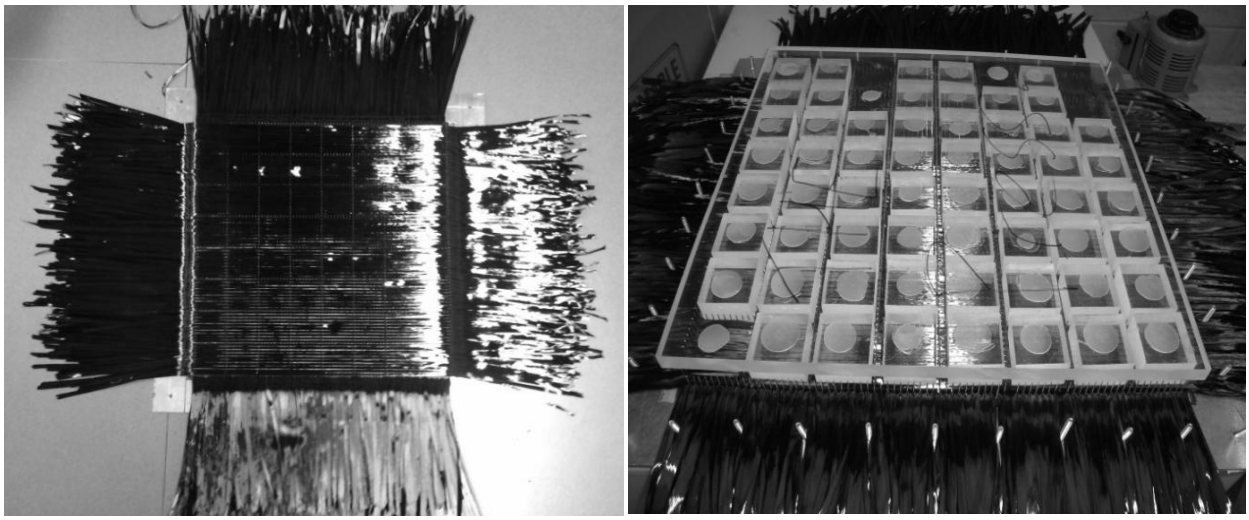

Figure 2.3: Carbon tows lay down (left) and manual preform compaction (right)

Each one of the stratified 18 carbon fibre plies were compacted manually using a clear acrylic (PMMA) platen. The platen, shown in Figure 2.3, featuring 3.5 cm × 3.5 cm × 2 cm acrylic blocks glued on. These penetrated between the pins to apply pressure on the carbon plies, resulting from gravity only. Compaction reduced the overall thickness and out-of-plane waviness. Having fibre tows as flat and spread out as possible improved surface coverage, made the lay down of subsequent layers easier, as well as the eventual stitching of the complete stack. Good surface coverage kept the surface density of the final dry preform constant. Once all plies were laid down as scheduled, they were clamped by fastening a second aluminum frame to the

first one shown in Figure 2.2, as shown in Figure 2.4. Clamping the plies stack aimed at providing a mechanical bond for enabling handling and reducing tow warpage during the stitching stage.

Figure 2.4: Clamped preform still in the pin-board

The next step was to pull out the clamped stack of plies from the pin-board. This was done with great care as carbon tows might be retained and damaged through getting caught in the pins. This problem might cause a whole assembly of carbon tows to split and shear in-plane as well as out-of-the-plane. Such shear caused some tows to slide out from the clamping frame longitudinally and transversely. When such slippage was minor, loose tows were repositioned manually by partially unscrewing the clamping frame and stretching the tows.

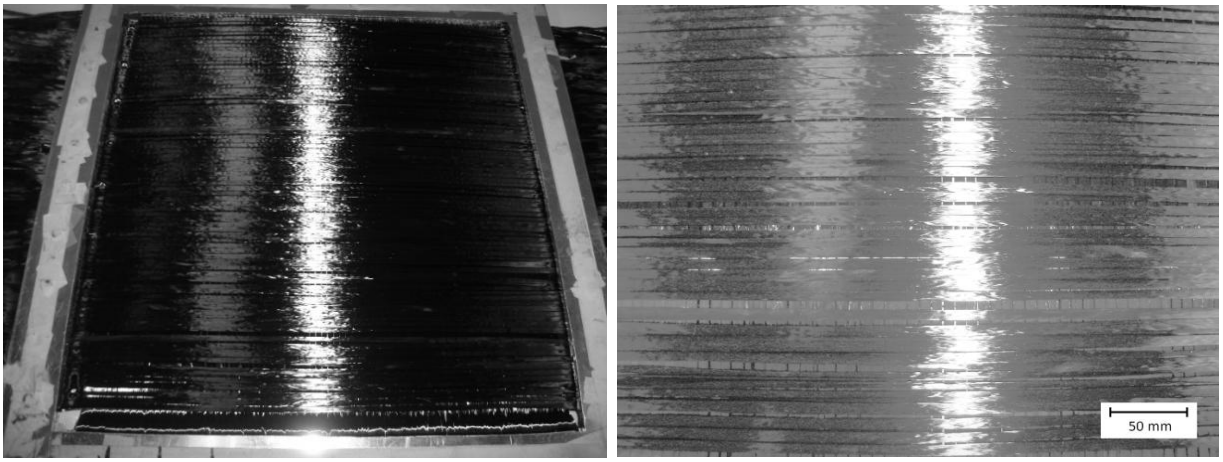


Figure 2.5: Clamped preform (left) and zoom-in on some loose fibres (right)

Assembly of 2D dry preforms was done through stitching. Stitching provided mechanical bonding between the tows, enabling subsequent preforming operations. A commercially available lock-stitch sewing machine was modified to accommodate the nature and dimensions of the materials to be stitched, Figure 2.6. A variable transformer (VARIAC) was used for regulating the feed voltage of the sewing machine. Voltage and timing were set so that by pressing the pedal only once, the needle traveled a complete stroke down to penetrate the preform and create the stitch knot, and then back to its initial position. A direction guide was fixed to the sewing machine for ensuring stitching along a straight line over the clamped preform. This allowed for having straight path seams with constant interspacing. Feed dogs initially present on the machine were removed for protecting the fibres, as these can be damaged by getting stuck in their teeth. Commercially available 100% polyester white thread was used for stitching the preforms. The same thread was used for the needle and bobbin. Seam interspacing was set to about 4 cm for the PMC plate preforms, and about 1.5 cm for the PMC demonstrator part preform.

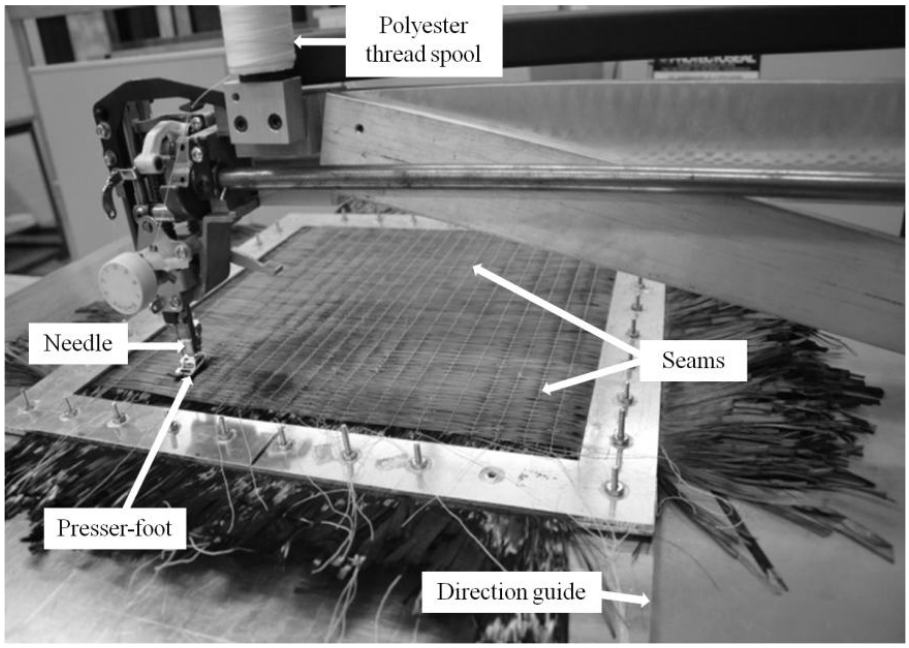


Figure 2.6: Sewing of a dry preform

The stitching process for a single seam started by positioning the direction guide and clamped preform adjacently so as to have a straight seam. Some tension was applied manually on both of the needle and bobbin threads to allow the interlacing of the threads and hence for making the first stitch knot. Then the frame was carefully pushed forward to the position of the next stitch knot. This operation was done manually owing to the absence of feed dogs. Once the first stitch was done, the threads being held manually were released and the frame was pushed forward by roughly 5 mm to the next knot position. This process cycle was repeated until the end of the seam was reached. Attention was given to keeping the stitch length as constant as possible. Needle thread tension was manually adjusted at the beginning of each cycle for keeping a roughly constant needle thread tension along the seam. Preforms were stitched along one direction only. After the completion of a seam, the clamped preform was translated to the next seam location. Completion of a single seam took roughly 15 minutes. A stitch bonded preform appears in Figure 2.7. This stage of the preforming process ensured better handling and minimal preform fray.

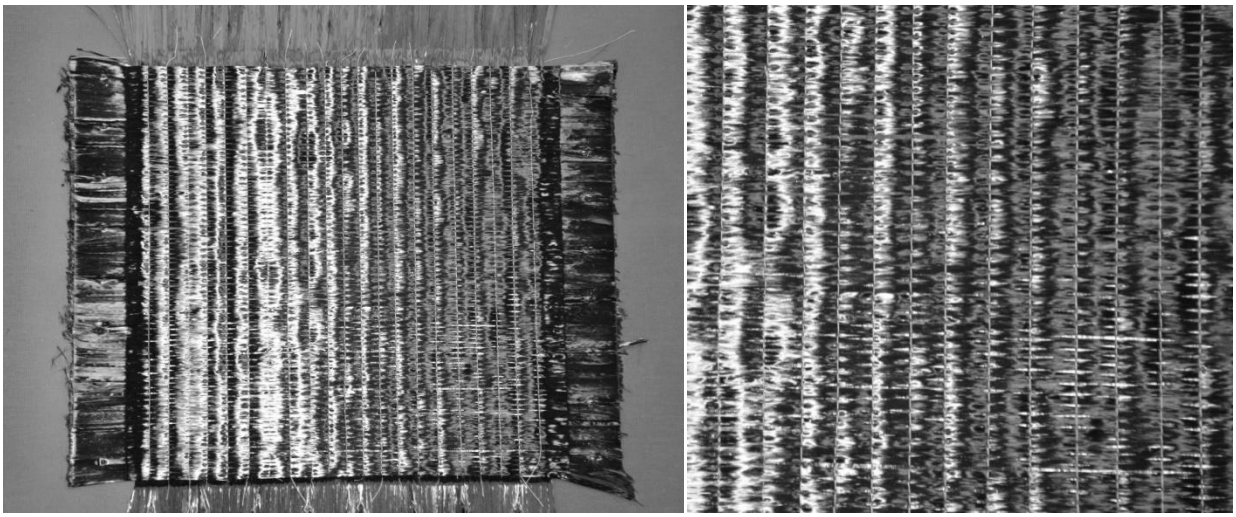

Figure 2.7: Dry carbon fibre stitched preform

The stitching process compressed the preform locally under the seams. Compression had a remarkably higher extent around the stitch pitch and caused the undulation of the fibre tows, hence contributing to the out-of-plane waviness. This undulation, also called crimp, is illustrated in Figure 2.7. Again, part of the out-of-plane waviness was generated during the tow lay down stage of the preforming process.

Stitching also introduced a limited amount of in-plane local tow dislocations (LTDs) resulting from tow clustering or tow split. Such LTDs appear in Figure 2.8. On the left side of the figure, owing to a high needle thread tension, a stitch clusters the fibrous tows creating in-plane voids. These voids had parallelogram geometry. On the right side of the figure, fibrous tows were split after needle penetration. Adding the effect of a high needle thread tension, some fibrous packages were carried over as shown in Figure 2.8. This kind of dislocation did not only contribute to the in-plane waviness but also to the out-of-plane waviness as well. Overall, defects resulting from high needle tension were more prevalent than those where tows were carried over. Seam having LTDs exceeding allowed tolerances were re-done as this can reduce the reproducibility of the RTM manufacturing process by disrupting the local resin flow and creating resin rich zones. Hence, local thermal behaviour of PMCs made using these preforms might be

affected.

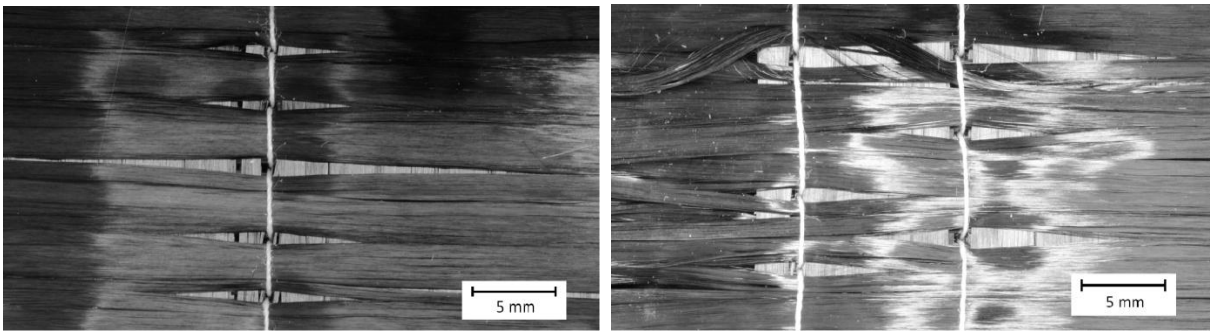


Figure 2.8: Stitch-induced defects in NCF dry preforms

Once all the seams were done, the bobbin thread tension was adjusted manually to produce a modified lock-stitch geometry, as previously shown in Figure 1.3. Thanks to the modified lock-stitch geometry, the stitch knots were produced on the back-surface of the preform as shown in Figure 2.9. This considerably reduced LTDs in the lower-side of the preform relative to the upper-side. Figure 2.9 shows the bobbin thread laid down on the back-side of the dry preform on a straight path with the needle thread looping around it.

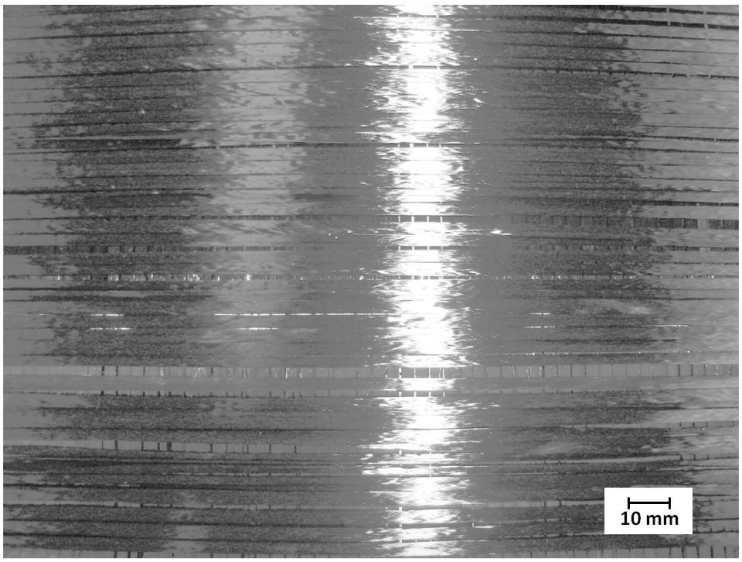


Figure 2.9: Tows arrangement around bobbin thread side of a seam

Some issues could not be controlled such as defects imparted to brittle tows during the different steps of the preforming process or inherent tow misalignment. Others were difficult to control manually such as tow twist as an outcome of the tow cutting and rolling operations. These problems were considered inherent to the preforming process. From the point of view of textile structures it was clear that the different stitched dry preforms made in the context of this thesis had some technical differences. Differences included seam interspacing and stitch length. Nevertheless, in-house made PMC components were deemed comparable in terms of their thermal behaviour, when reaching the same impregnation of the different preforms.

#### 2.1.1.2. Epoxy resin

The resin used was L-1911 two-component epoxy system, namely resin and hardener, supplied by Tri-Tex Co, Inc. (Saint-Eustache, Quebec, CANADA). The mixed epoxy was clear and had a relatively low viscosity at 25°C ranging from 200 mPa.s to 300 mPa.s which made it a good candidate for the present application, owing to its good preform wetting and long working time advantages. The gel time of 150 g of epoxy at 22°C was about one hour according to the

supplier. Trials carried out in this work showed longer gel times, reaching approximately 2 hours. The recommended cure schedule was 8 hours at 80°C. The resin was mixed with the hardener at 1 to 0.34 by weight. Detailed specifications of the epoxy resin are presented in Appendix A.


Figure 2.10: Epoxy resin components and mixing tools

### 2.1.2. RTM setup and manufacturing process

#### 2.1.2.1. RTM setup

The layout of the main components of the RTM injection setup is shown in Figure 2.11. The setup can be split into two sections: the injection system and the mould. A photograph of the injection setup is shown in Figure 2.12. It consisted of a vacuum pump, a hydraulic cylinder, a resin catch pot, a resin container, three-way valve $V_1$ and two shut-off valves $V_2$ and $V_3$. All technical information pertaining to equipment appears in the following pages. The hydraulic cylinder was attached to an Instron 4482 floor model universal testing machine (Norwood, MA, USA) available at the Department of Mechanical Engineering of the University of Ottawa. The assembly formed the resin pumping system, where the Instron machine effectively pushed resin

out of the hydraulic cylinder. The machine and hydraulic cylinder were used in injecting resin at a selected, accurate volumetric flow rate. The high load capacity and the good accuracy of the Instron machine, as well as the relatively low cost of the hydraulic cylinder, led to the choice of the current resin pumping system over a conventional resin pump.

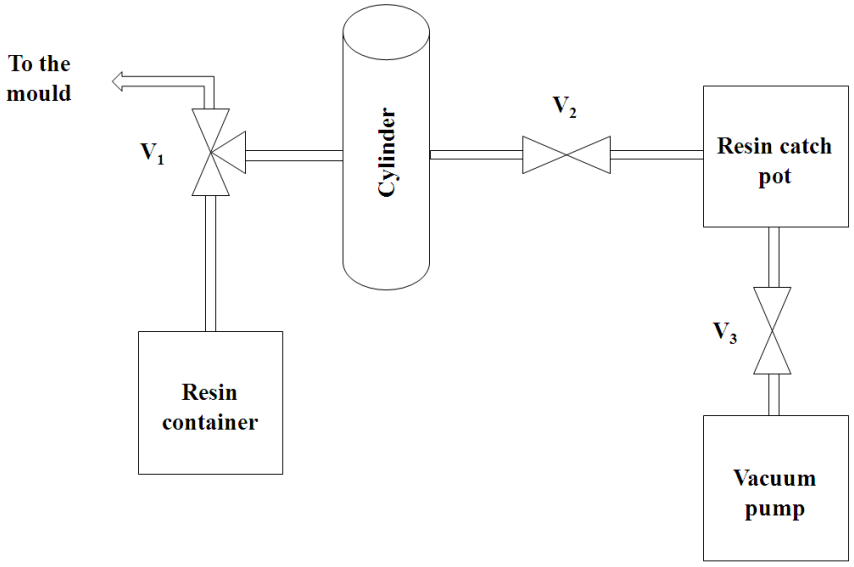


Figure 2.11: Schematic of the injection system


Figure 2.12: RTM injection setup


Figure 2.13: Hydraulic cylinder mounted on the INSTRON machine

The hydraulic cylinder, from Hy-spec hydraulik (Lachine, QC, CANADA), had a 7.6 cm bore and 20 cm stroke with maximum operating pressure of roughly 172 bars. The cylinder, shown in Figure 2.13, was attached to the load cell of the Instron using a clevis fastener-pin system. The

Instron was equipped with a 100 kN capacity load cell with a load measurement accuracy of +/- 0.5% of the reading. The Instron machine was controlled using the Bluehill 2 software installed on a computer connected to the Instron machine, Figure 2.12. The built-in data acquisition system provided load and extension measurements with respect to time at a sampling frequency up to 1 kHz.

Vacuum was applied to the injection setup to remove trapped air molecules and therefore minimise voids in the PMC component. It is worth noting that the vacuum was up to valve $V_1$ and did not connect to the mould. A DAA-V715A-EB oil-less diaphragm vacuum pump from GAST Manufacturing, Inc (Benton Harbor, MI, USA) was used for this purpose, Figure 2.14. The vacuum pump is capable of achieving a minimum absolute pressure and maximum flow rate of 31 mbar and 32.5 L/min, respectively.

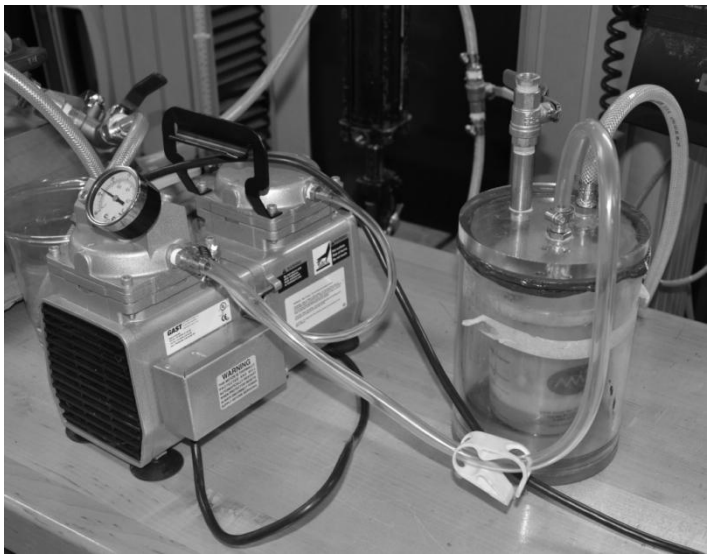

Figure 2.14: Vacuum pump and resin catch pot

The resin catch pot shown on the right side of Figure 2.14 served to prevent resin flowing under the action of vacuum during the fill of the mould, from reaching the inlet of the vacuum pump. It

was located between the vacuum pump and the cylinder. It consisted of a closed transparent plastic bucket and a cap. The catch pot cap had an inlet, an outlet and a vacuum release ball valve $V_3$. The valve was vacuum-rated and used for cancelling the vacuum whenever needed. Vacuum hose barb fittings were screwed into the inlet and outlet to ensure an airtight seal. A Teflon tape layer was applied on the threads to enhance the seal. The cap was then attached to the bucket using sealant tacky tape from Schnee-Morehead (Irving, TX, USA) to ensure vacuum integrity of the resin catch pot.

The second section of the RTM setup was the mould. Although the mould played an important role in harvesting the benefits of RTM, it was an interchangeable component in the setup. The mould cavity shape that hosted the dry preform and the dry preform inherent properties were actually the main factors that influenced the choice of the injection parameters, such as the choice of the injection flow rate. The mould cavity gave its final shape to the component and governed important in-process and post-process behaviour of the component. Its major impact on the resin flow pattern, infusion time, presence and position of voids as well as on the repeatability of the process was taken into account in establishing injection flow rates.

As very high pressures were expected during injections, fibreglass braided fabric reinforced plastic hoses with a pressure limit of about 19 bars were used for connecting the components of the injection setup. High pressure vacuum hose barb fittings, nipples and bushings with an overall safety pressure limit of about 14 bars were used for joining hoses to the different components of the injection setup in the first three trials. Teflon tape was rolled on all male threads to ensure sealing of the flow circuit.

Two moulds with different cavity shapes were used in this thesis, referred to as the 2D and 3D shapes. The 2D mould shape was a 4 mm deep cavity designed for producing flat squared composite plates with a side length of roughly 30.5 cm. The mould was CNC machined from two

41 cm side length and 2.5 cm thick square 6061-T6 aluminum plates, Figure 2.15.

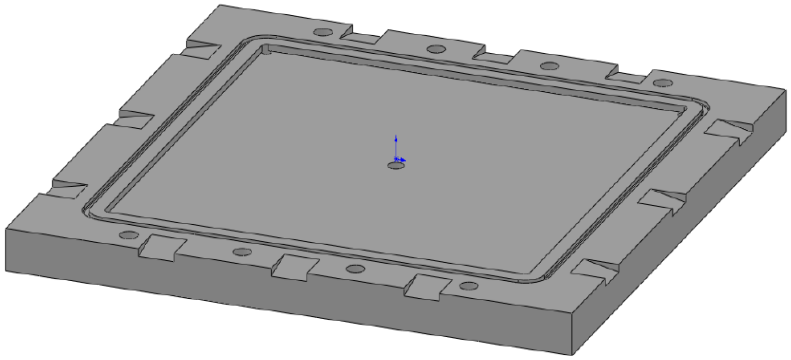

Figure 2.15: Solid model of the 2D mould

The first mould half hosted the mould cavity surrounded by a groove meant to hold a sealing o-ring in place, Figure 2.15. The resin injection port as well as the four outlet ports were machined with 3/8” diameter, and were NPT threaded to increase the seal. The outlet port diameters had a reduction to 1/4” diameter at the mould cavity surface, and were positioned at the corners of the cavity. NPT vacuum hose barb fittings were screwed into each port for allowing the hoses to be plugged into the mould while keeping an airtight seal. The second mould half surface was machined to eliminate surface waviness and improve the surface finish of the part. The 1/4” diameter o-ring placed in the groove ensured mould seal when subjected to high injection pressures. The Buna-N o-ring was made from silicone that stands temperatures from -7°C up to 100°C. Following loading with the preform, both mould halves were bolted together using 10 1/2” diameter grade five bolts to form a sealed mould cavity. The mould was then put on a table and secured to four support pods holding it in place, Figure 2.16. The table was used for the safety and mobility of the equipment. It was meant to keep all RTM setup components easily accessible and mobile while avoiding heavy lifting. The table supported the mould and positioned it at a convenient and workable height.

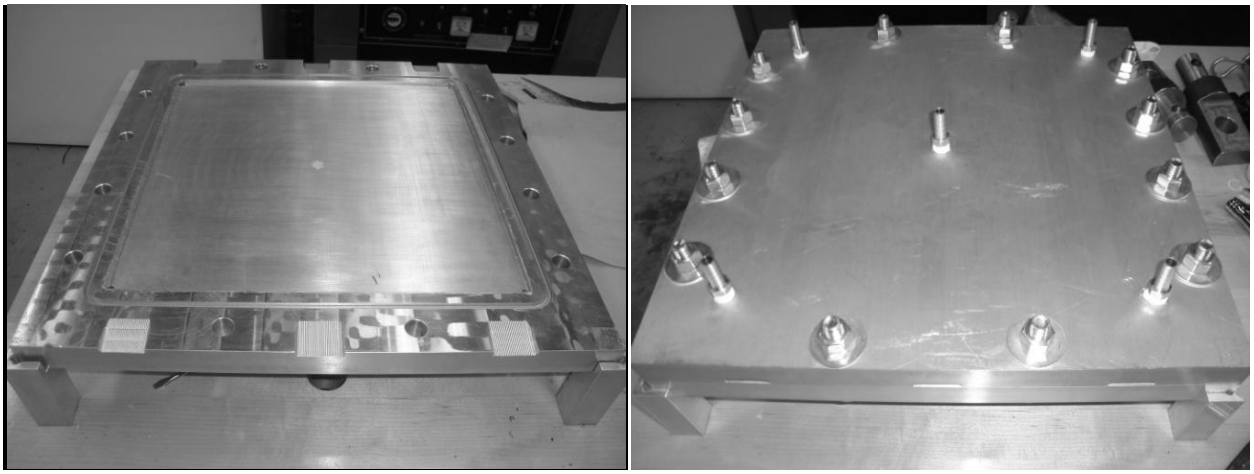

Figure 2.16: 2D aluminum mould for making PMC plates

The 3D mould consisted of a female and a male mould shown in Figure 2.17. Both mould halves were machined from approximately 10 cm thick 6061-T6 aluminum blocks. A groove was machined to host the sealing silicone o-ring. Mould halves were bolted together to form a mould cavity of thickness 4 mm able to host a preform. The male mould half housed the inlet and the outlet ports as shown in Figure 2.18. The inlet and the four outlet ports were machined at the centroid and corners of the cavity, respectively. NPT threaded vacuum hose barb fittings were screwed into all ports to allow inlet and outlet hoses to be plugged to the mould while keeping an airtight seal.

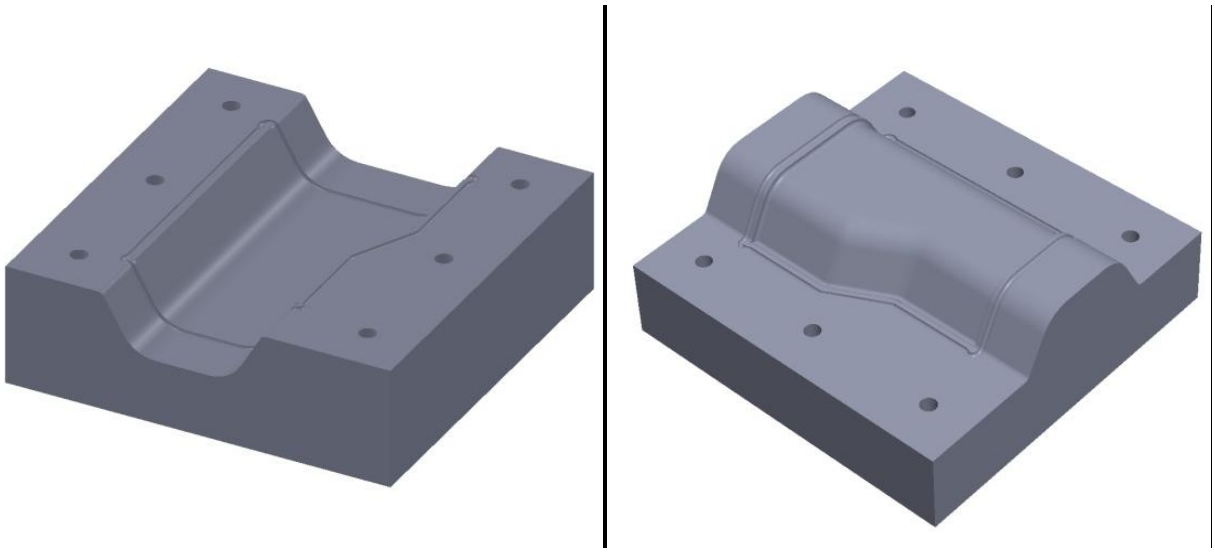

Figure 2.17: Solid model of the 3D mould: female mould (left) and male mould (right)

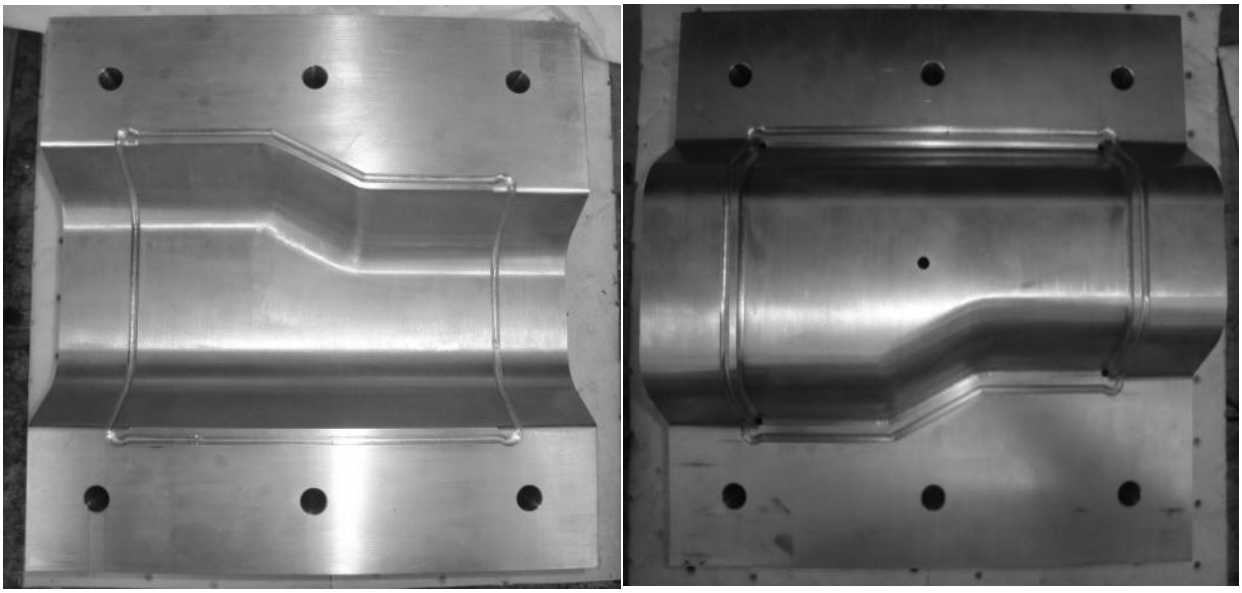

Figure 2.18: Top view the machined 3D mould: female mould (left) and male mould (right)

### 2.1.2.2. Preliminary injection

To assess the performance of the RTM setup and its ability to infuse dry preforms fully in the 2D mould, a preliminary constant flow rate injection was done using polydimethylsiloxane, a pure

silicone oil from Clearco Products (Bensalem, PA, USA), Figure 2.19. It is worth mentioning that this preliminary injection was part of a series of injections performed with fellow graduate students Andrew Stewart and Scott Audette. This silicone oil was chosen essentially due to its viscosity being comparable to that of the resin used in this thesis. The silicone oil had a viscosity of 0.485 Pa s. However, because of its colorless nature an Lx6258 polykrome bright blue dye from Pylam Products Company, Inc (Tempe, AZ, USA) was added to improve visibility of the flow front through the dry preform, Figure 2.19. According to the supplier, the dye has a good affinity to the silicone fluid, and does not alter its viscosity.

Figure 2.19: Silicone fluid used for the preliminary injection

With the same objective of improved visibility, a fibre glass preform was prepared according to the procedure described in section 2.1.1.1, Figure 2.20. A $V_f$ of 0.63 was sought in this injection. The preform contained 6 layers laid down as $[0°/90°/0°]_s$ . Again, great care was taken when cutting the preform in order to fit the dimensions of the mould cavity. This would minimise race-tracking along cavity edges associated with smaller preforms, and negate mould closure difficulties associated with larger preforms. Nevertheless, some difficulties were encountered in holding the tows near the edges in place while moving the preform manually. As shown in Figure 2.20, some tows slid out of the preform. These were put back in place manually.

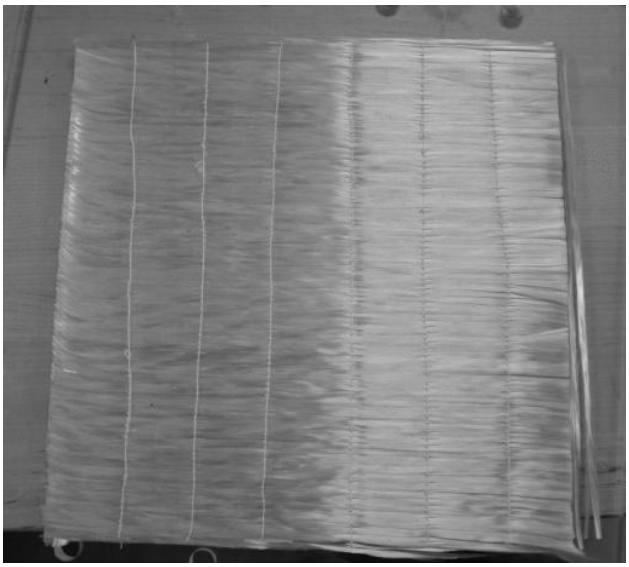

Figure 2.20: Fibreglass dry preform

The o-ring was placed in the groove and a 1.25 cm thick clear acrylic flat plate was used for closing the mould. Four steel beams were used for reinforcing the acrylic plate given the relatively high injection pressures expected. The beams, plastic plate and aluminum mould base were bolted together using 8 grade five bolts, as shown in Figure 2.21. The assembly was then placed on the table.

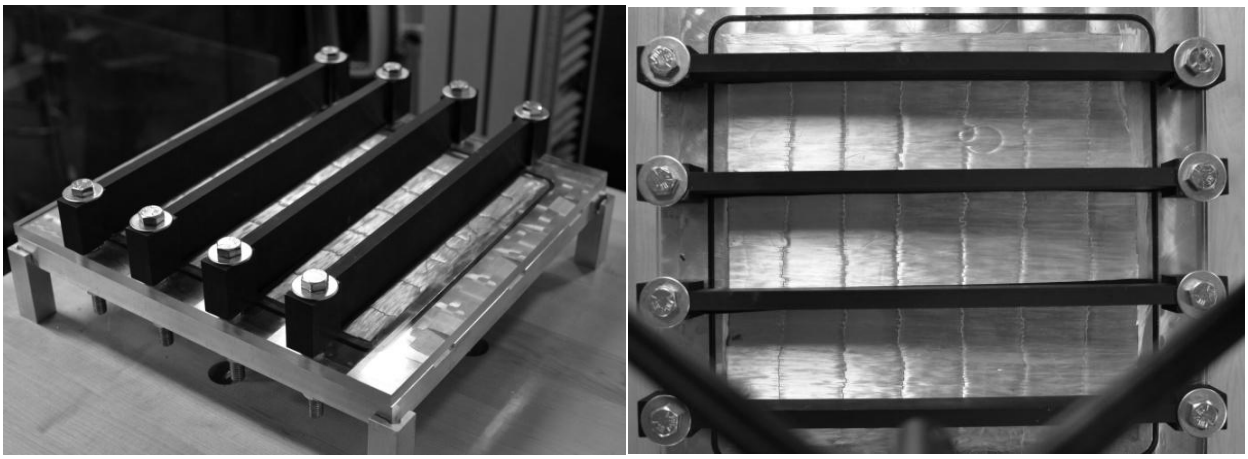

Figure 2.21: Closed mould: isometric view (left) and top view (right)

The injection system was used as described earlier in Figure 2.11 with a minor change consisting of the addition of two pressure transducers located upstream of the mould but downstream of three-way valve $V_1$. Both pressure transducers were from Cole-Parmer (Vernon Hills, IL, USA). The first pressure transducer measured pressures up to roughly 7 bars, while the second measured pressures up to roughly 20 bars. These pressure transducers were used simultaneously for providing good accuracy on measurements and accommodate any change in pressure magnitude. Figure 2.22 shows the pressure transducers mounted on a cross hose fitting, as well as the silicone fluid catch pot and vacuum pump. Changes in pressure values with time were recorded using Labview software from National Instruments Corporation (Austin, TX, USA). The closure speed of the cylinder was calculated using the law of conservation of mass, making the assumption of incompressible silicon oil:

$$V_{in}\, A_{in} = V_{cyl}\, A_{cyl} \qquad 2.1$$

where $V_{in}$ and $V_{cyl}$ are the silicone fluid flow velocity at mould inlet and in the vicinity of the piston respectively, while $A_{in}$ and $A_{cyl}$ are the inlet cross-section area and piston area, respectively. Based on a 0.2 cc/s injection flow rate, the closure rate was set to a constant 2.63 mm/min. This caused the silicone oil to flow at a constant flow rate out of the cylinder. The injection was done from the bottom of the mould to have a good top view visibility during infusion; the injection was also videotaped from the top. Outlet hoses from which silicone oil escaped the mould were diverted into plastic bottles. Figure 2.22 is a view from below the mould which shows the silicone fluid container, the three-way valve $V_1$ and the pressure transducer.

Figure 2.22: Setup below the mould: side view

Preparation for the injection started with opening the cylinder about 15 cm with valve $V_1$ closed, and valves $V_2$ and $V_3$ open. Vacuum was drawn so as to remove air trapped in the hoses and cylinder, up to a vacuum of roughly 99%. At an acceptable vacuum level, $V_1$ was opened slightly to allow silicone oil to flow into the cylinder under the effect of the vacuum, and eventually fill the cylinder. When the silicone oil flow front was seen downstream of $V_2$, both $V_1$ and $V_2$ were closed. At this stage, the cylinder was filled with silicone oil and ready for injection. A new Labview data acquisition session was started to record pressures read by the transducers.

The injection process started with simultaneously opening $V_1$ upstream of the mould and starting the closing of the cylinder. Pressure magnitudes displayed on the Labview station, as well as the load profile displayed by the Bluehill 2 software, were constantly monitored, with in the intention of tracking the progress of the injection as well as ensuring that injection pressures stayed within the safety limits of the RTM setup. Upon opening $V_1$, some air travelled by gravity through the injection hose, to reach the cylinder outlet. Most of this air was simply vented as

silicone oil was pumped by the cylinder into the mould. The injection was left to continue until the mould was filled.

Impregnation progress at 80 s, 140 s, 280 s and 390 s appears in Figure 2.23. The figures show that silicone oil race-tracked along the seams as well as in the channel formed between the preform and o-ring. This channel was formed owing to some tows that slipped out of the mould cavity to prevent the mould from being firmly closed at the exact cavity thickness. Hence, a channel was created around the preform where silicone oil flow met less resistance compared to the dense porous preform.

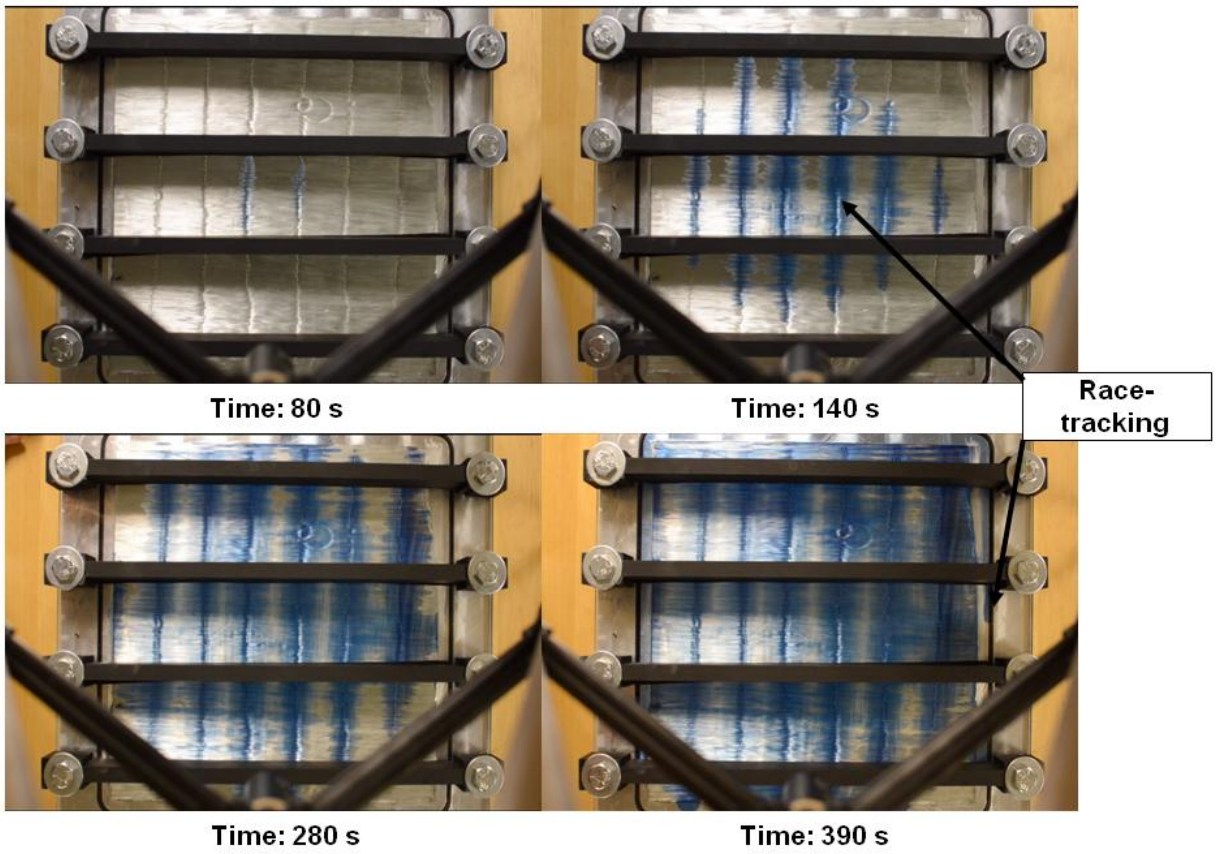


Figure 2.23: Impregnation of the glass preform at different time steps

Mould filling time was roughly 8.5 min in this preliminary experiment. The inlet injection pressure profile is presented in Figure 2.24. The pressure profile starts with a plateau at 1 bar until about 240 s. Next, pressure jumped linearly from 1 bar to roughly 3 bars in about 20 s. This big jump in pressure can be explained by the flow front reaching areas of higher resistance to flow: this marks the start of flow through the preform, in the though-thickness and in-plane directions. Subsequently, a small drop in pressure is seen where pressure reached roughly 2.6 bars at 260 s. This drop can be tentatively explained by the release of a flow front pressure build-up underneath the dry preform while trying to penetrate the preform in the though-the-thickness direction. Silicone oil starts to flow in-plane, translating in pressure increases up to roughly 3 bars. The pressure plateaued afterwards for the last 1 min of mould filling.

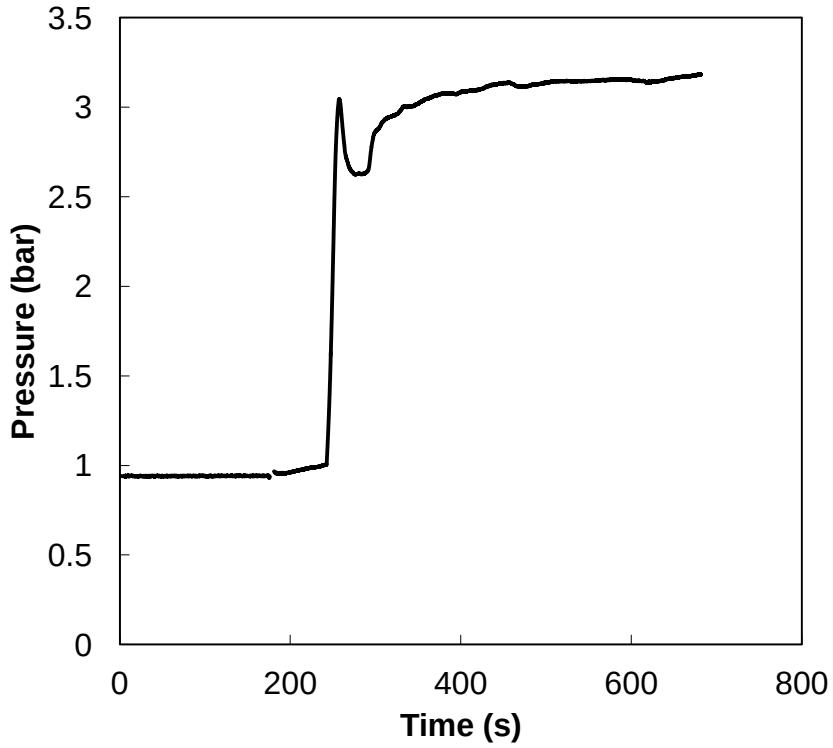


Figure 2.24: Mould inlet injection pressure profile

A top view of the filled mould appears in Figure 2.25. Silicone fluid is seen to be agglomerated

along the seams, though this may be an optical effect resulting from the volume of resin concentrated above the seams. Dry lines can be observed between the seams. Dry sections in an impregnated preform constitute a major issue. The general impregnation behaviour was expected as stitching compressed the preform along the seams to form channels between the preform and the mould walls. In the vicinity of the seams, permeability seemed lower than in these channels. This drove the silicone oil to flow in these channels and by-pass higher $V_f$ zones.

Figure 2.25: Top view of the infused preform

Silicone oil bypassed the o-ring, which was supposed to give an airtight seal. The o-ring failed to provide the required seal owing to the mould not being closed properly. Fibres which slid out of the mould cavity were trapped between the two mould halves, prevented proper closure. This brought up the importance of cutting preforms, used later on in this thesis to manufacture PMC components, with precise dimensions and minimal fray.

#### 2.1.2.3. Manufacturing of PMC components

The RTM setup described earlier was used in manufacturing PMC components in this thesis. Assessment of setup performance and safety was presented in the previous section. A total of 5 PMC components were manufactured in this thesis; 4 flat plates and a 3D demonstrator component.

##### 2.1.2.3.1. Preform draping and loading

Carbon fibre preforms used for manufacturing the PMC components were made according to the procedure highlighted in section 2.1.1.1. The demonstrator PMC component was made from a dry carbon fibre preform draped over the demonstrator mould. No draping was necessary for the PMC plates. All preforms were cut and loaded in the moulds following the same procedure described in this section.

In case of the demonstrator preform, the choice of ply orientations was made after shear angle analysis of the draped preform over the demonstrator mould. UO Drape software tool developed by Burnford [106] at the PMC Manufacturing Laboratory, University of Ottawa was used for simulating the shear angle distribution in draped preforms. A triangle surface mesh was generated and imported into UO Drape software where the first geodesics were generated. The geodesics according to -45°/45° directions are shown in Figure 2.26.

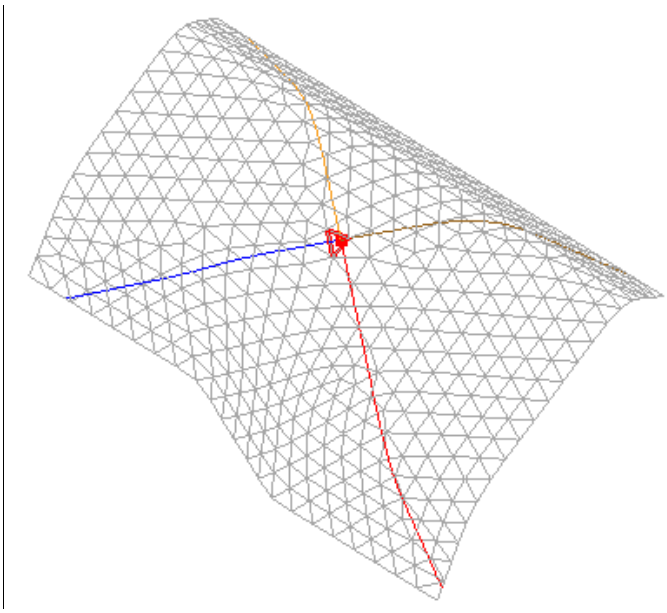

Figure 2.26: Surface mesh and geodesics of the 3D demonstrator solid model

The next step involved the drape simulation of a -45°/45° dry preform. 4 mm spacing between adjacent tows was set for purposes of display clarity. Simulation of the draped -45°/45° dry preform showing the tow paths appears in Figure 2.27.

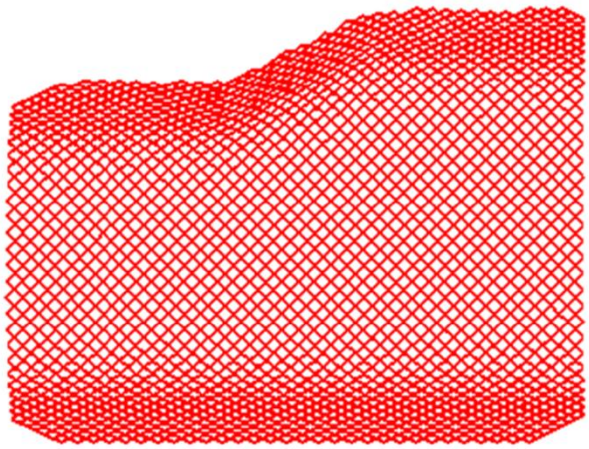

Figure 2.27: Simulated tow paths of a draped -45°/45° dry preform

As previously discussed in section 1.2.2.5, a cross-directional lamination sequence ensures in-plane thermal isotropy in a PMC component. Owing to the draping of a preform over a 3D shape, in-plane shear can modify the angle between the stacked carbon fibre plies locally. Figure 2.27 shows the tow paths of the draped preform. The extent of in-plane shear effect on the local shear angle was assessed using UO Drape. Shear angle distribution for two different ply lamination sequences were simulated, namely $[0°/90°/0°/90°/0°/90°/0°/90°/0°]_s$ and $[45°/-45°/45°/-45°/45°/-45°/45°/-45°/45°]_s$. Figure 2.28 below shows the shear angle distribution for both preforms.

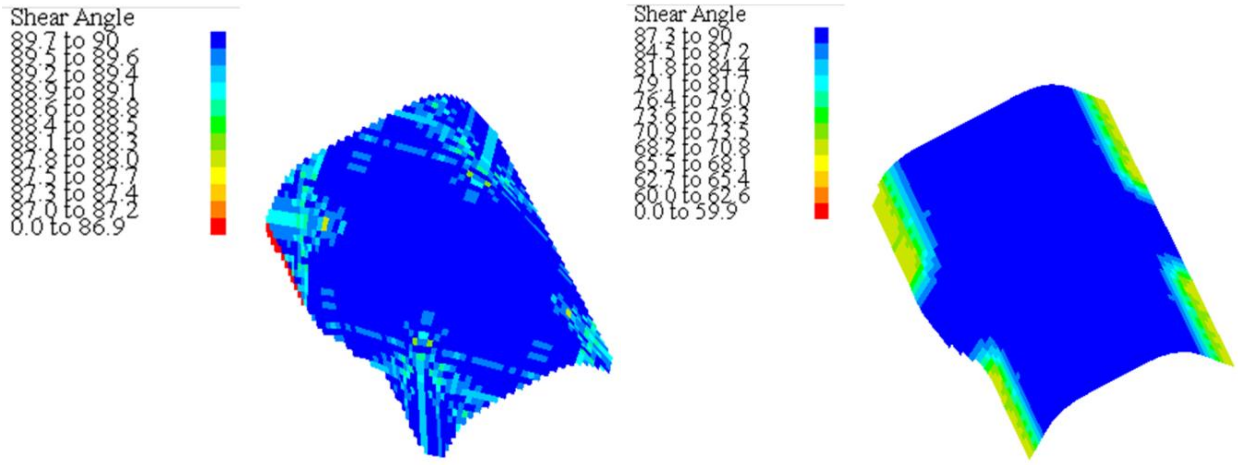


Figure 2.28: Shear angle of a draped dry preform: -45°/45° (left) and 0°/90° (right)

Starting from an initial situation where the flat, undraped preform is characterised by 90° inter-yarn angle throughout, simulation results presented above suggested that the -45°/45° draped preform features very limited surface areas where tows are sheared significantly. Tow shear angles did not drop below a 87° threshold. Conversely, the 0°/90° draped preform exhibited large areas where the tow shear angle distribution varied from 90° (no shear) down to 63°. These areas were located near the corners of the preform. Seeing this important discrepancy in shear angle distributions with larger shear angles found in the case of 0°/90° lamination sequence, the -

45°/45° lamination sequence was chosen for manufacturing the demonstrator PMC preform and component. Unwrapping of the demonstrator 3D solid model was done using UO Drape. The outcome was a 2D contour with dimensions appearing in Figure 2.29.

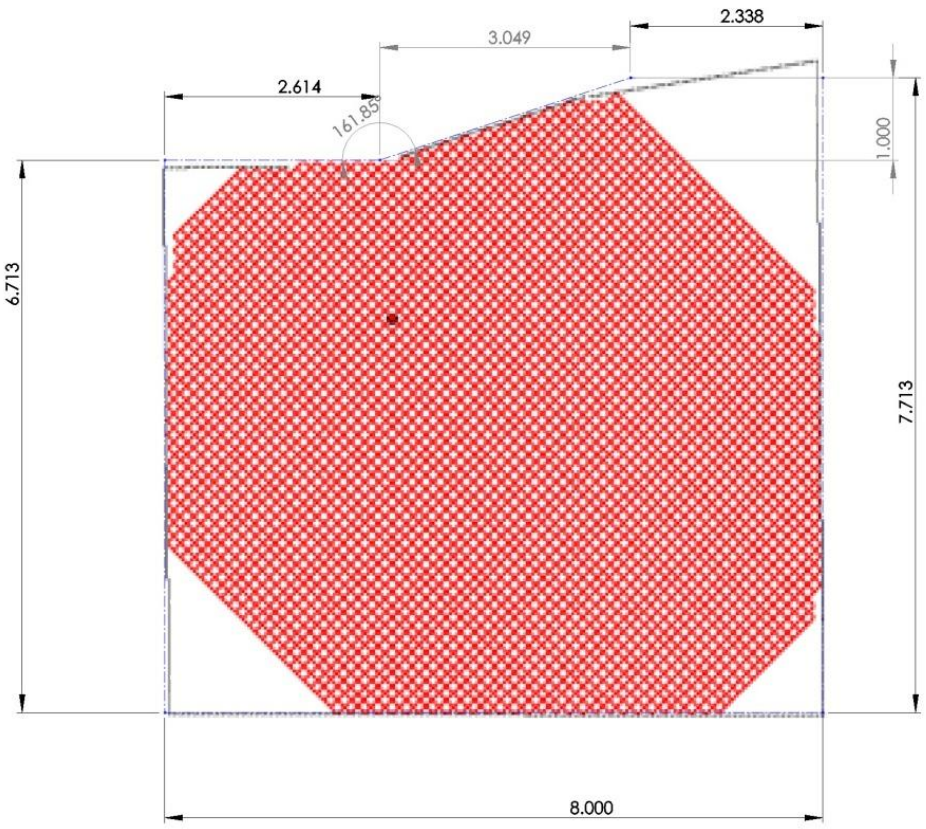


Figure 2.29: Contour dimensions of the demonstrator dry preform (inches)

Cutting the dry preform to the contour dimensions conforming to the mould cavity once draped was a crucial step in the preforming process as it was implemented when this thesis work was conducted. After placing the dry preform in the mould cavity, RTM requires the mould to be closed without any fibres present outside of the actual cavity to avoid resin leakage during the injection, or defects in the PMC component. Complete mould closure might not be achievable if the dry preform overlaps the cavity. On the other hand, a preform with noticeably smaller

dimensions than required would cause the resin to race-track along its edges.

In this thesis, dry preforms were clamped between a wood slab covered with a flexible plastic sheet and an aluminum plate, using C-clamps. The aluminum plate had dimensions slightly smaller than those of the mould cavity, to account for potential irregularities introduced by the manual cutting operation, Figure 2.30. Relatively high and uniformly distributed clamping pressure was exerted onto the dry preform to keep the fibrous tows from shearing in-plane during the cutting operation. The assembly was placed on a bench to ensure a workable height.

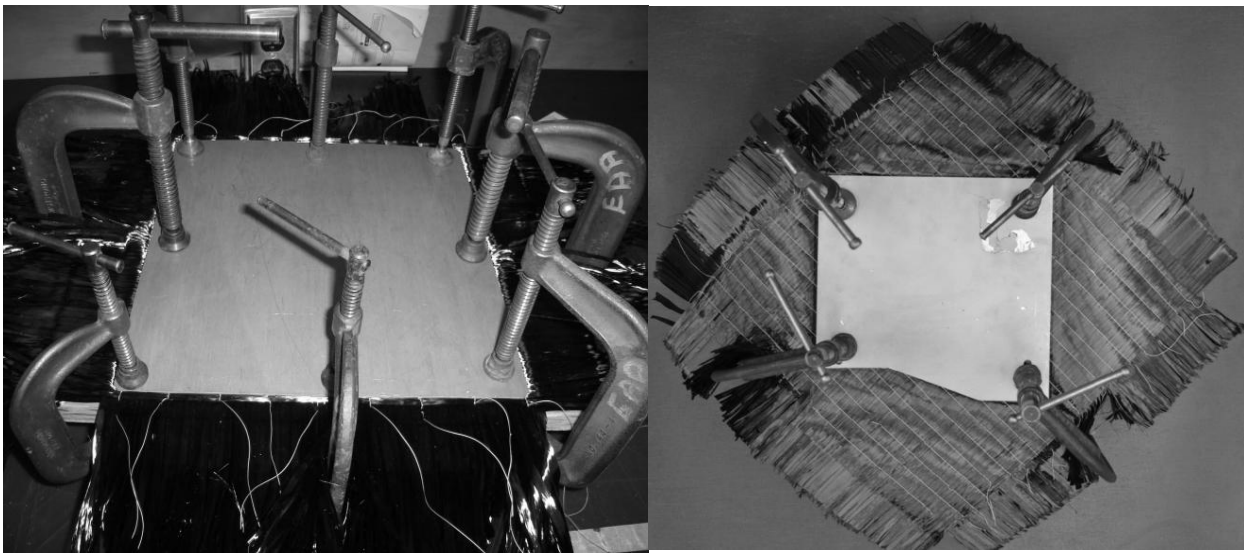

Figure 2.30: Clamped stitched dry preforms, ready to be cut

A snap-off high-duty blade was used for cutting the dry preforms as shown in Figure 2.31. The blade was forced to penetrate the dry preform, then it was pulled backwards in a continuous motion. A considerable downwards pressure was applied on the blade during the cutting operation. Great care was given to keeping the blade tip in motion as closely as possible to the aluminum plate. This was done for reducing in-plane edge waviness, so as to ensure easy mould closure. A cut 2D dry preform destined at manufacturing the demonstrator PMC component is

shown in Figure 2.32.

Figure 2.31: Cutting of dry preform using a snap-off blade

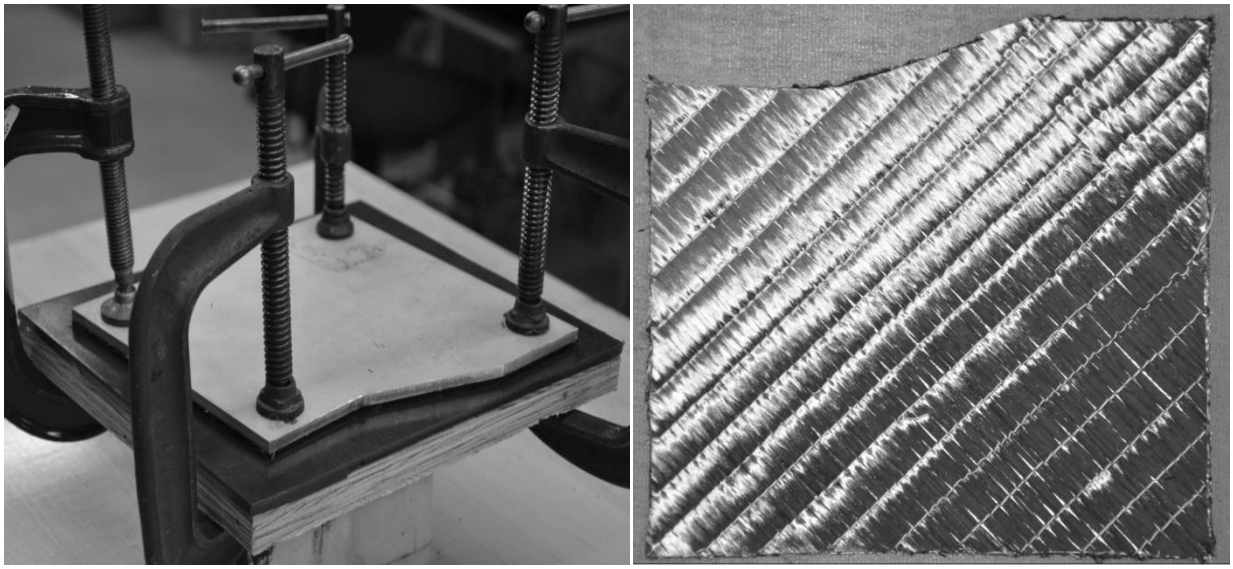

Figure 2.32: A stitched dry preform, cut

Dry preform handling and loading was a delicate task. Following the cutting operation, some

preforms had seamless areas which made them fray. Reduction of fray during preform handling was achieved by sliding a thin and strong flat plastic sheet underneath. The plastic sheet was used as a support for the dry preforms until their positioning in the mould cavity. Preform loading was carried out by slowly sliding the preform supported by the thin plastic sheet inside the cavity while aiming at the cavity edges. Then the preform was gently pushed down using gloved fingertips and fitted manually inside the mould cavity.

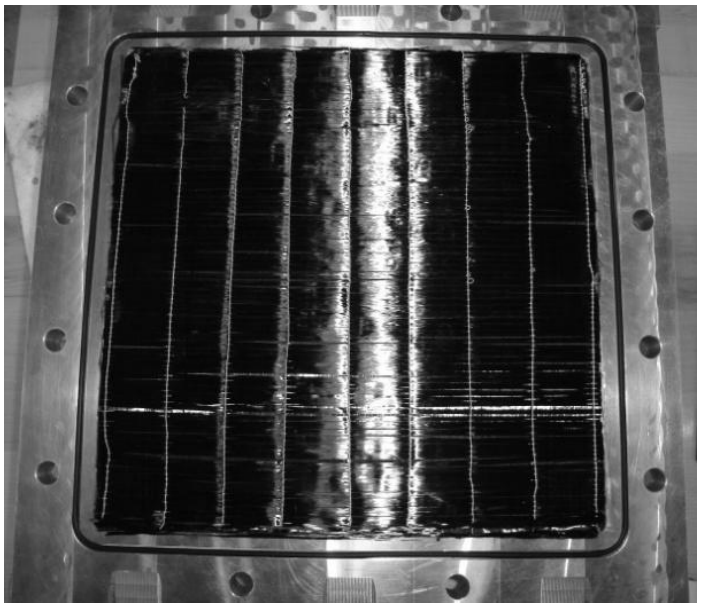

Figure 2.33: Dry preform placed in the 2D mould

Preform loading was somewhat delicate in the case of the demonstrator component. The preform was gently slid from the plastic sheet used as a support and positioned on the top of the male mould half as shown in Figure 2.34. It was positioned so that when draped, it would fit into the mould cavity. Then, a clear acrylic female mould half was used for pressing on the dry preform, bending it to the 3D demonstrator shape. Before placing the aluminum mould half, good positioning of the dry preform inside the mould cavity was ensured. The setup shown in Figure 2.34 was left to stand for approximately 1 hour before the acrylic female mould half was removed and replaced by the one made from aluminum.

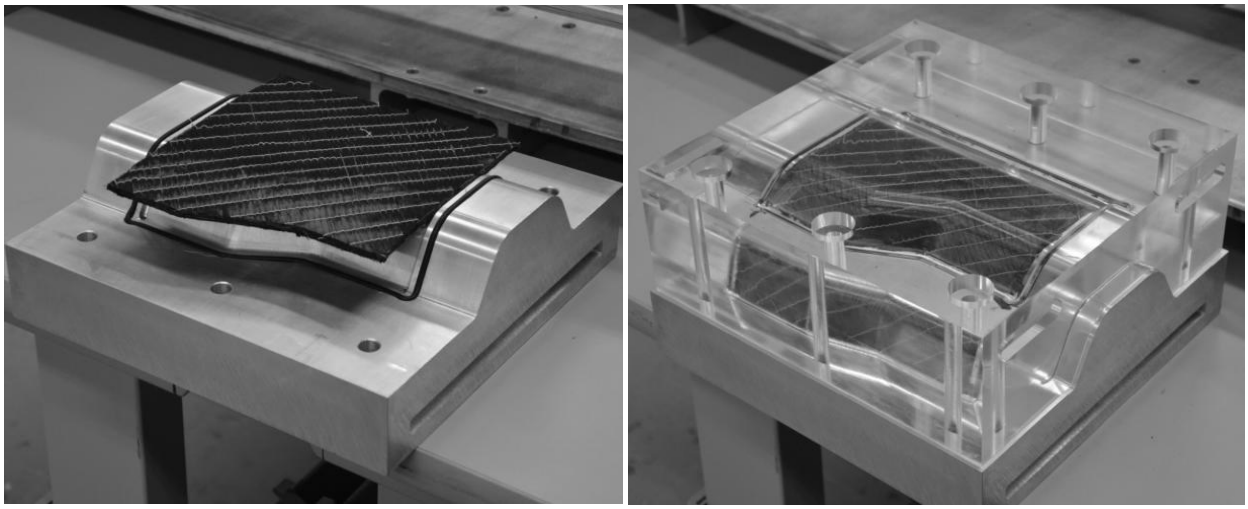

Figure 2.34: Draping of the demonstrator dry preform

Tow waviness and misalignment were observed after draping of the preform over the mould. The preform deformed in shear and created local tow distortions or enlarged existing ones. Overall the draping method used in this thesis lead to good results.

#### 2.1.2.3.2. Resin injections

Injection process steps were similar to those of the preliminary injection though it is worth mentioning that resin injections were made from the top of the mould. The flow rate was set via the Bluehill 2 software by setting up the cylinder compression speed. One additional difference with the preliminary injection was that only data for load applied on the cylinder was available, since pressure transducers could not be used during PMC components manufacturing. Mould release was applied on mould surfaces as well as on the hose fittings before each injection. A new o-ring was placed upon every injection to keep the same seal quality for all injections. High temperature silicone was also added for sealing the demonstrator mould. New hoses and valves were necessary for every injection.

The mould was closed after preform loading as shown in Figure 2.35. Once the injection setup was prepared according to the instructions in section 2.1.2.1, a sufficient amount of resin was mixed. The amount of mixed resin was overestimated for allowing the resin to flow as long as possible in the venting hoses after having the mould cavity filled. This was done in the aim of allowing trapped air in the mould cavity to be expulsed.

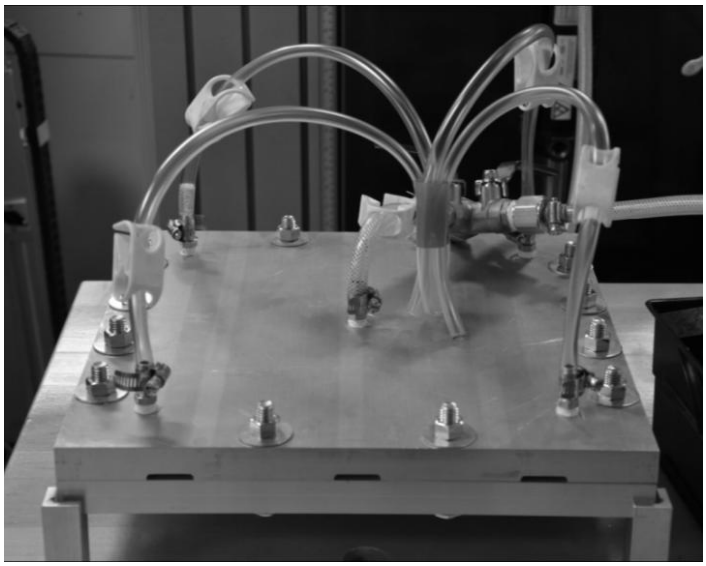

Figure 2.35: 2D mould setup

Resin was injected and then clamps were positioned on venting hoses for blocking resin flow once it had travelled at least 5 cm out of the mould, along the venting hose. Injection flow rates for the different PMC components are presented in Table 2.2. The profile of the load exerted on the cylinder was continuously monitored to ensure a safe and good progress of the injection. Venting hoses were clamped one by one whenever resin was seen to exit the mould cavity. Clamping venting hoses forced the resin to flow in the direction of other vents where the preform had larger dry areas. The last venting hose was kept open while the resin was still being pumped into the mould for allowing air bubbles to be vented, Figure 2.36.

Table 2.2: Injections flow rates

| Component | Injection flow rate (cc/s) |
|---|---|
| PMC plate N°1 | 0.2 |
| PMC plate N°2 | 0.1 |
| PMC plate N°3 | 0.1 |
| PMC plate N°4 | 0.1 |
| Demonstrator | 0.08 |

Figure 2.36: Air bubbles leaving the mould

The injection was stopped either when the pressure safety limit or resin gel time was reached. Resin was considered to have gelled after about 2 hours and 15 min after mixing. The remaining venting hoses and the inlet hose were clamped to maintain resin pressure inside the mould. This prevented resin under pressure from popping up from the inlet once this was disconnected from the cylinder. Subsequently, remaining resin in the cylinder was vented back in the resin container and the inlet hose was disconnected from the injection setup. Load profiles applied by the Instron machine on the cylinder for injections corresponding to PMC plates N°1, N°2 and N°3 appear in Appendix C. Considerable variability was observed in load profiles during the first 2000 s of the injections. Load increase behaviours also varied significantly. These discrepancies were hard to explain since resin injection pressure data was not available.

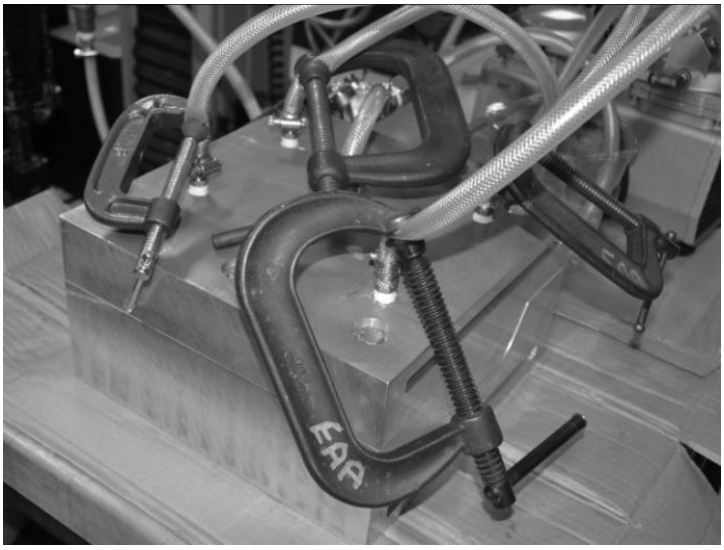


Figure 2.37: Clamped hose vents of demonstrator mould

The PMC component was then left to cure inside the mould for 8 hours at 80°C. The cure was done in a furnace, Figure 2.38. Mould inlets and vents were kept clamped during the cure process. Following every injection, components such as fittings, valves and bushings were flushed manually in an acetone bath. Cleaning the valves was difficult since even very small amounts of resin left in the valve caused total dysfunction once cured. Hence, valves were discarded after use. Resin remaining inside the cylinder was left to cure for a few days. The cylinder was dismantled and cleaned. All o-rings were checked and replaced if necessary. Cylinder inlet and outlet were drilled out and mould release was applied on the inner surface of the cylinder.

Figure 2.38: Cure of PMC components

The mould was left to cool down after completion of cure. The next step was removal of the PMC component, or demoulding. Demoulding constituted a delicate task since one had to avoid damaging the PMC component and mould surface. All fittings were removed first, and then the mould was opened. Figure 2.39 shows an open mould after cure. Cured epoxy resin at the inlet and vents held the PMC component in place owing to the presence of threads and geometry of the ports. Cured epoxy was drilled out and punched while great care was given to protect the threads. Then, using a punch the PMC component was hammered from the vents and inlet. This was done gradually until one or more corners popped out so they could be wedged out. Metallic and plastic wedges were used for demoulding PMC components. The use of metallic wedges was avoided as much as possible since these would easily damage the mould surface and delaminate the PMC component. Demoulding the demonstrator PMC component appearing below in Figure 2.39 was easier than the PMC plates since it was subject to fewer constraints from mould cavity edges.

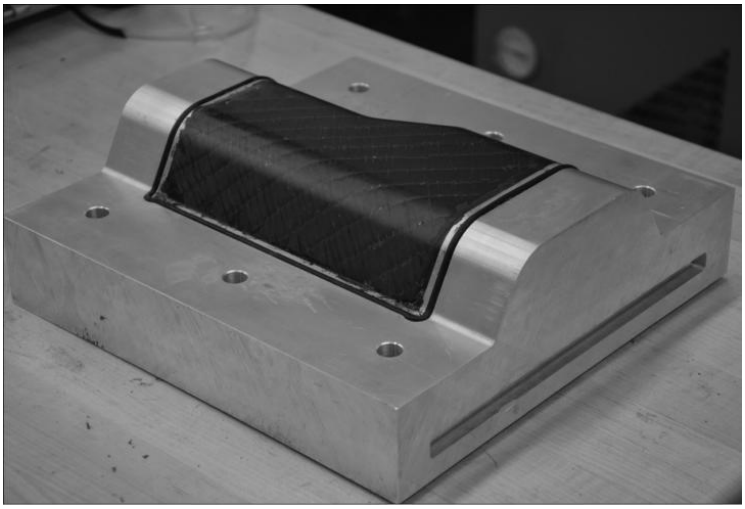

Figure 2.39: Opened mould after cure

#### 2.1.2.4. Inspection of PMC components

After removing the PMC component from the mould, edges were trimmed using a snap-off blade. Cured resin in the inlet and vents took the form of epoxy pins attached to the PMC component. These epoxy pins were cut and filed while protecting the surface of the PMC component with adhesive tape. A flat plate and demonstrator PMC components are shown in Figure 2.40 and Figure 2.41, respectively.

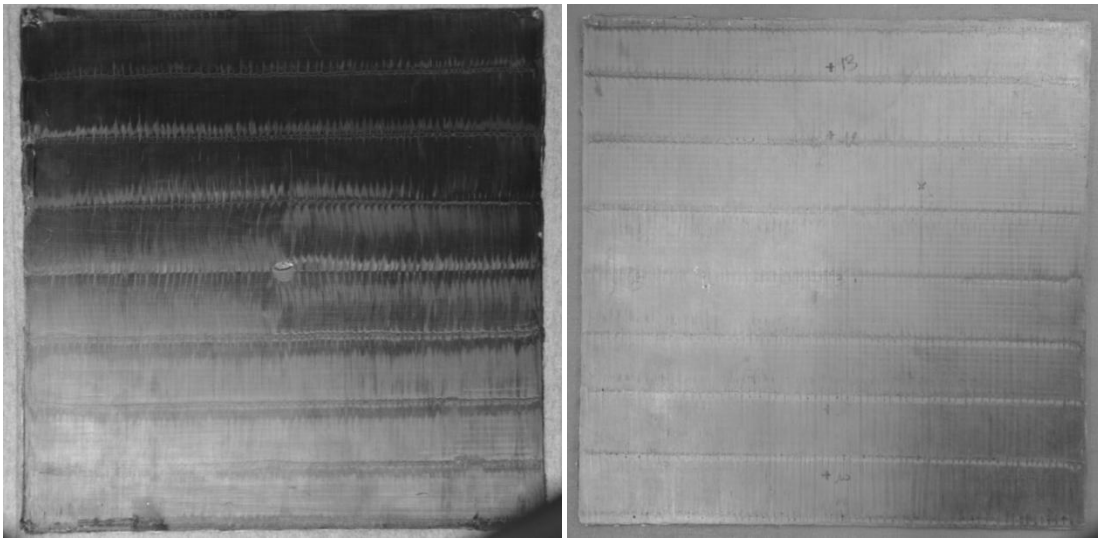

Figure 2.40: PMC plate N°4: top view (left) and bottom view(right)

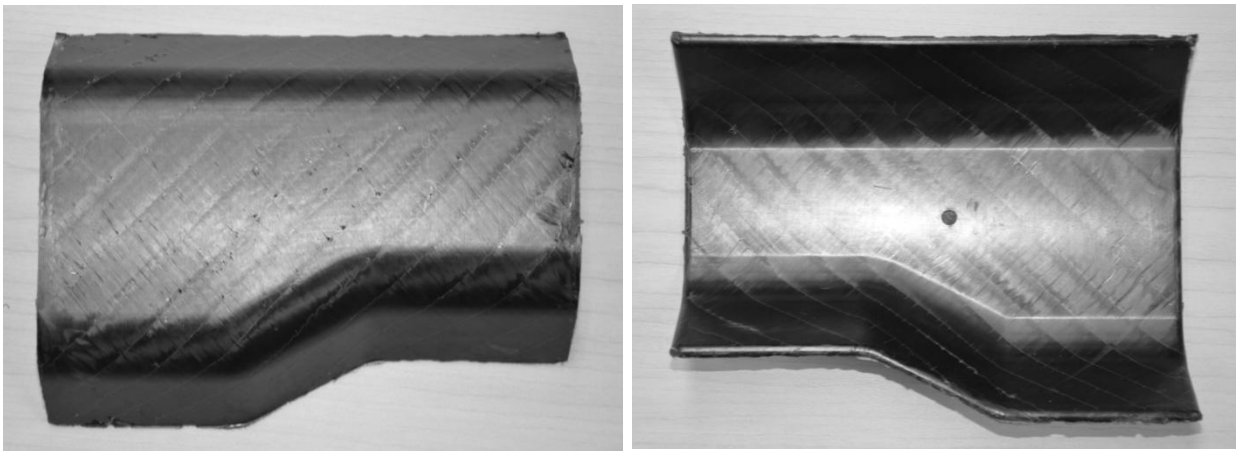

Figure 2.41: Demonstrator PMC component: top view (left) and bottom view (right)

Different macroscopic defects were noticed on the PMC components. For the PMC plates, common defects were minor dry spots in-between the seams, Figure 2.42, and bent tows in the vicinity of the injection inlet as well as near the corners, Figure 2.43. Areas in the vicinity of seams were clearly resin rich zones.

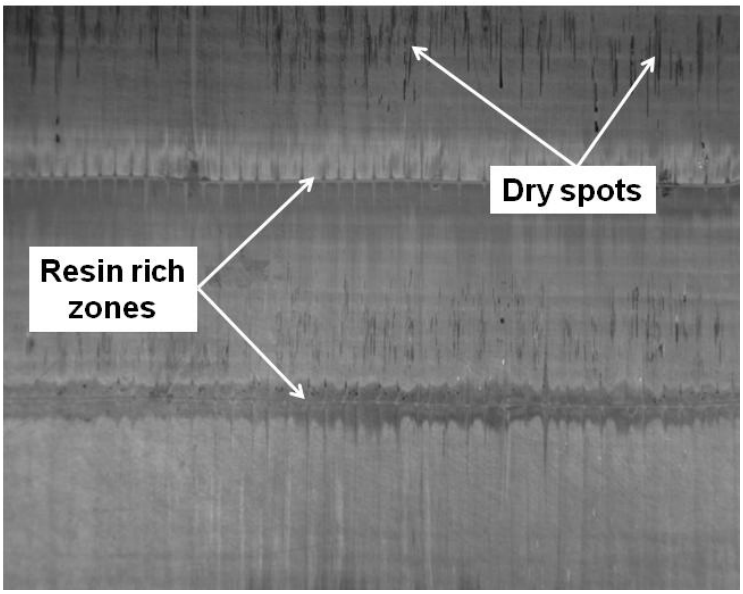


Figure 2.42: Dry spots and resin rich zones in a PMC plate

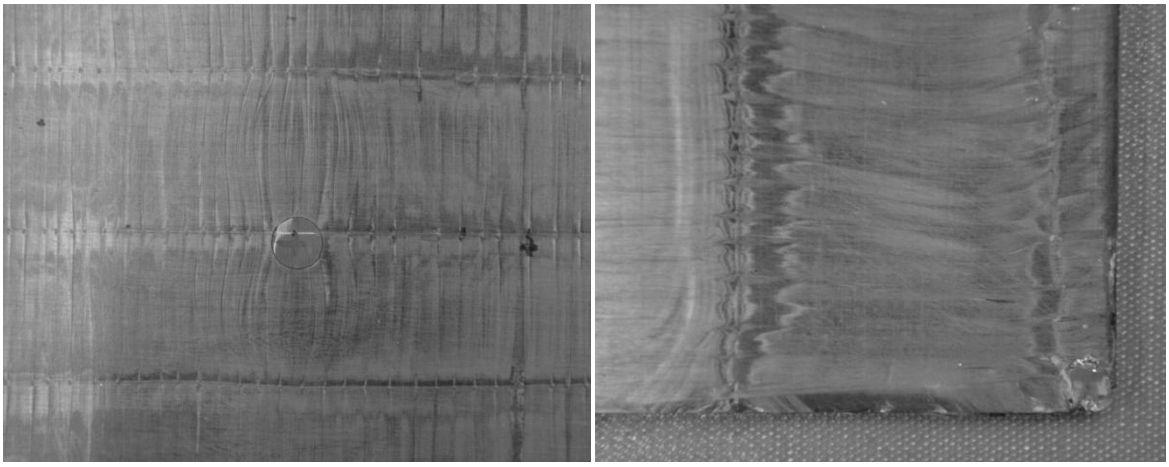

Figure 2.43: Bent tows around the inlet (left) and near a corner (right)

Dry spots can be explained by the out-of-plane tow crimp introduced by the compression exerted by seams on the dry preforms. On the other hand, tow bending in the vicinity of the inlet was explained by the relatively high injection pressures. Nevertheless, one cannot conclude reliably on this issue since pressures were not recorded directly. Buckled tows were observed at the corners of the plates as illustrated in Figure 2.43. Another type of defects was the delamination

of corners caused by the demoulding process, Figure 2.44.

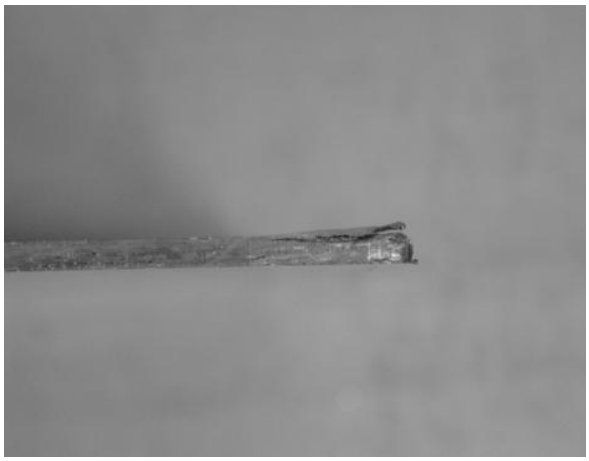

Figure 2.44: Delaminated corner in a PMC plate

Small dry spots were also present in the demonstrator PMC component. Nevertheless, these were mainly located in the vicinity of the vents. Resin rich zones were present in some corners owing to the draping process or preform fray, Figure 2.45. Bent tows were also observed in the vicinity of the injection inlet, Figure 2.46. Overall defects were small and components reached good impregnation with few trials needed for achieving good results.

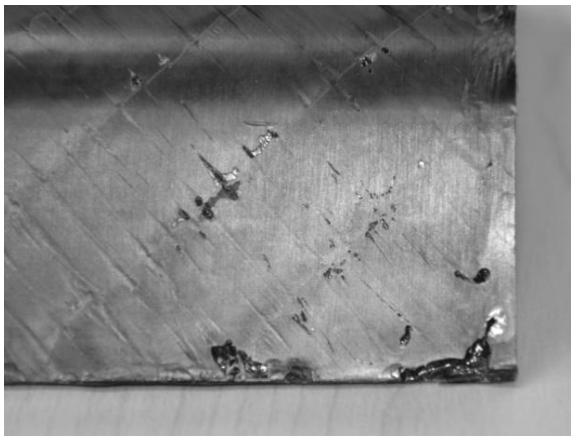

Figure 2.45: Dry spots in the vicinity of a vent

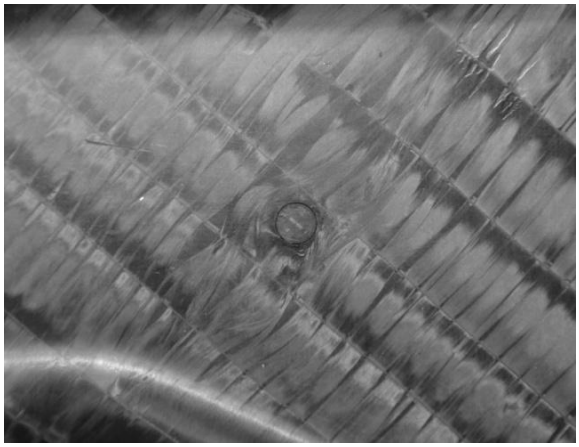

Figure 2.46: Bent tows in the vicinity of the inlet

To characterize PMC components at the microscopic level, a number of 12 square samples with roughly 1.5 cm side length were prepared. Four samples were taken from each of the first PMC plates N°1, N°2 and N°3. Cutting the samples was done using a diamond table saw at speed of 2200 rpm. The diamond saw was equipped with a water jet for cooling and flushing away dust particles. Two samples were taken from a distance of 2 cm from the edge while the remaining 2 samples were taken from a distance of 12 cm from the edge. Each sample was fixed with a clip then placed in a 3 cm diameter sample plastic cup treated with release agent. Having 2 samples from each location allowed for placing one at 0° and the other at 90°. A fluorescent epoxy resin was carefully poured to fill the sample cups. Epoxy was left to cure overnight at room temperature and then the assembly was demoulded. Following curing, the epoxy plugs hosting the samples were polished in a 3-steps process to gradually reach a 3µm roughness. This roughness was found to give good visibility during micrography of the samples. A micrograph of a sample taken from PMC plate N°2 at a distance of 12 cm off the edge is shown in Figure 2.47.

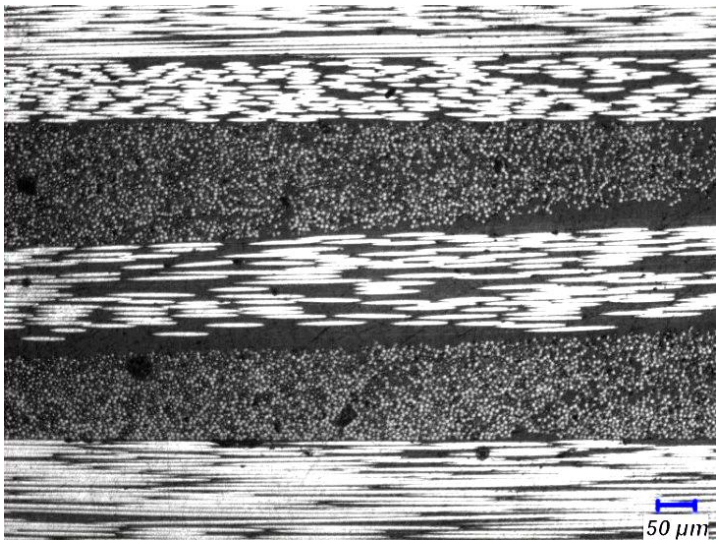


Figure 2.47: Micrograph of a PMC sample

The micrograph shows the carbon fibres plies in the 0° and 90° directions. Good proximity is observed between the carbon fibre plies with some rich resin zones which vary in extent. Minor resin rich zones are observed within plies in the 0° direction. On the other hand, in-plane waviness can be noticed in the 90° plies. It appears that discontinuities in the stranded fibres constituting a given ply were compensated by the presence of resin. Scanning electron microscopy of the same sample is shown in Figure 2.48. Carbon fibre plies can be easily distinguished in the figure and fibre packing appears to be fairly uniform. Figure 2.49 shows a higher magnification of the same sample. One can easily notice the good bonding between the fibres and the matrix. Void content appears to be very limited and some fibre cross-sections appear to be damaged because of the cutting process during sample preparation.

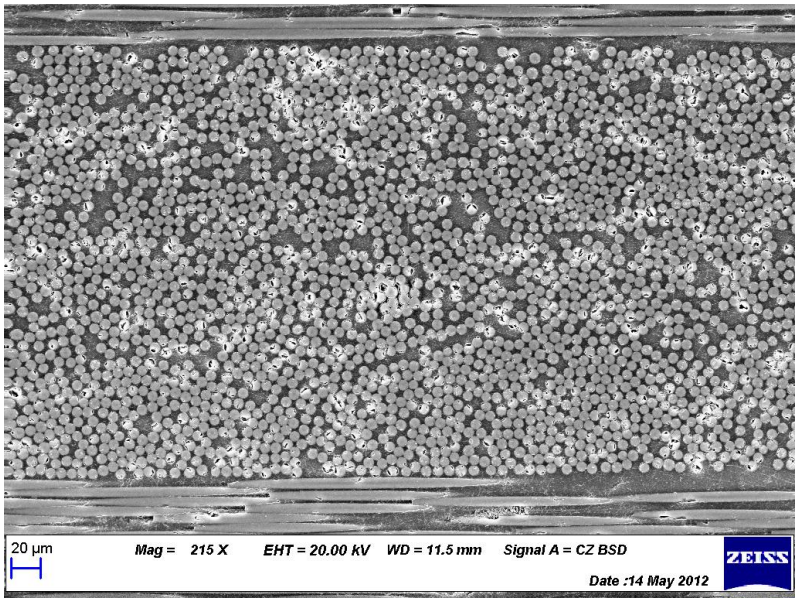


Figure 2.48: Scanning electron microscopy of fibre packing in PMC plate N°2

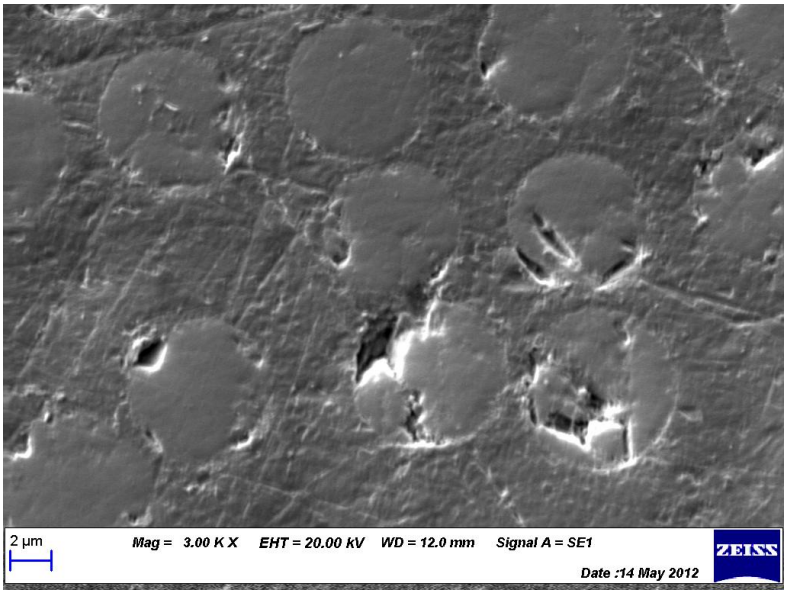


Figure 2.49: High magnification SEM image of fibre-resin interface areas in PMC plate N°2

Compression of preforms from the stitching process was evaluated using micrography. A micrograph of a PMC sample in the vicinity of a stitch is shown in Figure 2.50. It can be clearly

seen that the carbon plies are aggregated in the vicinity of the stitch under the action of high thread tension. The channel created along the seams discussed earlier in section 2.1.2.2 appears as resin rich zone.

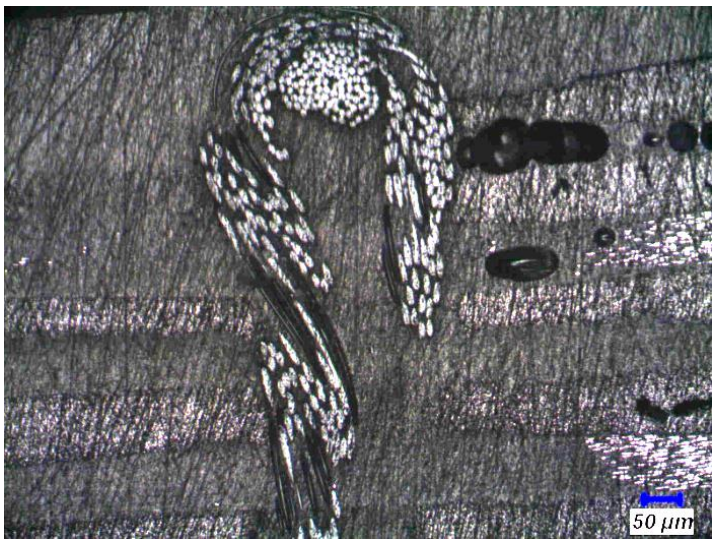


Figure 2.50: Micrograph of the vicinity of a stitch

Resin rich zones extend through-the-thickness along the sewing thread. The needle penetrating the strand of arranged tows created a hole causing damage to the carbon fibre bed. The damaged area was filled with resin upon injection. Another microscopic defect caused by the stitch was the aggregation of air bubbles in its vicinity. Air bubbles travelling under the pressure gradient towards the mould vents were blocked by the seams and the relatively low permeability of its surrounding.

## 2.2. Experimental investigation of temperature distribution through PMC components made in-house

Exposure of thin composite components to discrete heat sources was investigated for assessing

the thermal behaviour and repeatability of PMC components manufactured in the course of this thesis. The intent was also to explore the effect of the PMC component material on the temperature distribution. Temperature history was recorded during heating of a given PMC component using thermocouples and/or IR thermography. Tested PMC components included, in addition to 3 PMC plates and the demonstrator component discussed in the previous section, an emulation of the IHCT assembly presented in section 1.3.4. The IHCT assembly was made using a PMC plate manufactured in-house. Its temperature distribution was compared to the IHCT prototype made by the NRC-IAR and described by Maksoud [97], section 1.3.4. At least 3 repetitions were performed for each trial for ensuring the repeatability of measurements.

### 2.2.1. Experimental setup

PMC components were heated using Minco Thermofoil$^{TM}$ 0.2 mm × 76.2 mm × 101.6 mm flexible heaters from Minco (Fridley, Minnesota, USA). These were thin and flexible strips consisting of an etched-foil resistive element laminated between layers of flexible fibreglass-reinforced silicone rubber insulation, Figure 2.51. They offered an operating range extending from -45°C to 235°C. The supplier indicated a heater resistance of 8.6 ohms while measured resistance was about 9 ohms. All power calculations were performed according to specification sheets presented in Appendix B.

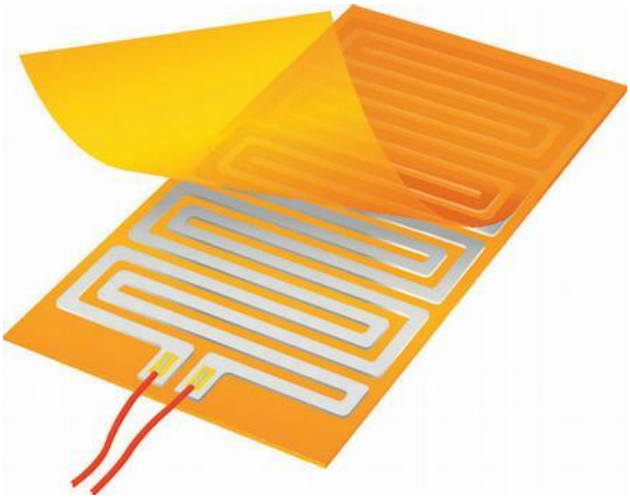

Figure 2.51: Minco Thermofoil$^{TM}$ heater [103]

Heaters were mounted on the surface of a given PMC component using Minco #12 pressure-sensitive adhesive film. The silicone-based thermosetting adhesive film was applied after removing the backing sheets using tweezers, and under manual pressure using gloved fingertips as recommended by the supplier, Figure 2.52. Next, the heater was placed on top of the adhesive film and rubbed manually. Following supplier instructions for curing the thermosetting adhesive film the assembly was put in a furnace for 15 minutes at 150°C, then left to wet-out for at least 24 hours before using the heater. It was observed that the longer the adhesive film was left to cure at room temperature, better was the bonding, with 24 hours sufficient to maintain good and thorough contact between the heater and surface.

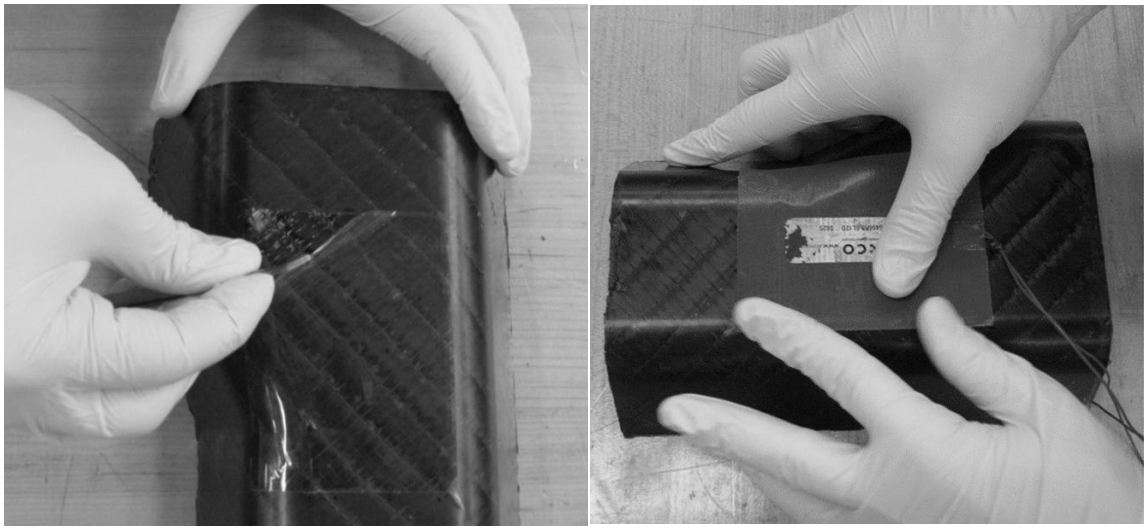

Figure 2.52: Heater bonding on the demonstrator component

11 K-type thermocouples were used for measuring the surface temperature at discrete locations on a given PMC component. These were attached to the plate using Flashtape 2R high temperature rubber polyester adhesive tape from Umeco Process materials, Inc. (Santa Fe Springs, CA, USA). The tape ensured good contact with the surface of the PMC component subjected to relatively high temperatures. Flashtape 2R withstands temperatures up to 204°C and can be released cleanly from the plate surface. Thermocouples were connected to a Labview computer via two data acquisition boards for recording the temperature history during heating. Temperature sampling frequency was 2 Hz. A control thermocouple was set at a reference location at the onset of each test, to keep the maximum temperature during heating below the glass transition temperature and within the heater operating range. The Labview acquisition board was connected to a solid-state relay which in turn was connected to a VARIAC. Once the control temperature was reached, the solid state relay stopped feeding power to the heater. The VARIAC connected to the heater enabled voltage variation and hence control of the generated heat flux.

Thermocouple positioning on the PMC plates appears in Figure 2.53. They were labelled as

TC#1 - TC#11. TC#1 was located on the back-face of the plate and served as reference. TC#2 was located on the surface of the heater and served as a safety thermocouple for protecting the heater from being burnt if temperatures beyond the operation range were reached. The rest of the thermocouples, namely thermocouples TC#3 – TC#11 were spread out on the opposite surface of the heater along its centreline and diagonal, Figure 2.53.

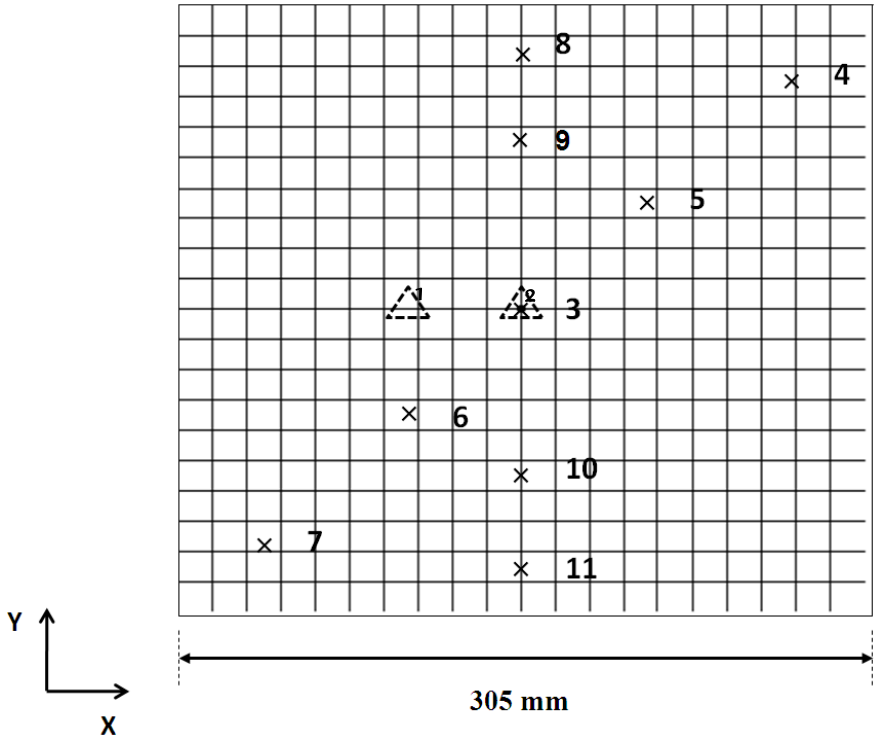


Figure 2.53: Positioning of thermocouples on PMC plates

The PMC component to be tested was fixed on a stand using a C-clamp pressing on small and thin wood slabs. The wood slabs acted as insulators and were used for reducing the heat sink through the C-clamp. Figure 2.54 shows a PMC plate positioned horizontally on the stand. During all trials conducted, the same room conditions were retained as constant as possible for ensuring repeatability of the measurements.

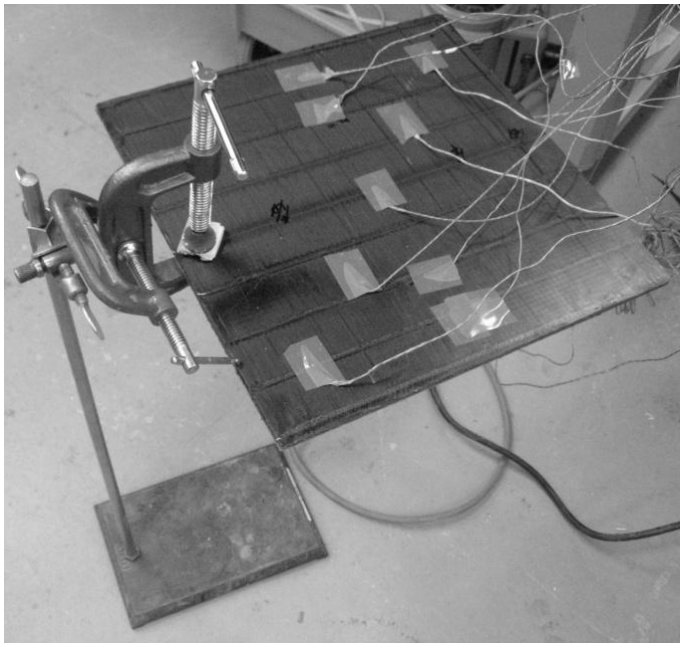

Figure 2.54: Thermocouples attached to a PMC plate positioned horizontally

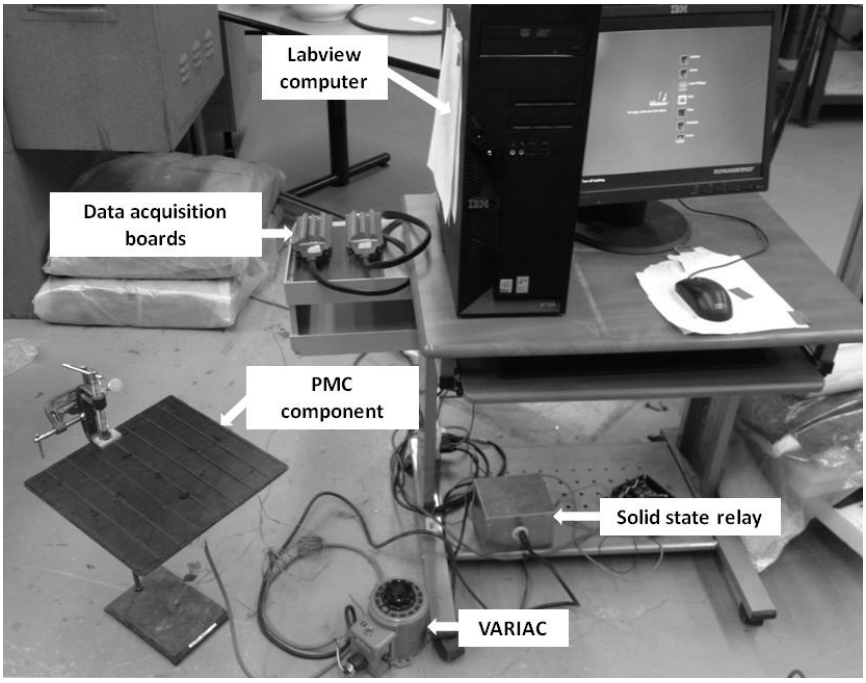


Figure 2.55: Thermal testing setup

To observe and record surface temperature distributions in PMC components, a FLIR i7 thermal imaging camera from FLIR Systems (Wilsonville, Oregon, USA) was used, Figure 2.56. The camera had a spectral range of 7.5 µm to 13 µm and was equipped with a 120 × 120 pixels uncooled micro-bolometer focal plane array. Image refresh rate was 9 Hz with a field of view of 25° × 25°. Minimum focal distance was 0.6 m. The manufacturer stated a thermal sensitivity of ±0.1°C and an error of 2% on readings at an ambient temperature ranging from 10°C to 35°C. The FLIR i7 camera had an internal temperature reference and was calibrated to give actual temperature readings over a temperature range of -20°C to 250°C [102].


Figure 2.56: FLIR i7 Infrared Camera [102]

Thermograms produced using FLIR i7 can be presented in a grey or color-coded scale. In the latter case, lower temperatures are represented in blue and warmer temperatures in red with highest appearing in white. A scale showing temperature versus color appears on the lower side of the display. This temperature scale can be adjusted during thermogram analysis using ThermaCAM Researcher PRO 2.10, a commercially available software package from FLIR Systems. The software was available in a trial version for extracting temperature data from thermograms. It allows for manual adjustment of the temperature range covered by the image, so that smaller temperature differences may be highlighted in cases where the scene covers a

relatively small temperature range.

### 2.2.2. Results

Experimental investigation of PMC material thermal behaviour was performed through a series of trials. Thermal repeatability for manufactured PMC plates was studied in trials 1.1 and 1.2. Emissivity of the PMC material was determined in trials 2.1 and 2.2, then a validation of the use of thermography was carried out in trials 3.1 and 3.2. Temperature distribution through PMC plates subjected to 4 discrete heaters was presented in trials 4.1 and 4.2 while thermal behaviour of IHCT assemblies was explored through trials 5.1 and 5.2. Finally, the thermal behaviour of the demonstrator PMC component subject to a concentrated heat source was presented in trial 6.

#### 2.2.2.1. Thermal repeatability of PMC plates

Quantification of thermal repeatability for manufactured PMC plates was performed by comparing heating histories of the PMC plates manufactured in-house. A power of 25 W was supplied to a heater fixed at the centre of the PMC plate, Figure 2.57. Temperature history was recorded for approximately 40 minutes (2500 s), ensuring that steady-state was reached. PMC plates were tested in the vertical and horizontal orientations in trials 1.1 and 1.2, respectively. The experimental data for trials presented in this section are the average of at least 3 repetitions.

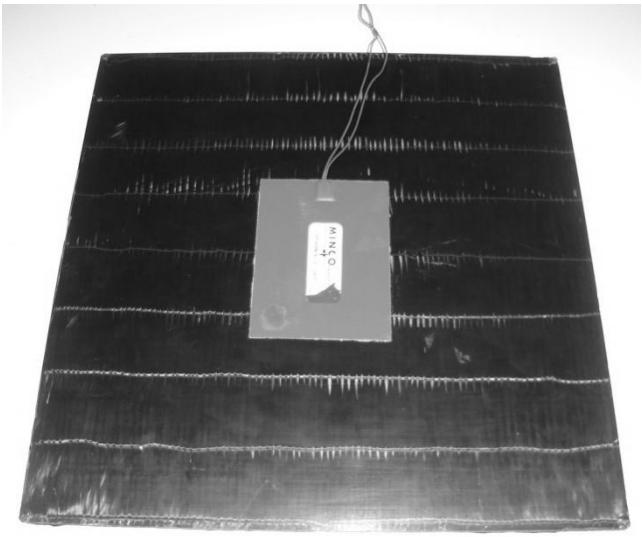


Figure 2.57: Minco heater attached to a PMC plate

#### 2.2.2.1.1. Trial 1.1: PMC plates aligned vertically

Heating histories of 3 PMC plates aligned vertically are discussed in this section. Results from all thermocouples for the 3 different PMC plates appear in Figure 2.58, in terms of relative temperature $T-T_0$, with $T_0$ being the initial temperature. Overall, relative temperature profiles corresponding to the 3 tested PMC plates and at each thermocouple location showed good concordance.

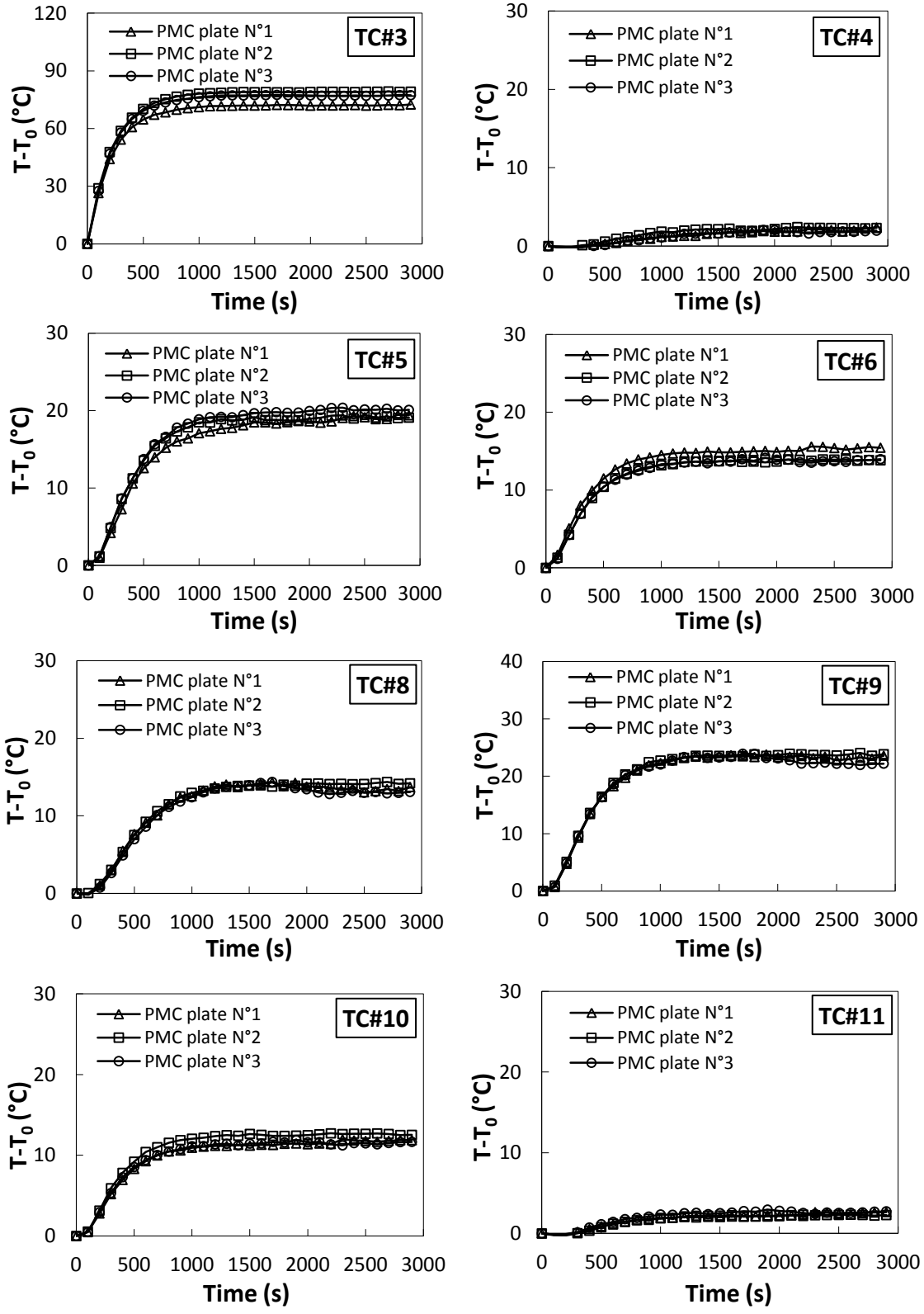


Figure 2.58: Relative temperature history, vertically aligned plates

Thermocouple TC#7 was omitted from the results shown in Figure 2.58 since no temperature change was sensed at that location. Steady-state relative temperature was reached at about 1200 s at all thermocouple locations. In general, relative temperature profiles corresponding to each thermocouple location showed limited discrepancies of about 2 °C, within the error margin of the thermocouples. Relative temperature profiles for the 3 PMC plates coincided except at thermocouple locations TC#3 during steady-state and TC#5 during transient state. Thermocouple TC#3 showed a relatively large discrepancy in the relative temperature profile corresponding to PMC plate N°1 while those corresponding to the 2 other plates were matching. The same behaviour was observed at TC#5 during the transient state. This could be explained by failure of the adhesive tape used for attaching the thermocouple to the PMC plate. The high temperature adhesive tape can peel if good bonding is not achieved before the start of a test.

#### 2.2.2.1.2. Trial 1.2: PMC plates aligned horizontally

In the case where PMC plates were aligned horizontally, the heater was bonded to the back face of the PMC plate while thermocouples were placed on the top face of the plate. Results at different thermocouple locations are summarized Figure 2.59. Relative temperature profiles during heating showed good consistency.

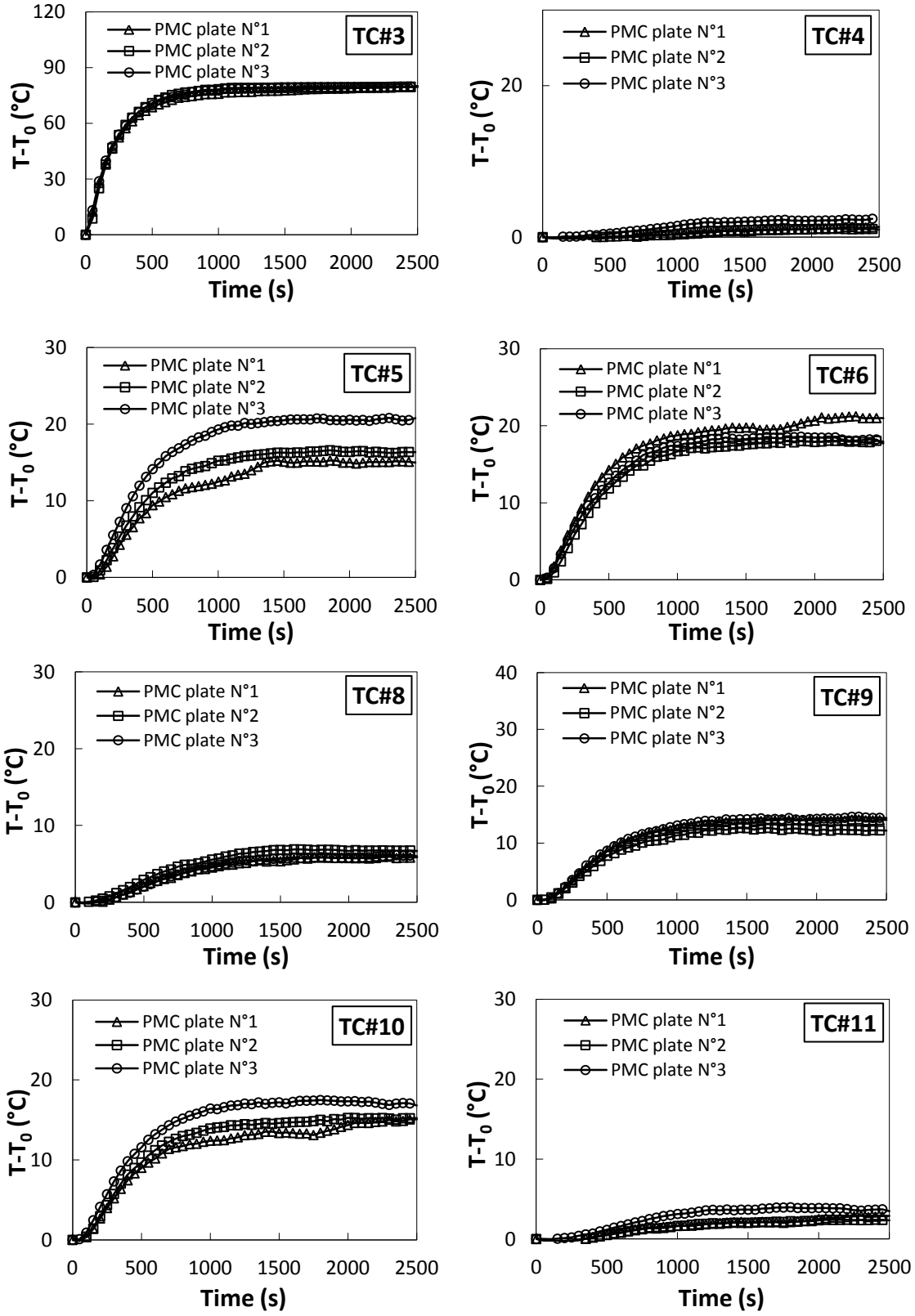


Figure 2.59: Relative temperature history, horizontally aligned plates

Steady-state was reached at approximately 1200 s as previously found with the vertical plates. Relative temperature values showed good concordance during transient and steady-state. Again, sudden changes were observed in relative temperatures and could be explained by poor bonding of the thermocouple to the plate surface.

Generally, all profiles recorded at a given thermocouple location for vertically and horizontally aligned PMC plates showed good consistency with variability within measurement error margins. High temperature pressure-sensitive adhesive failure was identified to be the main reason for relatively large discrepancies in relative temperature profiles at some thermocouple locations. Adhesive failure could be explained by the good surface finish of the PMC plates and relatively high temperatures reached during tests.

#### 2.2.2.2. Emissivity determination

The experimental trial and error method was used for determining the surface emissivity of PMC components manufactured in the course of this thesis. The thermography technique was also validated, so as to ensure acceptable accuracy of temperature readings in experiments. This was achieved through comparisons between thermogram data and direct thermocouple temperature measurements, for selected cases labelled Trial 2.1 and Trial 2.2 as follows. Trial 2.1 corresponded to testing the PMC plates oriented vertically while trial 2.2 corresponded to testing PMC plates oriented horizontally. In these trials, the PMC plates were heated as described in the previous section. After reaching steady state, temperatures were measured at selected locations on the face of the plate using thermocouples as shown earlier in Figure 2.53. Thermograms were also taken at steady-state with emissivity initially set to 0.9 in the IR camera. Then thermograms were analysed and temperature data was extracted using ThermaCAM researcher Pro software. The thermal emissivity was varied to match thermocouple temperature measurements. A value of 0.92 was eventually chosen for the surface emissivity of the PMC plates for the next phase of testing.

#### 2.2.2.2.1. Trial 2.1: PMC plates aligned vertically

A thermogram of the back face of PMC plate N°3 is presented in Figure 2.60. Emissivity was initially set to 0.9, and then varied to 0.92 and to 0.98. Temperature data along the centreline, showed in Figure 2.60, was obtained for the different emissivity values.

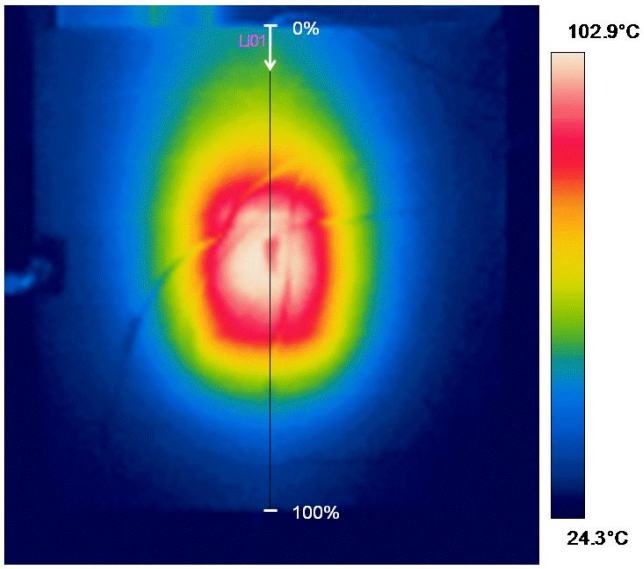


Figure 2.60: Thermogram of PMC plate N°3 aligned vertically

The temperature distribution was expected to show planar symmetry as the heater was centred on the plate. However, the centreline of the plate did not coincide with the centre of the temperature distribution through the plate in the thermogram above. This can be explained by imperfect orthogonality between the plate and camera axis. Temperatures varied from 24°C to about 100°C with considerable temperature gradients. Temperature profiles obtained from the thermogram were plotted and compared against thermocouple temperature measurements, Figure 2.61.

Overall, Figure 2.61 shows that changing the emissivity did not result in considerable changes in temperature values. Thermocouple measurements were generally close to the thermographic

temperature profiles. Nevertheless, thermocouple measurements were closest to the profile corresponding to an emissivity of 0.92. This is better visualized in the magnified region of the curves shown in Figure 2.61. Irregularities in the temperature profiles resulted from the presence of the adhesive tape used for attaching the thermocouples to the surface of the PMC plate. The adhesive tape has a different emissivity, which manifests as underestimated temperature values over its surface.

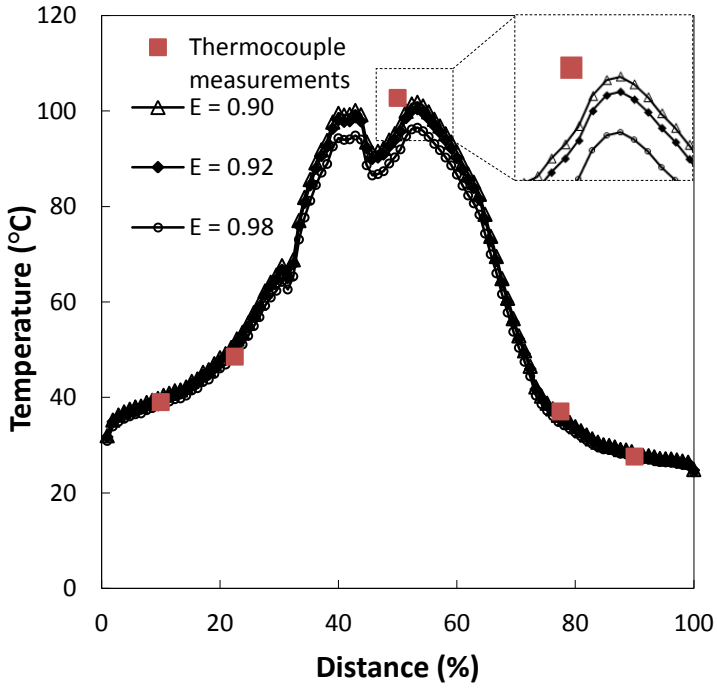


Figure 2.61: Comparison of temperature obtained from the thermogram and thermocouples for Trial 2.1

#### 2.2.2.2.2. Trial 2.2: PMC plates aligned horizontally

The same procedure was conducted on the same plate, aligned horizontally. The thermogram is presented in Figure 2.62. The temperature distribution showed planar symmetry coinciding with the centreline of the plate. The temperature range was larger than observed for the plate aligned

vertically. This is mainly because the contribution of buoyancy-driven convection heat transfer is more relevant in the case of vertical plates. The maximum temperature on the horizontal plate was about 110°C.

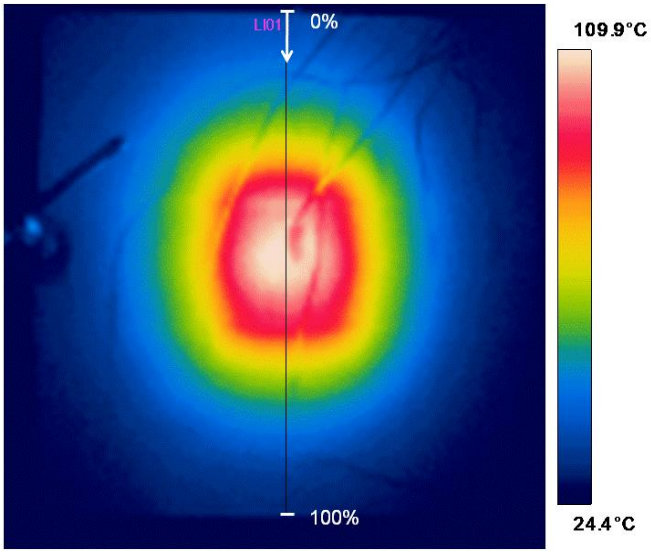


Figure 2.62: Thermogram of PMC plate N°3 aligned horizontally

Once again the temperature profiles along the centreline were obtained for the emissivity values of 0.90, 0.92 and 0.98. Temperature profiles appear in Figure 2.63. Temperature values did not vary extensively. Thermocouple temperatures were very close to all of the IR-measured temperatures. As in the previous case the temperature at the centre of the plate, corresponding to a distance of 50% in the Figure, showed the largest discrepancy between IR and thermocouple data. Again, this is explained by the presence of the adhesive tape, used for attaching the thermocouple.

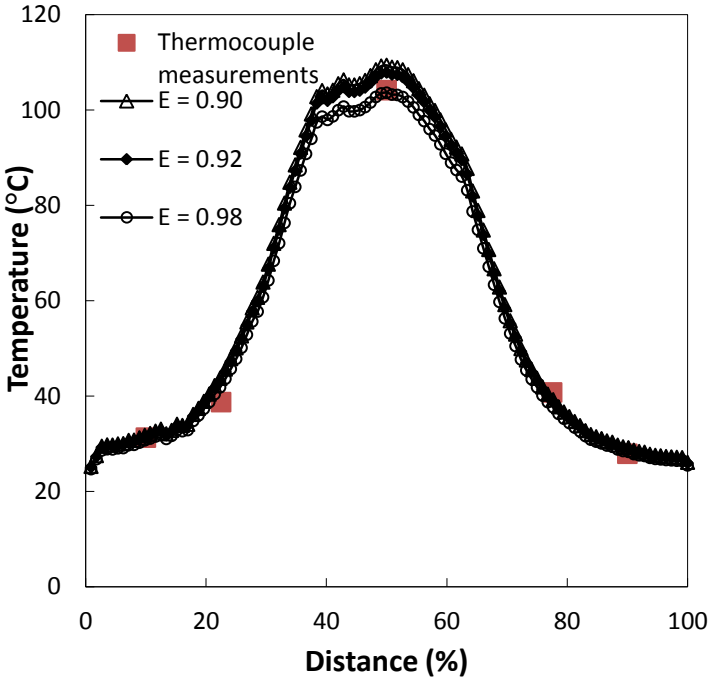


Figure 2.63: Comparison of temperature obtained from the thermogram and thermocouples for Trial 2.2

One can safely conclude that varying the emissivity of the PMC material did not affect temperature values significantly. The temperature profile of the plate aligned vertically and corresponding to an emissivity of 0.92 yielded results closest to those obtained from the thermocouples. Considering that the emissivity of organic materials has been reported to vary from 0.7 to 0.9 in the literature, an emissivity value of 0.92 was chosen for the PMC material tested in this thesis.

### 2.2.2.3. Validation of the thermography technique

The variability and repeatability of thermography measurements are explored in this section. As previously discussed in section 1.2.2.6, the surrounding environment can affect thermography temperature measurements. Thermography data is also sensitive to the distance and angle at which images are taken. In this thesis, thermograms were taken using the FLIR i7 IR camera

held manually, generally perpendicular to the surface to be measured. The potential effects of the environment, distance and measurement angle on IR temperature data were studied, and the usage of the present thermography technique was also validated.

Thermal history tests presented earlier in section 2.2.2.1 proved the repeatability of thermal behaviour for PMC components manufactured in-house. In the present tests, steady-state thermograms were collected from the 3 PMC plates, aligned vertically and horizontally, at an emissivity value of 0.92. Temperature data were extracted along the centreline of each PMC plate as previously shown in Figure 2.60 and Figure 2.62, respectively. The temperature profiles for the different PMC plates, labelled as Trial 3.1 for vertically aligned plates and Trial 3.2 for horizontally aligned plates, appear in Figure 2.64 and Figure 2.65 respectively. These were the result of averaged temperature data obtained from at least 3 thermograms.

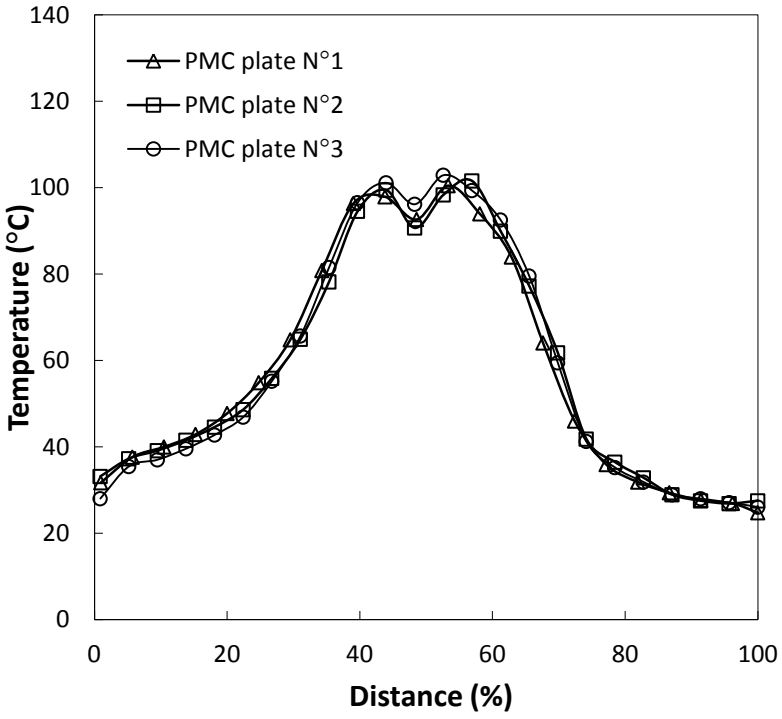


Figure 2.64: Thermographic temperature variability for Trial 3.1

Figure 2.64 shows temperature profiles along the centreline of the 3 different plates aligned vertically. The 3 curves coincide, with very little variation of local temperature values. As expected, the 0% - 50% part of PMC plates showed higher temperatures and smaller temperature gradients as seen in the thermogram appearing in Figure 2.60. Overall, all temperature profiles showed the same behaviour. The temperature profile corresponding to PMC plate N°1 is slightly shifted to the left of other curves. Thermograms taken at an oblique angle might be the main cause of this issue.

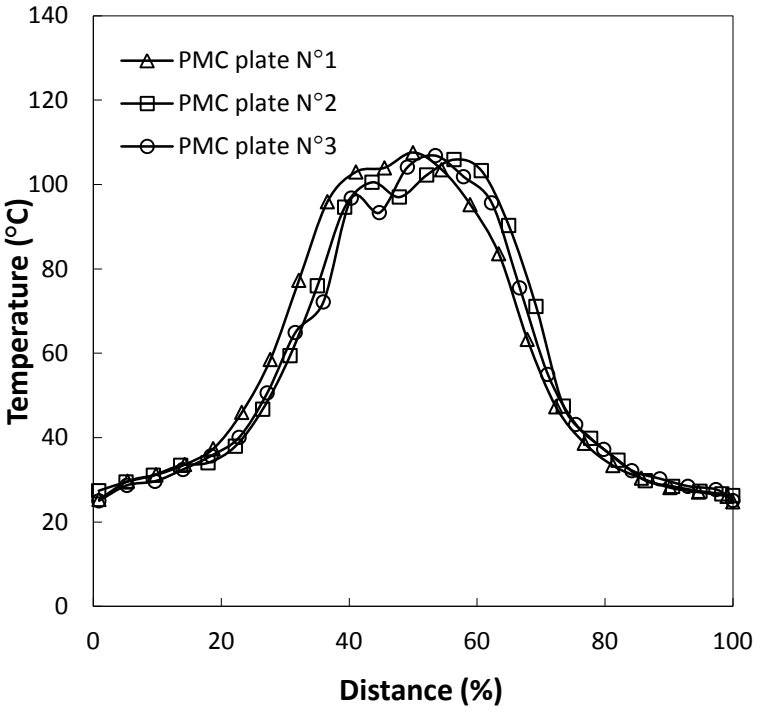


Figure 2.65: Thermographic temperature variability for Trial 3.2

Errors introduced by handling the IR camera manually were deemed acceptable. It is worth mentioning that resin rich zones along the seams did show discontinuity in temperature values. By looking at the temperature profiles in Figure 2.64 and Figure 2.65, one can conclude that thermography measurements showed good repeatability for both orientations of the PMC plates.

### 2.2.2.4. Temperature distribution through PMC plates subject to 4 discrete heat sources

This section presents the temperature distribution through PMC plate N°1 heated using a discrete arrangement of 4 heaters. The PMC plates were tested both vertically and horizontally, labelled as Trial 4.1 and Trial 4.2 respectively. Figure 2.66 shows a PMC plate N°1 with an arrangement of 4 heaters. The heaters contributed equally to deliver a total power of approximately 79 W. Thermograms were collected every 300 s until 3000 s for ensuring that steady-state was reached during heating and cooling processes. Temperature profiles were acquired from the thermograms along two straight lines Li01 and Li02, for assessing the effect of local variation in the convection coefficient on the temperature distribution through the PMC plate, Figure 2.67.

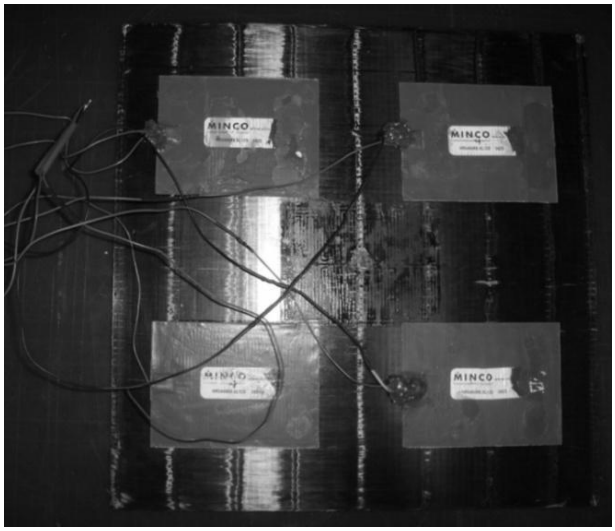


Figure 2.66: Discrete arrangement of heaters on the plate

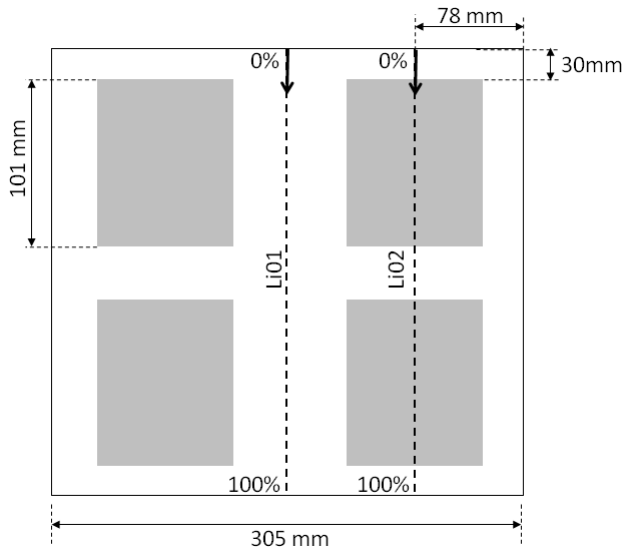


Figure 2.67: Location of temperature reading lines on the PMC plate

Thermograms of PMC plate N°1, positioned vertically during Trial 4.1, taken 300 s after first sending power to the heating elements, and in a steady-state regime, appear in Figure 2.68. Temperature distributions were characterised by symmetry along the vertical centreline of the plate. The upper half of the plate, corresponding to 0% - 50%, presented larger regions with higher temperatures than the lower half, corresponding to 50% - 100%. This was expected as heat loss to the atmosphere by natural convection in the upper half of the plates is reduced compared to the lower half, since the air in its vicinity gets heated by the lower half of the plate. Temperature profiles along lines Li01 and Li02 were extracted at every 300 s from the thermograms of vertical plates. The variation of these temperature profiles, in terms of relative temperature $T-T_{\infty}$, with respect to time is shown in Figure 2.69 and Figure 2.70 respectively.

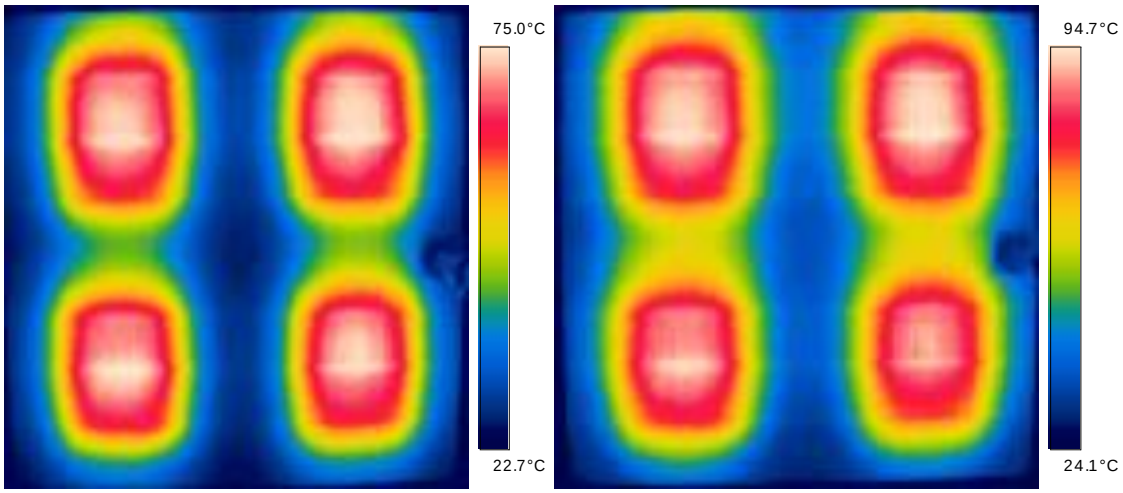


Figure 2.68: Thermograms taken during heating for Trial 4.1: at 300 s (left) and at steady-state (right)

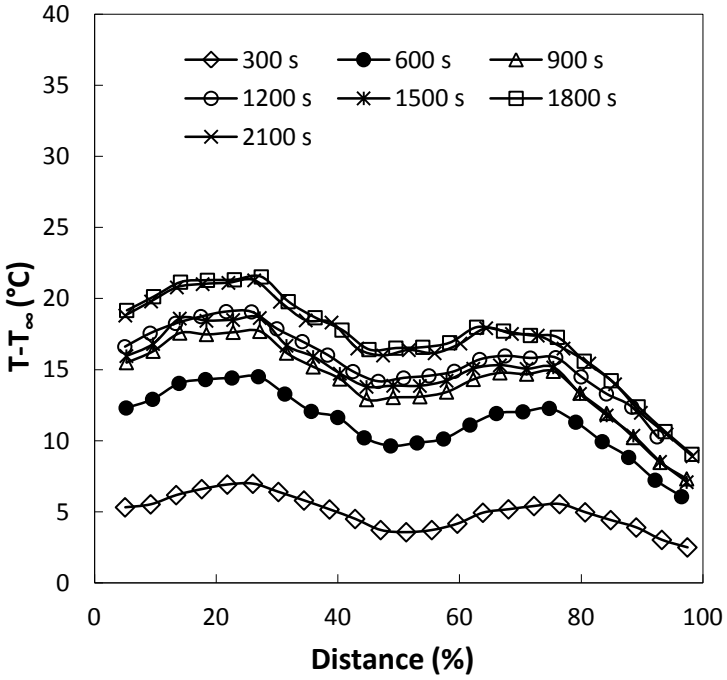


Figure 2.69: Temperature along line Li01 for Trial 4.1

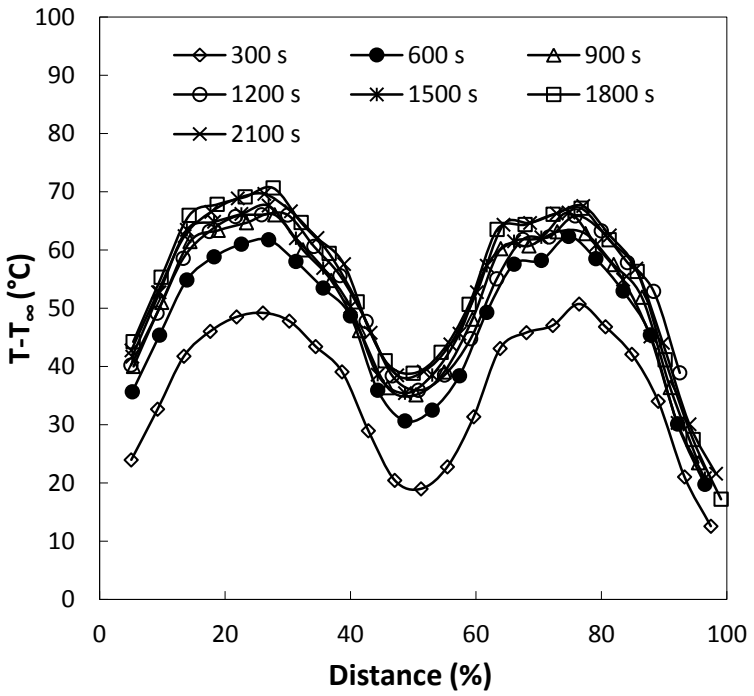


Figure 2.70: Temperature along line Li02 for Trial 4.1

The mismatch in temperature distribution between the upper half and the lower half of the plate can be seen clearly in Figure 2.69. Profiles maintain a trend at the different time steps; the trend is very consistent from 600 s to steady-state. Nevertheless, a slight increase in temperature gradient in the vicinity of the heaters can be observed between 300 s and 600 s. The temperature profile at 600 s exhibited larger differences between its local minima and maxima than the profile at 300 s. This was expected in the transient phase of heat conduction as the temperature distribution did not reach a fully developed stage. According to Figure 2.69, steady-state along Li01 was mostly reached at 900 s, while it was almost reached at 600 s along Li02, Figure 2.70.

Thermograms collected during the cooling process at 300 s and 900 s appear in Figure 2.71. For the thermogram corresponding to 300 s, temperatures varied from 23°C to 48°C approximately, while in the case of the thermogram taken at 900 s temperatures varied from 22°C to 29°C. Overall, the temperature distribution was more uniform in the sense that spatial temperature

gradients were significantly reduced. As opposed to the thermograms taken during the heating phase, one can easily notice the horizontal lines appearing as discontinuities in the temperature distribution, with slightly higher temperatures. These discontinuities correspond to the seams. The thermal conductivity of cured resin is significantly lower than the directional thermal conductivities of carbon fibres. This made heat diffusion slower in resin rich zones than in the rest of the PMC plate.

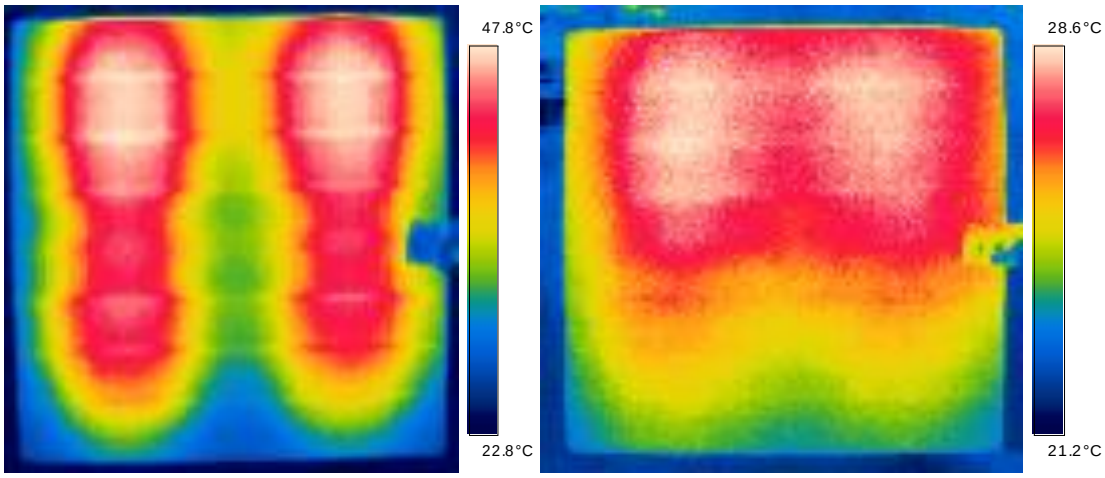


Figure 2.71: Thermograms taken during cooling for Trial 4.1: at 300 s (left) and at 900 s (right)

A quantitative analysis of thermogram data appears in Figure 2.72. The temperature profiles along lines Li01 and Li02 were almost linear with a moderate slope. This demonstrated again that the temperature field during the cooling phase was more homogeneous than during the heating phase. Because of the relatively low thermal conductivity of the PMC material it was difficult for the heat to distribute and for temperatures to even out, allowing heat to accumulate and leading to larger temperature gradients across the plate during the heating phase.

The uniformity of temperatures through the PMC plate during cooling can be confirmed from the temperature profiles along lines Li01 and Li02, Figure 2.72. All temperature profiles were

essentially linear with a limited slope. As expected, higher temperatures were observed in the immediate vicinity of the heaters, corresponding to line Li02, than in the centreline region at the beginning of the cooling process.

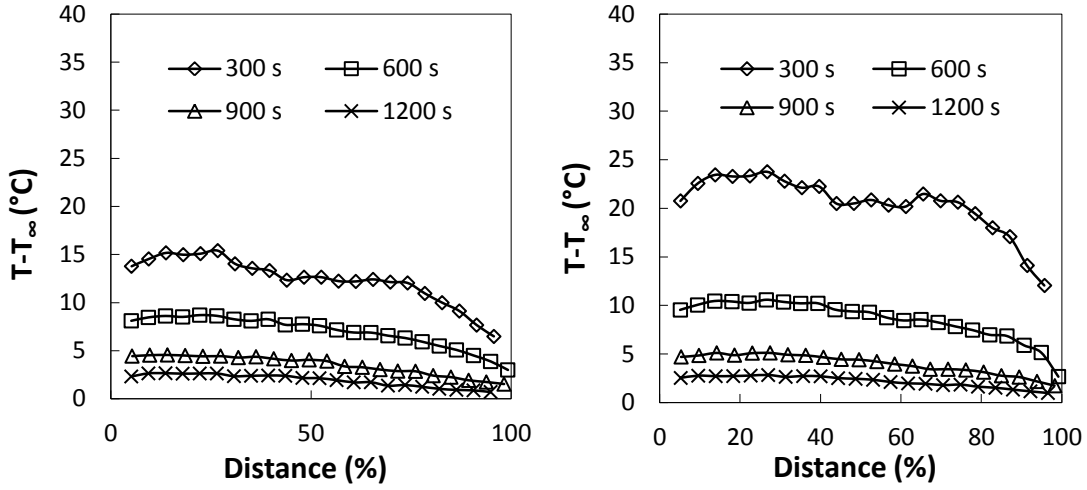


Figure 2.72: Temperature variation during cooling for Trial 4.1: Li01 (left) and Li02 (right)

The same testing procedure was performed on the same plate, namely PMC plate N°1, oriented horizontally. Thermograms corresponding to 300 s after provision of power to the heating elements and upon steady state are shown in Figure 2.76. The thermograms showed symmetry relative to two planes, namely the orthogonal planes penetrating the plate horizontally and vertically at its centre. Resin rich zones along the seams running in the vertical direction can be distinguished faintly in both thermograms.

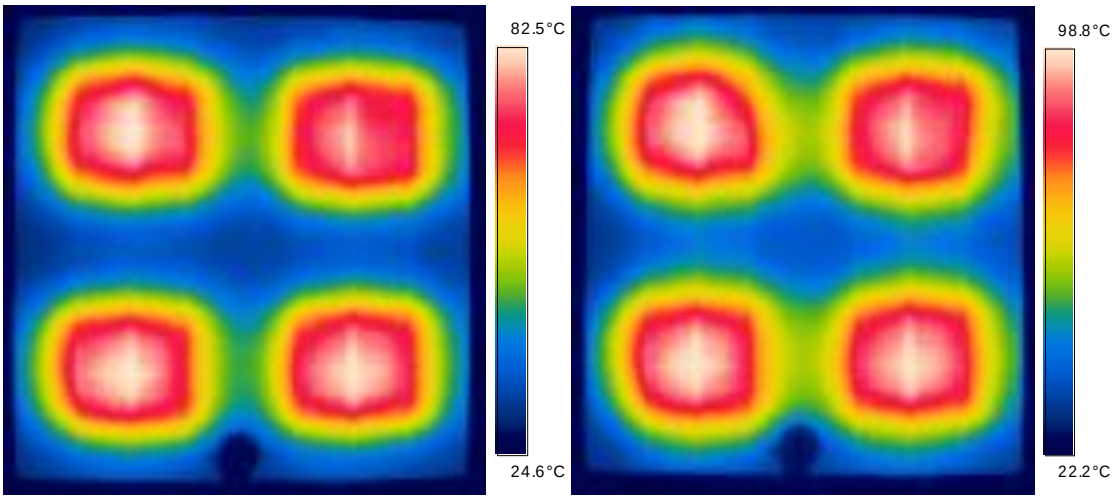


Figure 2.73: Thermograms taken during heating for Trial 4.2: at 300 s (left) and at steady-state (right)

Temperature profiles shown in Figure 2.74 and Figure 2.75 showed similar characteristics. The symmetry of the temperature distribution can be seen clearly through the symmetry of temperature profile along Li01 and Li02, Figure 2.74 and Figure 2.75 respectively. As observed earlier for the PMC plate aligned vertically, steady-state was reached starting at 900 s at line Li01 while it was mostly reached at 600 s in the vicinity of line Li02.

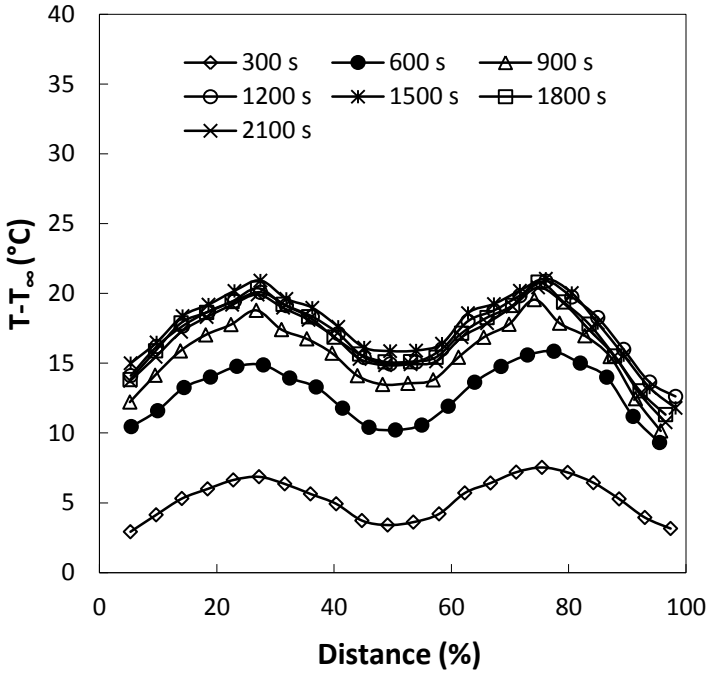


Figure 2.74: Temperature along Li01 during heating for Trial 4.2

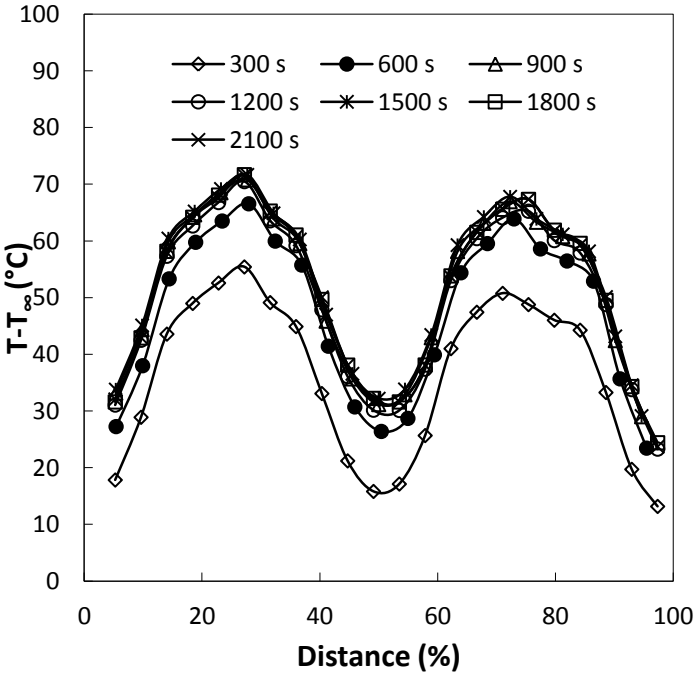


Figure 2.75: Temperature along Li02 during heating for Trial 4.2

The temperature distribution showed the same symmetry at the beginning of the cooling phase, Figure 2.76. The resin rich seams were clearly visible from the discontinuities introduced in the temperature distribution. The temperature distribution on the plate after 900 s was more homogeneous when compared to profiles at 300 s and 600 s. This can be seen in Figure 2.76 and quantitatively along lines Li01 and Li02, Figure 2.77. Temperature profiles at different time steps of the cooling phase exhibited a plateau with slightly lower temperatures observed at the edges of the plate. These lower edge temperatures can be explained by greater heat loss through natural convection around the edges for the temperature field of PMC plate aligned horizontally, as opposed to the vertical plate discussed earlier, where its effect could hardly be observed.

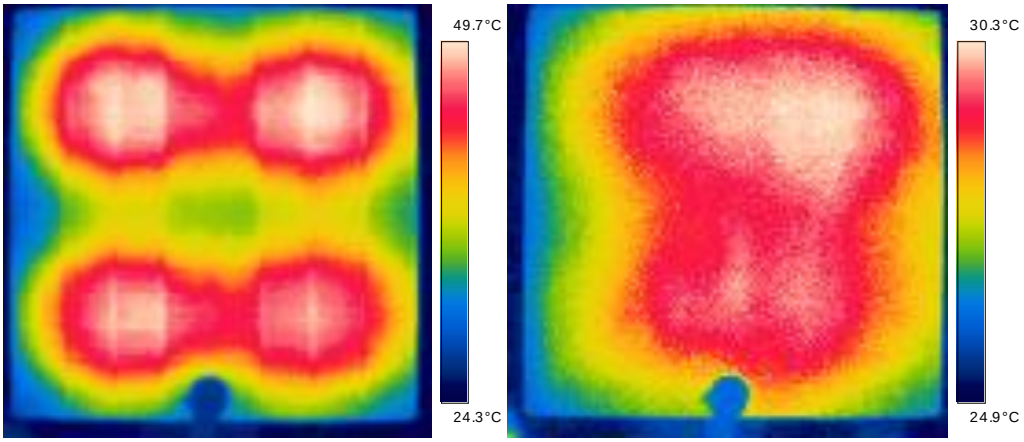


Figure 2.76: Thermograms taken during cooling for Trial 4.2: at 300 s (left) and at 900 s (right)

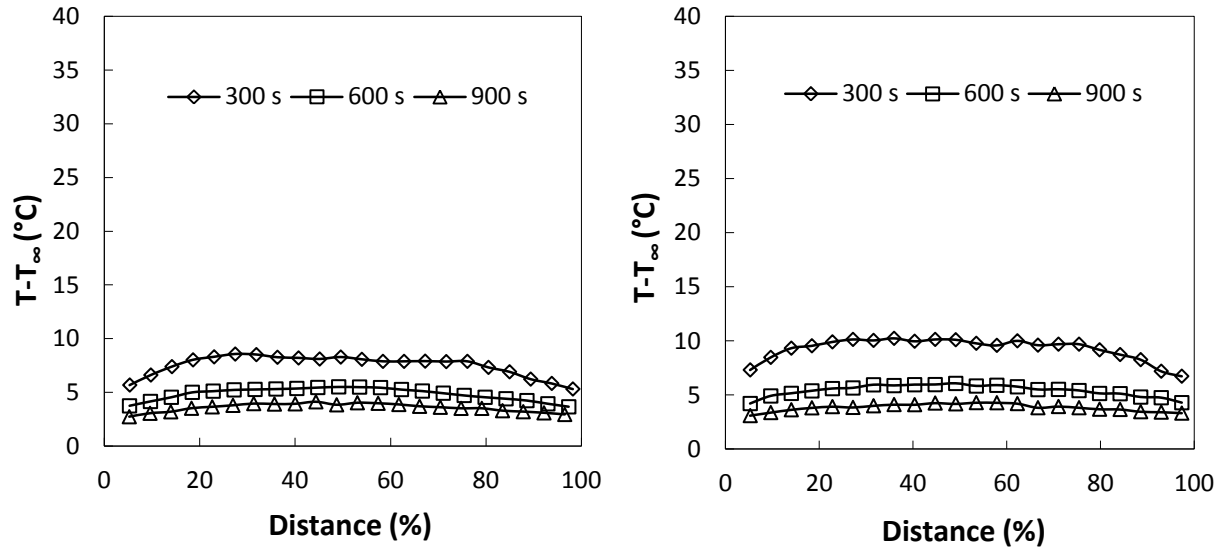


Figure 2.77: Temperature variation during cooling for Trial 4.2: Li01 (left) and Li02 (right)

### 2.2.2.5. Temperature distribution through integrally heated copper tooling assemblies

Duplication of the NRC-IAR IHCT assembly is presented in this section. An IHCT assembly was made using PMC plate N°4. Thermal conduction tests were performed on the original and duplicate assemblies, oriented vertically and horizontally. Temperature distributions were obtained using thermography for studying the bonding quality of the duplicate IHCT assembly.

The IHCT assembly manufactured by the NRC-IAR consisted of a 296 mm × 296 mm × 1.15 mm copper plate with a silicone rubber heating element fixed at the center on the top face. A combined layer of Kapton and 3M double sided tape was used for holding the heater in its position. The heater supplied a power of 25 W. The assembly was attached to a 296 mm × 296 mm × 5.68 mm AS4/3501-6 PMC plate using a layer of heat-resistant silicon adhesive, Figure 2.78. According to Maksoud [97], the thickness of the silicone adhesive cannot be determined since the technique with which the heater is attached to the plate does not allow for measurement of the layer thickness.

Figure 2.78: Original IHCT assembly manufactured by NRC-IAR

The duplicate IHCT assembly was made using a 305 mm x 305 mm PMC plate manufactured in-house. The PMC plate was bonded to a 1 mm thick flat copper sheet using high temperature silicone. The assembly was clamped to ensure even bonding throughout the silicone filled interface and to adjust the slightly bent copper sheet. The clamped assembly was left to cure for 48 hours, Figure 2.79.

One cannot evaluate the quality and uniformity of the silicone bonding from direct observation. Thermal conduction tests were carried out to allow for thermal assessment of the bonding and to investigate the thermal effect of the copper sheet on the temperature distribution through the PMC plate.

The duplicate IHCT assembly was heated using two heater configurations. A single heater was used in Trial 5.1, and a discrete arrangement of 4 heaters was used in Trial 5.2. Top views of the in-house manufactured IHCT assembly two heater configurations appear in Figure 2.80.

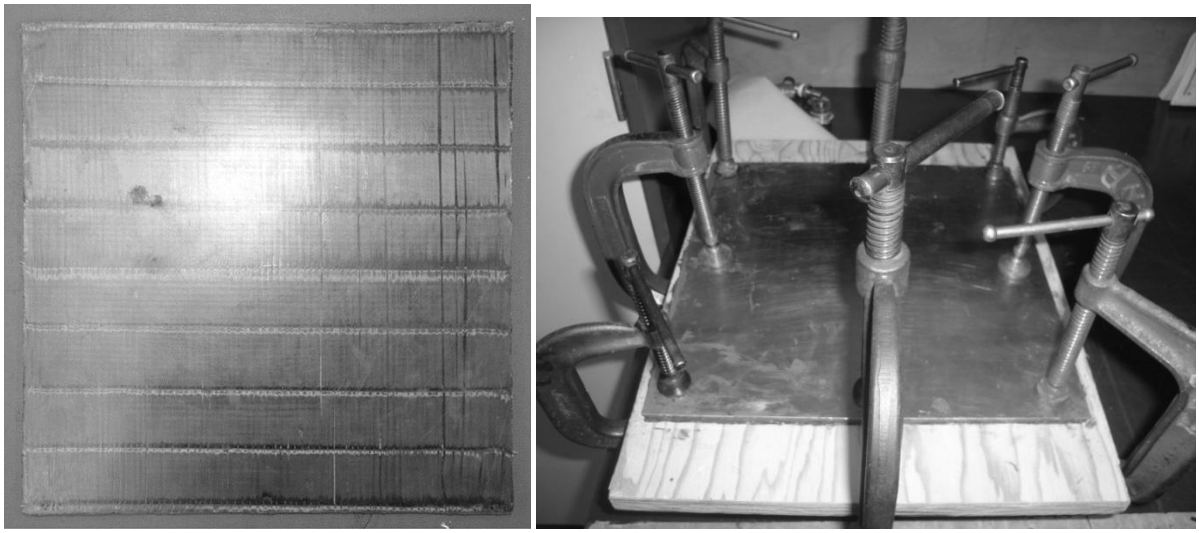

Figure 2.79: Manufacturing of the duplicate IHCT assembly

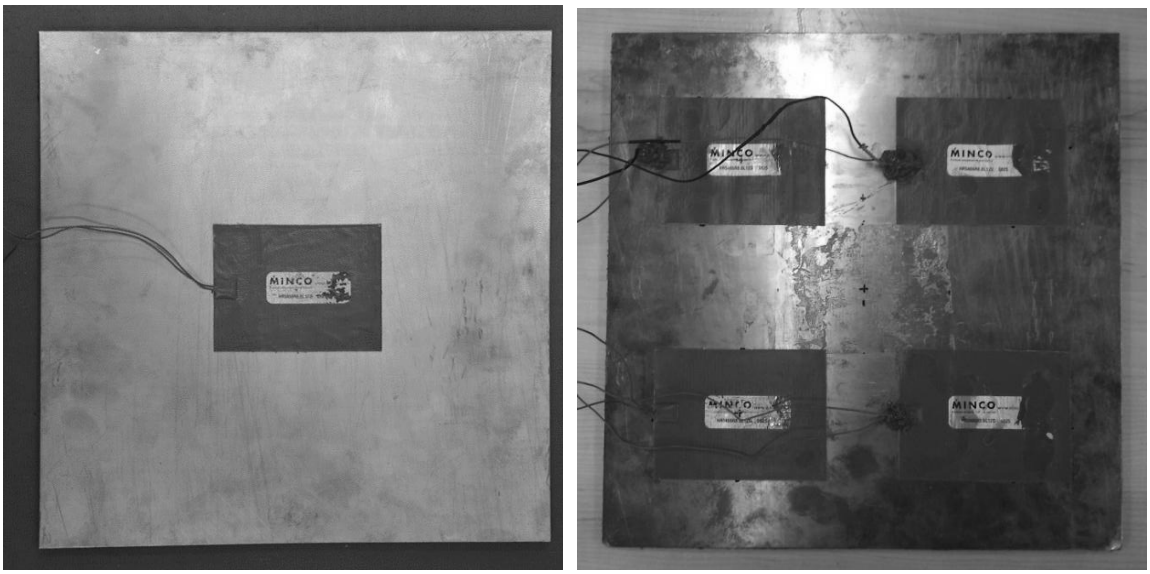


Figure 2.80: Heater configurations of the duplicate IHCT assembly

#### 2.2.2.5.1. Trial 5.1: Single heater temperature distribution

Steady state thermograms of the duplicated and original IHCT assemblies aligned vertically are shown in Figure 2.81 below. Temperature distributions were clearly different with a lack of

symmetry in the case of the duplicated IHCT assembly, as opposed to the original IHCT assembly. The left half of the plate assembly contained larger areas with temperatures exceeding 35°C. Maximum temperatures reached roughly 40°C in the duplicate IHCT assembly while temperatures reached roughly 50°C in the original IHCT assembly. This can be explained by the higher heat flux delivered by the heater of the original IHCT assembly. On the other hand, the original IHCT assembly exhibited areas with lower minimal temperatures. These areas are essentially located in the lower half of the assembly.

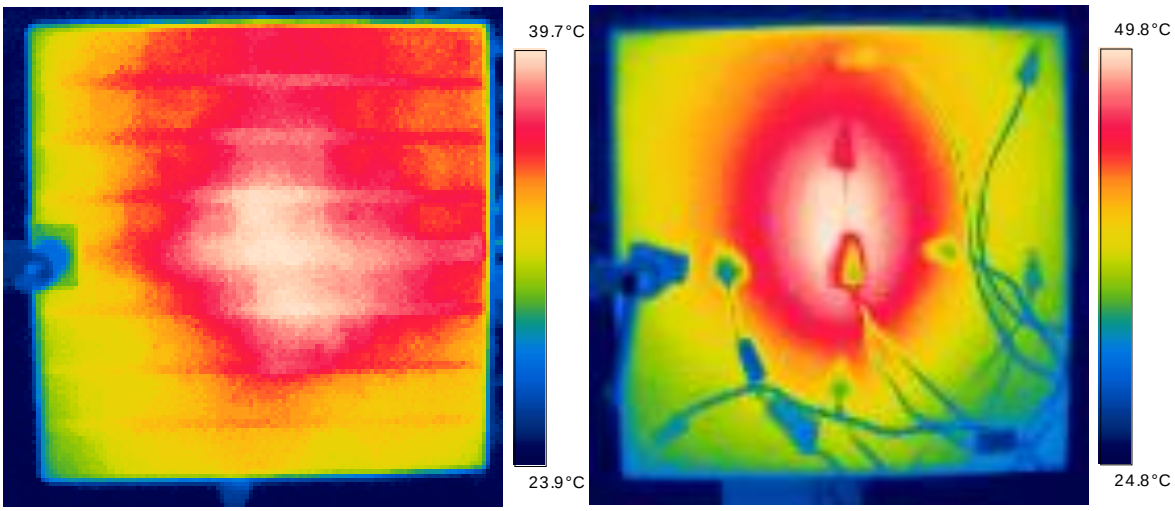


Figure 2.81: Thermograms of the vertical IHCT model in Trial 5.1: duplicate (left) and original (right)

The asymmetry was also observed in the case of the duplicate IHCT assembly aligned horizontally. Thermograms of the duplicate and original IHCT assemblies are presented in Figure 2.82 below. The temperature distribution in the original IHCT assembly was centered while it was shifted to the lower right corner of the duplicate IHCT assembly. Temperature maxima in both assemblies were similar to the previous case of the vertically aligned assemblies. Again, the original IHCT assembly temperature distribution presented larger areas of relatively low temperatures located around the corners of the plate.

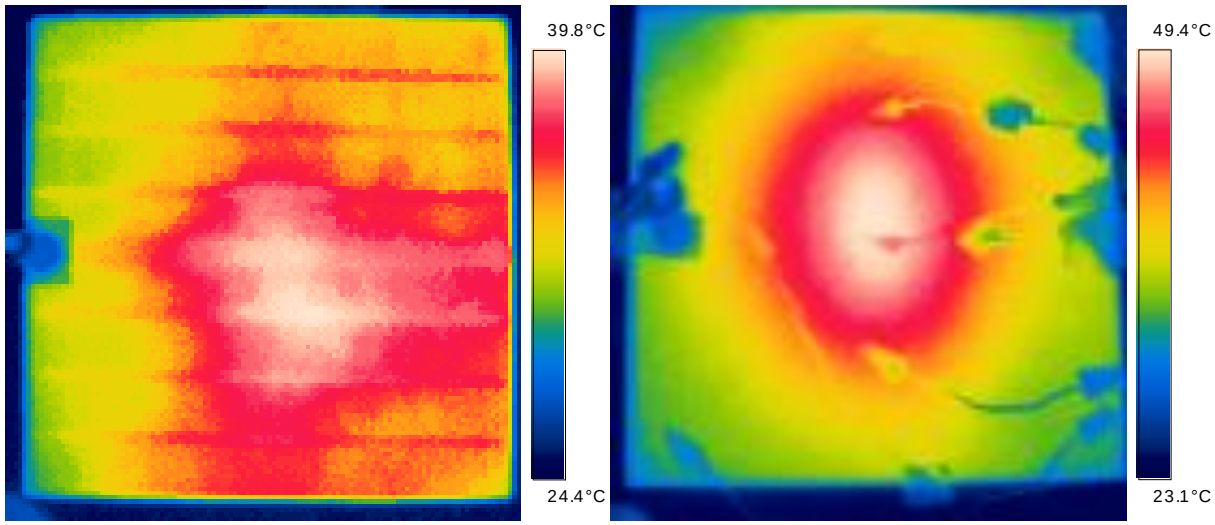


Figure 2.82: Thermograms of the horizontal IHCT assemblies in Trial 5.1: duplicate (left) and original (right)

Overall, the duplicate IHCT assembly showed lower temperatures than the original IHCT assembly. The observed asymmetry can be explained by the non-uniform application of the silicone serving for bonding the copper plate to the PMC plate. Hence, interfaces under areas with much lower temperatures may be empty or have minimal quantities of high temperature silicone.

#### 2.2.2.5.2. Trial 5.2: Discrete arrangement of 4 heaters

This section presents the temperature distributions in the duplicated IHCT assembly heated using a 4 heater arrangement and aligned in the vertical and horizontal directions. Figure 2.83 shows the steady-state thermograms of the duplicate IHCT assembly and PMC plate N°1. Temperature distributions showed different behaviours. The IHCT assembly had considerably lower temperatures than the PMC plate. Temperature reached a maximal value of approximately 95°C in the PMC plate while maximum temperature in the IHCT assembly was about 57°C.

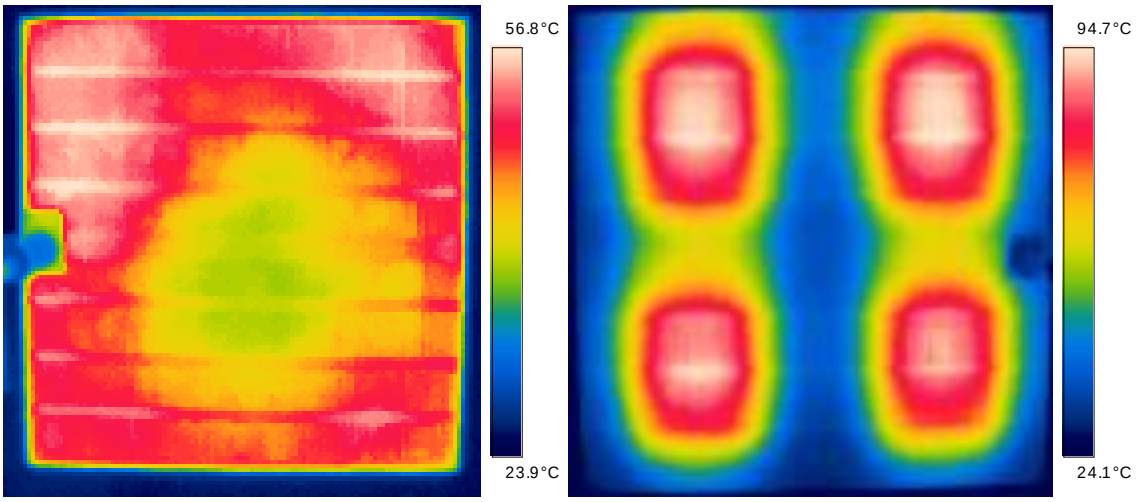


Figure 2.83: Steady state thermograms of IHCT assembly (left) and a PMC plate N°1 (right)

In the case of the IHCT assembly, high temperature areas were essentially located around its corners. The centre of the IHCT assembly had unexpectedly lower temperatures. While in the case of the PMC plate, higher temperatures were located in areas adjacent to heaters. The temperature distribution in the IHCT assembly was more uniform than in the PMC plate. This can also be concluded from Figure 2.84. The chart suggests that 94% of the IHCT assembly PMC surface area had temperatures ranging from 46°C to 60°C while different comparable surface area percentages were allocated to various temperature brackets extending from 24°C to 96°C.

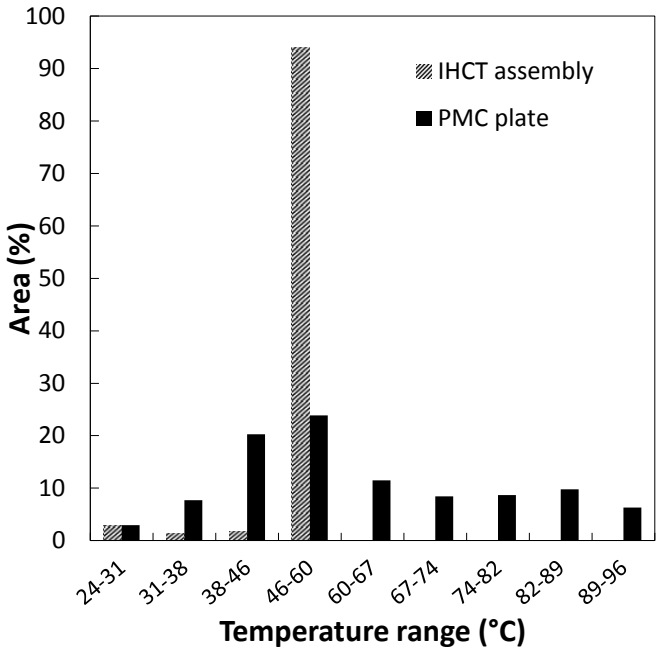


Figure 2.84: Temperature distribution comparison for the vertical orientation

The heating and cooling histories along the centreline of the IHCT assembly, appearing in Figure 2.85, were collected at 6 different time steps using thermography. Temperature profiles along the centreline of the IHCT assembly and at a given time step generally showed the same behaviour. This suggests that the spatial temperature gradient was mostly constant during the heating and cooling processes.

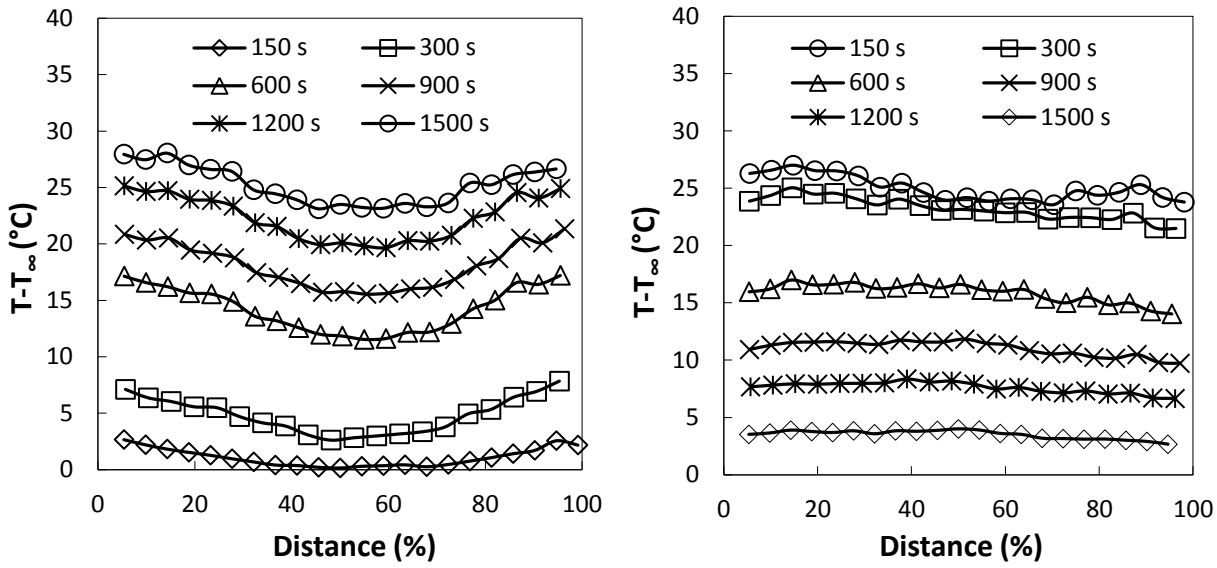


Figure 2.85: Temperature profiles along line Li01 of the vertically aligned IHCT assembly: heating (left) and cooling (right)

Similar conclusions can be drawn from the comparison of the steady-state thermograms corresponding to the IHCT assembly and PMC plate N°1 aligned horizontally. The IHCT assembly temperature distribution was more uniform than the PMC plate temperature distribution. Maximum temperature reached was roughly 99°C in the PMC plate while it was only 65°C in the IHCT assembly. High temperature areas were observed around the corners of the IHCT assembly while they were located in the heaters areas for the PMC plate.

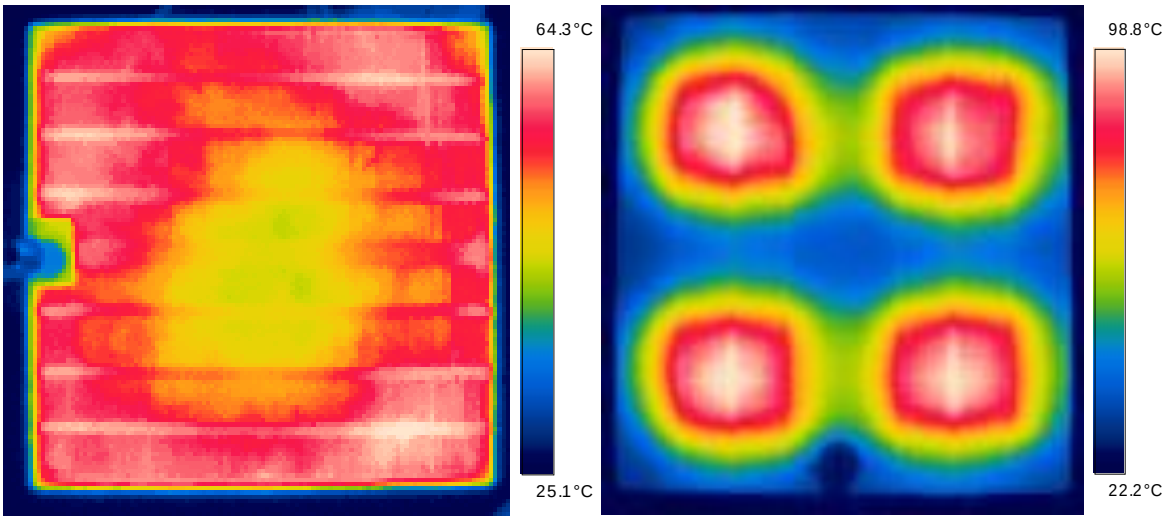


Figure 2.86: Steady state thermograms in the horizontal orientation: IHCT assembly (left) and PMC plate (right)

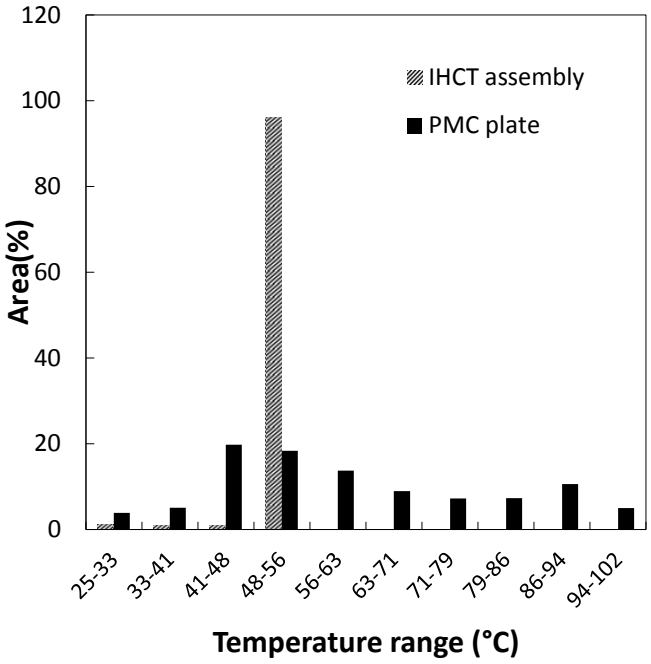


Figure 2.87: Temperature distribution comparison for the horizontal orientation

Temperature profiles on the IHCT assembly corresponding to given time steps of the heating and

cooling processes are presented in Figure 2.88. Temperature profiles for the different time steps had similar behaviour during heating and cooling. One can conclude that temperature gradients did not vary considerably across the IHCT assembly during the heating and cooling processes. Moreover, it is straightforward that temperature gradients were relatively low.

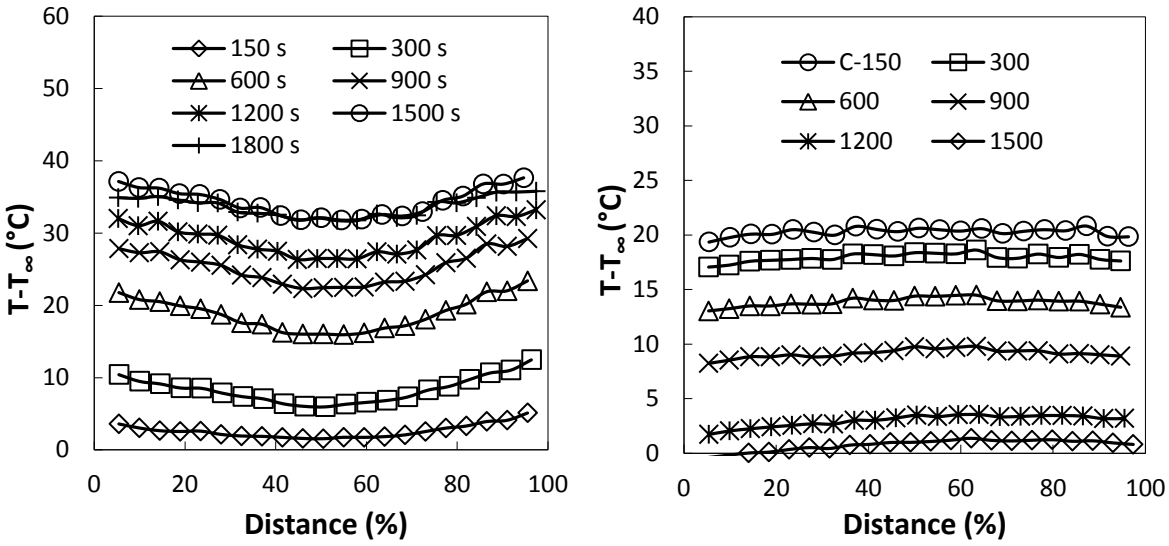


Figure 2.88: Temperature profiles along line Li01 of the horizontally aligned IHCT assembly: heating (left) and cooling (right)

### 2.2.2.6. Temperature distribution through the demonstrator PMC component

Temperature distributions through the demonstrator PMC component were obtained using thermography in Trial 6. The heater was positioned as in Figure 2.52. The demonstrator PMC component was aligned horizontally, attached to a stand with the heater facing down, Figure 2.89. Thermograms of the upper surface of the demonstrator PMC component were collected at several time steps. The steady-state thermogram of the demonstrator PMC component is presented in Figure 2.90. The thermogram shows that temperatures ranged roughly from 30°C around the corners areas to 111°C in the heater adjacent areas.

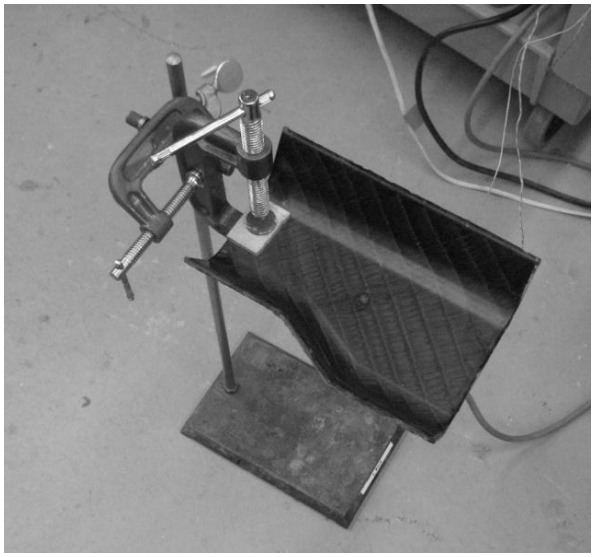

Figure 2.89: Demonstrator PMC component aligned horizontally

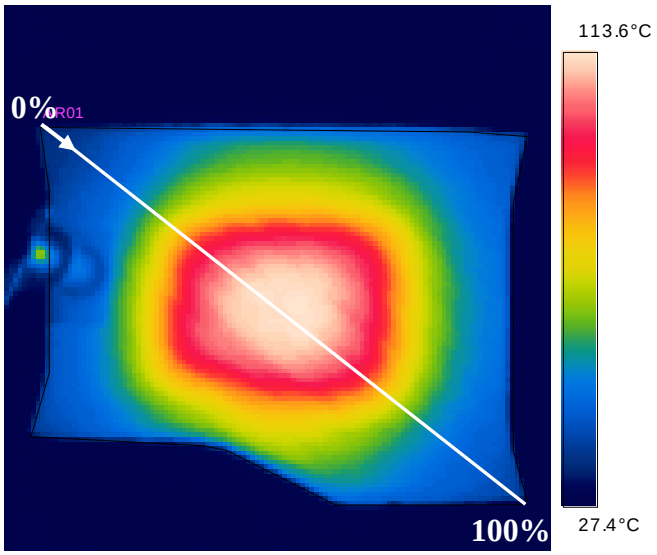


Figure 2.90: Steady-state thermogram of the demonstrator PMC component

Temperature profiles along the diagonal of the PMC component thermogram, shown in Figure 2.90, were extracted at different time steps. The temperature profiles corresponding to the different time steps are shown in Figure 2.91. The profiles presented symmetry around a distance of 50% of the diagonal. While the demonstrator PMC component was not symmetric along its

diagonal, the temperature distribution seen by the IR camera presented general symmetry. Overall, the temperature profiles had similar behaviours with maximum temperatures reaching roughly 111°C at steady-state.

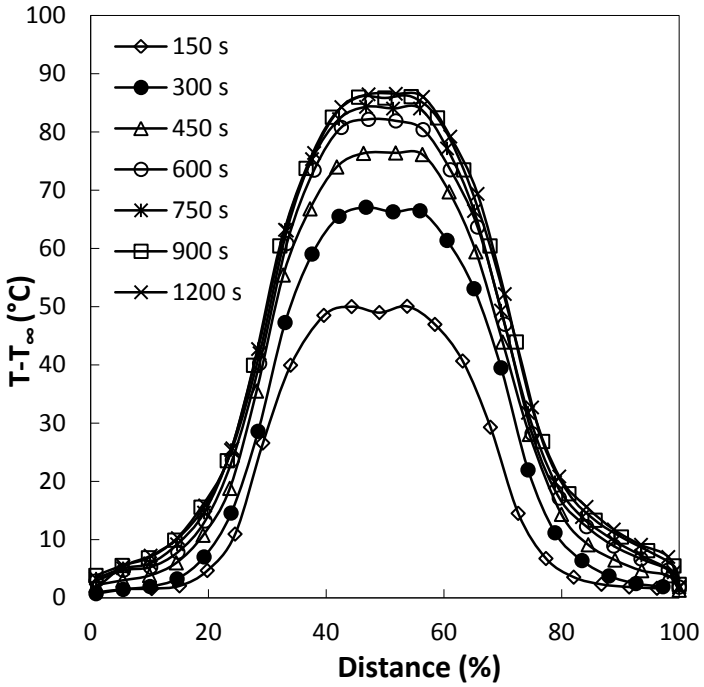


Figure 2.91: Temperature profiles during heating of the demonstrator PMC component

The area to temperature bracket allocation appears in Figure 2.92. A major portion of the projected demonstrator surface as captured by thermography, roughly 38%, was allocated to the 24°C - 34°C temperature bracket. More than 50% of the total projected area contained temperatures below 43°C. Allocated projected area percentages to temperature brackets were comparable for temperatures ranging from 43°C to 103°C. Allocated projected area percentages varied from 5% to 10% over this range. Projected area percentage was negligible for high temperatures ranging from 103°C to 111°C.

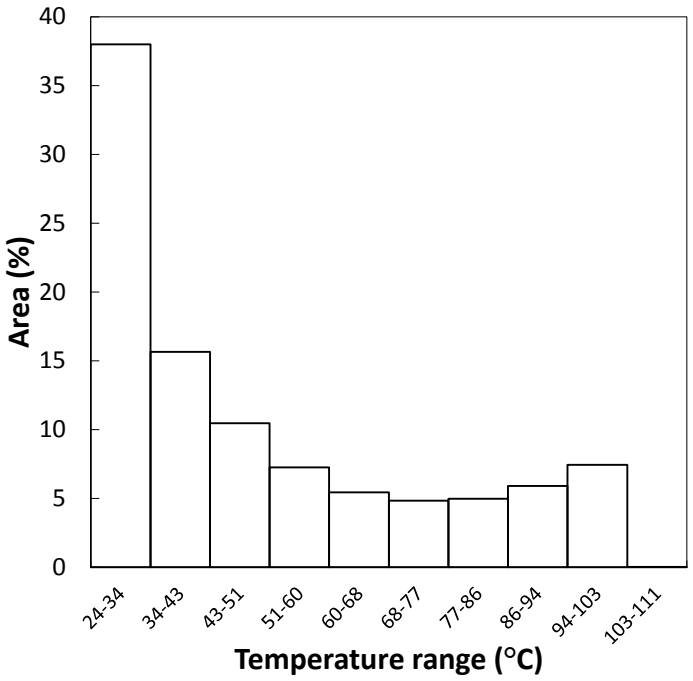


Figure 2.92: Area allocation of the demonstrator temperature distribution

### 2.2.2.7. Conductivity measurements

Following measurements on full plates were done they could be cut for measuring thermal conductivity. Thermal conductivities of the manufactured PMC plates were measured using the THISYS and THASYS instruments from Hukseflux (Delft, Netherlands). THISYS was used for measuring the bulk in-plane thermal conductivity while THASYS was used for measuring the through-thickness thermal conductivity.

Both of the THASYS and THISYS had similar general setups. Each of the setups was composed of a thin sample instrument (1), measurement and control unit (2), power cable (3), computer (4) and an RS 232 cable (5). A schematic of the setup is illustrated in Figure 2.93. The thin sample instrument was able to handle 70 mm × 110 mm specimens with less than 0.01 mm to 6 mm thickness. THASYS required the use of 2 specimens while THISYS required only one specimen.

Measurements were fully controlled via the computer. THASYS and THISYS devices were described thoroughly by Hind [101].

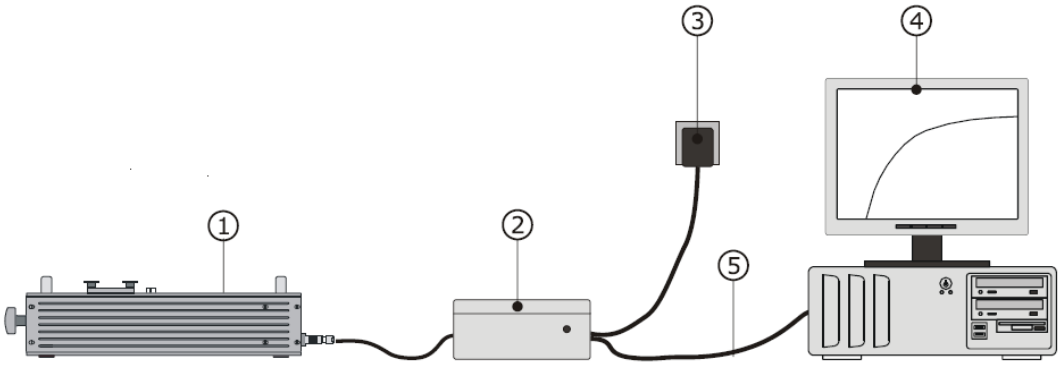


Figure 2.93: Schematic of the thermal conductivity measurement setup [107,108]

PMC plate surfaces were protected using adhesive tape before cutting with a band saw. Two specimens were cut from each of the 3 manufactured PMC plates, namely PMC plate N°1, PMC plate N°2 and PMC plate N°3 as shown in Figure 2.94. Using the band saw for cutting the PMC plates was found to give specimens with good edge quality and acceptable dimensional precision. Safety equipment, in the form of breathing mask and gloves, were used for avoiding carbon fibres dust hazards.

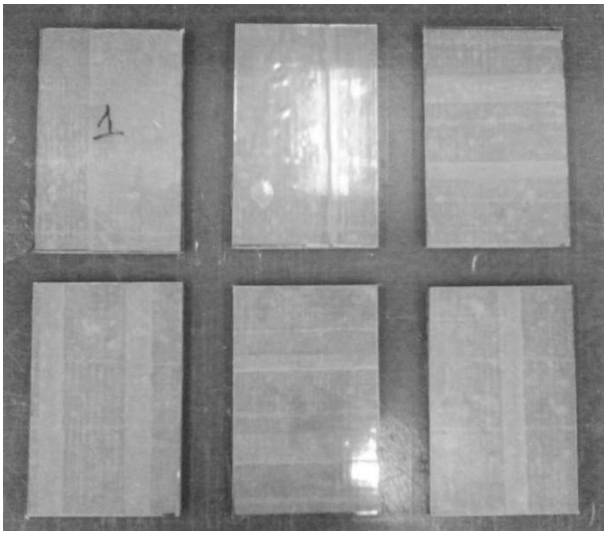


Figure 2.94: PMC specimens protected by adhesive tape

The computer software controlling the measurement operation required the input of specimen thicknesses. Benchmarking was successfully done using 5 mm thick Pyrex 7740 specimens with known thermal conductivities. A summary of results appears in Table 2.3. In-plane thermal conductivity of the specimens tested varied from 2.34 W/mK to 2.55 W/mK while through-thickness thermal conductivity varied from 0.510 W/mK to 0.487 W/mK.

Table 2.3: Thermal conductivities of the PMC plates

| | Plate N°1 | Plate N°2 | Plate N°3 | Mean value |
|---|---|---|---|---|
| Thickness (mm) | 4.30 | 4.20 | 4.30 | 4.27 |
| In-plane conductivity (W/mK) | 2.340 | 2.554 | 2.550 | 2.480 |
| Through-thickness conductivity (W/mK) | 0.510 | 0.502 | 0.487 | 0.500 |

# Chapter 3: Simulation of temperature distribution through PMC components subjected to discrete heat sources

## 3.1. ANSYS software package

The ANSYS 13.0 software package was used for simulating heat transfer through PMC components. The software package includes tools allowing the generation of solid models, meshing and CFD modelling. The CFD tool used was FLUENT, a numerical code based on the finite volume element method, for solving heat transfer equations numerically. FLUENT integrates the governing equations for heat transfer about each control volume. This integration leads to discrete equations that conserve a given physical quantity in a given control volume. The equations undergo spatial discretization according to the mesh, in addition to a temporal discretization in transient cases. FLUENT computes the solution iteratively with regards to the spatial and temporal degrees of freedom.

## 3.2. Simulation of heat conduction through PMC plates manufactured in-house

### 3.2.1. Simulation model

The solid models used for the simulations were created using the Design Modeller tool in ANSYS 13.0. Two solid models were used for simulations, namely $M_1$ and $M_2$. $M_1$ was the solid model of the PMC plate heated using one heater, Figure 3.1. The plate dimensions were 305 mm × 305 mm × 4.25 mm and the heater had 0.6 mm thickness. The second model $M_2$ was of the PMC plate heated using a discrete arrangement of 4 heaters, previously shown in Figure 2.67.

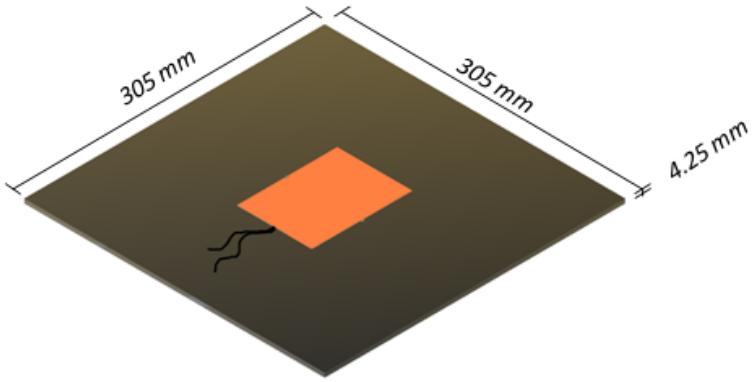


Figure 3.1: Isometric view of the PMC plate solid model $M_1$

The simulation of heat transfer by free convection to/from atmosphere at the outer surfaces required the division of the PMC plate surface into group zones, to account for the local variation of the free convection coefficient. Local variation of the free convection coefficient is justified, essentially by the effect of buoyancy. Convection coefficients were adjusted to the experimental data. The divided surfaces of the PMC plates for the $M_1$ and $M_2$ solid models are shown in Figure 3.2. Group zones were numbered only on one half of the plate as the convection boundary conditions were symmetric with respect to the vertical centreline.

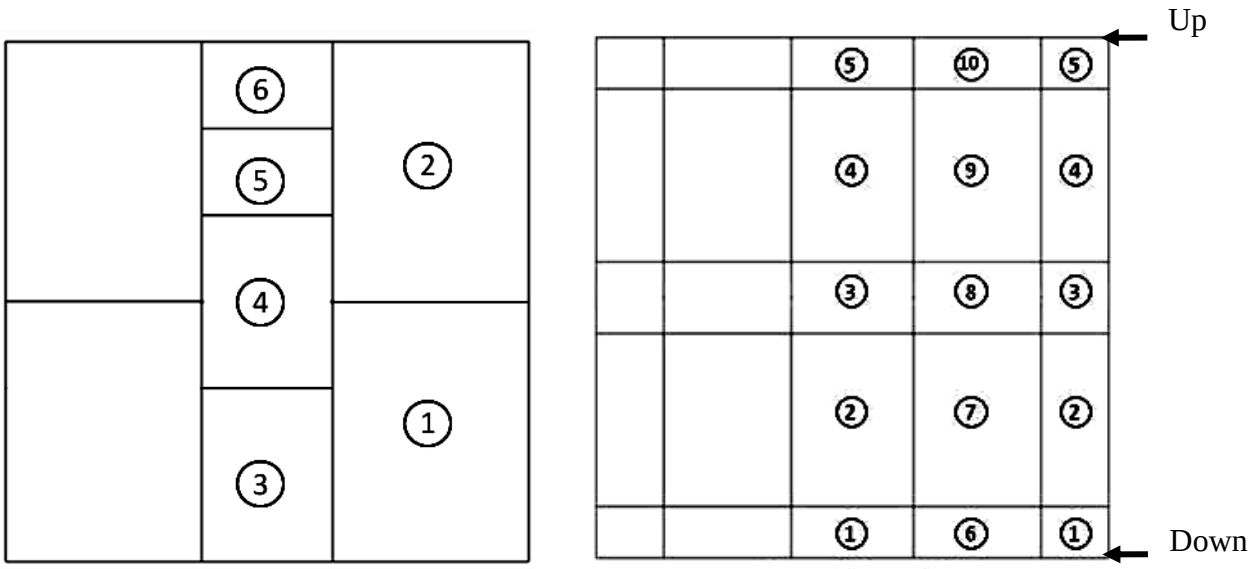


Figure 3.2: Surface zone division of the PMC plate solid models: $M_1$ (left) and $M_2$ (right)

Solid models were imported into ANSYS Mesh tool for mesh generation. A 3D structured mesh made of hexahedral linear elements was generated. The mesh featured 9500 nodes and 4560 elements in the case of solid model $M_1$ while solid model $M_2$ mesh contained 23620 nodes and 11325 elements. Generated meshes were deemed to be of good quality according to ANSYS documentation guidelines, based on parameters such as mesh skewness, aspect ratio and orthogonal quality.

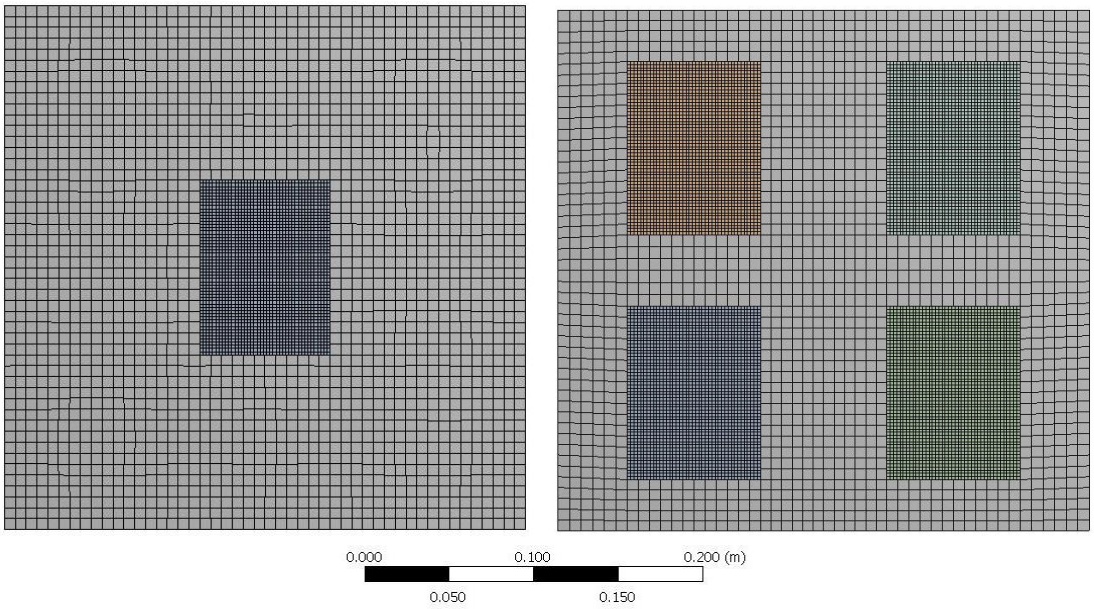


Figure 3.3: Bottom view of the PMC plate surface meshes

In all simulations the heater was assigned a volumetric heat generation rate of 5453 kW/m$^3$ so as to have the same generated heat rate as in previous experiments. Densities of the 6 PMC specimens used previously (Section 2.2.2.7) for thermal conductivity measurements were measured then averaged, Table 3.1. As the PMC material was unbalanced, in-plane thermal conductivity values measured previously (Section 2.2.2.7), were adjusted to get in-plane principal thermal conductivities reflecting the number of carbon fibre plies in each direction. Material properties of the diverse components of the model are listed in Table 3.1. Specific heat assigned to the PMC was obtained by trial and error method. Initial values were based on specific heat of epoxies presented in literature [109-111] and from AS4/3501-6 specific heat stated by Maksoud [97], namely 850 J/kg K. The latter value gave acceptable results but a final value of 950 J/kg K giving a better validation with the experimental data, was finally chosen.

Table 3.1: Material properties of the IHCT components

| | Heater (silicone rubber) [97] | PMC plate |
|---|---|---|
| Density (kg/m$^3$) | 1249 | 1405 |
| Specific Heat (J/kg K) | 1884 | 950 |
| Thermal Conductivity (W/mK) | 0.216 | $K_x$ = 2.61<br>$K_y$ = 2.34<br>$K_z$ = 0.5 |

Several trial and error simulations were performed for determining the free convection coefficients for each of the two models. Local allocations of free convection coefficients for both of the single heater and 4 heater arrangements appear in Table 3.2 and Table 3.3 respectively. The first simulations were based on results reported by Maksoud [97]. Preliminary simulations of the transient temperature distribution in horizontal plates based on a uniform free convection coefficient equal to 10 W/m$^2$ K showed good concordance except over the heater and area adjacent to the heater. It is important to mention that the plate was aligned with heaters facing down. In the case of vertical plates, the uniform free convection coefficient approach could not produce good results when compared with experimental data.

Table 3.2: Allocation of free convection coefficients for simulation model $M_1$

| Zone | Convection coefficient (W/m$^2$ K) | |
|---|---|---|
| | Vertical | Horizontal |
| 1 | 8 | 7 |
| 2 | 15 | 7 |
| 3 | 8 | 7 |
| 4 | 12 | 16 |
| 5 | 2 | 7 |
| 6 | 0.5 | 7 |

Table 3.3: Allocation of free convection coefficients for simulation model $M_2$

| Zone | Convection coefficient ($W/m^2$ K) | |
|---|---|---|
| | Vertical | Horizontal |
| 1 | 10 | 7 |
| 2 | 10 | 7 |
| 3 | 8 | 7 |
| 4 | 8 | 7 |
| 5 | 3 | 7 |
| 6 | 10 | 7 |
| 7 | 20 | 16 |
| 8 | 4 | 7 |
| 9 | 22 | 16 |
| 10 | 4 | 7 |

### 3.2.2. Results

Transient simulations of the heating process were performed for the single heater PMC plates, named model $M_1$, aligned vertically and horizontally. Again, heaters were facing down in the case of the horizontal plate. The aim of transient simulations was mainly to confirm the choice of the specific heat value of 950 J/kg K. Steady-state simulations of the temperature distribution were also done for simulation models $M_1$ and $M_2$ aligned vertically and horizontally. Steady-state simulations were then compared qualitatively and quantitatively to the temperature distributions obtained from the corresponding thermograms.

#### 3.2.2.1. Transient simulations

The heating process was simulated using the model described above. Temperature history was recorded and compared directly with thermocouple values at selected locations previously shown in Figure 2.58 and Figure 2.59. Temperature profile comparisons at locations N°3 - N°6 and N°8 - N°11 for the vertical plate and for the horizontal plate appear in Figure 3.4 and Figure 3.5, respectively. Temperature profiles were labelled as TC#3 – TC#6 and TC#8 – TC#11. Results

from TC#7 were omitted since no temperature change was observed.

Simulated temperature profiles matched thermocouple measured temperature profiles throughout the heating process within 3°C except for thermocouples TC#8 and TC#9. In the latter thermocouple locations, the transient phase of the simulations considerably underestimated the thermocouple values while in the steady-state, both sets of results concurred. Simulated temperature profiles at thermocouple locations TC#8 and TC#9 took longer to reach steady-state. This may be explained by the simultaneous local variation of the specific heat and the free convection coefficient with increasing temperatures. Buoyancy contributes to local free convection coefficients downstream of the heater on the vertical plate, while the specific heat of the PMC material changes driven by the change of the specific heat of the cured epoxy.

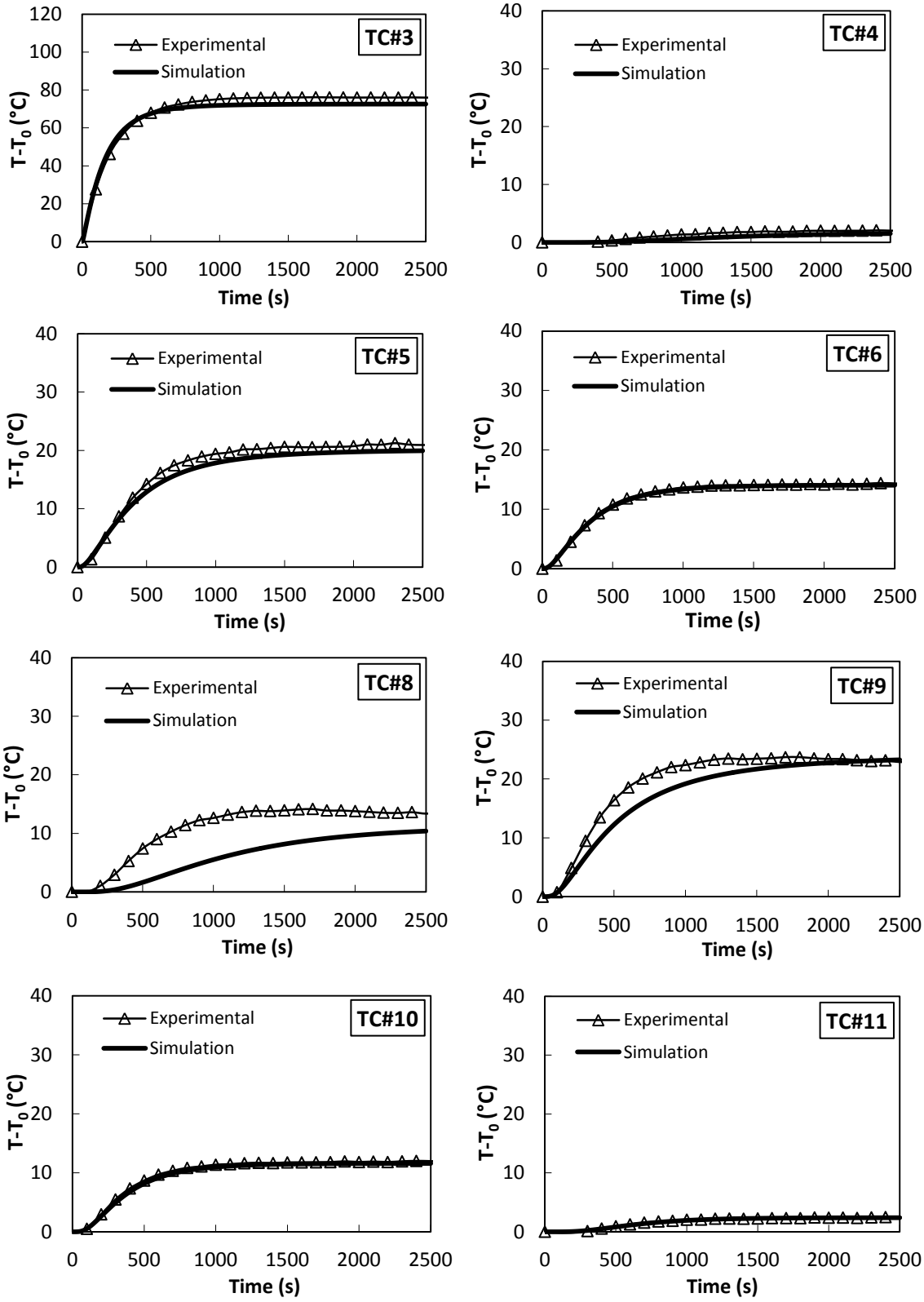


Figure 3.4: Temperature history comparison for the vertical plate

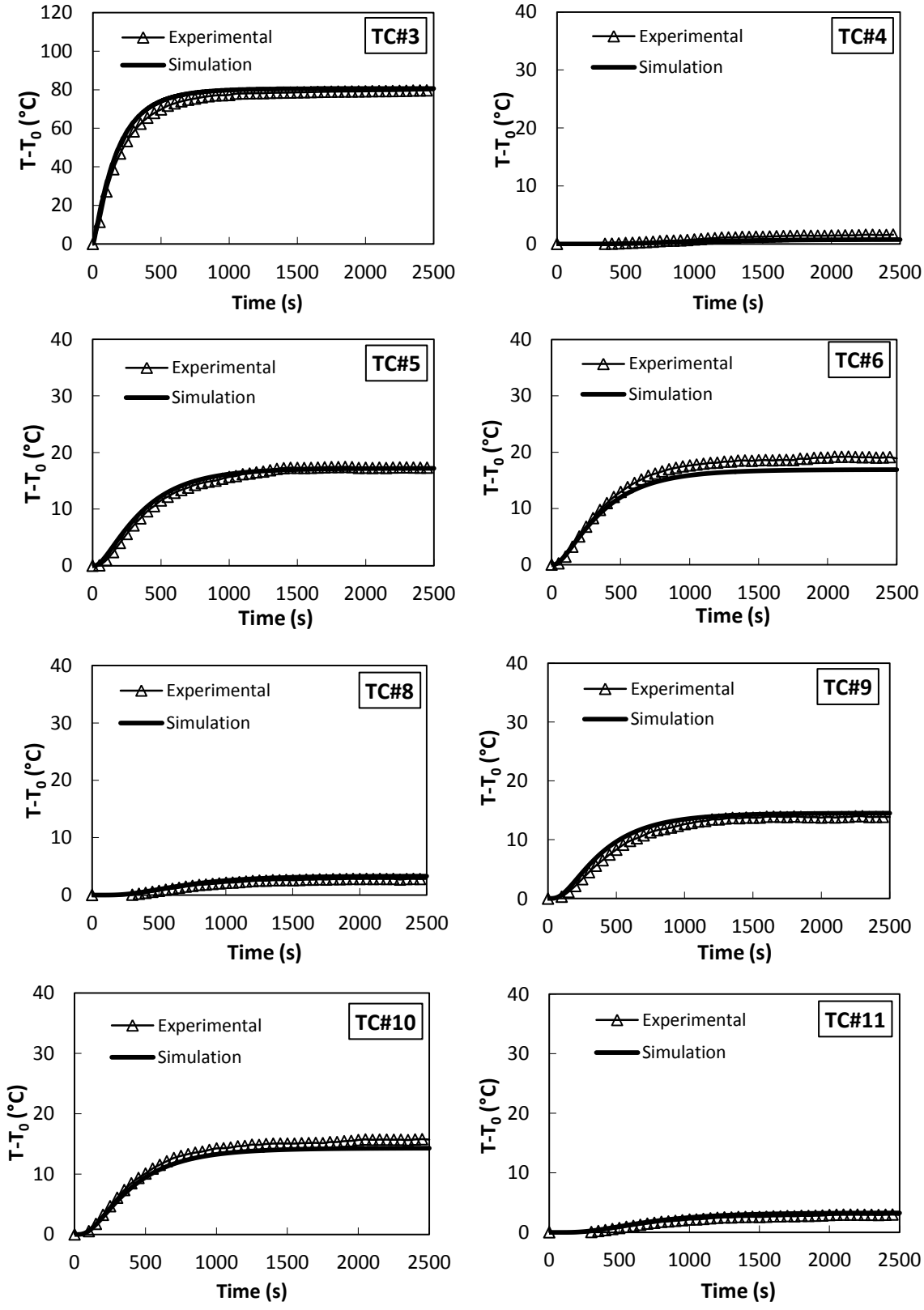


Figure 3.5: Temperature history comparison for the horizontal plate

Better agreement between the simulated and thermocouple temperatures was witnessed in the case of the horizontal plate. Temperature differences were within 3°C during the whole heating process. Thermocouple locations TC#8 and TC#9 showed good concordance as opposed to the case of the vertical plate.

#### 3.2.2.2. Steady-state simulations

Steady-state simulations were performed for the single heater and the 4 heater arrangement configurations, namely $M_1$ and $M_2$ solid models. Simulated steady state temperature distributions were compared to thermographic temperature distributions collected from the PMC plates N°1, N°2 and N°3. Thermograms were taken on opposite side of the heaters. Comparison was done along line Li01, for model $M_1$, while comparison was done along lines Li01 and Li02 for model $M_2$, Figure 2.67. Again, distance along a measurement axis is quoted in percentage from the upper edge of the plate appearing in a thermogram, and corresponding to 0%, while its lower edge corresponds to 100%. Temperature distributions obtained from simulation showed good concordance with those obtained by thermography. For simplicity purposes, only thermograms from PMC plate N°1 are presented in this section.

Temperature distributions from the PMC plate aligned vertically and heated using a single heater are presented in Figure 3.6. Temperature distributions showed similar behaviour and temperature gradients. Temperatures ranged roughly from 25°C to 100°C. Maximum temperature reached 98°C in the simulated temperature distribution while it was close to 103°C in the thermogram. Comparison of simulated and thermographic results appears in Figure 3.7.

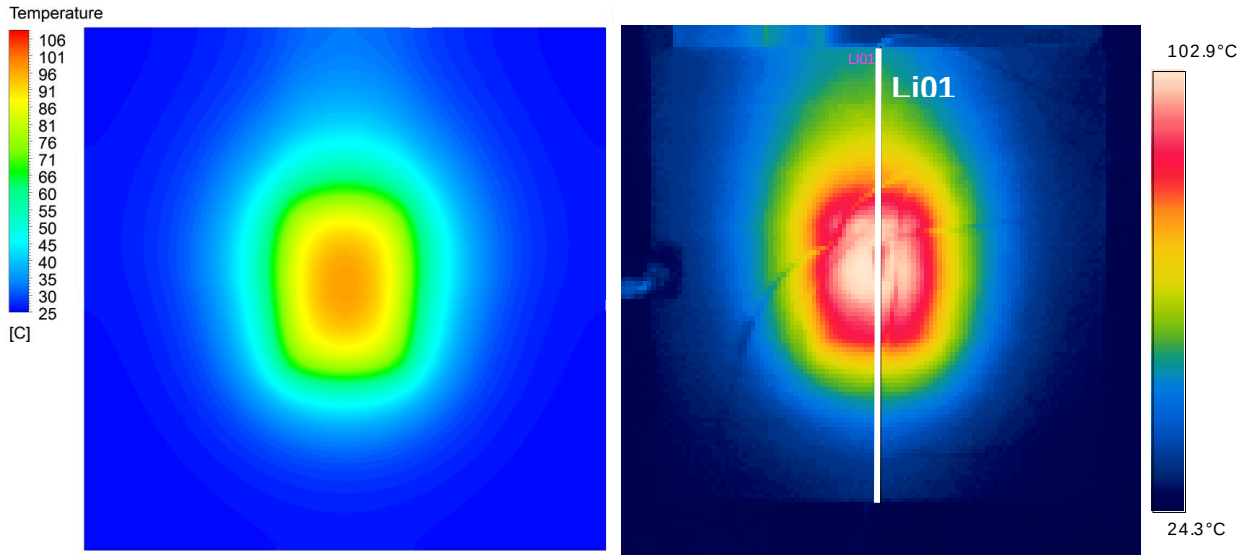


Figure 3.6: Temperature distribution in single heater vertical plate: simulation (left) and thermogram (right)

The simulated temperature profile recorded along the centreline showed good agreement with the corresponding thermographic temperature profile. Simulated temperatures slightly underestimated those obtained from the thermograms on the PMC plate surface from 0% to 35% and 65% to 100% of the measurement axis and in the heater area extending from 35% to 65% approximately.

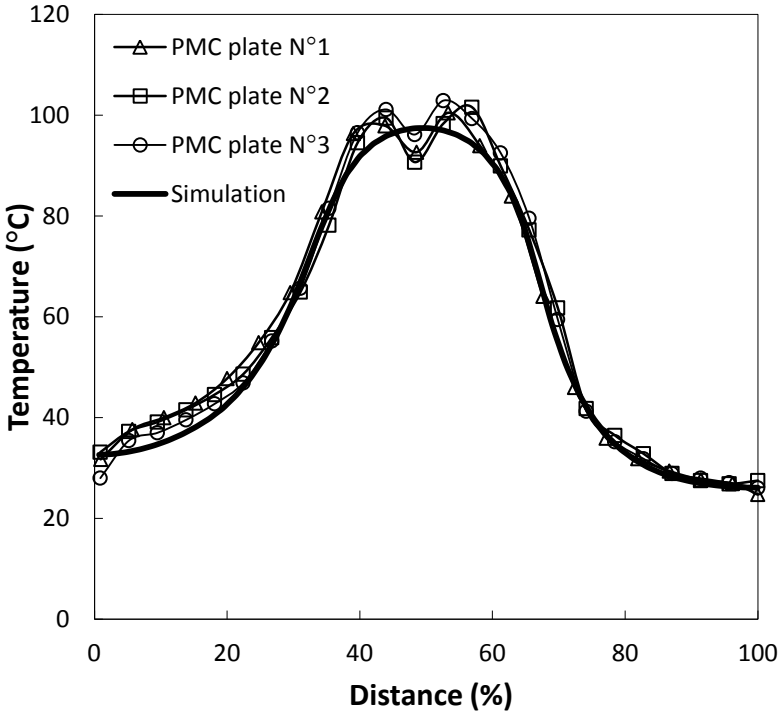


Figure 3.7: Temperature profile comparison along line Li01 of the vertical plate

Temperature distributions showed good agreement in the case of the same plate aligned horizontally. This can be observed in Figure 3.8. According to the graphs, maximum temperatures reached approximately 105°C in the simulated and thermographic temperature distributions. The comparison of the simulated temperature profile along line Li01 with the ones extracted from the thermograms of PMC plates N°1, N°2 and N°3 showed good concordance of the temperature values as well as the overall temperature distribution, Figure 3.9.

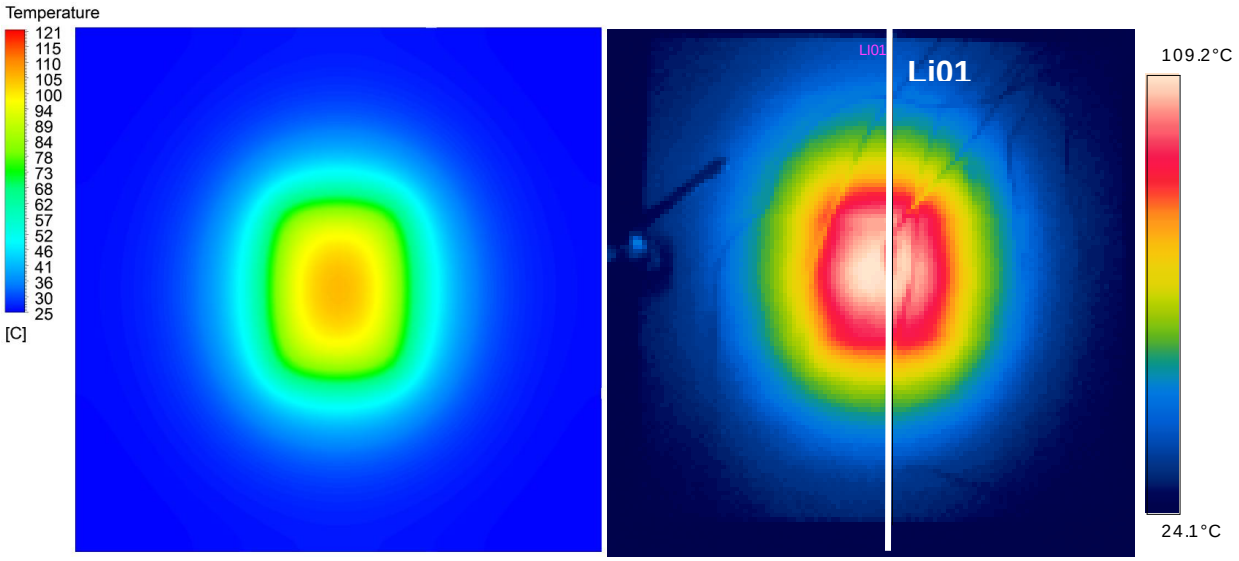


Figure 3.8: Temperature distribution in single heater horizontal plate: simulation (left) and thermogram (right)

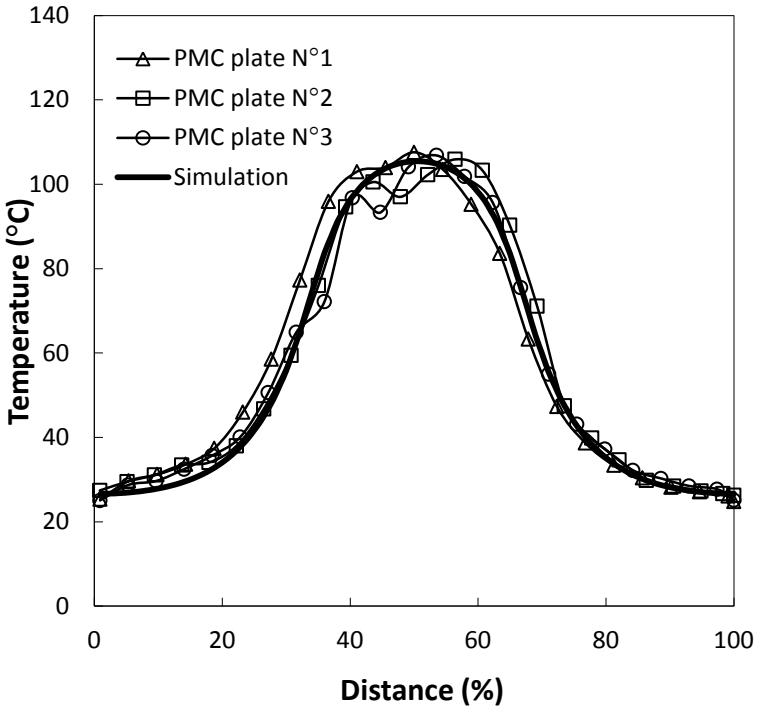


Figure 3.9: Temperature profile along line Li01 of the horizontal plate

The simulated and thermographic temperature distributions of the PMC plate with a 4 heater arrangement, labelled as model $M_2$, are shown in Figure 3.10. The initial intent was to apply directly the boundary conditions used in the single heater configuration to the 4 heater configuration plates. This approach gave acceptable results for the horizontal plate. However, the use of the same free convection coefficients did not lead to good agreement with the thermographic temperature data for the vertically aligned plate. The alternative allocation of free convection coefficients presented previously in **Error! Reference source not found.** resulted in emperature distributions shown in Figure 3.10.

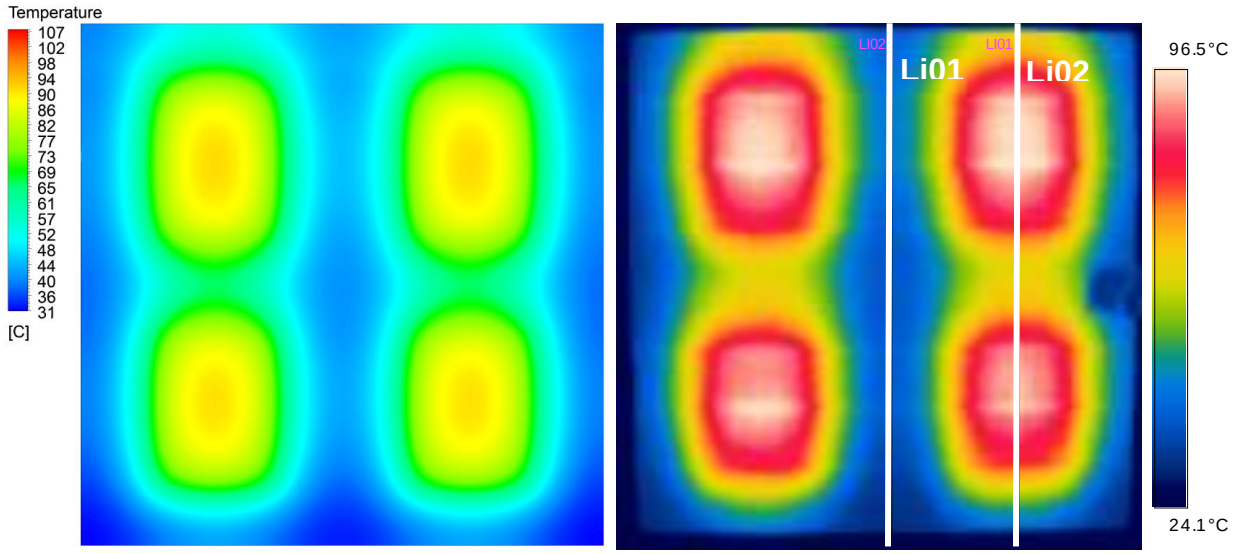


Figure 3.10: Temperature distribution in 4 heater arrangement vertical plate: simulation (left) and thermogram (right)

Temperature distributions showed a similar general behaviour. Temperature maxima were approximately 103°C and 97°C in the simulated temperature distribution and in the thermogram respectively. Temperature profiles obtained from simulations and thermography are compared in Figure 3.11. Data are presented in the form of actual and ambiant temperature difference, labelled as $T\text{-}T_\infty$. In general, simulation results showed good concordance with the thermographic results. Nevertheless, slight discrepancies were observed in temperature

distributions maxima and minima.

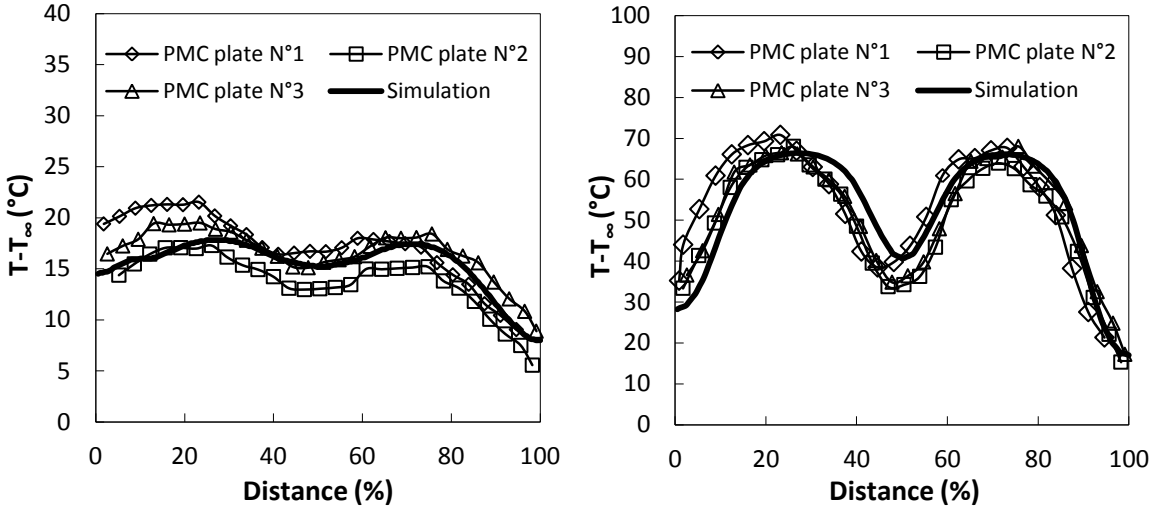


Figure 3.11: Temperature profiles comparison for the vertical plate: Li01 (left) and Li02 (right)

Figure 3.12 shows the simulated and thermographic temperature distributions in the horizontal PMC plates heated using a 4 heater arrangement. The use of the same zone allocation of free convection coefficients applied earlier to the single heater plate for simulating the temperature distribution generated acceptable results. Nevertheless, a discrepancy between the simulation and the thermogram in maximum temperature values can be noticed. Simulated temperatures reached roughly 106°C while thermographic temperatures reached about 102°C.

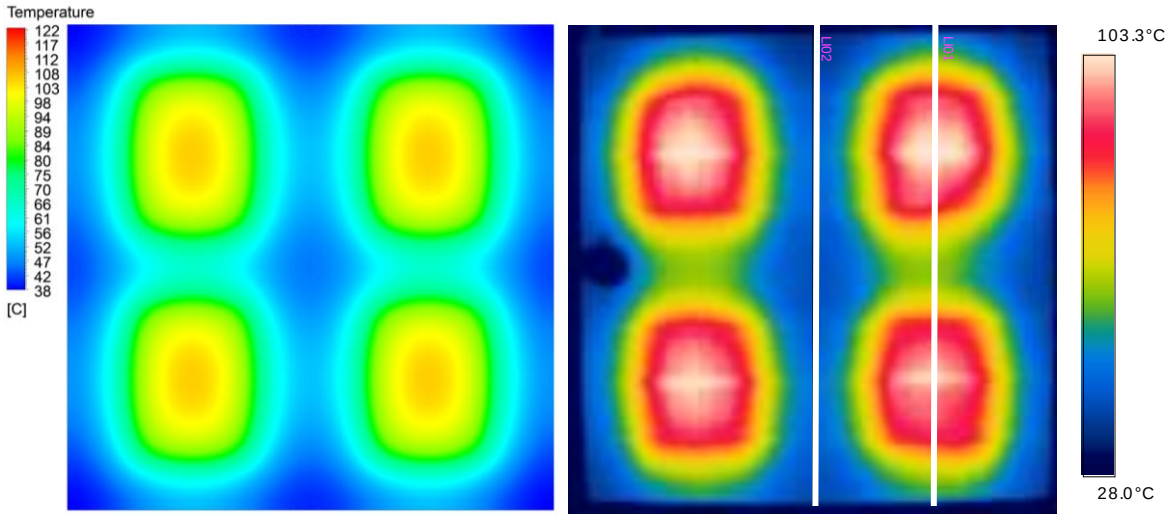


Figure 3.12: Temperature distribution in 4 heater arrangement horizontal plate: Simulation (left) and thermogram (right)

The discrepancy in maximum temperature values can also be seen in Figure 3.13. It is located in the heaters zones extending roughly from 20% to 40% and from 60% to 80% of the measurement axis Li01. Away from the heaters, the simulated temperature profile matched the thermographic temperature profiles.

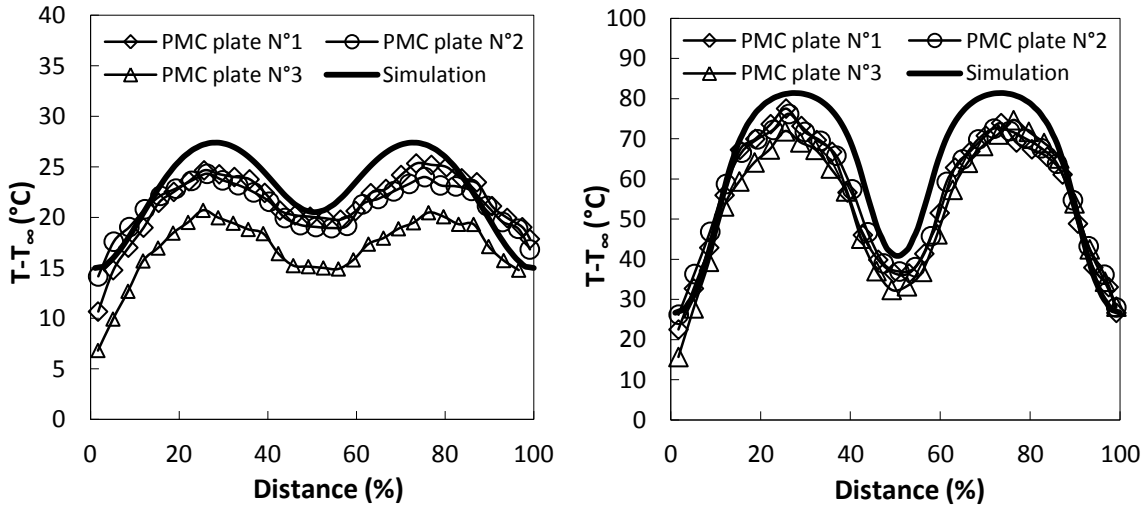


Figure 3.13: Temperature profiles comparison for the vertical plate: Li01 (left) and Li02 (right)

### 3.3. Simulation of heat transfer through demonstrator PMC component

#### 3.3.1. Simulation model

The solid model of the demonstrator PMC component is shown in Figure 3.14. The model geometry was relatively complex. It was divided to 6 zone groups for enabling allocation of PMC orthotropic thermal conductivities. Orthotropic thermal conductivities for each zone were assigned in local coordinate systems. Details of local coordinates axes for to each zone goup are presented in Appendix D. This partition scheme was done to replicate, as closely as possible, the real temperature distribution while minimizing the number of zones. The heater zone was omitted for showing the limits of the materials zone groups.

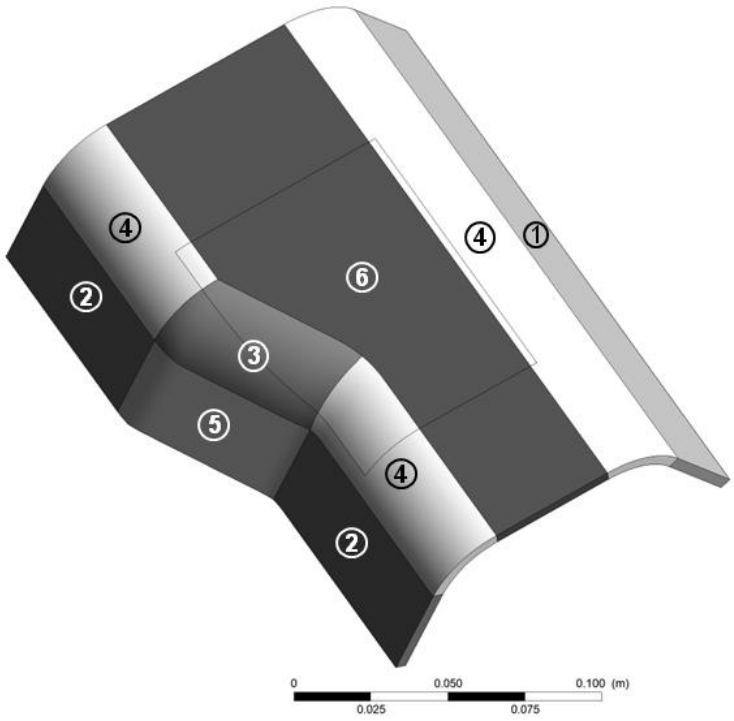


Figure 3.14: Solid model and zone partitions

The solid model shown above was imported to ANSYS mesh. A predominantly hexahedral mesh was generated. It was an unstructured multi-zone mesh with mostly linear elements. The mesh contained 8779 elements with an average 1.44 nodes per element. As opposed to the PMC plates, generating an integrally hexahedral mesh with elements of the same size was not possible because of the geometry. Nevertheless, the mesh was considered to meet the criteria of a good quality according to ANSYS Mesh documentation guidelines.

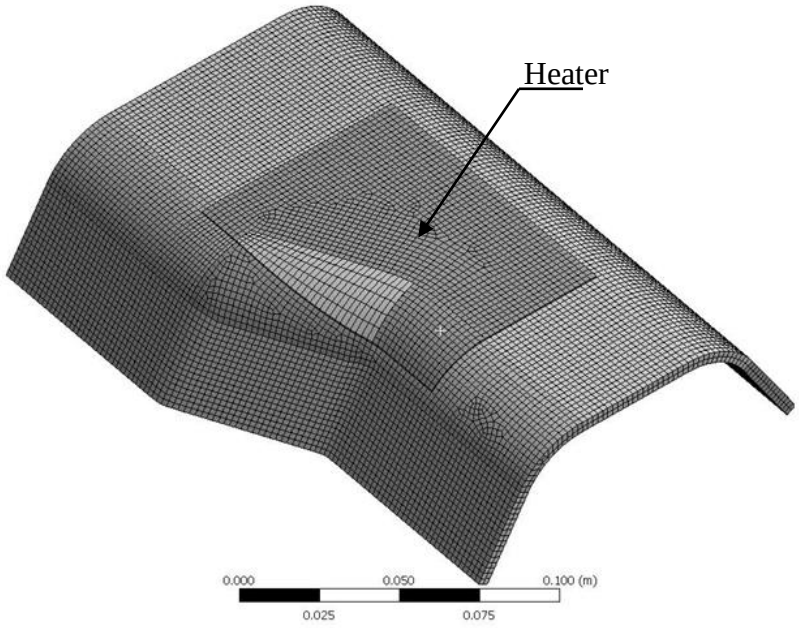


Figure 3.15: Demonstrator component mesh

Directional thermal conductivities were assigned values shown earlier in Table 2.3. Shear of the dry preform upon draping over the demonstrator geometry was previously found to be negligible, Figure 2.28. Consequently, specific heat and density were assigned the same values as in the simulations of the PMC plates, shown in Table 3.1. Volumetric heat generation rate similar to the experiment, described in section 2.2.2.6 as a value of 5453 kW/m$^3$, was assigned to the heater.

Several trial and error simulations of steady-state temperature distributions were done for obtaining the free convection coefficient matching each zone. The first simulations were based on the results obtained earlier from the simulations of temperature distribution in PMC plates aligned horizontally. For simplicity, oblique and curved zones in the demonstrator component were assigned the same convection coefficient values. Allocations of free convection coefficients for the zones appear in Table 3.4.

Table 3.4: Allocation of free convection coefficients for the demonstrator component

| Zone | Convection coefficient ($W/m^2$ K) |
|---|---|
| 1 | 7 |
| 2 | 7 |
| 3 | 7 |
| 4 | 7 |
| 5 | 7 |
| 6 | 10 |

### 3.3.2. Solution and results

Steady-state trial and error simulations were performed and the final temperature distribution was compared to the thermographic temperature distribution. Simulations took around 15 minutes to complete with typically 1000 iterations for convergence. Graphic comparison between the simulated temperature distribution and the thermographic temperature distribution is shown in Figure 3.16. Temperature distributions were displayed in greyscale to match the temperature scales obtained from simulations and from the thermogram. Overall, temperature distributions showed similar temperature gradients locally. Maximum temperatures obtained from simulations exceeded those collected from thermography by about 3°C while simulations underestimated temperatures in the minimum temperatures regions roughly by 5°C.

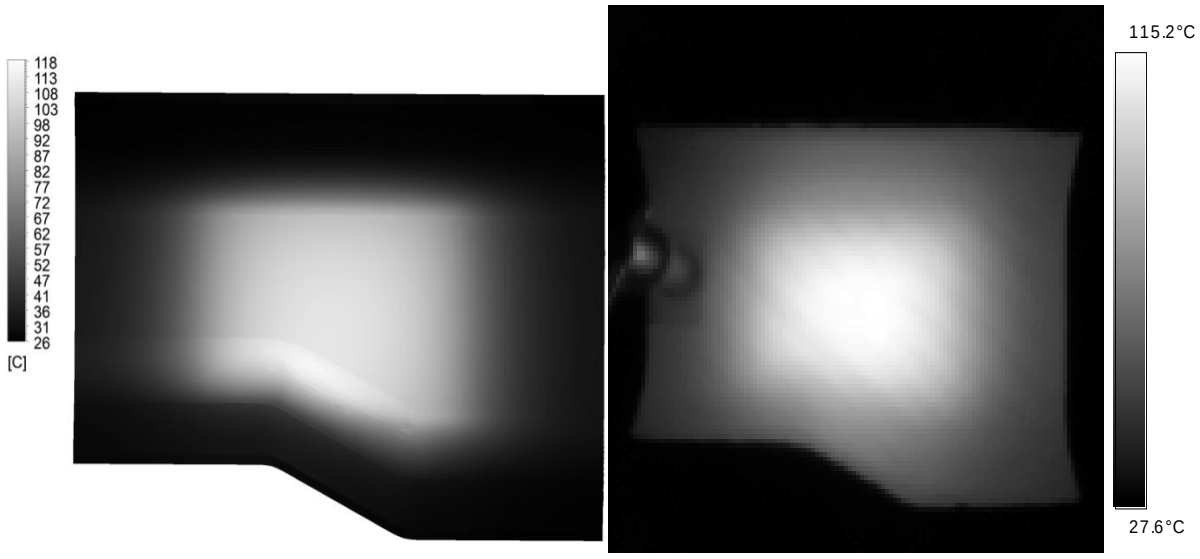


Figure 3.16: Comparison of simulated and thermographic temperature distributions

Comparison of the temperature distributions shown above appears in Figure 3.17. The comparative study of temperature distributions was done based on the area corresponding to a given temperature range. It is worth mentioning that comparison was based on projected areas. The low temperature range extending from 24°C to 34°C occupied the majority of the surface area. 44% of the simulated temperature distribution was in that bracket as opposed to 38% for the thermographic temperature distribution. Moving to the higher temperature ranges up to a temperature of 103°C, both of the temperature distributions showed good concordance. Temperature zones in simulations occupied smaller areas for all of the temperature ranges except for the 34°C - 43°C temperature range where the area percentages had nearly the same value. Discrepancies in the area percentages within a given temperature bracket over temperatures ranging from 34°C to 103°C were less than 2%. At the highest temperature range extending roughly from 103°C to 115°C, the area occupied in the simulated temperature distribution was roughly 5% while the occupied area obtained from the thermogram was only 2%. Most of the temperature ranges exhibited less than 3% area difference between the simulated and thermographic temperature distributions. The exception was a 6% area difference in the 24°C - 34°C temperature range. In general, the simulated temperature distribution was deemed to be matching the temperature distribution collected by thermography. The larger discrepancy in the

24°C - 34°C temperature range can be explained by the fact that areas with the lowest temperatures were oblique with respect to the camera axis. The surface of these areas was not integrally seen by the IR camera as opposed of the simulations where the area percentage occupied by the same temperature bracket was accurately evaluated. On the contrary, areas with the highest temperatures were mainly located on the flat surface of the demonstrator PMC component.

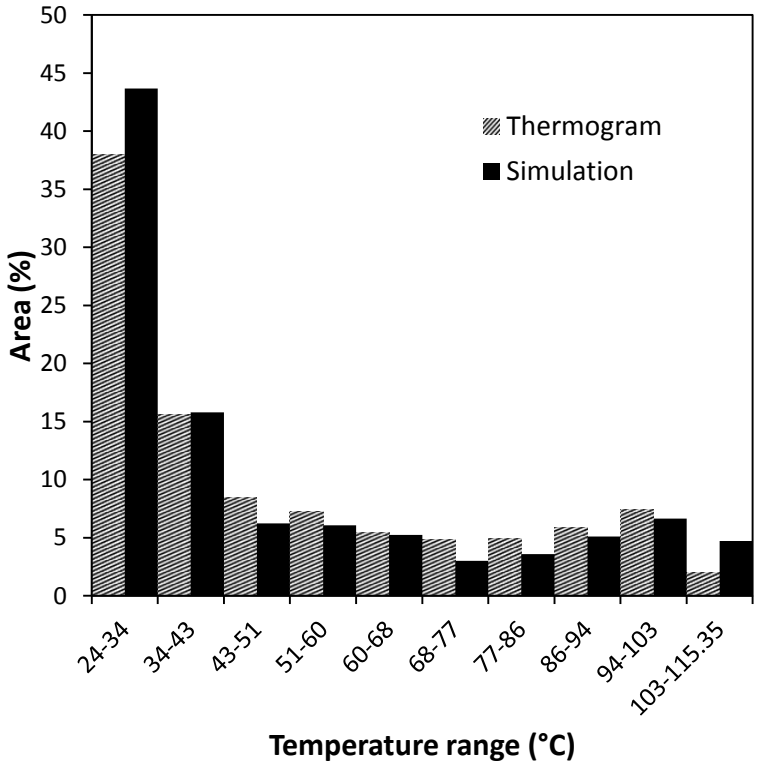


Figure 3.17: Comparison of temperature distributions obtained from simulation and thermography

The same model was used for simulating the temperature distribution in the demonstrator component while changing the PMC material to aluminum. The intent was to expose the effect of the low conductivity of the PMC material. Figure 3.18 shows the surface temperature distributions in the PMC component and in the simulated aluminum component.

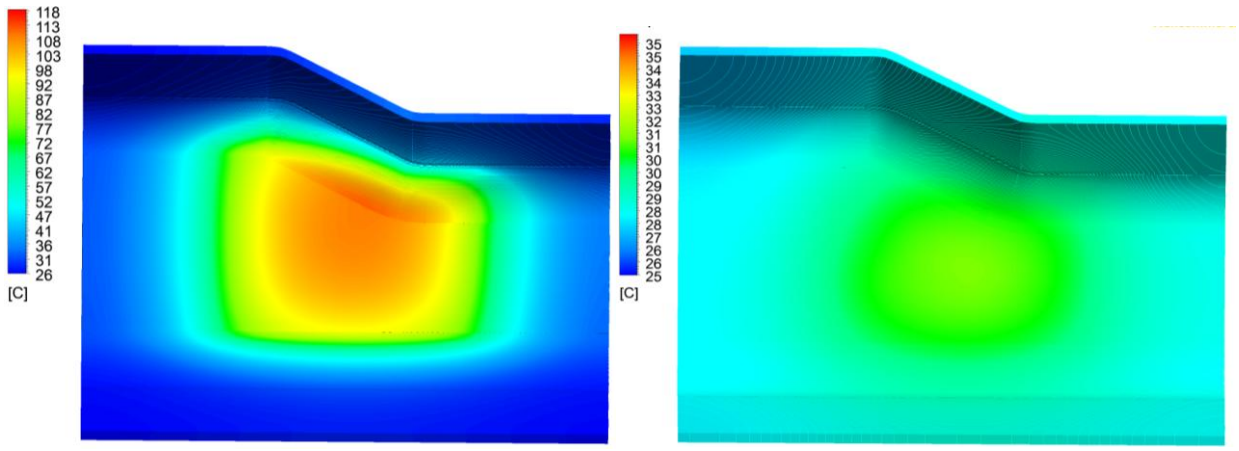


Figure 3.18: Effect of material change on the temperature distribution: PMC component (left) and aluminum component (right)

One can clearly notice that the PMC component had considerably higher temperature gradients. Maximum temperatures reached 118°C in the PMC component while in the aluminum component temperatures did not exceed 35°C. This can be explained by the relatively low in-plane and through-thickness thermal conductivity of the PMC material. The isotropic thermal conductivity of aluminum, evaluated at 237 W/m K at room temperature [21], is relatively high when compared to the in-plane and the through-thickness thermal conductivity of the PMC material. High temperature gradients present load bearing PMC components mounted into a larger structure might cause stress problems. Prediction of stresses is a paramount parameter in the design of PMC structures.

# Chapter 4: Conclusion

In the course of this thesis, an entire process was setup for producing PMC components using RTM. The process included preforming, moulding and post processing. Manual preform manufacturing was a tedious task adding considerable cost to the process. This urged the research group to give priority to the development of an automated tow lay-down device now functional at the PMC Manufacturing Laboratory, University of Ottawa. Dry preform impregnation in RTM was studied through silicone oil injections with specific emphasis on race-tracking. Finally, the developed RTM apparatus produced good quality 2D and 3D PMC components with a suitable $V_f$, namely 52%. Capital costs of the process were relatively low owing to the use of the Instron-cylinder pumping system as an alternative to a commercial RTM machine. Challenges faced during the development of the process were overcome by both research and trial and error. Challenges included preform fray, trapped air in the resin and delamination of the component edges during de-moulding.

Manufactured PMC components showed good repeatability in terms of thermal behaviour. The use of thermography with the manufactured PMC material was validated. Emissivity variation within the range indicated for organic materials was found to have minor effects on temperature readings. A value of 0.92 was found to give thermographic results concurring with thermocouple measurements. Variability of thermographic measurements was within error margin indicated by the infrared camera supplier. All expected advantages of thermography were realised, including instant temperature mapping of large surfaces and straightforward data processing.

Thermography was a key tool for evaluating the thermal effect of bonding an outer copper sheet to a manufactured PMC plate on the temperature distribution through the IHCT. The thickness of high temperature silicone thickness applied manually for bonding was impossible to control.

Nevertheless, the temperature distribution exhibited lower temperature gradients and considerably lower overall temperatures, when compared with the temperature distribution through another PMC plate subjected to similar heating conditions. This technique known as the integrally heated copper tooling is therefore well suited to mould applications. Manufacturing IHCT moulds using the same PMC material may resolve the issue of the coefficient of thermal expansion mismatch between the mould and the manufactured PMC component.

Simulation models were developed for predicting the temperature distribution through PMC components. ANSYS 13.0 software package was used for simulating heat transfer through PMC components. Orthotropic thermal conductivity was measured while specific heat was determined by trial and error using experimental data. Benchmarking with experimental measurements was the only way to reduce uncertainty introduced by simulations. Transient and steady-state simulations led to a good agreement with experimental data despite airflow in the laboratory. Developed simulation models can be used for reducing potential costs related to conceptual design of IHCT and PMC structures, but more accurate models need to be developed for designing accurately engineered structures.

The main contribution of this work was the development of a low cost RTM process capable of producing relatively large PMC components with high fibre volume fraction. The process can be used for numerous future studies and experiments. Mechanical testing should be done next on manufactured components. It is worth mentioning that more work can be done for improving the process. Potential improvements include optimizing the stitching process for better permeability uniformity, less fray and local tow dislocations during preforming as well as during impregnation. Improvement of impregnation of dry preforms during the RTM process can also be done through optimising the gating of the mould and the resin flow pressures through the preform.

# References


1 . Chung, D L. *Carbon fibre composites.* Butterworth-Heinemann, 1994.

2 . Baker, A, S Dutton, and D Kelly. *Composite materials for aircraft structures.* American institute of aeronautics and astronautics, Inc, 2004.

3 . Matthews, F L, and R D Rawlings. *Composite material: Engineering and science.* Oxford: Chapman & Hall, 1994.

4 . Frank, Ko. *Toughening of composites by 3-D fibre architecture.* Drexel University, 1993.

5 . Wamba, P M, and R Anandjiwala. "A review of preforms for the composites industry." *Journal of industrial textiles*, 2011.

6 . Weimer, C, P Mitschang, and M Neitzel. "continuous manufacturing of tailored reinforcements for liquid infusion processes based on stitching technologies." *The 6th International Conference on Flow Processes in Composite Materials.* Auckland, New Zealand, 2002.

7 . Ogale, A, and P Mitschang. "Tailoring of Textile Preforms for Fibre-reinforced Polymer Composites." *Journal of industrial textiles* (Journal of industrial textiles), 2004.

8 . Schuster, M, A Ogale, and L Peetz. "Analysis of sewed preforms by visual on-line monitoring of stitch-hole variations under compaction." *Composites science and technology*, 2008.

9 . Ogale, A, and P Mitschang. "Compaction behavior of assembled fiber reinforced preforms." *Journal of industrial textiles*, 2007.

10 . Mitschang, P, and A Ogale. "Manufacturing of tailored reinforcement for liquid composite molding processes." In *Polymer composites: from nano- to macro-scale*, by K Friedrich, S Fakirov and Z Zhang. Springer, 2005.

11 . Long, A C, B J Souter, F Robitaille, and C D Rudd. "Effects of fibre architecture on reinforcement fabric deformation." *Plastics, Rubber and Composites*, 2002.

12 . Loendersloot, R, S V Lomov, R Akkerman, and I Verpoest. "Carbon composites based on multiaxial multiply stitched preforms. Part V: geometry of sheared biaxial fabrics." *Composites: Part A*, 2006.

13 . Robitaille, F, and R Gauvin. "Compaction of textile reinforcements for composites manufacturing. III: Reorganization of the fiber network." *Polymer composites*, 1999.

14 . Hashin, Z. "Analysis of properties of fibre composites with anisotropic constituents." *ASME Applied Mechanics*, 1979.

15 . Mazumdar, S K. "Composites manufacturing: materials, product, and process engineering." CRC Press, 2002.

16 . Hoa, V S. *Principles of the manufacturing of composite materials.* DEStech Publications, 2009.

17 . Potter, K D. "The early history of the resin transfer moulding process for aerospace applications." *Composites: Part A*, 1998.

18 . Bickerton, S, E M Sozer, P J Graham, and S G Advani. "Fabric structure and mold curvature effects on preform permeability and mold filling in the RTM process. Part I. Experiments." *Composites: Part A*, 2000.

19 . Mouton, S, D Teissandier, P Sebastian, and J P Nadeau. "Manufacturing requirements in design: The RTM process in aeronautics." *Composites: Part A*, 2010.

20 . Edgren, F. *Physically based engineering models for NCF composites.* Stockholm: Department of Aeronautical and Vehicle Engineering, School of Engineering Sciences, Kungliga Tekniska Högskolan, 2006.

21 . Incropera, F P, T L Bergman, A S Lavine, and D P DeWitt. *Fundamentals of heat and mass transfer.* 6th edition. John and Wiley & Sons, 2006.

22 . Springer, G S, and L P Kollar. *Mechanics of composite structures.* Cambridge University Press, 2003.

23 . Anagnostopoulos, G, J Parthenios, and C Galiotis. "Thermal stress development in fibrous composites." *Materials letters*, Elsevier, 2008.

24 . Rastogi, N, R Soni, and A Nagar. "Thermal stresses in aluminum-to-composite double-lap bonded joints." *Advances in engineering software*, 1998: Elsevier science.

25 . Deheegera, A, C Badulescua, J D Mathiasb, and M Grediac. "Experimental study of thermal stresses in a bonded joint." *7th international conference on modern practice in stress and vibration analysis.* Journal of physics: Conference series, 2009.

26 . Barroso, A, D Vicentini, F Paris, and V Mantic. "Representativity of thermal stresses in designing composite joints based on singular stress states at multimaterial corners." *Composites: Part A*, 2011.

27 . Hetnarski, R B. *Thermal stresses.* Elsevier, 1996.

28 . Chawla, K K. *Fibrous materials.* Cambridge university press, 1998.

29 . Lim, T C. "Unified practical bounds for the thermal conductivity of composite materials." *Materials letters*, 2002.

30 . Nicilais, L, M Meo, and E Milella. *Composite materials: A vision of the future.* Springer-Verlag London Limited, 2011.

31 . Dasgupta, A, and R K Agarwal. "Orthotropic thermal conductivity of plain-weave fabric composites using a homogenization technique." *Journal of composite materials*, 1992.

32 . Pilling, M W, B Yates, M A Black, and Tattersall. "The thermal conductivity of carbon fibre-reinforced composites." *Journal of materials science* 14, 1979.

33 . Al-Sulaiman, F A, Y N Al-Nassar, and E M Mokheimer. "Numerical prediction of the thermal conductivity of fibres." *Journal of heat and mass transfer*, 2006.

34 . Thornburgh, J D, and C D Pears. "Prediction of the thermal conductivity of filled and reinforced plastics." *ASME*, 1965.

35 . Progelhof, R C, J L Throne, and R R Ruetsch. "Methods for predicting the thermal conductivity of composite systems: A review." *Polymer engineering and science* 16, no. 9, 1976.

36 . James, B W, G H Wostenholm, G S Keen, and S D McIvor. "Prediction and measurement of the thermal conductivity of composite materials." *Journal of physics D: Applied physics*, 1986.

37 . Springer, G S, and L P Kollar. *Mechanics of composite structures.* Cambridge University Press, 2003.

38 . Hashin, Z. "Analysis of composite materials: A survey." *Journal of applied mechanics*, 1983.

39 . Zinmeister, G E, and K S Purohit. "Comments on the Springer and Tsai's method predicting effective thermal conductivities of unidirectional materials." *Journal of composite materials*, 1970.

40 . Nielsen, L E. "The thermal and electrical conductivity of two-phase systems." *Industrial engineering chemical fundamentals*, 1974.

41 . Clayton, W A. "Constituent and composite thermal conductivities pf phenolic-carbon and phenolic-graphite ablators." *Structural dynamics and materials conference.* Anaheim, CA: AIAA/ASME 12th structures, 1971.

42 . Grove, S M. "A model of transverse thermal conductivity in unidirectional fibre-reinforced composites." *Composites science and technology*, 1990.

43 . Hasselman, D P, K Y Donaldson, and J R Thomas. "Effective thermal conductivity of

uniaxial composite with cylindrically orthotropic carbon fibers and interfacial thermal barrier." *Journal of composite materials*, 1993.

44 . Mirmira, S R, and L S Fletcher. "Comparison of Effective Thermal Conductivity and Contact Conductance of Fibrous Composites." *Journal of thermophysics and heat transfer*, 1999.

45 . Springer, G S, and S W Tsai. "Thermal conductivities of unidirectional materials." *Journal of composite materials*, 1967.

46 . Wakeham, W A. *Thermal conductivity measurement.* CRC Press, 2000.

47 . Department of defense handbook, USA. *Polymer matrix composites guidelines for characterisation of structural materials.* Vol. Volume 1. 2002.

48 . Parker, W J, and R J Jenkins. "Flash method of determining thermal diffusivity, heat capacity, and thermal conductivity." *Journal of applied physics*, 1961.

49 . Taylor, R E, J Jortner, and H Groot. "Thermal composites diffusivity of fiber-reinforced composites using the laser flash technique." *Carbon*, 1985.

50 . Graham, S, and D L McDowell. "Numerical analysis of the transverse thermal conductivity of composites with imperfect interfaces." *Journal of heat transfer*, 2003.

51 . Callister, W. *Materials science and engineering: An introduction.* John Wiley & Sons, 2003.

52 . Halliday, D, R Resnick, and J Walker. *Fundamentals of Physics.* 5th edition. John Wiley & Sons, 1997.

53 . Hunyar, C, L Feher, and M Thumm. *Simulations and experiments on the effects of millimetre-wave heating of orthotropic and anisotropic CFRP composites.* Universität Karlsruhe- Institut für Höchstfrequenztechnik und Elektronik.

54 . Advani, S G, and C Corlay. "Temperature distribution in a thin composite plate exposed to a concentrated heat source." *International journal of heat and mass transfer*, 2007.

55 . Davidson, M. *http://media.paisley.ac.uk/~davison/labpage/searle/searle.html.* April 15, 1992.

56 . Duncan, M, and M Jarratt. "Thermal conductivity of PTFE and PTFE composites." *28th conference of the North American thermal analysis society.* Orlando, Florida, 2000.

57 . Assael, M J, K D Antoniadis, and D Tzetzis. "The use of the transient hot-wire technique for measurement of the thermal conductivity of an epoxy-resin reinforced with glass fibres and/or carbon multi-walled nanotubes." *Composites science and technology*, 2008.

58 . Miller, M G, J M Keith, J A King, R A Hauser, and A M Moran. "Comparison of the guarded-heat-flow and transient-plane-source methods for carbon-filled nylon 6,6 composites: experiments and modeling." *Journal of applied polymer science*, 2006.

59 . Keith, J M, J A King, and M G Miller. "Thermal conductivity of carbon fibre/liquid crystal polymer composites." *Journal of applied polymer science*, 2006.

60 . Gowayed, Y, and J C Hwang. "Thermal conductivity of composite materials made from plain weaves and 3-D weaves." *Composites engineering*, 1995.

61 . Al-Sulaiman, F A, E M Mokheimer, and Y N Al-Nassar. "Prediction of the thermal conductivity of the constituents of fiber reinforced composite laminates." *Journal of heat and mass transfer*, 2006.

62 . Al-Sulaiman, F A, Y N Al-Nassar, and E M Mokheimer. ". Prediction of the thermal conductivity of the constituents of fiber-reinforced composite laminates: Voids effect." *Journal of composite materials*, 2006.

63 . Slesinger, N A. *Thermal Modeling Validation Techniques for Thermoset Polymer Matrix Composites.* Masters thesis, Vancouver: University of British Colombia, 2010.

64 . Loos, A C, and G S Springer. "Curing of Epoxy Matrix Composites." Journal of composite materials, 1983.

65 . Johnston, A. An integrated model of the development of process-induced deformation in autoclave processing of composite structures. PhD thesis, University of British Columbia, 1997.

66 . Hexcel Corporation. "HexTow AS4 product data sheet." Stamford, Connecticut, 2010a.

67 . Schuster, J, D Heider, K Sharp, and M Glowania. "Thermal conductivities of three-dimensionally woven fabric composites." Composites Science and Technology, 2008.

68 . Hexcel Corporation. "HexTow IM7 product data sheet." Stamford, Connecticut, 2010c.

69 . Hexcel Corporation. "HexTow IM10 product data sheet." Stamford, Connecticut, 2010b.

70 . Toray Inc. M35J product data sheet. Santa Ana, California: 2010a.

71 . Toray Inc. M40J product data sheet. Santa Ana, California: 2010b .

72 . Toray Inc. "M46J product data sheet." Santa Ana, California, 2010c.

73 . Toray Inc. "M50J product data sheet." Santa Ana, California, 2010d.

74 . Toray Inc. "M55J product data sheet." Santa Ana, California, 2010e.

75 . Toray Inc. "M60J product data sheet." Santa Ana, California, 2010f.

76 . Cytec Industries Inc. "Thornel P-25 product data sheet." Woodland Park, New Jersey , 2003a.

77 . Cytec Industries Inc. "Thornel P-30 product data sheet." Woodland Park, New Jersey , 2003b.

78 . Guo, Zhan Sheng, Shanyi Du, and Boming Zhang. "Temperature field of thick thermoset composite laminates during cure process." Composites Science and Technology, 2004.

79 . Toray Inc. "T300 product data sheet." Santa Ana, California, 2010h.

80 . Toray Inc. Toray industries Inc. 2005. http://www.torayca.com/en/techref/index.html (accessed April 22, 2012).

81 . Cytec Industries Inc. "Thornel P-300 product data sheet." Woodland Park, New Jersey , 2003c.

82 . Cytec Industries Inc. "Thornel T-650/35 product data sheet." Woodland Park, New Jersey , 2003d.

83 . Toray Inc. "T700S product data sheet." Santa Ana, California, 2010i.

84 . Toray Inc. "T800S product data sheet." Santa Ana, California, 2010j.

85 . Toray Inc. "T1000G product data sheet." Santa Ana, California, 2010g.

86 . Scott, E P, and J V Beck. "Estimation of thermal properties in epoxy matrix/carbon fiber composite materials." Journal of composite materials, 1992.

87 . Kalogiannakis, G, D Van Hemelrijck, and G Van Assche. "Measurements of Thermal Properties of Carbon/Epoxy and Glass/Epoxy using Modulated Temperature Differential Scanning Calorimetry." Journal of composite materials, 2004.

88 . Sweeting, R, and X Liu. "Measurement of thermal conductivity for fibre-reinforced composites." Composites-Part A: Applied science and manufacturing, 2004.

89 . Hind, S, and F Robitaille. "Measurement,Modeling, and variability of thermal conductivity for structural polymer composites." *Journal of polymer composites*, 2010.

90 . Herbert, Kaplan. Practical applications of infrared sensing and imaging equipment. Third edition. SPIE, 2007.

91 . Williams, T L. Thermal imaging cameras: Characteristics and performance. CRC Press, 2009.

92 . Kaviany, M. Principle of heat transfer. John Wiley & Sons, 2002.

93 . Hamrelius, T. "Accurate temperature measurement in thermography." QIRT seminar proceedings. 1992.

94 . Houde, M. "Carbon fibre composite tooling optimization for heat transfer using CFD modeling." Engineering report, University of Ottawa, 2007.

95 . Hind, S. "Using Plackett-Burman and Taguchi experimental designs to determine significant factors for the repair of thick section composite wing skins with aluminum substructure." Engineering report, University of Ottawa, 2007.

96 . Morton, J. "Modeling heat transfer through complex shapes using computational fluid dynamics." Engineering report, University of Ottawa, 2008.

97 . Maksoud, T. "Optimization of heat transfer in carbon fibre epoxy composite tooling." Engineering report, University of Ottawa, 2008.

98 . Brillant, M. "Simulation and experimental measurement of heat transfer through composite laminates with integrated copper sheets." Engineering report, University of Ottawa, 2008.

99 . El Karafi, I. "Geometric modeling and heat transfer simulations for the reverse engineering of an aerospace carbon / epoxy back seat tool." Engineering report, University of Ottawa, 2009.

100 . Hind, S. "Predicting and measuring thermal conductivity in carbon/epoxy unidirectional tape and textile reinforced composites." Masters thesis, University of Ottawa, 2008.

101 . Hind, S, and F Robitaille. "Measurement,Modeling, and variability of thermal conductivity for structural polymer composites." Journal of polymer composites, 2010.

102 . FLIR Systems. "FLIR i7 data sheet." 2010.

103 . MINCO products. http://www.minco.com/products/heaters.aspx? (accessed 04 22, 2012).

104 . Toho Tenax America, Inc. *http://www.tohotenaxamerica.com.* December 2009. http://www.tohotenaxamerica.com/contfil.php?conv=si (accessed April 25, 2012).

105 . Toho Tenax Europe GmbH. "Delivery programme and characteristics for Tenax® HTS filament yarn." Technical data sheet, 2011.

106 . Burnford, Nicolas. *Development of Drape Simulation Software and the Optimisation of Variable-Length Textiles.* Masters thesis, University of Ottawa, 2011.

107 . HUKSEFLUX THERMAL SENSORS. ***WWW.HUKSEFLUX.COM***. http://www.hukseflux.com/brochures/thermalConductivity/thisys.pdf (accessed 05 10, 2012).

108 . HUKSEFLUX THERMAL SENSORS.www.HUKSEFLUX.com. http://www.hukseflux.com/brochures/thermalConductivity/thasys.pdf (accessed 05 10, 2012).

109 . Hartmann, B, G Lee, and M Long. "Specific Heat Capacities of Some Polyepoxides." Polymer, 1982.

110 . McHugh, J, P Fideu, A Herrman, and W Stark. "Determination and review of specific heat capacity measurements during isothermal cure of an epoxy using TM-DSC and standard DSC techniques." Polymer Testing, 2010.

111 . Tamulevich, T W, and V E Moore. "The significance of glass transition temperature on epoxy resins for fiber optics applications." Epoxy Technology Inc., 1980.

# Appendix A: Materials technical sheets

TohoTenax

TEIJIN

**Delivery programme and characteristics for Tenax® HTS filament yarn**

| **Brand name** | | **Tenax®** | **Tenax®** | **Tenax®** |
|---|---|---|---|---|
| **Production site** | | **E** | **E** | **E** |
| **Fiber family & tensile properties** | | **HTS40** | **HTS40** | **HTS45** |
| Sizing properties | | F13 | F13 | E23 |
| Number of filaments | | 12K | 24K | 12K |
| Nominal linear density [1)] | [tex] | 800 | 1600 | 800tex |
| Twist | [t/m] | 0/10Z | 0/5Z | 0 |
| Running length per kg | [m/kg] | 1250 | 625 | 1250 |
| Package weight, net | [kg] | 2 • 4 • 6 | 2 • 4 • 6 • 8 | 2 • 4 • 6 |

1) ohne Präparationsauftrag

| **Tensile Properties (typical values)** | | | | |
|---|---|---|---|---|
| Tensile strength | [MPa] | 4300 | 4300 | 4500 |
| Tensile modulus | [GPa] | 240 | 240 | 240 |

| **Characteristics (typical values)** | | |
|---|---|---|
| Filament diameter | [µm] | 7 |
| Density | [g/cm$^3$] | 1,77 |
| Elongation at break | [%] | 1,8 |
| Specific heat capacity | [J/kgK] | 710 |
| Thermal conductivity | [W/mK] | 10 |
| Coefficient of thermal expansion [ | [ $10^{-6}$/K] | -0,1 |
| Specific electrical resistance | [Ω cm] | 1,6 x $10^{-3}$ |

**Sizing properties for fiber family HTS**

HTS is a classic Tenax® high performance carbon fiber. The high tenacity (HT) fibers provide excellent mechanical laminate properties.

E23 = Type with ca. 1,3 % sizing based on epoxy resin
F13 = Type with ca. 1,0 % sizing based on polyurethane

Please contact our sales team any time for choosing the right type. The stated numbers are typical values. For design purposes please request fiber specification.

Please note the application (aerospace or industry & sports) on your order.

The export or transfer of carbon fibers can be subject to authorization, depending on end-use and final destination.

Toho Tenax
Toho Tenax America, Inc.

TEIJIN

# RECOMMENDED STORAGE AND SHELF LIFE

A HTS Carbon Fiber Properties

Filament tensile strength, modulus of elasticity, coefficient of expansion, electric and thermal conductivities and yield are inherent properties of the HTS fiber and have indefinite shelf life.

B. HTS Carbon Fiber Processing

Typically, the original processing characteristics of E13 (EP01) and F13 (F301) sized yarn will be essentially constant for at least one year from date of delivery. The product should be stored indoors. The recommended storage conditions are 40°F-77°F (5°C-25°C) and less than 50 percent RH. Direct exposure to sunlight or rain should be avoided. The shrink wrap should not be removed until immediately prior to use.

If the roving is stored at high temperatures and/or high humidity conditions, it may become difficult to process. Roving that stiffens during storage should still be useable. However, a thorough evaluation of the processing characteristics (e.g., resin wet out, spreadability) relative to the customer's operation is strongly recommended.

## STANDARD PACKAGING AND SPOOL BUILD

| Spool designation | "A" | | "B" | | "Z" | | "H" | |
|---|---|---|---|---|---|---|---|---|
| | Inch-Pound | Metric | Inch-Pound | Metric | Inch-Pound | Metric | Inch-Pound | Metric |
| Net Weight | 2.2 lb | (1 kg) | 4.41 lb | (2 kg) | < 2.2 lb | (< 1 kg) | 8.82 lb | (4 kg) |
| Tube Length | 11.0 in | (27.9 cm) | 11.0 in | (27.9 cm) | 11.0 in | (27.9 cm) | 11.0 in | (27.9 cm) |
| Tube I.D. | 3.0 in | (7.6 cm) | 3.0 in | (7.6 cm) | 3.0 in | (7.6 cm) | 3.0 in | (7.6 cm) |
| Tube weight | 6.0 oz | (170g) | 6.0 oz | (170g) | 6.0 oz | (170g) | 6.0 oz | (170g) |
| Stroke | 10.0 in | (25.4 cm) | 10.0 in | (25.4 cm) | 10.0 in | (25.4 cm) | 10.0 in | (25.4 cm) |
| Outside dia. (OD) | 4.75±0.2 in | (12.1±0.5 cm) | 5.0±0.25 in | (12.7±0.6 cm) | Varies | | 6.4±0.3 in | (16.3±0.8 cm) |
| **Pallet Type** | Carton | | Carton | | Carton | | Carton | |
| Nominal length | 5400 yd | (4938 m) | 5400 yd | (4938 m) | Non-metered | | 5400 yd | (4938 m) |
| No. spools per carton | 20 | | 12 | | Varies | | 6 | |
| Carton weight | 44.1 lb | 20 kg | 52.9 lb | 24 kg | Varies | | 52.9 lb | 24 kg |
| Carton dimensions (LxWxH) | 24.8 x 20.1 x 11.6 in | 63 x 51 x 29.5 cm | Same | | Same | | 21.7 x 14.6 x 11.6 in | 55 x 37 x 29 cm |
| Pallet dimensions (LxWxH) | 40.6 x 50.8 x 41.5 in | 103 x 129 x 105 cm | Same | | Same | | 44.9 x31.9 x 37.2 in | 114 x 81 x 94 cm |
| Approx. Pallet weight | 529 lb | 240 kg | 635 lb | 288 kg | Varies | | 635 lb | 288 kg |

**Notes:**

- "A" spool is standard for 3K, "B" spool for 6K and "H" spool for 12K/24K. "Z" spool is un-metered.
- 12-14 cartons per pallet. Height of pallet not included in dimensions. The pallet size may be changed without notice.

**FICHE TECHNIQUE** **TECHNICAL DATA**

# MARINE SYSTEM
# L-1911 (Temporary)
# CLEAR LAMINATING/INFUSION SYSTEM
# (Low viscosity, good flow, short working time)

**Description:**

The L-1911 is a two component, 100% solid epoxy system, designed as a laminating/infusion resin. This low viscosity, good flow, long working time system is an excellent wetting agent for different fabric types. It is convenient for VARTM (Vacuum Assisted Resin Transfer Molding) process in fabrication of larger pieces. Though it gels hard at room temperature, this system requires an appropriate post cure to obtain the maximum properties.

**Uses:**

**Laminating resin:**
May be used to laminate fiberglass, carbon fibers, Kevlar and other similar fabrics.

**Infusion:**
May be used as an infusion system where reduction of wasted resin and elimination of wet lay up procedure is desired.

**Typical uncured properties:**

| Components | Mixing Ratio | | Specific Gravity | Viscosity | Packaging | | | | Color |
|---|---|---|---|---|---|---|---|---|---|
| | By weight # Parts | By volume # Parts | | Brookfield @ 25° C mPa.s (cps) | Liters | | | | |
| Resin | 100 | 100 | 1.15 | 700 - 1000 | | | | | Clear |
| Hardener | 34 | 41 | 0.96 | 10 - 50 | | | | | Clear |
| Mix | | | 1.10 | 200 - 300 | 0,00 | 0,00 | 0,00 | 0 | Clear |

**Shelf life:** **12 months**

**Gel time:**

| Minutes | Temp. °C | Mass (gr.) |
|---|---|---|
| 50 - 60 | 22 | 150 |

**Cure schedule:**
After gelling at room temperature, the following post-cure schedule is recommended:

| Number of hours | Temperature $^0C$ |
|---|---|
| 8 | 80 |
| | |

# IMPORTANT :

Temperature limitations of the mold or model will dictate whether it can be used as the supporting structure during post-cure cycle. If the tool must be withdrawn from the model for the post-cure, a supporting frame must be provided.

**Typical cured properties (Approx.):**

After curing schedule:

| | ASTM | | |
|---|---|---|---|
| Tensile strength, psi (MPa): | D-638 | ~10000 | (~70) |
| Tensile Modulus, psi (GPa) | D-638 | ~400000 | (~3) |
| Compressive strength, psi (MPa): | D-695 | 11 514 | 79.4 |
| Flexural strength, psi (MPa): | D-790 | ~17000 | (~120.0) |
| Flexural Modulus, psi (GPa): | D-790 | ~400000 | (~3) |
| Hardness, Shore D: | D-2240 | 88-89 | |
| Elongation, %: | D-638 | `4-5 | |
| Tg, °C | D-3418 | ~80 | |

**Mixing:**

1. Mix L-1911 resin only with L-1911 hardener.
2. Do not use damaged or leaking containers.
3. Premix resin and hardener separately. Then place the hardener into the resin container according to the required mixing ratio.
4. Blend the hardener into the resin thoroughly using a paddle attached to a low speed heavy duty electric drill at 300-600 rpm. Continue to mix for a minimum of 3 minutes or until the mix becomes homogenous
5. Never dilute with solvents.

**Cleaning of tools:**

Tools and equipment should be cleaned immediately after use with #17 solvent or with ''Clean tool'' #4 for a safer use.

**Storage:**

Keep containers closed until just before use at a temperature above 15°C.

**Caution:**

Keep resin and hardener away from eyes and skin. Avoid breathing of vapors and use good ventilation. Like any reactive material, uncured resin and hardener may irritate sensitive skin. Wear protective clothing, goggles and gloves.

**FIRST AID:**

**Eyes:**

Flush immediately with plenty of water for 15 minutes and obtain medical aid.

**Skin:**

Clean skin with warm water and a soft soap. Never use solvents to remove material from skin.

**11/2006**

**NOTE:**

PRODUCT DATA

# Chemlease® 70-90

## Release Agent

### Description
Chemlease® 70-90 is a unique semi permanent mold release system developed specifically for the polyester molding industry. Chemlease® 70-90 is a high slip version of Chemlease® 70; primarily for closed molding of abrasive, low draft parts, where a quality finish is still required.

### Benefits
- Multiple releases between applications
- Provides excellent gloss
- Easy to apply
- High temperature stability 850°F-450°C
- Eliminates the use of wax
- Does not build up on the mold surface
- Reduces labor time and costs
- Minimal transfer to molded part

Chemlease ® solvent carriers contain no Class I or II registered ozone depleting substances

### Mold Preparation
1. Mold surfaces should be thoroughly cleaned to remove all traces of wax, release agents, sealers and buffing compounds.
2. Do a final cleaning of mold surface with Chemlease ® Mold Cleaner.
3. Seal mold with Chemlease ® 15 Sealer. (See Chemlease ® 15 Sealer Technical Data Sheet for details.)

### Application For Base Coats
1. Mold surface must be thoroughly cleaned to remove all traces of wax, release agents, and other sealers.
2. Surface should be dry and free of contaminants.
3. Saturate clean cotton cloth (not dripping) and wipe on a smooth continuous film. Apply no more than a few square feet at a time.
4. Wait 15-20 seconds. While film is still wet, wipe the surface with a second clean dry cotton cloth using a circular motion from the outside, working inwards until film is left dry and clear. See Notes below.
5. Repeat above procedures until entire mold surface has been covered.
6. Apply 4-5 coats, allowing 10 minutes between each complete coat.
7. Allow 20-30 minutes for full cure. Proceed with production.

Notes: Time will vary with room and mold temperature. Wipe off as the solvent begins to evaporate. If the release agent is left on too long, you may notice some smearing or streaking. To remove the smear or streak, rub the affected area with the recommended Chemlease® release agent, simply remove the excess sooner than you had before.

### Test To Ensure Proper Application
Attach a small strip of masking tape to different areas of the mold. There should be very little resistance when removing the tape if proper release is applied. Compare to an untreated mold. (Tape should adhere to untreated mold).

### Touch-Up Coats
Once in production the release film will begin to wear. Rather than applying a touch-up coat once the parts begin to stick, it is better to do preventative maintenance. For example, if trials determine that 20 releases are obtainable between touch-up coats, it is better to reapply a touch-up coat after every 15 cycles or at the end of every second shift if you are, for example, turning the molds 8 times per shift. The above-described action will keep the molds in production longer and help establish a routine of quality preventative maintenance.

### Coating Patch Reparis
Prior to repairing a patch, make sure the release is removed for 3-4 inches around the area to be repaired. Note: Semi permanent releases must be removed with mild abrasion as well as a solvent wipe. If not, the patch will not bond to the surface and break out. Once the patch is cured, treat the area as a new mold:
1. Clean with Chemlease® Mold Cleaner;
2. Apply Chemlease® 15 Sealer and cure per instructions;
3. Apply 5 coats of Chemlease® 70-90 release agent and cure.

Touch up the patched area with Chemlease® 70-90 every other cycle for the first 4-6 releases. Remember, the patch is weaker than the rest of the mold and will require extra attention for the first few cycles. Further, a touch-up coat (other than patch repair) should usually be done over the whole mold. This prevents having to re-touch another area that is wearing on the next cycle. However, there may be some areas of surface draft, etc. That may require a touch up more frequently. For example:
- Touch up complete mold every 16 cycles;
- Touch up small areas with difficult draft angles every 8 cycles.

The Chemlease® 70-90 is designed to blend into itself very easily and operator experience will quickly determine the number of cycles between spot and complete touch-up. For a spot touch-up, only the 10-minute room temperature cure time is needed. Whenever the mold is stripped, reapply Chemlease® 15 Sealer and/or the Chemlease® 70-90 base coats as described.

**Important**

The recommended number of coats and cure times are a general guideline found to be more than sufficient in a broad spectrum of molding conditions. When molding products with extreme geometries or experiencing low-humidity conditions in the shop, the customer may find the need to extend the cure time between coats and increase the number of coats applied to the mold. The efficiency of a release film is best determined through a combination of tape tests and experimentation.

### Packaging
Chemlease® materials are available in 1, 5, and 55 gallon containers. It is important that the materials be left in the factory containers as the product is susceptible to moisture contamination if the container is left open or the material is stored in the wrong type of container. The material should always be clear. If cloudiness is detected, please contact a Chemlease® Technical Representative.

### Safety Data
Material Safety Data Sheets are available for all Chemlease® products and should be consulted prior to use of the product

# Appendix B: Technical sheets of selected equipment

## FLIR i7

P/N: 39301-0305

| General description |
|---|
| Affordable infrared camera with 120x120 pixel FPA with high quality image, high accuracy, area max/min, isotherm (above/below), focus free viewing, and storage on miniSD card. |
| Key features: |
| • Extremely lightweight, 0.34 kg (0.75 lb.)<br>• 2% high accuracy and thermal sensitivity of 0.1°C<br>• Area (max/min), isotherm(above/below) or centerspot measurement<br>• Large 2.8 in. color LCD with quality images saved on miniSD card<br>• Long, 5 hour battery life<br>• Focus free lens for quick and convenient viewing |

| Imaging and optical data | |
|---|---|
| Field of view (FOV) | 25° × 25° |
| Minimum focus distance | 0.6 m (2 ft.) |
| Spatial resolution (IFOV) | 3.7 mrad |
| F-number | 1.5 |
| Thermal sensitivity/NETD | < 0.1°C (0.18°F) / 100 mK |
| Image frequency | 9 Hz |
| Focus | Focus free |

| Set-up | |
|---|---|
| Color palettes | Black and white, iron and rainbow |
| Set-up commands | Local adaptation of units, language, date and time formats |

| Storage of images | |
|---|---|
| Image storage type | miniSD card |
| File formats | Standard JPEG, 14-bit measurement data included |

| Data communication interfaces | |
|---|---|
| Interfaces | USB Mini-B: Data transfer to and from PC |

| Power system | |
|---|---|
| Battery type | Rechargeable Li Ion battery |
| Battery voltage | 3.6 V |
| Battery operating time | Approx. 5 hours at +25°C (+77°F) ambient temperature and typical use |
| Charging system | Battery is charged inside the camera. |
| Charging time | 3 h to 90% capacity |
| Power management | Automatic shut-down |
| AC operation | AC adapter, 90–260 VAC input, 5 VDC output to camera |

| Environmental data | |
|---|---|
| Operating temperature range | 0°C to +50°C (+32°F to +122°F) |
| Storage temperature range | –40°C to +70°C (–40°F to +158°F) |
| Humidity (operating and storage) | IEC 60068-2-30/24 h 95% relative humidity |
| EMC | • EN 61000-6-2:2005 (Immunity)<br>• EN 61000-6-3:2007 (Emission)<br>• FCC 47 CFR Part 15 Class B (Emission) |
| Encapsulation | Camera housing and lens: IP 43 (IEC 60529) |
| Bump | 25 g (IEC 60068-2-29) |
| Vibration | 2 g (IEC 60068-2-6) |

| Physical data | |
|---|---|
| Camera weight, incl. battery | 0.34 kg (0.75 lb.) |
| Camera size (L × W × H) | 223 × 79 × 83 mm (8.8 × 3.1 × 3.3 in.) |

| Detector data | |
|---|---|
| Detector type | Focal plane array (FPA), uncooled microbolometer |
| Spectral range | 7.5–13 µm |
| IR resolution | 120 × 120 pixels |

| Image presentation | |
|---|---|
| Display | 2.8 in. color LCD |
| Image adjustment | Automatic adjust/lock image |

| Measurement | |
|---|---|
| Object temperature range | –20°C to +250°C (–4°F to +482°F) |
| Accuracy | ±2°C (±3.6°F) or ±2% of reading, for ambient temperature 10°C to 35°C (+50°F to 95°F) |

| Measurement analysis | |
|---|---|
| Spotmeter | Center spot |
| Area | Box with max./min. |
| Isotherm | Above/below |
| Emissivity correction | Variable from 0.1 to 1.0 |
| Emissivity table | Emissivity table of predefined materials |
| Reflected apparent temperature correction | Automatic, based on input of reflected temperature |

| | |
|---|---|
| Material | Polycarbonate + acrylonitrile butadiene styrene (PC-ABS)<br>Thixomold magnesium<br>Thermoplastic elastomer (TPE) |
| Color | Blue and gray |

| Certifications | |
|---|---|
| Certification | UL, CSA, CE, PSE and CCC |

| Scope of delivery | |
|---|---|
| Packaging, type | Hard case |

- Hard transport case (including padlock)
- Infrared camera
- Battery (inside camera)
- Calibration certificate
- FLIR QuickReport CD
- Hand strap
- miniSD card (512 MB), with SD card adapter
- Power supply/charger with EU, UK, US and Australian plugs
- Printed Getting Started Guide
- Printed Important Information Guide
- USB cable
- User documentation CD-ROM

**Optional Accessories**

- 1910423 USB cable Std A <-> Mini-B
- T910711 Power supply/charger with EU, UK, US and AU plugs
- T126024 Pouch
- T197619 Hard transport case for ix
- T197410 Battery

# Standard Kapton & Rubber Heaters

In the following pages you'll find more than 400 standard foil heaters, suitable for prototype or production. Contact Minco for custom designs.

Each model is available with several resistance values. The wattage output at a particular resistance depends on voltage applied, per Ohm's law:

| R Ohms (Ω) | | | P Watts (W) | | | I Amps (A) | | | E Volts (V) | | |
|---|---|---|---|---|---|---|---|---|---|---|---|
| $\frac{E}{I}$ | $\frac{E^2}{P}$ | $\frac{P}{I^2}$ | $EI$ | $I^2R$ | $\frac{E^2}{R}$ | $\sqrt{\frac{P}{R}}$ | $\frac{P}{E}$ | $\frac{E}{R}$ | $\sqrt{PR}$ | $\frac{P}{I}$ | $IR$ |

## Type (configuration)

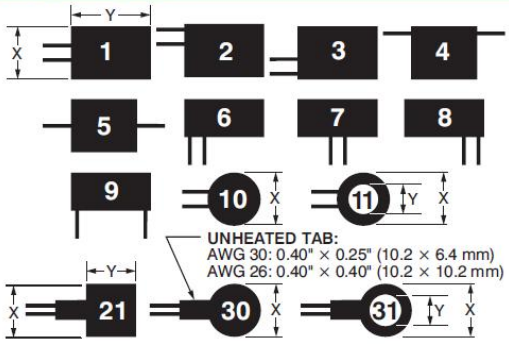


*Types 21, 30, and 31 have lead connections on an external tab. The tab produces negligible heat and, in most cases, need not be adhered to the heat sink.*

## How to order standard heaters

Specifications on pages B-1 (Kapton) and C-1 (rubber).

| | |
|---|---|
| HK | **Insulation:**<br>HK = Kapton<br>HR = Silicone rubber |
| 5200 | **Model number from tables on following pages** |
| R17.4 | **Heater resistance in ohms** |
| L12 | **Lead length in inches**<br>12" (305 mm) is standard<br>Contact Minco for other lengths |
| A | **Heater backing option (see page A-9)** |

| | HK | HR |
|---|---|---|
| A = No adhesive | -200 to 200°C | -45 to 235°C |
| B = PSA backing | -32 to 100°C | -45 to 177°C |
| D = Foil backing | -200 to 150°C | -45 to 235°C |
| E = Foil/Acrylic PSA | -32 to 150°C | -32 to 150°C |
| F = Foil/#12 PSA | -73 to 150°C | -45 to 204°C |

| | |
|---|---|
| U | **U = Marked for UL component recognition:** Ⓤ<br>Omit for no UL marking (lower cost)<br>UL limits: 220°C for rubber heaters |
| HK5200R17.4L12AU ← Sample part number | |

## Temperature sensitive elements

Heaterstats™ (page K-2) require temperature sensitive heating elements, such as those found in the "NiFe" and "Ni" columns. Their resistance increases with temperature. The resistances listed are measured at 0°C (32°F).

## How to use the table of Standard Kapton & Silicone Rubber Heaters

*Overall heater size in inches. Listed in ascending order, first by dimension X, then Y. Round heaters are last.*

*Heater type (lead exit configuration).*

*Element resistance options in ohms. Select resistance to produce desired wattage with available voltage (see Ohm's law)*

*Effective heating area. Use this value for calculating watt density.*

*Available heater insulation options for this model. K = Kapton R = rubber*

| Size (in) X | Size (in) Y | Size (mm) X | Size (mm) Y | Type | Resistance options in ohms* R(0°C) [May be used with Heaterstat] → | | | | NiFe | Ni | Effective area (in²) | Lead AWG | Insulation | Model number |
|---|---|---|---|---|---|---|---|---|---|---|---|---|---|---|
| 0.40 | 2.60 | 10.2 | 66.0 | 1 | 123 | 62.5 | 37.8 | 18.2 | | 19.1 | 0.74 | 30 | K | 5215 |
| 0.41 | 4.80 | 10.4 | 121.9 | 6 | 100 | 50.1 | 30.2 | 14.5 | | 15.5 | 1.40 | 26 | K, R | 5218 |
| 0.41 | 8.30 | 10.4 | 210.8 | | 61.9 | | | | 6.2 | | 2.50 | 26 | K, R | 5219 |

*Overall heater size in millimeters. Listed in ascending order, first by dimension X, then Y. Round heaters are last.*

*Temperature sensitive element resistance options (at 0°C) for use with Minco Heaterstat. Rubber (HR) models are not available with NiFe element.*

*Leadwire size. Maximum current capacities are listed on pages B-1 and C-1.*

*Base model number.*

*Resistance tolerance is ±10% or ±0.5 Ω, whichever is greater

Rubber (HR) models not available with NiFe element

# Kapton & Silicone Rubber Heaters

| Size (in) X | Size (in) Y | Size (mm) X | Size (mm) Y | Type | Resistance options in ohms* R(0°C) [May be used with Heaterstat] → | | | | | | NiFe | Ni | Effective area (in²) | Lead AWG | Insu-lation | Model number |
|---|---|---|---|---|---|---|---|---|---|---|---|---|---|---|---|---|
| 3.00 | 3.10 | 76.2 | 78.7 | 1 | 44.4 | 22.2 | 13.4 | 6.5 | 4.4 | | 6.9 | | 7.98 | 24 | K, R | 5465 |
| 3.00 | 4.00 | 76.2 | 101.6 | 1 | 62.1 | 30.9 | 19.4 | 8.6 | 5.7 | 4.1 | 9.6 | | 10.14 | 24 | K, R | 5466 |
| 3.00 | 4.00 | 76.2 | 101.6 | 7 | 35.1 | 17.1 | 10.8 | 4.6 | | | 5.4 | | 10.14 | 24 | K, R | 5488 |
| 3.00 | 5.00 | 76.2 | 127.0 | 1 | 176 | 88.2 | 49.4 | | | | 27.3 | 6.1 | 14.23 | 30 | K, R | 5175 |
| 3.00 | 5.00 | 76.2 | 127.0 | 1 | 77.7 | 38.7 | 24.2 | 10.3 | 7.1 | 5.1 | 12.0 | | 12.94 | 24 | K, R | 5467 |
| 3.00 | 5.00 | 76.2 | 127.0 | 7 | 36.1 | 19.5 | 12.6 | 5.9 | 3.7 | | 5.6 | | 12.94 | 24 | K, R | 5507 |
| 3.00 | 6.00 | 76.2 | 152.4 | 1 | 93.8 | 46.1 | 29.1 | 12.9 | 8.6 | 6.1 | 14.5 | | 15.74 | 24 | K, R | 5468 |
| 3.00 | 7.00 | 76.2 | 177.8 | 1 | 109 | 53.4 | 33.9 | 14.3 | 10.1 | 7.1 | 16.9 | | 18.54 | 24 | K, R | 5469 |
| 3.00 | 8.00 | 76.2 | 203.2 | 1 | 125 | 60.9 | 38.8 | 16.1 | 11.4 | 8.1 | 19.4 | | 21.34 | 24 | K, R | 5470 |
| 3.00 | 9.00 | 76.2 | 228.6 | 1 | 141 | 68.3 | 43.5 | 18.9 | 12.9 | 9.1 | 21.9 | | 24.14 | 24 | K, R | 5471 |
| 3.00 | 9.00 | 76.2 | 228.6 | 1 | 407 | 203 | 123 | 59.2 | 40.5 | 28.3 | 63.1 | 14.2 | 25.50 | 26 | K, R | 5472 |
| 3.00 | 10.00 | 76.2 | 254.0 | 1 | | 340 | 190 | 88.2 | 67.9 | 53.8 | 103 | 23.1 | 28.75 | 24 | K, R | 5176 |
| 3.00 | 10.00 | 76.2 | 254.0 | 1 | 156 | 75.8 | 48.3 | 20.3 | 14.9 | 10.2 | 24.2 | 5.4 | 26.94 | 24 | K, R | 5473 |
| 3.00 | 11.00 | 76.2 | 279.4 | 1 | 172 | 83.6 | 53.1 | 22.3 | 15.7 | 11.1 | 26.7 | 6.0 | 29.74 | 24 | K, R | 5474 |
| 3.00 | 12.00 | 76.2 | 304.8 | 1 | 188 | 91.1 | 57.7 | 23.9 | 16.7 | 12.1 | 29.1 | 6.5 | 32.54 | 24 | K, R | 5475 |
| 3.00 | 15.00 | 76.2 | 381.0 | 1 | | 226 | 126 | 58.8 | 45.3 | 35.9 | 68.2 | 15.3 | 43.30 | 24 | K, R | 5177 |
| 3.03 | 3.03 | 77.0 | 77.0 | 3 | 1317 | 658 | 350 | 175 | | | 204 | 46.8 | 8.34 | 30 | K | 5476 |
| 3.10 | 4.10 | 78.7 | 104.1 | 1 | 306 | 153 | 92.7 | 43.8 | 18.1 | 12.7 | 47.4 | 10.7 | 11.40 | 26 | K, R | 5477 |
| 3.10 | 6.10 | 78.7 | 154.9 | 1 | 88.6 | 44.4 | 26.9 | 12.9 | 8.8 | 6.2 | 13.7 | | 16.60 | 24 | K, R | 5478 |
| 3.10 | 7.10 | 78.7 | 180.3 | 3 | 104 | 52.3 | 31.6 | 15.2 | 10.4 | 7.3 | 16.1 | | 19.80 | 24 | K, R | 5479 |
| 3.10 | 9.10 | 78.7 | 231.1 | 1 | 1500 | 750 | 454 | 218 | | | 233 | 52.7 | 25.60 | 26 | K, R | 5480 |
| 3.10 | 12.10 | 78.7 | 307.3 | 1 | 445 | 222 | 135 | 63.9 | 44.3 | 31.1 | 69.0 | 15.5 | 33.90 | 24 | K, R | 5481 |
| 3.25 | 3.25 | 82.6 | 82.6 | 7 | 172 | 86.1 | 52.1 | 25.1 | 17.1 | 12.1 | 26.7 | 6.0 | 9.80 | 26 | K, R | 5482 |
| 3.50 | 7.35 | 88.9 | 186.7 | 1 | 252 | 126 | 76.3 | 36.7 | 25.1 | 17.6 | 39.1 | 8.8 | 23.30 | 24 | K, R | 5483 |
| 3.63 | 16.27 | 92.2 | 413.3 | 1 | 795 | 398 | 212 | 106 | 70.5 | 52.9 | 123 | 27.7 | 56.00 | 24 | R | 5484 |
| 3.75 | 4.75 | 95.3 | 120.7 | 6 | 72.5 | 36.3 | 21.9 | 10.5 | 7.2 | 5.1 | 11.2 | | 15.60 | 26 | K, R | 5485 |
| 3.80 | 8.60 | 96.5 | 218.4 | 1 | 243 | 121 | 73.6 | 35.4 | 24.2 | 16.9 | 37.7 | 8.4 | 29.80 | 24 | K, R | 5486 |
| 4.00 | 4.00 | 101.6 | 101.6 | 1 | 330 | 165 | 92.4 | 42.9 | | | 51.2 | 11.5 | 15.20 | 30 | K, R | 5178 |
| 4.00 | 4.00 | 101.6 | 101.6 | 1 | 46.5 | 23.3 | 14.3 | 6.1 | 4.9 | | 7.2 | | 13.94 | 24 | K, R | 5489 |
| 4.00 | 5.00 | 101.6 | 127.0 | 1 | 57.9 | 27.7 | 17.7 | 7.6 | 5.5 | 3.8 | 9.0 | | 17.74 | 24 | K, R | 5490 |
| 4.00 | 5.00 | 101.6 | 127.0 | 7 | 48.5 | 25.9 | 16.8 | 7.3 | 5.1 | 3.5 | 7.5 | | 17.74 | 24 | K, R | 5508 |
| 4.00 | 6.00 | 101.6 | 152.4 | 1 | 69.3 | 33.2 | 21.3 | 9.4 | 6.4 | 4.6 | 10.7 | | 21.54 | 24 | K, R | 5491 |
| 4.00 | 7.00 | 101.6 | 177.8 | 1 | 80.7 | 38.6 | 24.7 | 10.9 | 7.2 | 5.3 | 12.5 | | 25.34 | 24 | K, R | 5492 |
| 4.00 | 8.00 | 101.6 | 203.2 | 1 | | 318 | 178 | 82.7 | 63.7 | 50.4 | 96.0 | 21.6 | 30.84 | 24 | K, R | 5179 |
| 4.00 | 8.00 | 101.6 | 203.2 | 1 | 92.3 | 43.9 | 28.3 | 12.3 | 8.4 | 6.1 | 14.3 | | 29.14 | 24 | K, R | 5493 |
| 4.00 | 8.00 | 101.6 | 203.2 | 3 | 378 | 189 | 114 | 55.1 | 37.6 | 26.3 | 58.6 | 13.1 | 30.30 | 24 | K, R | 5494 |
| 4.00 | 9.00 | 101.6 | 228.6 | 1 | 103 | 49.5 | 31.7 | 13.4 | 9.3 | 6.8 | 16.0 | | 32.94 | 24 | K, R | 5495 |
| 4.00 | 10.00 | 101.6 | 254.0 | 1 | 114 | 55.1 | 35.3 | 14.8 | 10.8 | 7.6 | 17.7 | | 36.74 | 24 | K, R | 5496 |
| 4.00 | 11.00 | 101.6 | 279.4 | 1 | 126 | 60.6 | 38.8 | 16.2 | 11.7 | 8.3 | 19.5 | | 40.54 | 24 | K, R | 5497 |
| 4.00 | 12.00 | 101.6 | 304.8 | 1 | | 212 | 118 | 55.1 | 42.4 | 33.6 | 64.0 | 14.3 | 46.48 | 24 | K, R | 5180 |
| 4.00 | 12.00 | 101.6 | 304.8 | 1 | 137 | 66.1 | 42.1 | 17.6 | 12.2 | 9.1 | 21.2 | | 44.34 | 24 | K, R | 5498 |
| 4.00 | 15.50 | 101.6 | 393.7 | 2 | 445 | 223 | 135 | 64.8 | 44.3 | 31.1 | 69.0 | 15.4 | 58.70 | 24 | K, R | 5499 |
| 4.00 | 16.80 | 101.6 | 426.7 | 6 | 720 | 360 | 218 | 105 | 71.6 | 50.1 | 112 | 25.0 | 63.00 | 24 | R | 5500 |
| 4.00 | 20.00 | 101.6 | 508.0 | 1 | 851 | 426 | 257 | 120 | 84.6 | 59.3 | 132 | 29.6 | 74.50 | 24 | R | 5501 |
| 4.05 | 8.05 | 102.9 | 204.5 | 1 | 617 | 312 | 186 | 89.9 | 61.4 | 43.1 | 95.6 | 21.5 | 30.40 | 26 | K, R | 5502 |
| 4.05 | 9.05 | 102.9 | 229.9 | 1 | 1400 | 700 | 420 | 210 | 139 | 97.1 | 217 | 49.0 | 34.10 | 26 | K, R | 5503 |
| 4.05 | 11.90 | 102.9 | 302.3 | 8 | 290 | 145 | 87.8 | 42.2 | 28.9 | 20.2 | 45.0 | 10.1 | 45.00 | 24 | K, R | 5504 |
| 4.50 | 19.40 | 114.3 | 492.8 | 1 | 30.1 | 15.1 | 9.1 | 4.3 | | | | | 81.30 | 24 | R | 5505 |
| 5.00 | 5.00 | 127.0 | 127.0 | 1 | | 407 | 227 | 106 | 81.5 | 64.5 | 123 | 27.7 | 24.02 | 24 | K, R | 5181 |

*Resistance tolerance is ±10% or ±0.5 Ω, whichever is greater

Rubber (HR) models not available with NiFe element

Richmond Aerovac
umeco composites

**TECHNICAL DATA** 8/16/2010

# *FLASHTAPE 2R*

## High Temperature Pressure Sensitive Rubber Adhesive Polyester Tape

### DESCRIPTION:

**FLASHTAPE 2R** is a multipurpose .002" thick, green, polyester tape with a .0015" thick, high temperature rubber adhesive.

### APPLICATION:

**FLASHTAPE 2R** is designed for use in areas where a thicker, stronger flash tape is required. Like our **FLASHTAPE 1R**, it releases cleanly from most surfaces, with no residue. **FLASHTAPE 2R** cuts labor costs by allowing easier removal of excess resin and adhesive flash from metal and composite details.

---

| | | |
|---|---|---|
| **PHYSICAL PROPERTIES:** | | |
| Backing: | Polyester | |
| Color: | Green, translucent | |
| Adhesive: | High temperature rubber | |
| Thickness: | Film: .002" (.051mm) | Adhesive: .0015" (.038mm) |
| **MECHANICAL PROPERTIES:** | | |
| Tensile: | 43 lbs./in. width | 19 kg/25.4mm width |
| Adhesion to steel: | 25 oz./in. width | .70 kg/25.4mm width |
| Stretch at break: | 100 % | |
| **THERMAL PROPERTIES:** | | |
| Maximum use temperature: | 400°F | 204°C |

---

**Flashtape 2R** is available in standard roll sizes at:
1" and 2" x 72 yds. 25.4mm and 50.8mm x 65.8m

Other sizes may be available as special order.

# Appendix C: Load profiles applied on the hydraulic cylinder during epoxy injections for PMC plates N°1, N°2 and N°3

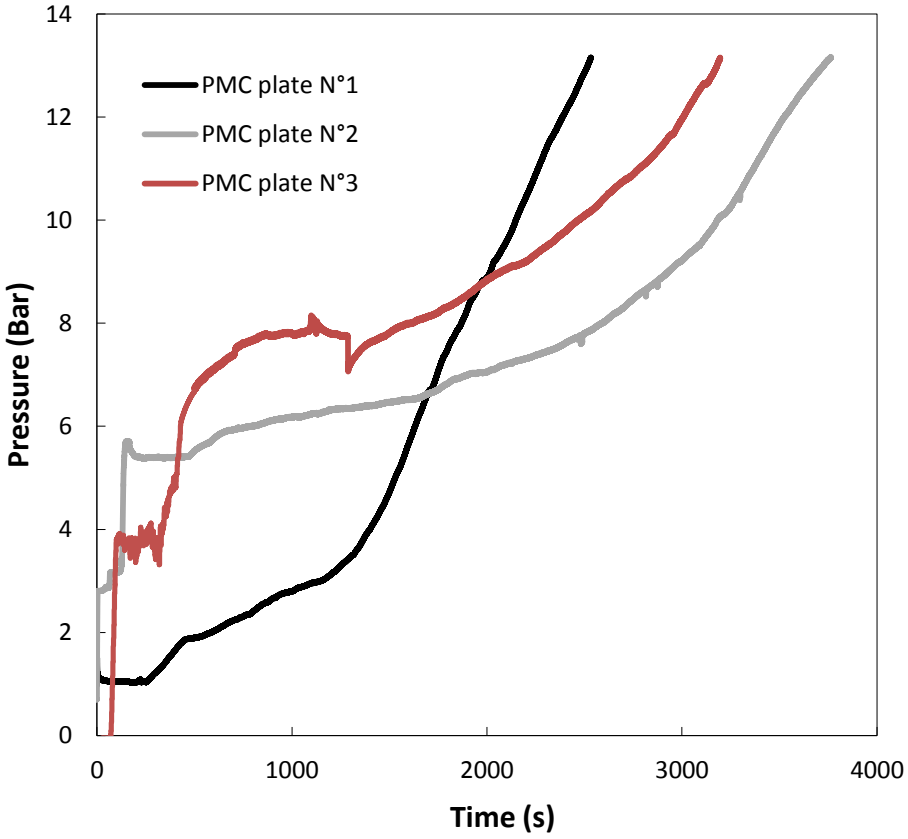

# Appendix D: Zone groups local coordinate systems

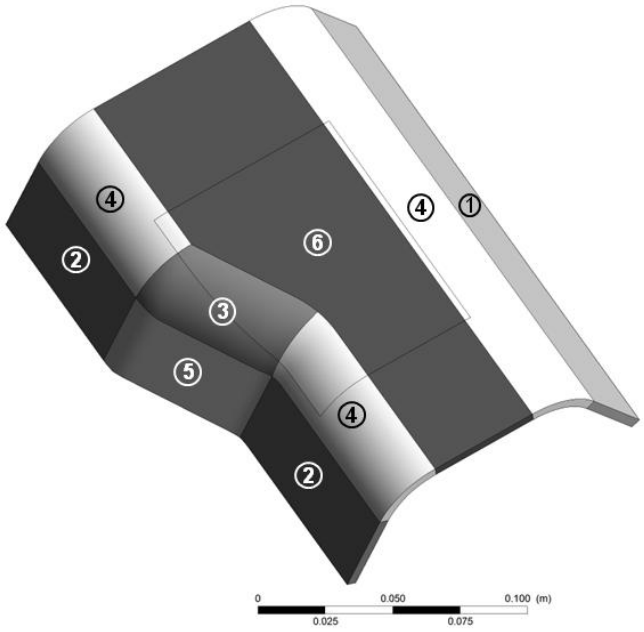


| Zone group | Type | Local coordinate system |
|---|---|---|
| 1 | Cartesian | $X_1$=(-0.5,0.866,0)<br>$X_2$=(-0.866,-0.5,0) |
| 2 | Cartesian | $X_1$=(0.5,0.866,0)<br>$X_2$=(-0.866,0.5,0) |
| 3 | Cylindrical | $X_3$=(-0.5,0,0.866) |
| 4 | Cylindrical | Global |
| 5 | Cartesian | $X_1$=(0.433,0.866,0.25)<br>$X_2$=(-0.75,0.5, -0.433) |
| 6 | Cartesian | Global |